



SAPIENZA
UNIVERSITÀ DI ROMA

Dottorato di ricerca in Scienze della Terra

Ciclo XXVI

Linking crystal chemistry and physical properties of
natural and synthetic spinels: an UV-VIS-NIR and
Raman study

Settore Scientifico Disciplinare GEO/06

Candidato

Veronica D'Ippolito

Docente guida:

Prof. Giovanni B. Andreozzi

Anni 2010-2013

“La mineralogia è una scienza di elite, ha pochi sbocchi professionali. Ma, come in tutte le cose della vita, se ci metti passione e determinazione, una strada vedrai che te la crei”

Prof. Sergio Lucchesi

“Success is getting what you want. Happiness is liking what you get.”

H. Jackson Brown

Index

| | |
|---|----|
| Introduction | 1 |
| | |
| Chapter 1- The Spinel Group | 5 |
| | |
| 1.1- Crystal chemistry..... | 5 |
| 1.2- Structure..... | 8 |
| 1.3- Relevance of spinels in the geological field..... | 16 |
| 1.4- Relevance of spinels in the gemological field | 19 |
| 1.5- Relevance of spinels in the technological field | 20 |
| | |
| Chapter 2- Spectroscopic methods | 22 |
| | |
| 2.1- Introduction to spectroscopy..... | 22 |
| 2.2- Raman spectroscopy..... | 25 |
| 2.2.1- Symmetry, Group theory, Normal Modes and Selection rules ... | 30 |
| 2.2.2- Applications..... | 33 |
| 2.2.3- Raman spectra of Spinel Group compounds..... | 36 |
| 2.2.4- Luminescence spectroscopy using Raman spectrometer..... | 40 |
| 2.3- Optical absorption spectroscopy..... | 42 |
| 2.3.1- Crystal Field Theory (CFT)..... | 45 |
| ➤ <i>One-electron systems</i> | 45 |
| ➤ <i>Crystal field splitting</i> | 47 |
| ➤ <i>Many-electron d^N systems</i> | 50 |
| ➤ <i>Tanabe-Sugano diagrams</i> | 50 |
| 2.3.2- Qualitative measurements in optical absorption spectra..... | 52 |
| ➤ <i>Causes of color</i> | 53 |
| 2.3.3- Quantitative analysis in optical absorption spectra..... | 56 |
| ➤ <i>Structural relaxation</i> | 57 |

| | |
|---|--------|
| Chapter 3- Materials and methods | 60 |
| 3.1- Materials..... | 60 |
| 3.2- Synthesis by Flux growth method..... | 68 |
| 3.2.1- Experimental conditions..... | 70 |
| 3.3- Single-Crystal X-Ray Diffraction..... | 75 |
| 3.4- Electron microprobe analysis..... | 78 |
| 3.5- X-ray mapping technique in SEM/EDS analysis..... | 79 |
| 3.6- Cation distribution procedure..... | 80 |
| 3.7- LA-ICP-MS instrument..... | 81 |
| 3.8- Raman spectroscopy instruments..... | 82 |
| 3.8.1- Polarized Raman spectra..... | 84 |
| 3.9- Optical absorption spectroscopy instrument..... | 86 |
| 3.9.1- Experimental conditions of synthetic spinels..... | 86 |
| 3.9.2- Experimental conditions of natural spinels..... | 87 |
| Chapter 4- Results and discussion | 89 |
| 4.1- Synthetic blue Co-spinels..... | 89 |
| 4.1.1- Synthesis and chemical characterization..... | 92 |
| 4.1.2- Structural and spectroscopic characterization..... | 100 |
| 4.2- Natural multicolor spinels..... | 113 |
| 4.2.1- Chemical characterization..... | 114 |
| 4.2.2- Spectroscopic characterization..... | 126 |
| ➤ <i>Fourier transform infrared spectroscopy</i> | 126 |
| ➤ <i>UV-VIS-NIR-MIR spectroscopy</i> | 132 |
| 4.3- Synthetic (Mg,Co,Fe)(Al,Cr) ₂ O ₄ spinels: Raman study..... | 153 |
| 4.3.1- The spinel s.s. (MgAl ₂ O ₄) end-member..... | 153 |
| 4.3.2- The MgAl ₂ O ₄ – CoAl ₂ O ₄ spinel series..... | 157 |
| 4.3.3- The MgAl ₂ O ₄ – FeAl ₂ O ₄ spinel series..... | 165 |
| 4.3.4- The MgAl ₂ O ₄ – MgCr ₂ O ₄ spinel series..... | 172 |
| 4.4- Raman spectra of natural spinels..... | 183 |
| 4.4.1- Comparison between natural and synthetic spinels..... | 188 |

| | |
|--|------------|
| 4.5- A multi-analytical study of a natural blue gahnite (ZnAl_2O_4)..... | 194 |
| 4.5.1- Chemical and structural characterization..... | 195 |
| 4.5.2 Spectroscopic characterization..... | 201 |
| Chapter 5- Conclusion and Implications..... | 206 |
| 5.1- Optical properties..... | 206 |
| 5.2- Vibrational properties..... | 208 |
| 5.3- Implications..... | 209 |
| Acknowledgments..... | 212 |
| References..... | 214 |

Introduction

The goal of the present work is the development of an empirical model of optical and vibrational properties of natural and synthetic spinels. Single crystals of natural and synthetic spinels have been studied in detail by a combination of complementary methods with the aim to explore their physical properties, which in turn have been interpreted on the basis of spinel crystal chemistry.

Multiple oxides with spinel structure represent minerals largely occurring in rocks as well as materials of high relevance from a technological point of view. To understand their physical properties the complete chemical, structural and crystal-chemical study is necessary.

This study can be inserted in a multidisciplinary context, shown schematically in the tetrahedron in Figure 1, where every vertex is closely correlated to another.

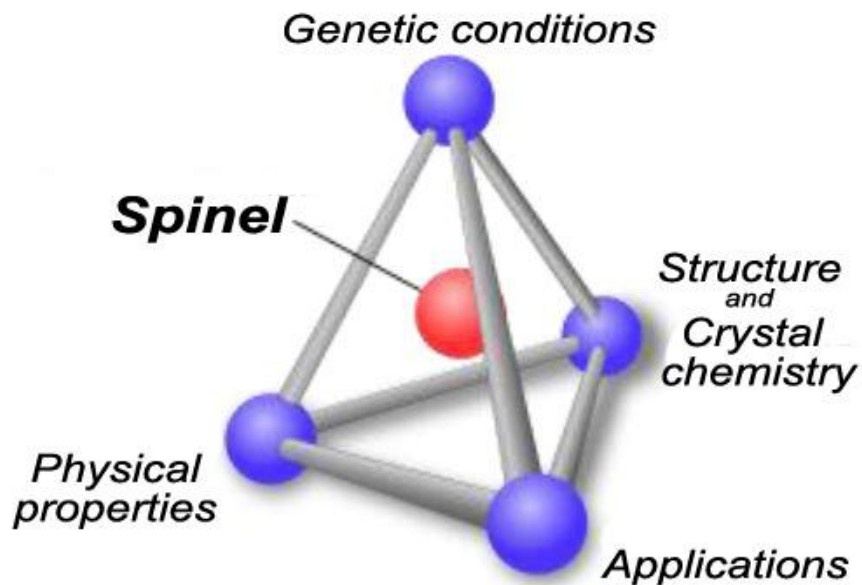


Fig. 1. Streamlined scheme of the multidisciplinary context in which the study of spinels is inserted.

Understanding the relationships among environmental conditions (P, T, etc.), crystal chemistry (e.g., cation distribution), cation distribution and physical properties can help to exploit the spinel potential, both in Earth Sciences and in Materials Sciences.

One of the characteristics of the spinel structure is the flexibility in the range of cations and cation charge combinations that can be accommodated, making it a structure adopted by over a hundred compounds, many of them either important minerals or important commercial materials.

On the Earth, many varieties of spinels occur as main or accessory minerals in different rocks, from the upper mantle to the crust, and their properties need to be understood in order to model the Earth interior. Being sensitive to temperature, pressure, oxygen fugacity, and bulk rock and fluid composition, intra- and inter-crystalline equilibria in spinel are extremely useful for constructing mineral geothermometers, geobarometers and oxygen fugacity sensors (Della Giusta et al., 1986; Ballhaus et al., 1991; Sack and Ghiorso, 1991; Princivalle et al., 1999; Lenaz and Princivalle, 2005).

Spinel oxides have been also discovered in extraterrestrial materials, as for example in Martian meteorites. The identification and compositions of the spinels on Mars provide information and constraints on conditions of rock genesis and alteration. In addition, they can provide evidence for magnetism on the “red planet” or can give information about oxygen fugacity and the possibility of life on Mars (Wang et al., 2004; Richter et al., 2009; Mayhew et al., 2013).

Gem-quality natural spinels are appreciated as attractive and brilliant gemstone all over the world for their color range and vivid tone. Indeed thanks to the ability of accepting different cations with different valence in the structure, spinels exhibit a wide range of compositions and then a wide range of color.

From a technological point of view, spinel oxides are suitable for a large variety of applications, from semi-conductors to catalysts, from refractory material to electrode for batteries, from magnetic devices to pigments for their electrical, mechanical, magnetic, thermochemical and optical properties (Shukla et al., 1999; Fernandez and de Pablo, 2002; Fierro et al., 2005; Gedam et al., 2009).

Among the large variety of useful physical properties shown by spinels, this study deals with the optical and vibrational properties, through a multi-methodological approach using Electron MicroProbe, Single-Crystal X-ray Diffraction, Optical

Absorption and Raman spectroscopies. In particular, this study investigates how the minerals of the spinel group absorb or scatter radiation in the visible and infrared part of the electromagnetic spectrum, and the relationships with crystal chemistry.

A large amount of natural spinels showing various colors and tone has been analyzed in the present work. Causes of color in minerals may be different, and Nassau (1987) provided a good overview of the various causes, most of them being related to transition metal ions, their valence and their coordination. However, more complex coloring mechanisms are difficult to characterize and often remain unexplained. To fully comprehend the origin of color in spinels, an accurate chemical and spectroscopic study has been performed using the optical absorption spectroscopy, which investigates the absorption of the ultraviolet, visible and infrared region of the electromagnetic spectrum (UV-VIS-NIR-MIR). It is concerned with transitions of electrons between outermost energy levels and can be used to identify the electronic transitions responsible for color and pleochroism in minerals. In addition this spectroscopy can provide information about the local structure around the chromophore ion such as the type of coordination, its symmetry and distortions, degree of covalency of bond distance and interactions with neighboring anions and cations.

A larger set of spinel single crystals, including synthetic samples, has been investigated through the Raman spectroscopy, which is a non-destructive technique used to interpret atomic vibrations, with the aim to establish the correlations between the spectra and compositions. Raman spectra consist in unique vibrational fingerprints useful in routine identification of a multitude of materials, without necessarily knowing the structural origin of the individual spectral peaks. Several catalogues of Raman spectra of standard compounds have been published already, and many spectra collections can be found on the internet, but a significant number of these spectra are incorrect. In particular, dealing with spinels the study of natural samples is rather difficult, due to the ubiquitous presence of minor elements and the rarity of compositions close to the end-members. Synthetic single crystals belonging

to solid solutions have been investigated in this study and the results have been used to interpret the spectra of natural samples.

The successful conclusion of the present study represents a marked increase of knowledge about the spinel system, and will have significant consequences in both Earth Sciences and Materials Sciences. In fact, the results of the present work extend the database of the Raman and optical spectra of spinels with different compositions, and the increased knowledge may be used:

- for geological purposes, to define a method to obtain the main composition of spinels directly from the Raman spectra;
- for gemological purposes, to clarify color mechanisms in spinels and to distinguish natural from thermally treated or synthetic spinels using the Raman and photoluminescence spectra;
- for technological purposes, to interpret the color and improve chromophore efficiency of spinel-based ceramic pigments.

Chapter 1

THE SPINEL GROUP

1.1. Crystal chemistry

Spinel minerals belong to a large group of composite oxides with a cubic symmetry (space group $Fd\bar{3}m$) and the general chemical formula of AB_2O_4 , where A and B are cations with variable valence. In natural spinels usually A represents divalent cation as Mg, Fe^{2+} , Zn, Mn^{2+} , while B represents trivalent cation as Al, Fe^{3+} , Cr, and V ($A^{2+}B^{3+}_2O_4$, so-called 2-3 spinels). Moreover, natural spinels may host also monovalent and tetravalent cations as Li, Ti^{4+} and Ge^{4+} , giving compositions like $A^{4+}B_2^{2+}O_4$ and $A^+B_5^{3+}O_8$. In addition, thanks to the flexibility of the spinel structure in the range of cations and cation charge combinations, more than 150 oxide spinels with alternative compositions have been synthesized in literature (Hill *et al.*, 1979). Following Palache et al. (1944) the classification of the naturally occurring members of the spinel group is based on the trivalent cation species (Al, Fe, Cr) and is shown in Table 1.1.

Tab. 1.1. Classification of the main spinel end-members based on the trivalent cation species.

| | Spinel <i>sensu stricto</i> series (AAI_2O_4) | Magnetite series ($AFe^{3+}_2O_4$) | Chromite series (ACr_2O_4) |
|-----------|--|---|-----------------------------------|
| Mg | Spinel | Magnesioferrite | Magnesiochromite |
| Fe^{2+} | Hercynite | Magnetite | Chromite |
| Zn | Gahnite | Franklinite | Zincochromite |
| Mn | Galaxite | Jacobsite | Manganochromite |
| Ni | | Trevorite | Nichromite |
| Co | | | Cochromite |

In addition to the end-members reported in Table 1.1, the spinels maghemite (γ - Fe_2O_3), ulvöspinel ($\text{TiFe}^{2+}_2\text{O}_4$) and qandilite (TiMg_2O_4) are also naturally occurring, the former having a cation deficiency ($(\frac{1}{3}\text{Fe}^{3+}_{2/3})\text{Fe}^{3+}_2\text{O}_4$), the latter's having the replacement $2\text{Fe}^{3+} \leftrightarrow (\text{Fe}^{2+}, \text{Mg}) + \text{Ti}^{4+}$. Furthermore, the V cation is often present in natural spinels as coulsonite, $\text{Fe}^{2+}(\text{V}^{3+})_2\text{O}_4$, magnesiocoulsonite, $\text{Mg}(\text{V}^{3+})_2\text{O}_4$, and vuorelainenite ($\text{Mn})(\text{V}^{3+})_2\text{O}_4$. In the spinel group the pure end-members are rare in nature; in fact these minerals exhibit a wide range of solid solutions, the crystal-chemistry and thermodynamics of which have been extensively studied (O'Neill and Navrotsky, 1984 and references therein). Results revealed that every considered join has a specific behavior and physical properties dependent on composition (e.g., Della Giusta et al., 1996; Redfern et al., 1999; Andreozzi and Lucchesi, 2002; Lenaz et al., 2004; Bosi et al., 2009; Lenaz and Skogby, 2013). The spinels may be subdivided on the basis of the dominant A^{2+} and B^{3+} ions, the varieties being designated by the next most dominant constituent. The ranges of composition of the main members of the spinel group are plot in the modified Johnston spinel prism (Fig. 1.1). The historical name picotite is conventionally used to describe Cr-bearing spinel and pleonaste for spinel containing some Fe^{2+} .

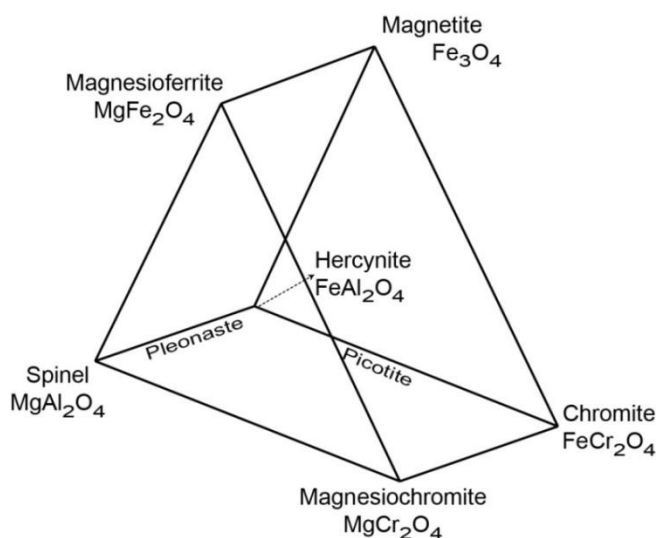


Fig. 1.1. Nomenclature and projection of different compositions in the Johnston spinel prism (after Haggerty, 1991).

The members of the spinel group are almost ubiquitous in most geological environments in the Earth's lower crust and upper mantle, as well in extraterrestrial and even interplanetary materials. In our planet, spinel-bearing mineral associations are frequent accessory minerals of both igneous intrusive and volcanic rock suites, regional and contact metamorphic rocks, and occur also as detrital grains in many sediments. Generally, $MgAl_2O_4$ -rich spinel is considered the characteristic mineral of the uppermost lherzolite facies of the mantle. Moreover, spinels in which chromium is a non-negligible constituent are nearly ubiquitous, accessory minerals in low-pressure, basic and ultramafic igneous and metamorphic rocks. The magnesium-rich silicate spinel (Mg_2SiO_4) is generally considered to be the dominant component of the lower part of the upper mantle.

Typically mineral spinels can be found in three geologic situations: 1) as crystals in limestones and dolomites that have been subjected to contact metamorphism; 2) irregularly-shaped grains in basic igneous rocks; and, 3) as water-worn pebbles in alluvial deposits.

Spinel is very resistant to chemical and physical weathering. It often occurs in marbles which are much less resistant to weathering. Spinel easily weathers out of the marble and is transported by streams. This places spinel in alluvial deposits which are often worked for gemstones. Most of the spinels are produced from alluvial deposits in Sri Lanka, Thailand, Cambodia, Vietnam, Myanmar. Other countries where spinel is mined include: Afghanistan, Nepal, Tajikistan, Australia, Madagascar, Nigeria, and Tanzania.

As extraterrestrial material, the spinels are important constituent of many lunar rocks and meteorites. Magnetite, titanomagnetite, spinel, chromite and ulvöspinel were found in many Martian meteorites (Taylor et al., 2002; Xirouchakis et al., 2002; Yu and Gee, 2005) and lunar meteorites (Arai et al., 1996; Gross and Treiman, 2011). A new mineral with post-spinel structure "xieite" has recently been approved by the Commission on New Minerals, Nomenclature and Classification of the International Mineralogical Association (Chen et al., 2008). It occurs in the Suizhou meteorite

which underwent a strong collision in space, and is a high pressure polymorph of chromite.

Studies of pre-solar grains in meteorites showed that Cr-bearing MgAl_2O_4 spinel is an abundant constituent of stardust (Gyngard et al., 2010). Besides, reflectance spectra of spinels indicate they may be present at the surface of some asteroids (Hiroi et al., 1994; Sunshine and Cloutis, 1999).

1.2. Structure

The spinel structure ($Fd\bar{3}m$) is made up an approximately cubic close-packed (CCP) array of O atoms with a unit cell containing eight formula units. The unit cell contains 32 anions, 64 tetrahedrally coordinated sites and 32 octahedrally coordinated sites, but A and B cations are distributed only in one-eighth of all tetrahedrally coordinated (T) and half of all octahedrally coordinated (M) sites to give the cell content of $\text{A}_8\text{B}_{16}\text{O}_{32}$. In the spinel structural framework, M sites share half of their polyhedral edges, M and T sites share polyhedral corners, and tetrahedra show no mutual ligands. Perpendicular to each triad axis, layers of O atoms alternate with layers containing the cations, which, in turn, are made of layers occupied only by edge-sharing octahedra (M) and layers with two isolated tetrahedral (T) occupied for every octahedra (Fig. 1.2).

With the origin of the unit cell taken at the center of symmetry ($\bar{3}m$), the cations are fixed at special positions 8a (T) and 16d (M) at $1/8, 1/8, 1/8$ and $1/2, 1/2, 1/2$ fractional coordinates, respectively. Single oxygen atom also occupies a special position, 32e, with $3m$ symmetry but with a variable fractional coordinate (u, u, u) . The oxygen parameter u is the distance of the nearest anion from the origin and can be used to define the distortion of the CCP array.

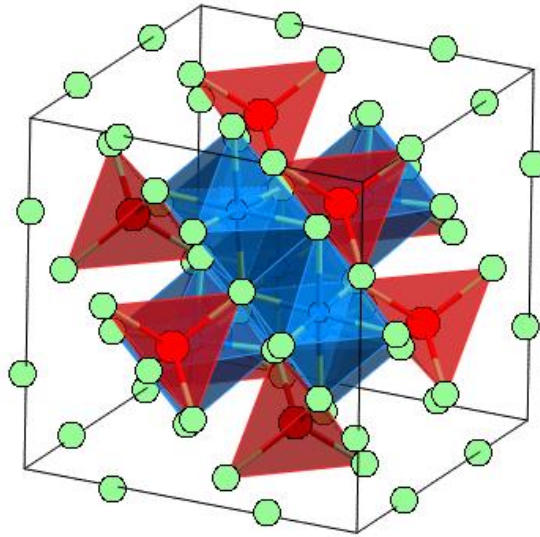


Fig. 1.2. Spinel structure, with cubic unit cell outlined in black, oxygen ions in green, tetrahedra and T sites in red and octahedra and M sites in blue color.

For the ideal close packed structure, $u = 0.25$, the anions form an exactly cubic close packed array, and define a regular tetrahedral coordination polyhedron about the 8a sites (point symmetry $\bar{4}3m$) and a regular octahedron about the 16d sites (point symmetry $\bar{3}m$). A distortion of the CCP arises when $u \neq 0.25$, with the range of parameters u spanning from 0.24 to 0.27. When u increases, oxygen moves along the [111] direction, so the octahedral site becomes smaller and the tetrahedral site larger until, at $u = 0.2625$ they are equal in size. As the positions of cations A and B are fixed, the oxygen array expands (or contracts) around them. In this way, the octahedron undergoes angular distortion and its symmetry degenerates to $\bar{3}m$ (trigonally distorted octahedra), whereas the tetrahedron remains regular (Bosi et al., 2007). The presence in T and M sites of transition elements with unpaired external electronic levels can cause large distortions in both sites, due to the Jahn-Teller effect (Fregola et al., 2012). In particular, cations with 3d_9 or 3d_4 orbitals such as Cu^{2+} and Mn^{3+} produce a reduction of octahedral site symmetry from $\bar{3}m$ to $4/m$ or lower. For example, in the cubic spinels, when $^M\text{Mn}^{3+}$ is present in low concentrations, the octahedra are deformed but don't produce macroscopic effects such as point

symmetry modifications, since this distortion occurs random along the equivalent [100] directions. When a critical Mn^{3+} concentration and critical temperature are reached, mutual interactions between second-coordination spheres become important and all octahedra are deformed along the same direction, as in hausmannite ($MnMn_2O_4$), lowering the symmetry to tetragonal $I4_1/amd$ (Bosi et al., 2002).

In the spinel structure, only two parameters may vary with chemical composition and/or physical conditions: the oxygen fractional coordinate u and the cell edge a . Many studies on different spinel samples highlighted that a is affected principally by the chemical composition of compounds, whereas u depends mainly on the cation distribution (Della Giusta et al., 1986; Princivalle et al., 1989; Lucchesi and Della Giusta, 1994). From the geometrical point of view, the unit-cell parameter is dependent only on the tetrahedral and octahedral bond distances, with the octahedral bonds exerting the greater influence, following the equation:

$$a = \frac{8}{11\sqrt{3}} \left[5(T-O) + \sqrt{33(M-O)^2 - 8(T-O)^2} \right] \quad (1)$$

The u parameter is geometrically related to the ratio of the bond distances, following the equation:

$$u = \frac{0.75R - 2 + \sqrt{\left(\frac{33}{16}\right)R - 0.5}}{6(R-1)} \quad (2)$$

where $R = (M-O)^2 / (T-O)^2$.

Every variation of u and a determines modifications of T-O and M-O bond distances, allowing for accommodation of various chemical components and/or cation ordering (Lavina et al., 2002). Similarly the octahedral and tetrahedral bond distances can be used to determine the two structural parameters, a and u .

$$T-O = a\sqrt{3}(u-1/8) \quad (3)$$

$$M-O = a\sqrt{3u^2 - 2u + 3/8} \quad (4)$$

Figure 1.3 shows relations that T-O and M-O distances have with a and u . Many studies on different spinel samples highlighted that a is affected principally by the chemical composition of compounds, whereas u depends on the cation distribution in the unit cell, connected with thermal history of spinel and with physic and chemical conditions of the geologic environment (Della Giusta et al., 1986; Lucchesi and Della Giusta, 1994).

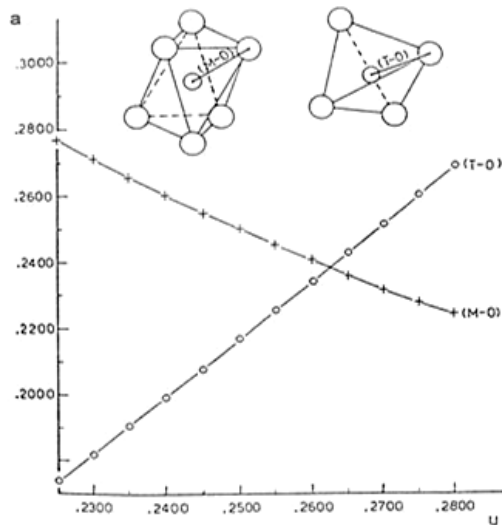
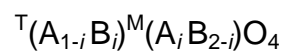


Fig. 1.3. Relationships between T-O and M-O distances, expressed as fractions of a , and u .

It is well known that u strongly depends on thermal history of spinel and on physical and chemical conditions of the geologic environment. Princivalle et al. (1989) observed that u displays a constant value within the spinels from individual geological settings, even if there is a variation in bulk chemistry, whereas spinels with similar bulk chemistry but belonging to different geological environments exhibit a wide range of u values. Furthermore, Della Giusta et al. (1996) and Redfern et al. (1999) observed that u must preserve geologic history. Thermal experiments employing natural Mg-Al-Fe²⁺-Fe³⁺ spinels showed that the most sensitive parameter during changes in temperature is the oxygen coordinate, with u in normal spinels decreasing significantly during heating and increasing during cooling.

In general, cations can reside on both types of sites, thus giving rise to a disordered cation distribution. If all A cations are in the T sites and all B cations are in the M sites, the spinel is called *normal spinel*. When half of the B cations occupy the T sites and the rest, together with the A cations occupy the M sites, the spinel is called *inverse spinel*. There are many examples of intermediate cases between normal and inverse spinel where a fraction of A and B cations are inverted and they are termed as *partially inverse spinels*. The cation distribution in spinels can be described by the general formula:



where i represents the so-called inversion parameter which can be defined as the fraction of B-type cations in the tetrahedral site and can vary from 0 to 1 from normal to inverse spinels, assuming the value of 2/3 for a completely random distribution (i.e. each single site displays the same occupancy: ${}^T(A_{1/3}B_{2/3}){}^M(A_{1/3}B_{2/3})_2O_4$), that is maximum disorder. However, the order-disorder of spinels is “non-convergent”, that is the same symmetry is maintained at any inversion, because it only involves a redistribution of cations over sites which are already differentiated. In this way i may be used as a measure for cation disordering since it asymptotically approaches the value of 2/3 at elevated temperature for every composition (Sack and Ghiorso, 1991; Redfern et al., 1999). The cation distribution of natural and, above all, synthetic

spinel has been extensively studied using different techniques and different experimental conditions (O'Neill and Navrotsky, 1983; Della Giusta et al., 1996; Lucchesi and Della Giusta, 1997; Princivalle et al. 1999; Andreozzi et al. 2000; Andreozzi and Lucchesi, 2002; Bosi et al., 2009).

The inversion parameter is affected by the temperature and thermal history, by chemical composition and by the cation site preference.

The dependence of cation distribution on the equilibration temperature has been estimated for several end-members of the spinel group with various techniques (Della Giusta et al., 1986; O'Neill and Dollase, 1994; Waerenborgh et al. 1994; Harrison et al., 1998; Redfern et al., 1999; Andreozzi et al., 2000; Carbonin et al., 2002; Uchida et al., 2005). Although the values of the inversion degree reported in the literature are sometimes very different, all studies agree that increasing the temperature, the cations may be disordered between T and M sites: the higher the temperature the higher the disordered state. In this way, the cation distribution of spinel reflects the thermal history of the host rock and can be used as geothermometer (see paragraph 1.3.).

The cation distribution is also greatly influenced by the chemical composition, which is by cation radii and charge. The relationship between inversion parameter and chemical composition has been studied in several spinel solid solution series. The trend of the inversion parameter in a spinel solid solution series is influenced by the difference of the substituting cation radii (Andreozzi et al., 2001a; Andreozzi and Lucchesi, 2002; Lenaz et al., 2004; Lenaz et al., 2006; Bosi et al., 2007; Bosi et al., 2009; Bosi et al., 2011; Fregola et al., 2011). Cation radii and charge effects have a tendency to counteract each other. In 2-3 spinels the B^{3+} cations generally possess small ionic radii and, thus, they may occupy the smaller tetrahedrally coordinated sites, involving the change of an inverse configuration. However, according to the Verwey–Heilmann principle of maximal charge neutralization, the charge is neutralized efficiently by numerous anions in the first coordination shell, thus cations of high valence (B^{3+}) may also occupy sites with higher coordination numbers (M

sites). This behavior is favorable to the normal configuration. It was shown that the effective radius of cation depends on the type of anions in the first coordination shell, and on the coordination number. Shannon and Prewitt (1969) were the first authors to examine the variations of ionic size in function of the coordination number and entered into a list of effective ionic radii (Tab. 1.2), improved later by O'Neill and Navrotsky (1983) and Lavina et al. (2002).

Table 1.2. Effective ionic radii in tetrahedral and octahedral sites reported in literature.

| | Shannon and Prewitt (1969) | O'Neill and Navrotsky (1983) | Lavina et al. (2002) |
|--|-------------------------------|---------------------------------|-------------------------|
| Cationic radii in the tetrahedral site | | | |
| Mg | 0.57 | 0.585 | 0.586 |
| Zn | 0.60 | 0.58 | 0.58 |
| Fe ²⁺ | 0.63 | 0.615 | 0.62 |
| Mn ²⁺ | 0.66 | 0.655 | 0.656 |
| Co ²⁺ | 0.58 | 0.58 | 0.592 |
| Ni | 0.55 | 0.565 | 0.56 |
| Al | 0.39 | 0.39 | 0.394 |
| Fe ³⁺ | 0.49 | 0.485 | 0.495 |
| Si | 0.26 | 0.275 | 0.247 |
| Cationic radii in the octahedral site | | | |
| Al | 0.535 | 0.53 | 0.528 |
| Cr | 0.615 | 0.615 | 0.615 |
| Fe ³⁺ | 0.645 | 0.645 | 0.645 |
| Mn ³⁺ | 0.645 | - | 0.65 |
| V | 0.64 | 0.645 | 0.642 |
| Ti | 0.605 | 0.60 | 0.582 |
| Mg | 0.72 | 0.715 | 0.702 |
| Zn | 0.74 | 0.73 | 0.75 |
| Fe ²⁺ | 0.78 | 0.74 | 0.77 |
| Mn ²⁺ | 0.83 | 0.8 | 0.811 |
| Co ²⁺ | 0.745 | 0.72 | 0.73 |
| Ni | 0.69 | 0.69 | 0.68 |

Another explanation for the observed behavior for which the smaller B^{3+} cation is found in the larger octahedra and larger A^{2+} cation in the smaller tetrahedra is represented by *octahedral site preference energy* (OSPE). The OSPE is the difference between the crystal field stabilization energy (CFSE) for the octahedral and tetrahedral coordination and is a measure of a cation preference for the octahedrally coordination relative to the tetrahedral one (Tab. 1.3).

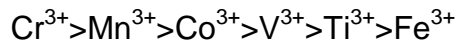
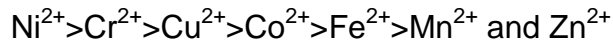
Table 1.3. Crystal Field Stabilization Energy (CFSE) in T and M sites and Octahedral Site Preference Energies (OSPE) for Transition Metals in Oxide Structures (Burns, 1993).

| Number of 3d electrons | Cations | Octahedral CFSE (kJ/mole) | Tetrahedral CFSE (kJ/mole) | OSPE (kJ/mole) |
|---------------------------|-----------------------------|---------------------------------|----------------------------------|-------------------|
| 0 | $Ca^{2+}, Sc^{3+}, Ti^{4+}$ | 0.0 | 0.0 | 0.0 |
| 1 | Ti^{3+} | -87.4 | -58.6 | -28.8 |
| 2 | V^{3+} | -160.2 | -106.7 | -53.5 |
| 3 | Cr^{3+} | -224.7 | -66.9 | -157.8 |
| 4 | Cr^{2+} | -100.4 | -29.3 | -71.1 |
| 4 | Mn^{3+} | -135.6 | -40.2 | -95.4 |
| 5 | Mn^{2+}, Fe^{3+} | 0.0 | 0.0 | 0.0 |
| 6 | Fe^{2+} | -49.8 | -33.1 | -16.7 |
| 6 | Co^{3+} | -188.3 | -108.8 | -79.5 |
| 7 | Co^{2+} | -92.9 | -61.9 | -31.0 |
| 8 | Ni^{2+} | -122.2 | -36.0 | -89.2 |
| 9 | Cu^{2+} | -90.4 | -26.8 | -63.7 |
| 10 | $Zn^{2+}, Ga^{3+}, Ge^{4+}$ | 0.0 | 0.0 | 0.0 |

As example, high-spin Cr^{3+} has one of the highest values for CFSE of any transition metal in octahedral coordination, which means that Cr^{3+} *really prefers* to be in octahedral coordination, thus Cr-spinels usually have normal configuration. Similarly, both Ni^{2+} and Cu^{2+} have relatively large values of OSPE, forming inverse spinel. Cations like Fe^{3+} and Mn^{2+} have zero OSPE, therefore, don't have preference for

either tetrahedral or octahedral coordination, and thus will form both normal and inverse spinels depending on the site preferences of the other coexisting cations.

It's possible to determine orders of preference of divalent and trivalent cations for the octahedral site:



This method is not always successful, and there are unsolved problems when d^0 , d^5 , and d^{10} ions are present because of lack of crystal field preference energy. For example, in the case of zinc spinels one could postulate an excess energetic stabilization for the zinc ion in the tetrahedral site, derived from its formation of sp^3 -type covalent bonds, which would explain why all 2-3 zinc spinels are normal.

The covalence character of a mineral is also influenced by the effect of the polarization. When large cation in the lattice, especially with a large charge, and a small anion with a large charge, are close to each other, the anion may attract part of the negative charge on the cation to itself, thus distorting the shape of the anion. This is called polarization, and indicates an increasing covalent character in the bond. In fact, greater charge and smaller size of the cation greater will be its polarizing power and the covalence nature of the bond length.

In conclusion, the cation order–disorder effects in spinels give rise to important consequences in their thermodynamics and properties. Therefore, the study of the local structure of these compounds is of primary importance (Šepelák et al., 2007).

1.3. Relevance of spinels in the geologic field

Within the spinel group there is a wide variety of compositions, each showing different properties and interest. As already seen, the cation distribution is a function of the closure temperature and the cooling rate of spinels in host rocks. During crystal cooling, divalent and trivalent cations progressively order at T and M sites, respectively. The temperature at which such an exchange stops is defined as closure

temperature (T_c) and depends on cooling rate. The closure temperature depends on the cooling rate of the host rock so that, for rapid cooling, the closure of intracrystalline exchange between T and M sites occurs at a higher temperature, whereas a slow cooling allows a strong ordering and low T_c (Princivalle et al. 1989; Della Giusta et al. 1996; Lucchesi and Della Giusta 1997; Lucchesi et al. 1998; Princivalle et al. 1999; Uchida et al., 2005).

Thermal experiments employing spinels of fixed chemistry showed that the most sensitive parameter during changes in temperature is the oxygen coordinate, u . As observed by Princivalle et al. (1989), spinels that underwent the same cooling history show rather constant u values in spite of their wide compositional ranges. On the other hand, in normal spinels u decreases significantly during heating and increases during cooling. In general, u less than or close to 0.2625 cooled more quickly than those with u higher than 0.2625. For example, chromian spinels from various suites of ultramafic rocks commonly show u values ranging from 0.2625 to 0.2631 (Della Giusta et al. 1986, Princivalle et al. 1989; Lenaz and Princivalle, 2005). Thanks to this temperature dependence, the spinels have been proposed as a potential geothermometer. Since olivine and spinel coexist in many igneous and metamorphic rocks such as peridotites, primitive basalts, and some type of meteorites, an Mg-Fe exchange geothermometer applicable to olivine-spinel assemblages was made (O'Neill and Wall, 1987; Ballhaus et al., 1991). An olivine-spinel thermometer was used also in ordinary chondrites by Votyakov et al., 1998.

While the geothermometer described by Princivalle et al. (1999) allows calculation of the closure temperature for magnesium spinels from their cation distribution. It is based on the temperature-dependent intracrystalline exchange reaction ${}^M\text{Al}+{}^T\text{Mg} = {}^T\text{Al}+{}^M\text{Mg}$. The closure temperature can be obtained by the equation:

$$T_c (\text{°C}) = 6640 * B$$

where $B = {}^T\text{Al}/\text{Al}_{\text{tot}} + 0.101(1 - {}^T\text{Mg} - {}^T\text{Al}) + 0.041(2 - {}^M\text{Al} - {}^M\text{Mg})$. The coefficients take into account the compositional influence of the other cations. The uncertainty associated with this geothermometer is ± 20 °C.

Given the influence of the chemical composition on the cation distribution, different regions have been delineated based on the composition of spinels according to their tectonic settings (Barnes and Roeder, 2001). Some minerals of the group, particularly chromites, can be used as “petrogenetic indicators” (Irvine, 1965, 1967; Sack and Ghiorso, 1991). This is due to the fact that chromites associated with mafic–ultramafic rocks are very sensitive to conditions present during the crystallization of these rocks; therefore, they provide information regarding the tectonic settings in which their host rocks were formed. An example of relations between environment of rock formation and spinel composition could be the spinel-based classification for ophiolites from Dick and Bullen (1984) based on the ratios $\text{Cr}/(\text{Cr}+\text{Al})$ and $\text{Mg}/(\text{Mg}+\text{Fe}^{2+})$. The Cr contents of homogeneous spinels could also provide a sensitive indicator of the degree of fractionation and of interactions between host liquids and wall rocks for the MORB-type basalts (e.g., Allan et al., 1988).

Chromites are also major collector of the platinum group elements (PGE) and Ni-Cu-PGE, which are of strategic importance due to their growing use in advanced technologies and the use of Pt, Pd, and/or Rh in automobile catalyst converters (Economou-Eliopoulos, 1996).

The quantity of V in spinel can be used as a sensor of oxygen fugacity of terrestrial rocks, meteorites and asteroid. For example in chromites studied via XANES spectroscopy by Rigther et al., 2009, V pre-edge peak intensity and energy vary with $f\text{O}_2$. The partitioning between spinel and olivine can be used as oxybarometer.

Furthermore, the spinels, especially iron-spinels, are responsible of the most magnetism in rocks. In nature the most important magnetic spinel phase is the solid solution between magnetite (Fe_3O_4) and ulvöspinel (Fe_2TiO_4). The occurrence of magnetite is particularly important for palaeomagnetic reconstructions of the drifting continents over geological time and to provide information on the timing and the magnitude of the Martian dynamo, studying Martian meteorites (Antretter et al., 2003; Yu and Gee, 2005). The thermodynamic properties of this system are again a function of magnetic ordering in the magnetite-rich compositions, which yields a

ferrimagnetic spin structure below the Curie temperature with magnetic moments on octahedral sites aligned antiparallel to those on tetrahedral sites (Néel, 1948).

Due to magnetic properties of the spinels, they are of great interest in geophysical research. Because spinels exhibit pressure-induced phase changes, they are often used as model minerals for deep-Earth mineralogy. The importance of the presence of spinel-type phases in the Earth's mantle has recently led to high-pressure experimental studies of phase transformations (Winell et al., 2006) and measurements of sound velocities and elastic constants (Yoneda, 1990; Pasternak et al., 1994; Reichmann and Jacobsen, 2004, 2006).

Recently a team of researchers from the University of Colorado (Department of Geological Sciences and Laboratory for Atmospheric and Space Physics) and the University of Alaska (Department of Chemistry and Biochemistry) hypothesizes that the spinels play an important role in the water-rock reaction producing hydrogen gas to sustain life in cool parts of the ocean's crust or on Mars (Mayhew et al., 2013). These authors propose that H₂ production is promoted by the transfer of electrons occurring at the surface of spinel mineral phases. Spinel phases that possess Fe(II) in their mineral structure may transfer electrons from those structural Fe(II) atoms to water (H₂O) or protons (H⁺) adsorbed to the mineral surface, producing H₂ gas. Spinel-bearing rocks, such as basalts are common on the surface of Mars and minerals diagnostic of the occurrence of water-rock reactions have also been detected on Mars' surface, so the spinels could play a role in supporting putative microbial habitats on other terrestrial planetary bodies.

1.4. Relevance of spinels in the gemological field

Natural spinels are actively sought as gemstones by gem collectors for their excellent hardness (8 on Mohs scale), high clarity, high refraction index and wide palette of attractive colors. In fact, thanks to and the ability of accepting different cations with different valence in the structure, spinels exhibit a wide range of compositions. Most gems spinels have compositions close to spinel s.s., including the so-called ruby

spinel, one of the best examples of which is the “Black Prince’s ruby” in the Imperial State Crown. Chemically pure spinel s.s. is colorless, but minor amounts of coloring elements (chromophores) such as Cr, Co, Mn, Fe, V and Cu are responsible for a broad spectrum of colors from pink to red, purple to violet, light blue to vivid blue, green to bluish grey. Most appreciated are red spinels, but also pink to purple and blue are amongst the favorite colors on the gemstone market. Synthetic spinel is often used to imitate a variety of other gemstones, like ruby and sapphire.

1.5. Relevance of spinels in the technological field

Spinel is significant not only for the Earth Sciences but they are also some of the most studied substances in the Solid State Science, thanks to their remarkable mechanical, thermal, electrical, magnetic, and physical properties. For these properties, synthetic spinel materials are suitable for large varieties of applications as:

- *Pigments.* Synthetic spinels are widely utilized by the ceramic industry as pigments for the coloration of ceramics, glazes, porcelain enamels, glass, paint, fibers, paper, cement, rubber, plastics, and cosmetics. In fact, spinel shows all the fundamental characteristics of a good ceramic pigment: thermal and chemical stability at high temperature, high chemical resistance (inert to the action of molten glass, frits or sintering aids), strong refractoriness (melting point $>1500^{\circ}\text{C}$) and high refractive indices ($>1,7$). The solid solutions $(\text{Mg,Fe})(\text{Al, Ti, Cr, Fe})_2\text{O}_4$ are the most essential to ceramic technology because of their colors and stability (Maslennikova, 2001). Furthermore, cobalt-zinc aluminate spinels CoAl_2O_4 and $(\text{Co,Zn})\text{Al}_2\text{O}_4$ are the only high-temperature blue pigments widely used in ceramic industry.

In addition, spinel crystal doped with Cr^{3+} ions ($\text{Cr:MgAl}_2\text{O}_4$) has been proposed as substitute of ruby crystal as the sensor probes of the fibre-optic thermometers, because of high melting temperature ($T = 2378 \text{ K}$), visible PL ($\lambda = 690 \text{ nm}$), and long PL lifetime (in ms order) (Aizawa et al. 2002).

- *Refractory material.* Spinel is a highly refractory material for its high melting point, excellent mechanical strength at ambient and elevated temperatures, superior corrosion, erosion, abrasion resistance and thermal spalling resistance. The major application areas of spinel refractory are burning and transition zones of cement rotary kilns, side-walls and the bottom of steel teeming ladles and checker work of glass tank furnace regenerators as it is resistant to corrosion by slag (Dal Maschio et al., 1988). Being an important refractory material it may also be used in advanced application like high-temp arc-enclosing envelops, humidity and infrared sensors, transparent windows, domes and armor material (Ghosh et al., 2004).
- *Semi-conductors.* Recently, the spinel oxides, for example ZnFe_2O_4 , Zn_2TiO_4 and NiFe_2O_4 , were widely used as gas sensor materials to detect, measure and control the atmospheric pollution, because of their stability in thermal and chemical atmosphere and the good sensitivity to a variety of different gases (Gedam et al., 2009).
- *Catalysts.* Among the transition metal oxides, chromium oxide has been known to be the most active component. MCr_2O_4 chromites with $\text{M} = \text{Cu}, \text{Co}, \text{Zn}, \text{Mg}, \text{Mn}$ are bifunctional catalysis, which accelerate both the oxidation of hydrocarbons and CO and the reduction of NO_x , with an activity sequence $\text{CuCr}_2\text{O}_4 > \text{MnCr}_2\text{O}_4 > \text{CoCr}_2\text{O}_4 > \text{MgCr}_2\text{O}_4 > \text{ZnCr}_2\text{O}_4$ (Pirogova et al., 2001). Also iron-cobalt-zinc manganites are efficient catalysts for the reduction of NO to N_2 by both propane and propene (Fierro et al., 2005).
- *Batteries.* The spinel phase LiMn_2O_4 is well known as alternative electrodes for rechargeable lithium batteries. The main advantages of the spinel lithium manganese oxide are the low cost of manganese (because of its abundance in nature), better cell safety performance, and low toxicity to environment. (Julien and Massot, 2006).

Chapter 2

SPECTROSCOPIC METHODS

2.1. Introduction to Spectroscopy

Spectroscopic methods are complementary techniques or sometimes even an alternative to the traditionally applied diffraction methods. The diffraction and chemical analysis are of great importance for a material characterization, but many problems are not amenable to such techniques and a spectroscopic characterization is required. Indeed, the X-ray diffraction analyses depend on the long-range periodicity of a crystal structure producing an average description. While the spectroscopic methods provide short-range information about the local structure around each cation, such as the coordination number, local chemical and crystallographic environment and site symmetry. One should regard these techniques as complementary, and use them in combination with structural and chemical analysis to the study of minerals.

Although there are many different spectroscopic techniques, they all are concerned on the same basic principle: the interaction between various types of radiation (mainly electromagnetic radiation) and matter. Because of quantum mechanical wave-particle duality, the electromagnetic radiation can either be described as a wave or a particle, a photon. As a wave, it is represented by velocity, wavelength (λ), frequency (ν) and a wave vector (\mathbf{k}). As a particle, it is represented as a photon, which transports energy. When a photon is absorbed, the electron can be moved up or down an energy level. When it moves up, it absorbs energy, when it moves down, energy is released. Thus, since each atom has its own distinct set of energy levels, each element emits and absorbs different frequencies. Four types of radiation-matter interaction can be defined (modified from Geiger, 2004):

- 1) There is no interaction between the incident radiation and matter. The radiation is transmitted with no change in its properties.

- 2) The interaction involves only a change in the wavevector, while the frequency of radiation remains the same. The incident radiation is scattered or diffracted elastically over a range of wavevectors.
- 3) The incident radiation causes some internal excitation or transition, which can be vibrational, electronic or nuclear. Thus, the radiation is selectively absorbed by the matter promoting particles to a higher energy level. These are the absorption spectroscopy. For example the IR and optical absorption spectroscopy involve vibrational and electronic excitations, respectively, from E_1 to E_0 , where $E_1 > E_0$.
- 4) The incident radiation couples with an internal process, a transition occurs and a following decay back to the ground state cause an emission of radiation having a different frequency. This process makes possible a wide range of methods including inelastic scattering (Raman spectroscopy), luminescence spectroscopy, etc.

Normally, only the last two categories are considered to constitute different spectroscopic processes.

The radiation of appropriate frequency provoked changes in the energy levels of the material from the *ground state* (i.e. at lowest energy state) to the *excited states* (i.e. at higher energy), and it is usually referred to as a transition. When the particle changes from one energy state to another, it must absorb or release the energy corresponding to the difference between the states, that is:

$$\Delta E = E_1 - E_0 = h \nu = hc/\lambda \quad (6)$$

where E is the energy in joules, h is Planck's constant (6.6×10^{-34} Js), c is the velocity of light (3×10^8 ms⁻¹), ν is the frequency (Hz or cycles/s) and λ is the wavelength (cms). E_1 is the energy of the excited state while E_0 is the energy of the ground state, then the molecules absorbs ΔE when it is excited from E_0 to E_1 and emits ΔE when it reverts from E_1 to E_0 .

The energy difference between ground and excited states cover the entire range of the electromagnetic spectrum from radiofrequency ($\sim 10^6$ Hz) to X-ray and γ -ray frequencies (up to $\sim 10^{20}$ Hz) (Putnis 1992).

Each energy levels is associated with a different phenomenon involving for example nuclear spin resonance, electron spin resonance, molecular rotations and vibrations, valence electron transitions, core electron transitions, and nuclear transitions (Fig. 2.1). Different regions of the electromagnetic spectrum provide different kinds of information. For example the visible range gives information about the electronic transitions involving the valence electrons, while the infra-red range brief about the molecular vibration, which involve stretching and bending of atomic bonds.

Thus, the different spectra can provide compositional information, local structural and crystal-chemical properties. Often in order to fully understand the physical and chemical properties of some material, it is necessary applies a number of different techniques in a complementary mode.

In this work, the emphasis will be on the molecular vibrations and the valency electron transitions in the IR, visible and ultraviolet regions of the spectrum, characterizing the spinels through the Raman and UV-VIS-NIR spectroscopy.

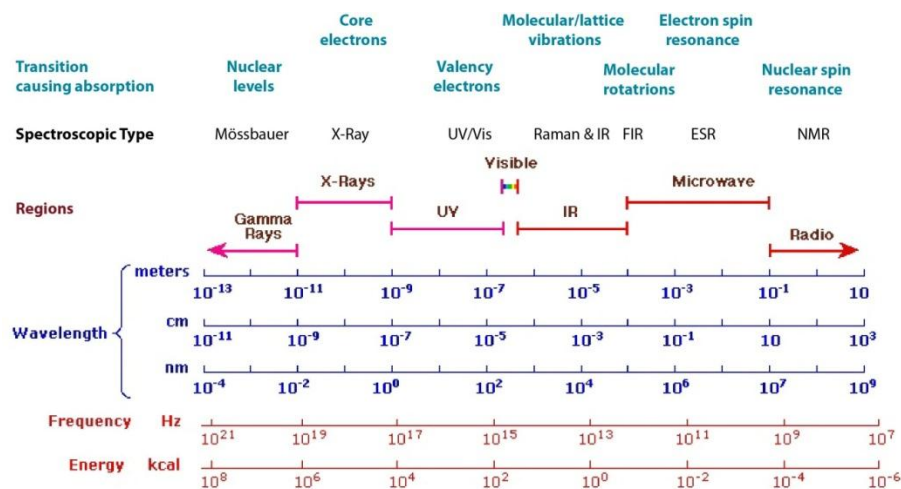


Fig. 2.1. The electromagnetic spectrum with the different regions. The various transitions causing the absorption with the corresponding spectroscopic type are shown (above). At the bottom, there are the wavelengths, frequencies and energy associated with each regions.

2.2 Raman Spectroscopy

The main spectroscopies employed to detect vibrations in molecules are based on the processes of infrared absorption and Raman scattering. They are widely used to provide information on chemical structures and physical forms, to identify substances from the characteristic spectral patterns ('fingerprinting'), and to determine quantitatively or semi-quantitatively the amount of a substance in a sample. Samples can be examined in a whole range of physical states; for example, as solids, liquids or vapors, in hot or cold states, in bulk, as microscopic particles, or as surface layers. Raman scattering is less widely used than infrared absorption, largely due to problems with sample degradation and fluorescence. However, recent advances in instrument technology have simplified the equipment and reduced the problems substantially. These advances, together with the ability of Raman spectroscopy to examine aqueous solutions, samples inside glass containers and samples without any preparation, have led to a rapid growth in the application of the technique (Smith and Dent, 2005).

Raman spectroscopy is a vibrational spectroscopy involving the use of light to probe the vibrational behavior of molecular systems and it is based on inelastic scattering, or Raman scattering, of monochromatic light, usually a laser in the visible. The Raman Effect occurs when light impinges upon a molecule and the oscillating electric field of the light polarizes (distorts) the electron cloud around the nuclei to form a short-lived state called a "virtual state" (Fig. 2.2). This unstable state is not necessarily a true quantum state of the molecule and the photon is quickly re-radiated. The photon excites the system to a virtual state before decaying to the ground state (Rayleigh) or an excited vibrational state (Raman). In detail, when a monochromatic beam of light of frequency ν_0 interacts with a molecule, most of the incident radiation is transmitted, refracted, reflected and scattered. Regarding the scattering, the most light is elastically scattered at the same frequency (ν_0) and wavelength as that of the incident beam. This process is called Rayleigh scattering and does not provide useful information. However a small fraction of the incident light

($\sim 10^{-5}$ – 10^{-8} of the incident beam intensity) can be inelastically scattered at different wavelengths and frequency ν_1 (and so different energy) as a result of the interaction between the incident beam and the vibrational modes of the molecule. This process is called Raman scattering and depend on the chemical structure of the sample. The Raman scattered light therefore loses or gains a small increment of energy which corresponds to the energy of the vibrational mode. The radiation that is scattered at lower frequencies than the incident beam ($\nu_0 - \nu_1$) is referred to as Stokes scattering while the light scattered at higher frequencies ($\nu_0 + \nu_1$) is referred to as anti-Stokes scattering.

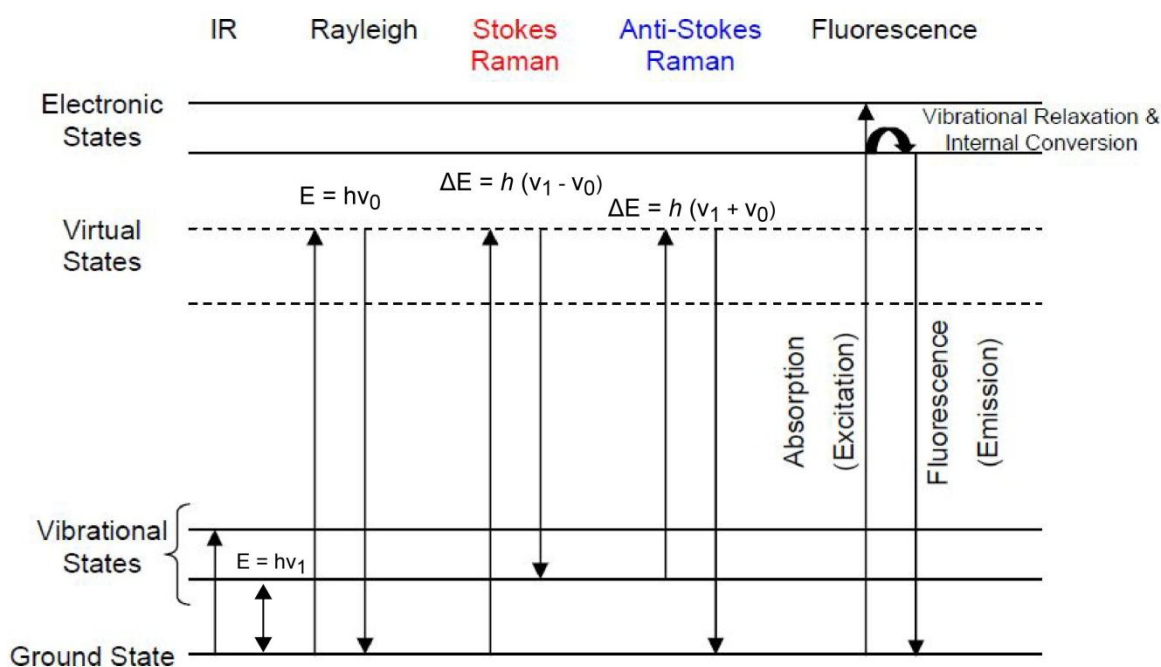


Fig. 2.2. Energy diagram showing the IR, Rayleigh, Raman scattering and fluorescence processes (modified from Smith and Dent, 2005).

Raman scattering is less intense than Rayleigh scattering and is directly proportional to the intensity of the incident beam and the concentration of the sample. According to the Maxwell-Boltzmann distribution law, the population of any excited level is always less than that of the ground state, therefore Stokes scattering is more intense

than anti-Stokes scattering provide similar information, normally only the Stokes side of the Raman spectrum is used to interpretation (Fig. 2.3).

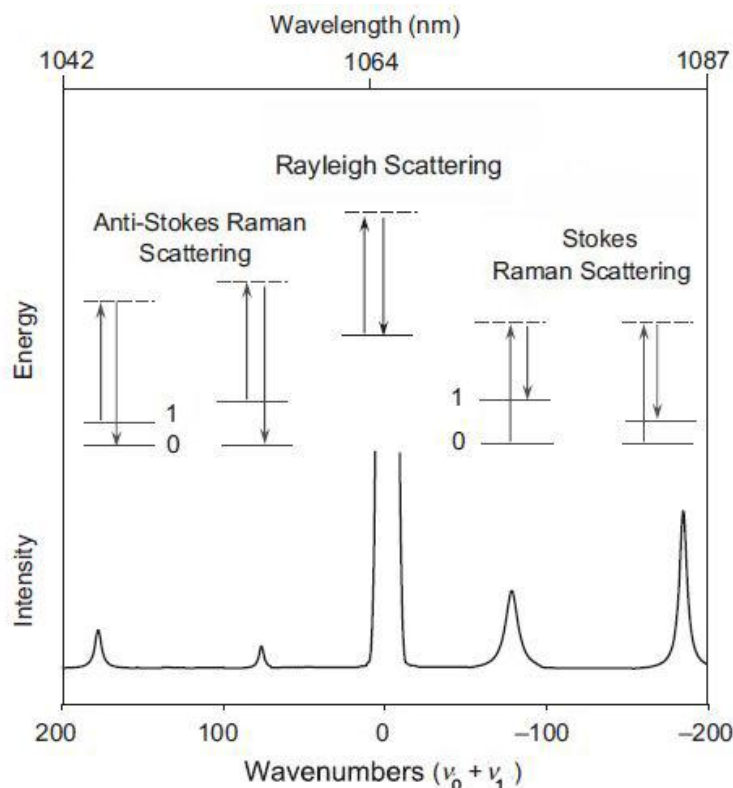


Fig. 2.3. Raman spectroscopy. Rayleigh, Anti-Stokes and Stokes scattering processes and the equivalent Raman bands.

A spectrum comprises one or more bands which reflect the vibrational energies of the molecules within the analyzed sample; these in turn are related to the nature of the bonding. The Raman spectrum can be plotted as light intensity (usually given in counts, counts per second or arbitrary units) versus photon energy, expressed in wavenumber ($\tilde{\nu}$). A wavenumber can easily be calculated from a known light frequency ν , using

$$\tilde{\nu} = \frac{1}{\lambda} = \frac{\nu}{c} \quad (7)$$

where ν is the frequency of the photon, and c is the speed of light in a vacuum, 2.998×10^{10} cm/s; the unit of the wavenumber is cm^{-1} . While wavenumbers are generally used in IR absorption spectra, in Raman spectroscopy, the use of absolute wavenumber would be impractical, because it must depend on the wavenumber of the incident light. A wavenumber shift relative to the wavenumber difference between the incident and scattered light can be plotted (Fig. 2.4). This is called Raman shift, $\tilde{\nu}$, can be calculated using the equation:

$$\tilde{\nu} = \frac{\Delta\nu}{c} = \frac{\nu_i - \nu_s}{c} \quad (8)$$

where ν_i and ν_s are the frequencies of the incident and scattered photons, respectively. So the Raman shift is the difference between the wavenumbers of the Raman-scattered photon and the Rayleigh-scattered photon. By convention, the Rayleigh line is set at 0 cm^{-1} and Stokes and anti-Stokes bands have positive and negative relative wavenumbers, respectively (Nasdala et al., 2004b).

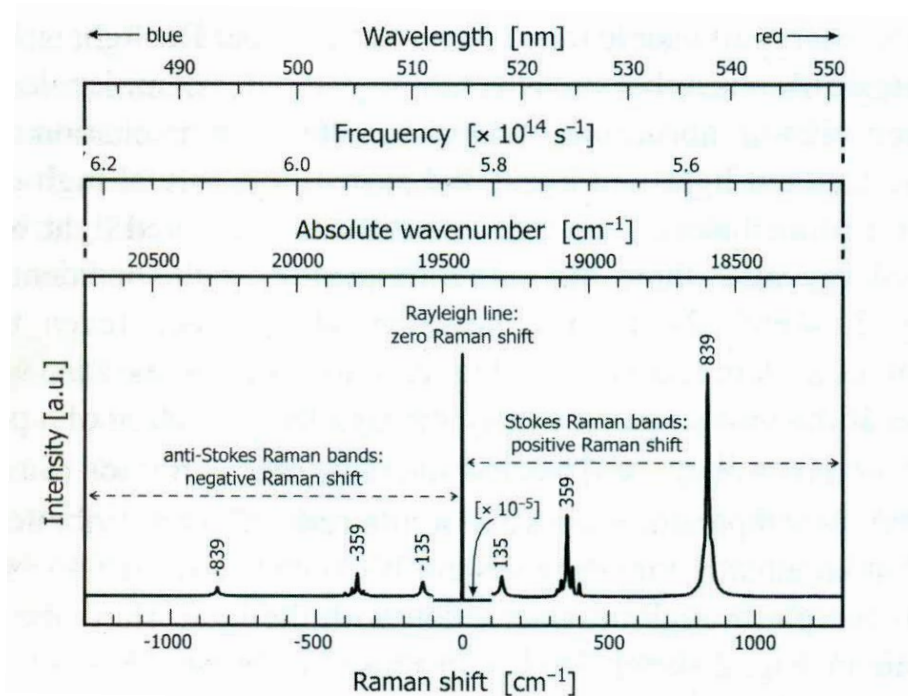


Fig. 2.4. Raman spectrum plotted in terms of Intensity (arbitrary unit) versus Raman shift. The x axis is given with three additional scales at the top to elucidate the relationship of the absolute and relative wavenumbers, frequencies and wavelengths (from Nasdala et al. 2004b).

Although different energy ranges are possible, the information of interest to most users is in the 4000-200 cm^{-1} , since this includes most modes which are characteristic of a molecule. On the other hand, most Raman spectrometers readily measure the spectrum down to 100 cm^{-1} , and often lower.

The intensity of bands in the Raman spectrum of a compound is governed by the change in *polarizability*, α , occurs during the vibration.

The deformation of the electron cloud induces an instantaneous dipole moment, μ , given by:

$$\mu = \alpha E_0 \cos(v_0 t) \quad (9)$$

in which α is the polarizability of the lattice and $E_0 \cos(v_0 t)$ describes the strength of the oscillating electric field at a given time (t) where E_0 is the amplitude and v_0 is the frequency of the radiation.

Electron clouds are three-dimensional entities, and an incident electric field can induce a dipole in directions perpendicular to the direction of polarization. Therefore, the Equation 9 must be a tensor to incorporate the x, y, and z directions. In matrix form, this equation can be written as:

$$\begin{pmatrix} \mu_x \\ \mu_y \\ \mu_z \end{pmatrix} = \begin{pmatrix} \alpha_{xx} & \alpha_{xy} & \alpha_{xz} \\ \alpha_{yx} & \alpha_{yy} & \alpha_{yz} \\ \alpha_{zx} & \alpha_{zy} & \alpha_{zz} \end{pmatrix} \begin{pmatrix} E_x \\ E_y \\ E_z \end{pmatrix} \quad (10)$$

where the 3x3 matrix is called the polarizability tensor.

Hence, Raman scattering will only occur when the molecular vibration produces a change in polarizability. If the polarizability does not change during a vibration, the vibration is not Raman-active.

This is the main difference to infrared (IR) absorption, where vibrations of light and vibrations of the sample have the same frequency and the interaction depends on the dipole moment μ .

The intensities of the bands in the Raman spectrum are also dependent on the nature of the vibration being studied and on instrumentation and sampling factors.

2.2.1 Symmetry, Group theory, Normal Modes and Selection rules

The complex vibrations of a molecule are the superposition of relatively simple vibrations called *normal modes* or *normal vibrations*. If a normal mode has an allowed IR transition, it says that it is IR active. Similarly if a normal mode has an allowed Raman transition, it says that it is Raman active.

The number of vibrations to be expected from a molecule with N atoms is $3N - 6$ for all molecules except linear systems where it is $3N - 5$. For simple mineral this equation can be used but when a mineral has a number of symmetry elements in its structure, it would have a huge number of degrees of vibrational freedom. In contrast, the number of observed vibrations is always limited. This is due to the periodic arrangement of atoms in the crystal lattice, which leads to a comparably small number of longitudinal and transversal lattice vibrations. So the vibration of a mineral lattice can be reduced to the corresponding primitive unit cell and its degrees of vibrational freedom. The number of vibrational modes in a highly symmetry crystal which may be observed in infrared and Raman spectroscopy is equal to $3n - 3$, where n is the number of atoms in the primitive unit cell.

The symmetries of the normal modes can be classified by group theory. Group theory provides a powerful mathematical tool for predicting the infrared and Raman activities of all vibrational modes of even complex molecules and crystals. A group is a set of elements and symmetry operations, which express certain spatial relations between different parts of the molecule.

Detailed explanation of Group theory is described by Rykhlin'skaya and Fritzsche (2004), but a few concepts need to be presented here as relevant terms will be used during the discussion of theory and data.

Symmetry operations are geometric transformations that leave a molecule indistinguishable from its original orientation. The symmetry of minerals can be described in terms of the following five symmetry elements:

- 1) The identity operator, E , leaves the structure unchanged;
- 2) The rotation operator, C_n , rotates the structure through an angle of $360^\circ/n$ about an axis, where n is an integer;
- 3) Vertical and horizontal mirror plane operators, σ_v and σ_h , reflect all atoms in the structure about a plane;
- 4) A center of inversion operator, i , reflects all points in the structure across a center of symmetry;
- 5) The rotation reflection operator, S_n , also known as an improper rotation, involves both a rotation and a reflection.

Any unit cell of a mineral contains some set of one or more of these symmetry elements. The symmetry operations can be represented by matrices. A set of matrices that describe the symmetry operations belonging to a point group is known as a representation. A representation will depend upon the choice of basis coordinates. To prevent confusion as to which representation is being used, irreducible representations are introduced. Any arbitrary representation can be described by a linear combination of these irreducible representations.

The symbols that refer to irreducible representations consist of a capital letters, and, in higher symmetry point groups where there is a center of symmetry, there would also be a g or a u subscript (for example, A_{1g} modes). The capital letter gives information on the degeneration (if two different vibrations have the same frequency, *i.e.*, they are equal in phonon energy, this is referred to one degenerate mode) and symmetry. There are four possible letters, A , B , E and F . A and B mean that the vibration is singly degenerate, with A modes being symmetric and B modes antisymmetric with respect to the main symmetry axis. E means it is doubly degenerate and F means it is triply degenerate. The subscripts g and u are used to

describe modes that are respectively symmetric ($g = \text{gerade}$) and antisymmetric ($u = \text{ungerade}$) with respect to the symmetry center (Nasdala et al., 2004b).

When two- and three-dimensional representations are present, instead of giving the full matrix form for the irreducible representation, it is more convenient to give only the character, which is the sum of the diagonal elements of a matrix. The number of irreducible representations belonging to a point group is equal to the number of symmetry classes of the point group. This allows the construction of a square character table, known as point group character table, which lists the characters of each symmetry class for every irreducible representation. The character table is the conventional way of tabulating symmetry information for molecular point groups. In the character table, as for example C_{2v} point group table in Fig. 2.5, the symmetry elements are shown across the top. The first column contains the irreducible representations and across the line from the symbols representing the irreducible representations, there are a series of numbers for each. The numbers are either 1 or -1 with the value of 1 usually for every symmetry element.

| C_{2v} | E | C_2 | $\sigma_v(xz)$ | $\sigma'_v(yz)$ | | |
|----------|-----|-------|----------------|-----------------|----------|-----------------|
| A_1 | 1 | 1 | 1 | 1 | z | x^2, y^2, z^2 |
| A_2 | 1 | 1 | -1 | -1 | R_z | xy |
| B_1 | 1 | -1 | 1 | -1 | x, R_y | xz |
| B_2 | 1 | -1 | -1 | 1 | y, R_x | yz |

Fig. 2.5. Character table of the C_{2v} point group.

The character table also contains information if a vibration is allowed or not. Not all fundamental vibrational transitions can be studied by both IR and Raman spectroscopy because they have different selection rules. Selection rules tell us if a transition is allowed or forbidden. An allowed transition has a high probability of occurring and will result in a strong band. Conversely a forbidden transition's probability is so low that the transition will not be observed.

Look at the character table for the point group of the molecule, the end column gives information on the allowed transitions. If the symmetry label of a normal mode corresponds to x , y , or z , then the fundamental transition for this normal mode will be IR active. If the symmetry label of a normal mode corresponds to products of x , y , or z (such as x^2 or yz) then the fundamental transition for this normal mode will be Raman active.

The basic selection rule is that Raman scattering arises from a change in polarizability in the molecule. This means that symmetric vibrations will give the most intense Raman scattering. This is in complete contrast to infrared absorption where a dipole change in the molecule gives intensity and, at a very simple level, this means asymmetric rather than symmetric vibrations will be intense.

One specific class of molecule provides an additional selection rule. In a centrosymmetric molecule, vibrations which are Raman active will not be infrared active, and vibrations which are infrared active will not be Raman active. This rule is known as the mutual exclusion rule. Only vibrations which are g in character can be Raman active and only vibrations which are u in character can be infrared active. This is because the g and u labels can be multiplied out and the final product must contain the totally symmetric representation and hence g . The rules are $g \times g = g$, $u \times u = g$ and $g \times u = u$. Since the Raman operators are g in character and the ground state is g , the excited state must be g if the vibration is to be allowed. In contrast, the infrared operator is u in character and so the excited state must be u if the vibration is to be allowed. In molecules without a centre of symmetry, there is no such specific rule.

2.2.2. Applications

Raman spectroscopy is a particularly attractive technique in many fields because is a non-destructive technique, suitable also for single crystals as small as a few hundred micrometers, no sample preparation is usually required, and Raman spectra are easy to obtain from solids, liquids, gases and from materials with low atomic weight elements. For these reasons, Raman spectroscopy is widely applied for routine

identification of materials, without necessarily knowing the structural origin of the individual spectral peaks.

In mineralogy, Raman spectroscopy is widely used as a fingerprint tool for the identification of minerals and related phases. In fact, recently Raman spectroscopy becomes established in the description of new species or their redefinition (e.g. Wallwork et al., 2002; Kolitsch, 2003). Tables and database of known band positions have been published for minerals (Frost et al., 1999, Table 2.1).

Table 2.1. Characteristic frequency regions for various anionic groups (from Frost et al., 1999).

| | | | | |
|-------------------|----------------------------|----------------------------|--------------------------|--------------------------|
| Sulphides | | | | <500 cm ⁻¹ |
| Hydroxides | 3000-4000 cm ⁻¹ | 600-1200 cm ⁻¹ | | |
| Oxides | | <1200 cm ⁻¹ | | |
| Carbonates | | 1300-1550 cm ⁻¹ | 800-890 cm ⁻¹ | 670-700 cm ⁻¹ |
| Nitrates | | ~ 1050 cm ⁻¹ | 800-850 cm ⁻¹ | 715-770 cm ⁻¹ |
| Borates | | 1250-1350 cm ⁻¹ | 600-900 cm ⁻¹ | |
| Sulphates | | 900-1250 cm ⁻¹ | | 570-680 cm ⁻¹ |
| Tungstates | | | 750-950 cm ⁻¹ | 250-450 cm ⁻¹ |
| Chromates | | | 800-950 cm ⁻¹ | 350-500 cm ⁻¹ |
| Molybdates | | | 750-950 cm ⁻¹ | 250-450 cm ⁻¹ |
| Phosphates | | 900-1150 cm ⁻¹ | | 400-600 cm ⁻¹ |
| Arsenates | | | 770-900 cm ⁻¹ | 350-400 cm ⁻¹ |
| Vanadates | | | 700-900 cm ⁻¹ | 300-400 cm ⁻¹ |
| Silicates | | 800-1200 cm ⁻¹ | | |

One advantage of Raman spectroscopy is that polymorphs with the same chemical composition can be easily distinguished (Etchepare et al., 1974; Rodgers, 1993)

Today, Raman can also be a semi-quantitative tool that not only identifies which species are present but also the amounts. Semi- quantitative chemical information on

the composition of a mineral belonging to a solid solution can be obtained through a relationship between concentration of a particular end-member and Raman shifts. This approach uses the Raman shift and not at all the intensities because the Raman shift is independent of a crystal orientation and hence of polarization effects and is a viable indicator of chemical composition (Nasdala et al., 2004b).

Furthermore, structural information can be obtained in the study of the variation of Raman spectra with order-disorder phenomena in minerals (Keramidas et al., 1975).

Thanks to the small size of the beam and the confocal optics, Raman spectroscopy can also use to characterize fluid and mineral inclusions in host minerals. Studying fluid inclusions, it's possible to identify their gaseous, liquid, supercritical and solid components and to estimate the origin and formation conditions of solid phases inside inclusions (Burke, 2001).

The study of inclusions find also geological applications in investigating both terrestrial (Kawakami et al., 2003) and extra-terrestrial (Popp et al., 2001) materials. Raman spectroscopy provides a powerful technique for identifying geological materials (minerals, glasses, melts and fluids) and for probing their behavior under extreme pressure and temperature conditions. Raman technique is commonly used to calculate the density of CO₂ fluids, the chemistry of aqueous fluids, and the molar proportions of gaseous mixtures present as inclusions. Raman spectroscopy has been applied to measure the *pH* range and oxidation state of fluids (Frezzotti et al., 2012). Recently, coupling vibrational spectroscopic techniques with studies in the diamond anvil cell (DAC) has permitted direct experimental investigation of minerals under extreme pressure and temperature conditions especially those of the Earth's upper and lower mantle or those produced during impact of asteroids on the Earth's surface. So Raman spectroscopy can be used to observe phase transitions and to model thermodynamic properties at both pressure and temperature of the Earth's and planetary interiors. The measurement of the thermodynamic properties of minerals stable at high pressures is not straightforward because of the minute amounts available and because they are highly metastable at ambient pressure and high

temperature (Gillet, 2006). For instance, the most abundant mineral stable in the Earth's lower mantle, (Mg,Fe)SiO₃ perovskite, transforms upon heating above 600 K (Durben and Wolf, 1992).

Recently, NASA and ESA currently consider Raman spectroscopy, either separately or in combination with laser induced breakdown spectroscopy (LIBS) or fluorescence, as a fundamental next generation instrument for the characterization of mineralogical and organic material during the exploration of Mars. During planetary surface exploration, a high priority is to identify and characterize surface materials, especially to do definitive mineralogy, in order to understand Mars evolutionary history. The ExoMars mission, a European mission to Mars scheduled to fly in 2018, will search for evidence of life. The spacecraft will carry an instrument to perform Raman spectroscopy on selected rock samples, to determine mineralogy and organic components. The knowledge of Mars through Raman spectroscopy also covers other aspects such as the study of potential terrestrial Martian analogues.

Because the sensitivity of the Raman analysis to short-range order, silicate glasses and melt have been studied to provide information about differentiation of Earth materials and on the formation of natural glasses.

In the field of gemology, both Raman and photoluminescence analyses has become extremely employed to verify the nature of the gemstones, to examine treatments, to detect synthetic and imitation stones and to explore solid and fluid inclusions. These features in turn sometimes identify the provenance of a stone. To identify inclusions, fillers, waxes and other treatments is very important because they have an impact on gem valuation.

2.2.3. Raman spectra of Spinel Group compounds

Looking the point group character table in Table 2.2 and according to the group theory, spinel group should exhibit the following normal modes:

$$A_{1g}(R) + E_g(R) + F_{1g} + 3F_{2g}(R) + 2A_{2u} + 2E_u + 5F_{1u}(IR) + 2F_{2u}.$$

The (R) and (IR) identify Raman- and infrared-active vibrational species, respectively.

Table 2.2. The character table of the O_h point group, to which the spinel system belongs.

| O_h | E | 8C₃ | 6C₂ | 6C₄ | 3C₂ | i | 6S₄ | 8S₆ | 3σ_h | 6σ_d | |
|-----------------------|----------|-----------------------|-----------------------|-----------------------|-----------------------|----------|-----------------------|-----------------------|-----------------------|-----------------------|---------------------------------|
| A_{1g} | 1 | 1 | 1 | 1 | 1 | 1 | 1 | 1 | 1 | 1 | $x^2+y^2+z^2$ |
| A_{2g} | 1 | 1 | -1 | -1 | 1 | 1 | -1 | 1 | 1 | -1 | |
| A_{1u} | 1 | 1 | 1 | 1 | 1 | -1 | -1 | -1 | -1 | -1 | |
| A_{2u} | 1 | 1 | -1 | -1 | 1 | -1 | 1 | -1 | -1 | 1 | |
| E_g | 2 | -1 | 0 | 0 | 2 | 2 | 0 | -1 | 2 | 0 | $(2z^2 - x^2 - y^2, x^2 - y^2)$ |
| E_u | 2 | -1 | 0 | 0 | 2 | -2 | 0 | 1 | -2 | 0 | |
| F_{1g} | 3 | 0 | -1 | 1 | -1 | 3 | 1 | 0 | -1 | -1 | (R_x, R_y, R_z) |
| F_{1u} | 3 | 0 | -1 | 1 | -1 | -3 | -1 | 0 | 1 | 1 | (x, y, z) |
| F_{2g} | 3 | 0 | 1 | -1 | -1 | 3 | -1 | 0 | -1 | 1 | (xz, yz, xy) |
| F_{2u} | 3 | 0 | 1 | -1 | -1 | -3 | 1 | 0 | 1 | -1 | |

Because the spinel structure is center symmetric, the active modes are mutually exclusive. Thus, the vibrational modes are either infrared- or Raman active. Spinel oxides have only five Raman active modes: $A_{1g} + E_g + 3F_{2g}$. A common notation exists in most of the literature to distinguish between the Raman modes belonging to the same representation, and will be used in the present work. The three Raman-active F_{2g} modes are labelled $F_{2g}(1)$, $F_{2g}(2)$, and $F_{2g}(3)$, where $F_{2g}(1)$ is the lowest Raman shift F_{2g} mode and $F_{2g}(3)$ is the highest Raman shift of this vibrational species.

The Raman spectra of minerals belonging to spinel group have been extensively studied in literature, Table 2.3 shows a summary of the Raman data from the literature.

Tab. 2.3. Raman data from the literature on AB₂O₄ spinels (modified from Hosterman, 2011). Shoulders of peaks are marked with *sh*.

| Spinel | F_{2g}(3) | E_g | F_{2g}(2) | F_{2g}(3) | A_{1g} |
|----------------------------------|--------------------------|----------------------|--------------------------|--------------------------|-----------------------|
| <i>Chromites</i> | | | | | |
| CdCr ₂ O ₄ | 134 | 343 | 499 | 600 | 647 |
| CoCr ₂ O ₄ | | 454 | | | 692 |
| CuCr ₂ O ₄ | 190 | | | 623 | 680 |
| FeCr ₂ O ₄ | | | | | 686 |
| MgCr ₂ O ₄ | 227 | 447 | 544 | 614 | 687 |
| MnCr ₂ O ₄ | | 457 | 511 | 600 | 685 |
| NiCr ₂ O ₄ | 181 | 425 | 511 | 580 | 686 |
| ZnCr ₂ O ₄ | 180 | 430,457 | 511 | 605 | 687 |
| <i>Ferrites</i> | | | | | |
| CoFe ₂ O ₄ | 210 | 312 | 470 | 576 | 624 <i>sh</i> , 695 |
| MgFe ₂ O ₄ | 217 | 333 | 486 | 554 | 646, 715 |
| Fe ₃ O ₄ | 193 | 306 | | 538 | 668 |
| NiFe ₂ O ₄ | | | 460 <i>sh</i> , 492 | 574 <i>sh</i> , 595 | 654 <i>sh</i> , 702 |
| ZnFe ₂ O ₄ | 221 | 246 | 355 | 451 | 647 |
| <i>Aluminates</i> | | | | | |
| CoAl ₂ O ₄ | 201 | | 516 | 615 | |
| MgAl ₂ O ₄ | 311 | 410 | 492 | 671 | 772 |
| ZnAl ₂ O ₄ | 197 | 417 | 509 | 658 | 758 |

Spinel oxides tend to exhibit Raman vibrational modes in the 100-800 cm⁻¹ spectral region. Generally, strong bands are observed around 400-500 cm⁻¹ and 700-800 cm⁻¹ region assigned to the E_g and A_{1g} modes, respectively. The bands around 600 cm⁻¹ are assigned to the third F_{2g} symmetry species, the bands around 480-520 cm⁻¹ are assigned to the second F_{2g} symmetry species, whereas, the bands around 200-300 cm⁻¹ are assigned to the first F_{2g} symmetry species.

In some spinels, more Raman modes have been observed than those predicted by group theory. It has been suggested that most of these extra features are related to cation disorder. For example, an extra mode has been observed at 727 cm^{-1} in synthetic and heat-treated natural spinels that are thought to be partially inverted. In addition, asymmetric broadening of the most intense mode at 410 cm^{-1} , E_g , has been related to cation disorder as it is observed only in synthetic or heat-treated natural spinel (Chopelas and Hofmeister, 1991; Cynn et al., 1992).

Many Raman studies of pure spinel oxides have appeared in the literature (Table 2.3), however, a systematic study of the changes of the line positions and their relative intensities into a solid solution is insufficient. The relationship between the vibrational modes and cation substitution is complicated, as the vibrational modes can be dependent upon the mass of the cations, the bonding forces, and the ionic radii. All these variables change with substitution of one cation with another (Hosterman, 2011). For example, Malavasi et al. (2002) examined the $\text{Mg}_{1-x}\text{Mn}_x\text{Mn}_2\text{O}_4$ spinel system and they support the A_{1g} mode is inversely proportional to the lattice parameter of the spinel, although the shift in wavenumber of the Raman-active mode is only approximately 1%. In addition to the information on the relationship between vibrational modes and structural parameters, such as unit-cell parameter, a detailed study of the change of the vibrational modes with the concentration of a particular end-member in a series could cause a semi-quantitative chemical analysis. For example Malézieux et al. (1983) examined the spinel–magnesiochromite series and obtained a variation of the Raman shift with the chemical composition close to linear.

Although there has been a large amount of experimental work on pure spinels, the literature is inconsistent with regard to the assignment of the specific atomic motions within the spinel lattice during the Raman-active vibrations.

For example, the important A_{1g} mode in literature has been assigned to:

1. The symmetric breathing mode of the AO_4 unit within the spinel lattice. The oxygen atoms move away from the tetrahedral cation along the direction of the

bonds. Neither the tetrahedral nor octahedral cations are in motion during this vibration (Cynn et al., 1992).

2. The symmetric breathing mode of the octahedral unit (Marinković Stanojević et al., 2007);
3. The random occupation of the octahedral sites by the A^{2+} and B^{3+} cations (Laguna-Bercero et al., 2007);
4. The stretching of AlO_4 tetrahedra (Barpanda et al., 2006).

Besides, there is little discussion of the role of the octahedral cations during the vibrations. Many researchers assume that all vibrational modes to motions involving solely the AO_4 unit with octahedral cations remaining at rest (O'Horo et al., 1973; Verble, 1974; Cynn et al., 1992). But every oxygen atom is bound to three octahedral cations and only a single tetrahedral cation, so even if the cations in M site remain at rest, the bonding force between octahedral cations and the oxygen atoms must be relevant for determining phonon energies. So some authors assign many vibrations to the octahedral cation, especially the high-frequency vibrations (Preudhomme and Tarte, 1971; Laguna-Bercero et al., 2007; Marinković Stanojević et al., 2007).

For the assignment of the vibrations in spinels important problems are that spectra are complicated by disordering of the cations and sample history and spinels can have a very large number of possible chemical compositions. Many researchers have worked to develop and use theoretical models by ab initio quantum chemical methods to calculate the vibrational modes of spinels (Johnson and Florián, 1995; de Wijs et al., 2002; Lazzeri and Thibaudau, 2006). Such calculations can provide crucial support in the assignment of vibrational modes as correct calculations could predict frequencies, intensities, and atomic motions of the vibrations of solid solution spinel systems.

2.2.4 Luminescence spectroscopy using Raman spectrometer

In the Raman spectra of minerals are observed additional spectral features not assigned to Raman modes but to luminescence features. The general term

luminescence describes the ability of minerals to emit light after being excited with different kind of energy. The ion responsible for a particular luminescence feature is called a luminescent center. The wavelengths of the lasers (514, 532, 780 and 785 nm) used to collect Raman spectra may excited multiple luminescence centers in various minerals.

When electromagnetic radiation (light) interacts with a luminescent material, an electron is excited to a higher energy state. When the electron drops back down to the ground state it releases light of a specific wavelength or range of wavelengths, called radioactive decay (Fig. 2.1). There exist several types of luminescence, which are usually subdivided according to the lifetime of the excited state and type of excitation. The first differentiation is between *fluorescence* and *phosphorescence* to emphasize the fast and slow response of a mineral to the excitation. Fluorescence describes the almost immediate emissive return of the excited electron to its ground state, whereas phosphorescence occurs with a larger delay. Regarding to the type of excitation, luminescence can be excited in minerals by radiation of many different wavelengths; luminescence induced by light sources in the UV-visible range is called *photoluminescence* (this is what we are observing in the Raman spectra of this study). Other means of exciting luminescence in minerals include excitation by a high-energy electron beam, called *cathodoluminescence*, excitation by corpuscular radiation, called *radioluminescence*, and excitation by heat, called *thermoluminescence*. Photoluminescence is an exceptionally sensitive technique because discrete energy levels of the sample can be excited separately with light of the respective wavelength, which makes it possible to distinguish among various luminescence centers (Nasdala et al., 2004a).

In contrast to the Raman effect, which is caused by inelastic scattering of the laser light by the crystal lattice, photoluminescence is caused by the absorption of the excitation laser light. By absorption of the laser light, electron, excited by the energy absorbed, jumps from a higher energy level to a lower one, emitting photons.

Generally, fluorescence prohibits the recording of a Raman spectrum, because if fluorescence is much more intense than Raman scattering, hiding Raman features, so usually Raman spectroscopist searches a method to avoid fluorescence emission, like change the laser wavelength to avoid electronic excitation. But photoluminescence (PL) spectroscopy obtained on a Raman spectrometer can have many practical applications, because it is sensitivity to the local environment around the luminescent center, providing information about short range order and trace element (REE and transition metal cation). In fact, PL analysis can give qualitative information, detecting trace element in extremely low concentrations. For example, the detection limit for Cr^{3+} can be as low as ppb level, or even better. To best characterize a material by PL spectroscopy it would be important to have a range of lasers of different wavelengths available because lasers of different wavelengths may excite completely different defects or trace elements. Considering the sensibility to the low-defect concentrations, PL spectroscopy is extremely used today in gemology to demonstrate defect distribution in a gem material, to separate among natural, treated and synthetic gems and to detect REE elements which are often tracers of genetic conditions.

2.3 Optical Absorption Spectroscopy

Optical spectroscopy is concerned with the qualitative and quantitative measurements of the absorption, reflection and emission of light in the spectral range from near-ultraviolet ($40\,000\text{ cm}^{-1}$) through visible ($26\,300\text{--}12\,800\text{ cm}^{-1}$) to near infrared (4000 cm^{-1}). Generally, studies of metal ion site occupancy, oxide states and concentrations are done on transparent minerals with the absorption spectroscopy in transmission mode. However, reflection measurements on samples totally absorbing the electromagnetic spectrum or on samples too thick for the transmission measurements are also possible.

When a monochromatic beam of intensity I_0 passes through a mineral, it leaves the sample with a smaller intensity I , because certain wavelengths are absorbed, often

leading to colored transmitted light. The amount of the radiation absorbed can be described by:

✓ Transmittance $T = I/I_0$ (11)

✓ Absorbance $A = \log (I/I_0) = \log (1/T) = -\log T$ (12)

Often, in optical absorption the amount of light absorbed is linearly related to the concentration of the absorbing species and to the thickness of the sample, according to the Beer-Lambert law:

$$A = \epsilon cd \quad (13)$$

Where ϵ is called molar absorption coefficient in units such as $\text{l mol}^{-1} \text{cm}^{-1}$ or $\text{cm}^2 \text{mol}^{-1}$, c is concentration expressed in mol l^{-1} and d is the thickness measured in cm. Molar absorption coefficient depends on the chemical species and the energy of radiation. Specific values of molar absorption coefficient for different chemical species at specific wavelengths of light can be found in chemical reference manuals.

Absorption spectra are obtained by passing light through a polished crystal slice which must be thin enough to transmit. An absorption spectrum shows the amount of radiation absorbed or transmitted at each energy. Energy units are often quoted in terms of wavelength, as well as wavenumber.

Five types of processes generally contribute to the absorption spectra of minerals:

1. Crystal field transitions: electronic transitions between unfilled d (or f) orbitals of transition metal such as Cr, V, Mn, Fe, Ni, Co and Cu. These transitions involve rearrangement of the valence electrons; an electron from one orbital is promoted to a higher energy orbital in the same atom. These transitions give rise to absorption in the ultraviolet, visible and near-infrared region ($40\,000 - 4000 \text{ cm}^{-1}$).

2. Charge transfer: electronic transitions which involve displacement of charge density from one ion of an atom to another of an adjacent atom. There are two ways in which this can occur
 - Ligand–metal and metal–ligand charge transfer (LMCT, MLCT): charge transfer between an anion and a cation. An example is the transfer of electron density from a filled oxygen p orbital to a partially occupied Fe^{3+} d orbital. These transitions occur in the ultraviolet region (mostly $> 30\,000\text{ cm}^{-1}$) with high probability and produce a very intense absorption, up to 10^3 to 10^4 times higher than those of crystal field transitions.
 - Intervalence charge transfer (IVCT) also called Metal–metal charge transfer (MMCT): electronic transfer involves movement of electron density between adjacent cations. The cations must have different oxidation states and, generally, they share edges or faces of coordination polyhedral. These transitions occur principally in the visible region ($24\,000\text{--}9000\text{ cm}^{-1}$) with intensities between 10^2 and 10^3 times stronger than transitions between $3d$ orbital energy levels.
3. Band gap transitions: electronic transitions between the top of a valence band and the bottom of the conduction band. Transitions between bands occur when the electrons in the valence band absorb light that provides a sufficient amount of energy for the electrons to jump over the band gap into the conduction band. These transitions occur principally in the visible region ($24\,000\text{--}4000\text{ cm}^{-1}$) and, usually, have less importance in minerals.
4. Color centers: electronic transitions between the states localized at electron or hole point defects giving rise to absorption in the visible spectral range ($25000\text{--}4000\text{ cm}^{-1}$).
5. Overtones of vibrational transitions. Overtones and combination modes of molecules or charged atomic groups. Vibrational overtones occur in the near-

infrared ($8000\text{--}4000\text{ cm}^{-1}$) and they are readily recognized because they have much smaller widths than electronic transitions which can occur in the same spectral region.

Most of these processes are responsible for the color of many minerals and synthetic compound. Crystal field $d\text{--}d$ transitions play a decisive role and will be discussed in detailed in the next paragraph.

2.3.1 Crystal Field Theory (CFT)

The crystal field theory is a model of chemical bonding applicable to transition metal and lanthanide ions, and it describes the origins and consequences of interactions of the surroundings on the orbital energy levels of a transition metal ion.

The description of the interaction of the d (or f) electrons of a transition ion with the crystal field generated by the surrounding ligands requires background knowledge of quantum mechanics (QM). A comprehensive and advanced essay of the crystal field theory can be found in Burns (1993), but basic ideas on QM indispensable for understanding some of the rule that govern electron systems are shortly given in the following subparagraph.

➤ ***One-electron systems***

The energy of the localized d or f electrons can be described by the time-independent one-electron Schrödinger equation:

$$\mathbf{H}\Psi = E\Psi \quad (14)$$

where \mathbf{H} is the so-called Hamiltonian, (i.e. the operator of the total energy of the system), and E is the total energy corresponding to the state (Ψ) under consideration. The position and energy of each electron surrounding the nucleus of an atom are described by a wave function, which represents a solution to the Schrodinger wave equation. In a spherical approximation and for a one-electron system the wave function for each electron in a spherical coordinate system (r, θ, φ), may be written as:

$$\Psi(r, \theta, \varphi) = R_n(r)Y_{lm_l}(\theta, \varphi)\chi_{m_s} \quad (15)$$

This equation comprises the radial function, $R(r)$, which depends only on the radial distance, r , of the electron from the nucleus, the angular functions Y which depends only on the angles θ and φ , and the spin function, χ , which is independent of the spatial coordinates r , θ and φ .

The various solutions describing the possible state of one-electron system are parameterized by the four *quantum numbers*:

1. The *principal quantum number*, n , describes the average distance of the electron from the nucleus and corresponds to the electron orbits or shell (e.g. K ($n = 1$); L ($n = 2$) M ($n = 3$) N ($n = 4$) etc.);
2. The *orbital quantum number*, l , reflects the shape of an orbital and have values between 0 and ($n-1$). Letter symbols are given to the orbitals according to the value of l : s ($l = 0$), p ($l = 1$), d ($l = 2$), f ($l = 3$) etc.
3. The *magnetic quantum number*, m_l , indicates how the orbital angular momentum is oriented relative to some fixed direction, particularly in a magnetic field. Its value can take all integral values from $+l$ to $-l$, or $(2l+1)$ values in all.
4. The *spin quantum number*, m_s , An electron then can have two kinds of spin, parallel or antiparallel orientation, characterized by the quantum numbers $m_s = +\frac{1}{2}$ and $m_s = -\frac{1}{2}$. Thus, each orbital can accommodate two electrons which spin in opposite directions.

Atomic orbitals represent the angular distribution of electron density about a nucleus. The shapes and energies of these amplitude probability functions are obtained as solutions to the Schrodinger wave equation. The s orbitals are spherical, the p orbitals are dumb-bell shaped and the d orbitals crossed dumb-bell shaped. Each orbital can accommodate two electrons spinning in opposite directions, so that the d orbitals may contain up to ten electrons (Burns, 1993). The d orbitals are divided into 5 orbitals d_{xy} , d_{yz} , d_{xz} , $d_{x^2-y^2}$ and d_{z^2} , and each orbital has four lobes in opposite quadrants (Fig. 2.6).

On the basis of their angular distribution, the 5 orbitals can be divided into 2 groups. Three of the orbitals, d_{xy} , d_{yz} and d_{xz} , have lobes projecting between the cartesian axes. This group is designated t_{2g} , where t refers to the three-fold degeneracy, whereas the subscript 2 indicates that the sign of the wave function does not change on rotation about the axes diagonal to the cartesian axes and the subscript g refers to the fact that the wavefunctions are symmetrical with respect to the octahedral center of inversion (*gerade*). The other two orbitals, $d_{x^2-y^2}$ and d_z^2 have lobes directed along the cartesian axes. They are termed e_g , where e stands for the two-fold degeneracy. The d_z^2 orbital appears to have a different shape from the other four, this difference is only apparent because the d_z^2 orbital is a linear combination of two orbitals, $d_z^2-x^2$ and $d_z^2-y^2$ having the same shape as the other d orbitals but which are not independent of them.

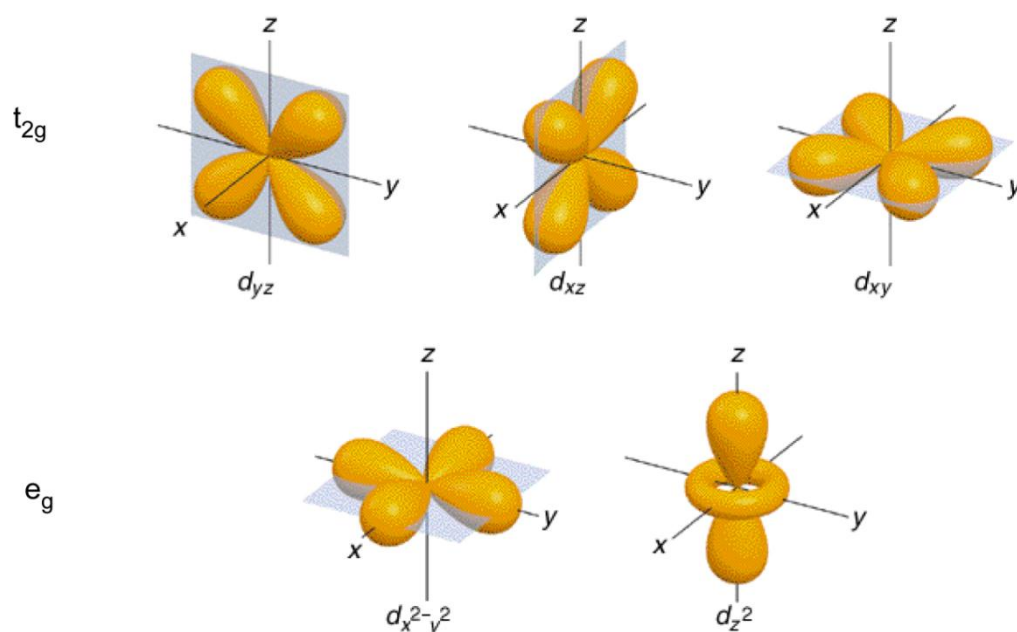


Fig. 2.6. The shapes of the d atomic orbitals, representing the regions which contain most of the electron density. The orbitals are divided into two groups, t_{2g} and e_g on the basis of their orientation relative to the x , y and z axes.

➤ **Crystal field splitting**

In a free transition metal ion, or an ion in a spherical field, all of the $3d$ electrons have an equal probability of being located in any one of the five d orbitals, since these

orbitals have the same energy. When such transition metal ion is in a crystal structure, however, the relative energies of the 3d orbitals are controlled by the different repulsive energies of the anions coordinated to it. The effect of a non-spherical electrostatic field on the five degenerate *d* orbitals is to lower the degeneracy by splitting the *d* orbitals into different energies about the center of gravity, or barycenter, of the unsplit energy levels. These energy splittings are described by the crystal field parameter Δ_i (or $10Dq$) where the subscript *i* refers to the polyhedral type (*i*: c = cube; t = tetrahedron; o = octahedron). The CF splitting depends on the symmetry and geometry of the coordination polyhedron as well as on the type of the central transition metal ion and of the ligands surrounding the transition metal. Generally, electrons in orbitals which point towards the anions are repelled to a greater extent and their energy is raised relative to orbitals which project between the anions. For example, in a regular octahedral coordination, since the lobes of the electron distribution of the two e_g orbitals point towards the anions, electrons in these two orbitals are repelled to a greater extent than are those in the three t_{2g} orbitals that lie between the ligands (Fig. 2.7). The three t_{2g} orbitals are lowered by $0.4\Delta_o$ below, and the two e_g orbitals raised by $0.6\Delta_o$ above, the barycenter. The value of Δ_o or $10 Dq$ is obtained directly, or may be estimated, from spectral measurements of transition metal-bearing phases in the visible to near-infrared region.

In a tetrahedral coordination, the crystal field of the *d*-orbitals again splits into two groups (Fig. 2.7). But since d_{xy} , d_{yz} and d_{xz} orbitals point towards the edges of the cube and the $d_{x^2-y^2}$ and d_z^2 orbitals towards the cube faces, the CF splitting is inverted as compared to the octahedral case. The tetrahedron don't have a center of symmetry, therefore the *g* indices are omitted from the representations (t_2 and *e*).

Furthermore, since the ligand electrons in tetrahedral symmetry are not oriented directly towards the *d*-orbitals, the energy splitting will be lower than in the octahedral case ($\Delta_t = - 4/9 \Delta_o$).

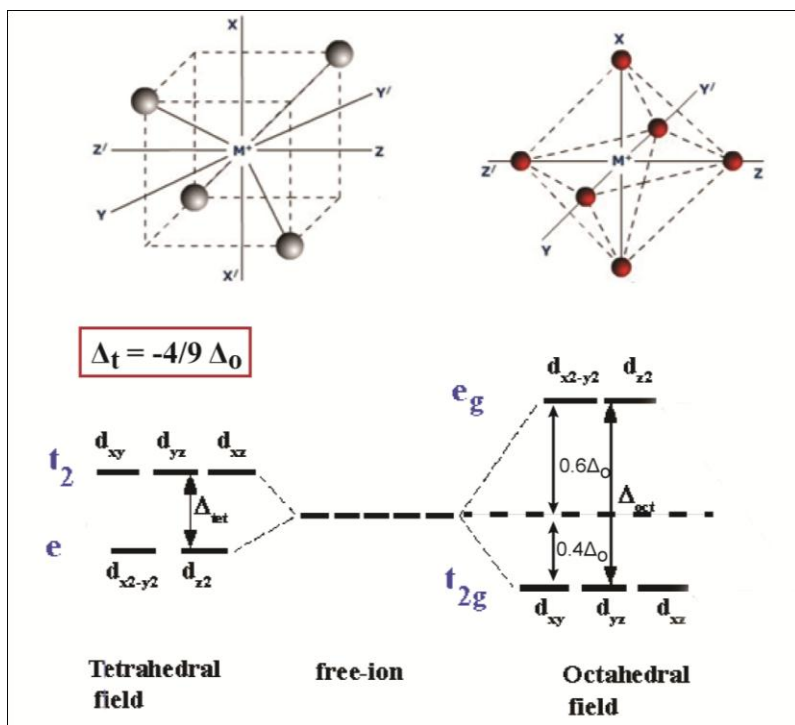


Fig. 2.7. Crystal field splitting of a transition metal ion (M^+) in tetrahedral and octahedral coordination.

The distribution of 3d electrons in a given transition metal ion is controlled by two opposing tendencies. First, repulsion and exchange interactions between electrons cause them to be distributed over as many of the 3d orbitals as possible with parallel spins. This is in accordance with Hund's first rule and lead to high-spine electronic configuration. Secondly, the effect of crystal field splitting is to cause electrons to populate 3d orbitals having the lowest energy, leading to the low-spin electronic configurations. The choice of electronic configuration occurs only in the ions possessing four, five, six and seven 3d electrons (such as Mn^{3+} , Mn^{2+} , Fe^{3+} , Fe^{2+} , Co^{3+} , Co^{2+}), the others possess only one electronic configuration.

In both tetrahedral and octahedral coordination, the resultant net stabilization energy gain is termed the crystal field stabilization energy and is designated by CFSE. For example in the octahedral coordination, each electron in a t_{2g} orbital stabilizes a transition metal ion in octahedral coordination by $0.4\Delta_0$, whereas every electron in an

e_g orbital destabilizes it by $0.6\Delta_o$. The CFSE represents the algebraic sum of these factors.

➤ **Many-electron d^N systems**

The methodical interpretation of optical absorption spectra of transition element compounds requires a many-electron d^N system, taking into account the inter-electron interactions (i.e. repulsions) between the d electrons within an open-shell orbital set. The full Hamiltonian for the d^N electrons in crystals must consider further perturbations in addition to the crystal field (CF):

$$\mathbf{H} = \mathbf{H}_{\text{spher}} + \mathbf{H}_{\text{ee}} + \mathbf{H}_{\text{CF}} + \mathbf{H}_{\text{SO}} + \mathbf{H}_{\text{SS}} \quad (16)$$

where $\mathbf{H}_{\text{spher}}$ denotes the free-ion Hamiltonian in the spherical approximation; \mathbf{H}_{ee} is the electron-electron repulsion effects within the nd^N configuration not included in $\mathbf{H}_{\text{spher}}$; \mathbf{H}_{CF} comprises the crystal field interactions (this contribution derives from the crystal field parameter $10Dq$ as explained above); $\mathbf{H}_{\text{SO,SS}}$ represent the spin orbit and electronic spin-spin interaction. In the $4d$ and $5d$ transition elements the CF splitting prevails over the other interactions.

➤ **Tanabe-Sugano diagrams**

Using the group theory one can predict how levels split in CF of a given symmetry and then use the irreducible representations as already seen for the Raman spectroscopy. Tanabe-Sugano (TS) diagrams are used to predict absorptions in the UV and visible electromagnetic spectrum of coordination compounds. TS diagrams show the crystal field parameter, $10Dq$, or Δ , divided by the Racah parameter B versus the energy, E , also scaled by B (Fig. 2.8).

Three Racah parameters exist, A , B , and C , which describe various aspects of interelectronic repulsion. A is an average total interelectronic repulsion, and being constant among d -electron configuration, it is not necessary for calculating relative energies (i.e. it is absent from Tanabe and Sugano's studies of complex ions), while B and C correspond with individual d -electron repulsions (B is the most important of Racah's parameters).

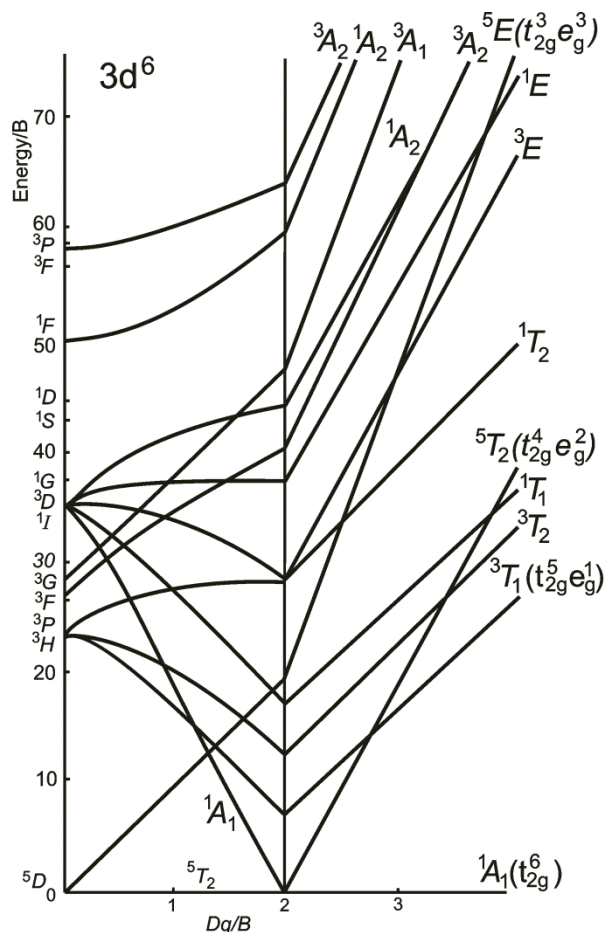


Fig. 2.8. Tanabe-Sugano energy level diagram for a 3d⁶ ion in an octahedral crystal field.

Each state is given and labelled by its symmetry (e.g. A_{1g} , T_{2g} , etc.). Term symbols (e.g. 3P , 1S , etc.) for a specific d^N free ion are listed, in order of increasing energy, on the y-axis of the diagram. In the diagrams are included not only the electronic transitions "allowed" but also the electronic transitions "spin-forbidden". Intensities of absorption bands are governed by probabilities of electronic transitions between the split 3d orbital energy levels. The probabilities are expressed by **selection rules**. The primary selection rule is related to the conservation of parity (*Laporte* or parity selection rule). On the basis of this selection rule, the transitions are allowed only between orbitals which differ in the symmetry of their wavefunction, that is, one state must have a symmetric (*g*) wave function and the other an antisymmetric (*u*) wave function. This means that LMCT, and MLCT (from an oxygen p orbital to a metal d

orbital) will occur with high probability and the resulting absorption band will be intense. While, since d orbitals have identical parities, electron transfer between two different d orbitals is forbidden. The second selection rules are related to *spin multiplicity* and states that the total number of unpaired electrons on an atom must remain unchanged during an electronic transition. The transitions between states with different spin multiplicity are forbidden. Hence, for the high-spin d^5 systems all transitions are spin-forbidden, leading to the light color of many Mn^{2+} and Fe^{3+} minerals.

The electron d-d transitions are parity forbidden, but some of them are spin-forbidden and some are spin allowed. The spin-forbidden transitions produce very weak absorption bands, which may gain intensity by spin-orbit coupling of electrons and magnetic interactions between neighboring cations. The spin-orbit coupling is an interaction between the electron's spin and the magnetic field generated by the electron's orbit around the nucleus. Effects of spin-orbit coupling become increasingly important with rising atomic number, they are thus more noticeable in compounds of Co and Ni than they are in V- and Cr-bearing phases.

2.3.2. Qualitative measurements in optical absorption spectra

An analysis of the optical spectrum and its absorption bands provide information about type of transition metal cation, its valence, its crystallographic site and bond types. The valence and coordination symmetry of a transition metal ion in a crystal structure govern the relative energies and energy separations of its 3d orbitals and, hence, influence the positions of absorption bands in a crystal field spectrum. Measurements of absorption spectra of transition metal compounds and minerals are used to obtain Δ_i ($10Dq$) and to evaluate the CFSE of the ions. The magnitude of Δ_i depends on various factors:

- types of the central transition metal ion: Dq increases with the oxidation state of the transition cation ($M^{2+} < M^{3+} < M^{4+}$) and with the high or low-spin configuration ($M_{hs} < M_{ls}$). The observed variation of Dq with the transition ion is

summarized in the *spectrochemical series of central atoms*:
 $Mn^{2+} < Co^{2+} \approx Ni^{2+} < Fe^{2+} < V^{2+} \approx Cu^{2+} < Fe^{3+} < Cr^{3+} < V^{3+} < Co^{3+} < Mn^{4+}$.

- the symmetry of the coordination polyhedron. The relationship for crystal field splittings in octahedral, tetrahedral, body-centered cubic is $\Delta_o : \Delta_c : \Delta_t = 1 : -\frac{8}{9} : -\frac{4}{9}$;
- types of the coordinating ligand atoms. A variation with the ligand type is observed and summarized in the *spectrochemical series of ligands*: $S^{2-} < Cl^- < F^- < O^{2-} \approx OH^- < H_2O$.
- degree of covalency of cation-anion bond. The Racah B parameter, which is a measure of interelectronic repulsion and exchange interactions, provides a qualitative indication of bond covalency. The nephelauxetic series represents the order of decreasing Racah B parameters and correlates with increasing covalent bonding characters of ligands coordinated to a transition metal. The nephelauxetic series of ligands is: free cation $> F^- > H_2O > OH^- > Si-O > O^{2-} > Cl^- > S^{2-}$, while the nephelauxetic series of central atoms is: $Mn^{2+} > V^{2+} > Ni^{2+} > Co^{2+} > Fe^{2+} > Cr^{3+} > V^{3+} > Fe^{3+} > Co^{3+} > Mn^{4+}$.

These factors may produce characteristic spectra for most transition metal ions, particularly when the cation occurs alone in a simple oxide structure. Each transition metal ions in a particular crystallographic site have specific absorption bands occurring in a part of the electromagnetic spectrum.

Attributing absorption to a particular cation in a crystallographic site is also useful to identify the electron transitions responsible for the color.

➤ **Causes of color**

Color is the response of the eye to the visible light range of the electromagnetic spectrum. We perceive color when the different wavelengths composing white light are selectively interfered (reflected, refracted, diffracted, scattered, absorbed, or simply transmitted).

Several mechanisms can contribute to the coloration of a mineral; there are at least fifteen causes of color summarized from Nassau (1987) on the base of the fundamental process involved. Most of the processes causing color, such as transition metal ions, charge-transfer phenomena and band theory, are discussed in the paragraph 2.3, with the first two mechanisms providing the colors in the most part of minerals. In the optical absorption, the positions of the absorption bands determine the actual colors observed, while the hue or vividness of color may be correlated with the intensities of the absorption bands. Regarding the transition metal ions, the oxidation state of a cation have a strong influence on both hue and the intensity of the color, for example, a beryl containing Mn^{2+} exhibits a delicate pink hue (morganite), while Mn^{3+} containing beryl occurs as bright red. Furthermore crystal field theory states that Mn^{2+} and Fe^{3+} transitions have a low probability of occurrence and hence they give rise to low-intensity absorptions and brighter colors. Drastic differences in color may arise when the same cation occurs in different coordinations. For example, Fe^{2+} in octahedral sites gives rise to the green color in peridot, while Fe^{2+} in distorted cube imparts a deep red color to almandine garnet. Also the nature of the neighboring atom of the cation can influence the color. For example, both green sphalerite and blue spinel are colored by Co^{2+} in tetrahedral sites, but the Co^{2+} ion in green sphalerite is connected to sulphur, while that of blue spinel is connected to oxygen (Fritsch and Roosman, 1987). The situation is complicated in those cases where the same cation with the same oxidation state and in the same coordination can produce different colors in different minerals even though it is surrounded by the same number of oxygen ions. For example, ruby and emerald owe their coloration to Cr^{3+} in octahedral coordination. This difference can be explained by the crystallographic environment around Cr^{3+} . The difference in the local cation-anion distance can cause different colors. Information on the short-range ordering and local structure can be obtained by spectroscopic methods (see structural relaxation, paragraph 2.3.4). For example, Hålenius et al. (2010) suggests that color changes from pale red to dark green in $Mg(Al_{1-x}Cr_x)_2O_4$ series, may be due to variations in Cr-O bond covalency, without or with very minor local Cr-O bond distance variation.

Regarding charge transfer, usually metal–ligand charge transfer absorptions are centered in the near ultraviolet band are broad enough to extend into the blue end of the visible spectrum, producing yellow to orange to brown colors (Fritsch and Rossman, 1988). For example, the deep yellow color of the heliodor, the golden variety of beryl, is caused by the $O^{2-} \rightarrow Fe^{3+}$ charge transfer. Besides, the IVCT processes have great importance for the ferromagnesian spinel group, because the $Fe^{2+}-Fe^{3+}$ IVCT is the prevailing mechanism color in these minerals, dominating the visible part of the spectrum with broad and intense absorption bands in the red end of the spectrum, producing a blue color (because also the violet light is suppressed by the $O^{2-} \rightarrow Fe^{3+}$ charge transfer). The IVCT also occurs between different metal ions. An important example is the $Fe^{2+}-Ti^{4+}$ IVCT that gives the characteristic blue color to the sapphire.

Color can also cause by electron transitions in magnetically exchange coupled pairs transitions (ECP) involving cations located at sites that share faces, edges, or just corners (e.g., Rossman 1975; Mattson and Rossman, 1987a; Taran et al. 2005). The spinels have a favorable structural basis for the formation of magnetically coupled $TFe^{3+}-MFe^{3+}$ clusters which can cause absorption bands (Andreozzi et al., 2001b). But also absorption bands due to exchange-coupled $Fe^{2+}-Fe^{3+}$ pairs generally occur in the iron-spinels close to or at the energies of the single-ion d–d transitions of the pair cations, and the extinction coefficients of the bands are strongly enhanced with respect to bands caused by single- ion d–d transitions (Hålenius et al., 2002).

Band gap colors are produced in insulating and semiconducting materials. If the energy band includes all wavelengths of light the material is white or clear and an insulator. If the band includes the energies of part of the visible spectrum the material is a semiconductor and colored. Examples of minerals colored by band gap mechanisms are cinnabar, and cuprite, in which all wavelengths from violet to orange are absorbed, so that only red light is transmitted.

Beside the processes already mentioned, also color centers and physical mechanisms, such as diffraction, dispersion and scattering, can determine color. For

example, internal scattering and interference phenomena cause iridescence in opal and some feldspars (e.g., moonstone).

Color centers are created when a mineral is exposed to a high-energy radiation, which can change the oxidation state of metal ions or interact with “defect” in the crystal, such as vacancies or additional atoms. A vacancy type of color center is responsible for the green color of diamonds. An example of variation of the oxidation state after an irradiation is the amethyst, where Fe^{3+} occupying the silicon site in quartz is changed into Fe^{4+} . Color centers are one of the few coloring mechanisms that can be removed by heating or exposing the mineral to strong light.

2.3.3. Quantitative analysis in optical absorption spectra

Quantitative relationship between intensity of an absorption peak and the concentration of an element in a crystallographic site can be established experimentally and it can be used to determine *site occupancies*. A constant correlation between the net linear extinction coefficients of the bands attributed to the ${}^{\text{M}}\text{Fe}^{2+}$ – ${}^{\text{M}}\text{Fe}^{3+}$ IVCT increase as a function of the sample $[{}^{\text{M}}\text{Fe}^{2+}] \cdot [{}^{\text{M}}\text{Fe}^{3+}]$ concentration product in the spinel s.s.–hercynite series (Hålenius et al., 2002), providing the possibility to determine the ferric concentration.

Intracrystalline Fe^{2+} - Mg^{2+} distributions in natural and synthetic orthopyroxenes have been determined from intensities of absorption bands in their polarized spectra (Steffen et al, 1988). Molar extinction coefficients of crystal field bands centered originating from Fe^{2+} ions located in pyroxene M2 sites enabled the iron contents to be estimated from the Beer-Lambert law equation.

Variations of extinction coefficients and spectrum profiles with changes in chemical composition of a mineral provide information on *cation ordering* in the structure. Cation ordering in silicate minerals may also be indicated by changes of spectrum profiles with changing chemical composition of a mineral. For example, Fe^{2+} ordering in Mg-Fe pyroxenes was investigated by Goldman and Rossman (1979) and linear correlations between the Fe^{2+} concentration and intensities of the Spin allowed band

of the Fe^{2+} were observed in the spectra. These correlations provide a means of quantitatively determining the distribution of Fe^{2+} between the M(1) and M(2) sites of orthopyroxene crystals.

Despite the fact that the CFSE constitutes only a minor contribution in regard to the total energy of a system, it can be the decisive force for the intra- and inter-crystalline transition ion distribution (Wildner et al., 2004). For example, as already seen in the chapter 1, the CFSE influences the intra-crystalline distribution of transition ions in octahedral and tetrahedral sites in the spinel group compounds. The intra-crystalline distribution is often predicted from the differences between the respective octahedral and tetrahedral CFSE, which are expressed as OSPE, octahedral site preference energy. For example, trivalent cations with high OSPE's are predicted to occupy octahedral sites in spinels and to form normal spinels.

Concerning the *inter-crystalline transition metal distribution*, the CFT predict the partition behavior of transition metals between various coexisting phases, but several other competing mechanisms like crystal chemical effects also have to be taken into account. For example, Langer and Andrut (1996) investigated the distribution of the Cr^{3+} ion among paragenetic coexisting minerals in various rocks, confirming a positively relationship between the Cr^{3+} concentration and its CFSE in the respective mineral phase.

➤ **Structural relaxation**

Spectroscopic methods have demonstrated that the local structure often differs from the average structure as determined by diffraction methods, and that Vegard's rule is not obeyed at the atomic scale due to lattice relaxation during atomic substitution (Galoisy, 1996). Vegard's rule states that in a binary solid solution $\text{A}_{1-x}\text{B}_x\text{O}$ the unit cell parameter a_x can be expressed as a function of its composition: $a_x = a_{\text{AO}}X_{\text{AO}} + a_{\text{BO}}X_{\text{BO}}$, where a_{AO} and a_{BO} represent the lattice parameter for the end-members, while $X_{\text{AO}}, X_{\text{BO}}$ their respective molar fractions. According to the Vegard's rule, the interatomic distance corresponds to an average value, equivalent to:

$$\langle \text{A}_{1-x}\text{B}_x - \text{O} \rangle = \langle \text{A} - \text{O} \rangle + x \cdot (\langle \text{B} - \text{O} \rangle - \langle \text{A} - \text{O} \rangle) \quad (17)$$

The model obeying this Vegard's rule is called "virtual crystal approximation" (VCA) and it assume that all bond distances are equal regardless of their individual occupancy by A or B.

Urusov (1992) proposed a geometrical model to quantify the deviation from Vegard's rule through the relaxation coefficient (ϵ), expressed as:

$$\epsilon = \frac{\langle B-O \rangle_x - \langle A-O \rangle}{\langle B-O \rangle - \langle A-O \rangle} \quad (18)$$

where $\langle A-O \rangle$ and $\langle B-O \rangle$ are the mean interatomic distances in the end-members in question and are measured by diffraction methods, whereas, $\langle B-O \rangle_x$ is the local mean distance for the $A_{1-x}B_xO$, estimated by optical absorption spectroscopy.

In a real crystals, the behavior of the exchanging cation in a solid solution falls between two extreme cases. The relaxation coefficient would be 0.0 for no relaxation, i.e., the case of the "virtual crystal" model obeying Vegard's rule, and 1.0 for complete relaxation, i.e., the case of the "hard-sphere" model (Fig. 2.9).

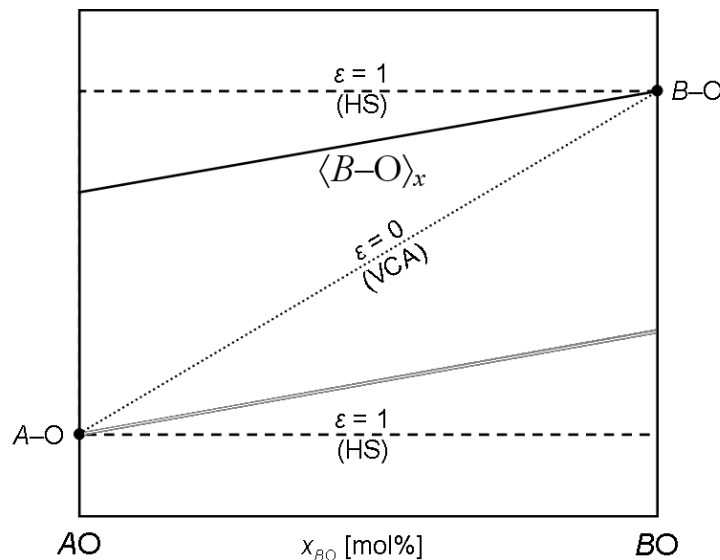


Fig. 2.9. A scheme of A-O and B-O bond distance changes dependent on composition. The dotted line indicates the VCA model ($\epsilon = 0$); the dashed lines indicate HS model ($\epsilon = 1$); the solid lines show the local bond distance (modified from Urosov, 1992).

The “virtual crystal” model assumes that the ions are located without local distortions at the “ideal” lattice sites of the average unit cell, and they are substituted without modification of the bond distances. In contrast, for the hard sphere model, the ionic radii are constant and the whole structure is expected to take up all modifications upon chemical substitution (Hålenius et al., 2010). In the case of absence of relaxation the individual bond distances in the mixed crystal are equal to their average values; it means $\langle B-O \rangle_x = \langle A-O \rangle$. In the case of full relaxation, instead, the interatomic bond distance will not change with the composition, it means $\langle B-O \rangle_x = \langle B-O \rangle$.

The local metal-oxygen distances in a solid solution can be achieved by optical absorption spectroscopy through the measurement the crystal field parameter $10Dq$. In fact, the $10Dq$ value, in a hypothetical AO-BO solid solution, depends on the mean metal-oxygen bond distances by the relationship:

$$10Dq = \frac{5 ZLe \langle r^4 \rangle}{3 \langle B-O \rangle^5} \quad (19)$$

Where ZLe is the effective charge of the ligands and $\langle r \rangle$ is the average radius of the d orbitals. These two values can be considered constant in the same metal ion in the same ligand environment (Burn, 1993) and then the equation 18 can be simplified as:

$$10Dq = const \frac{1}{\langle B-O \rangle^5} \quad (20)$$

Knowing the B-O bond distance, $\langle B-O \rangle_{x=1}$, and the crystal field splitting parameter for the 3d metal cation, $(10Dq)_{x=1}$, in the 3d metal-rich end-member ($x = 1$) of a binary solid solution, it is possible to calculate the local B-O bond distance $\langle B-O \rangle_x$ for any given composition ($x < 1$) on the binary from the recorded crystal field splitting $(10Dq)_x$ of that composition by applying the relation:

$$\langle B-O \rangle_x = [(10Dq)_{x=1}/(10Dq)_x]^{1/5} \quad (21)$$

Chapter 3

MATERIALS AND METHODS

3.1. Materials

In the present work natural and synthetic single crystals of spinels were studied. The examined **synthetic samples** consist of:

- ✓ Synthetic single crystals of spinel (10 samples) belonging to the MgAl_2O_4 (spinel sensu stricto) - CoAl_2O_4 (cobalt spinel) solid solution. These samples were synthesized through the synthesis procedure described in the paragraph 3.2. Then they were characterized using electron microprobe, single-crystal X-ray diffraction, optical absorption and Raman spectroscopies.

- ✓ Synthetic single crystals of spinel (10 samples) belonging to the MgAl_2O_4 (spinel sensu stricto) - FeAl_2O_4 (hercynite) solid solution. These samples were already synthesized and a chemical, structural and optical characterization was performed by Andreozzi and Lucchesi (2002) and Hålenius et al., 2002. In the present study the samples of this series were characterized by Raman spectroscopy.

- ✓ Synthetic single crystals of spinel (10 samples) belonging to the MgAl_2O_4 (spinel sensu stricto) - MgCr_2O_4 (magnesiochromite) and to ZnAl_2O_4 (gahnite) - ZnCr_2O_4 (zincchromite) solid solutions. These samples were already synthesized and a chemical and optical characterization was performed by Hålenius et al., 2010. In the present study the samples of these series were characterized by Raman spectroscopy.

Natural samples have different color, size and origin. They were characterized by Electron MicroProbe Analysis (EMPA) to obtain chemical composition and by Optical Absorption Spectroscopy (OAS) to investigate the causes of colors in the spinel group minerals. In addition, some samples were studied by the Laser Ablation-Inductively

Coupled Plasma-Mass Spectrometry (LA-ICP-MS) to obtain the quantitative chemical composition of the minor and trace elements, but in this study only the minor elements will be presented and discussed. Most of the natural samples were investigated by Raman spectroscopy to obtain chemical information and consideration of spinels from the study of the Raman active modes.

Natural spinels were kindly furnished by:

- ✓ Swedish Museum of Natural History (Naturhistoriska riksmuseet, NRM). A total of 19 samples coming from different geological environment were selected by the mineral collection of the NRM, among which 14 single crystals were extracted from the embedding rock, whereas 5 spinels were already in the form of single crystals.

- ✓ Museum of Earth Sciences, University of Bari. Five single crystals spinels belonging to the mineral collection of the Museum were taken.

- ✓ Private gemologists made available 4 gem-cut spinels with the equivalent rough samples, and 2 single crystal spinels.

The features of the natural spinels and a scheme of the techniques used to characterize them are summarized in Table 3.1.

Table 3.1. Natural spinels investigated and the techniques used to characterize them.

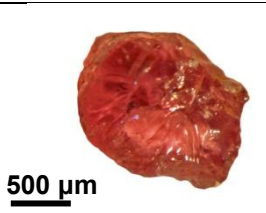

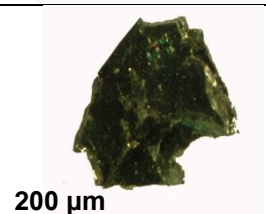
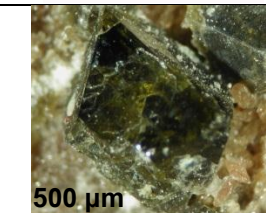
| Sample | Label | Color | Localities | Investigated by | | | |
|---|-------|-----------------|--------------------|-----------------|-----------|----------|------------|
| | | | | EMPA | LA-ICP-MS | OAS+FTIR | Raman + PL |
|  | ST | Pink-Red | Tanzania | ✓ | ✓ | ✓ | ✓ |
|  | SX | Violet | Unkonwn | ✓ | ✓ | ✓ | ✓ |
|  | 2366 | Blue-green | Dalarne, Sweden | ✓ | ✓ | ✓ | |
|  | 31081 | Yellowish-Green | Jakobsberg, Sweden | ✓ | ✓ | ✓ | ✓ |

Table 3.1. Continued.





| Sample | Label | Color | Localities | Investigation by | | | |
|---|--------|-------------------|-----------------|------------------|-----------|----------|------------|
| | | | | EMPA | LA-ICP-MS | OAS+FTIR | Raman + PL |
|  | 330763 | Light blue | Dalarna, Sweden | ✓ | | ✓ | ✓ |
|  | 330764 | Blue | Dalarna, Sweden | ✓ | ✓ | ✓ | ✓ |
|  | 420491 | Pink | Ceylon, India | ✓ | ✓ | ✓ | |
|  | 440238 | Violet-Light blue | Åker, Sweden | ✓ | | ✓ | ✓ |

Table 3.1. Continued.

| Sample | Label | Color | Localities | Investigation by | | | |
|---|--------|------------|---------------|------------------|-----------|----------|------------|
| | | | | EMPA | LA-ICP-MS | OAS+FTIR | Raman + PL |
|  | 440243 | Violet | Åker, Sweden | ✓ | ✓ | ✓ | ✓ |
|  | 510941 | Light blue | Levida, Spain | ✓ | | ✓ | ✓ |
|  | 510942 | Blue | Levida, Spain | ✓ | ✓ | ✓ | ✓ |
|  | 670275 | Lilac | Åker, Sweden | ✓ | ✓ | ✓ | ✓ |

Table 3.1. Continued.



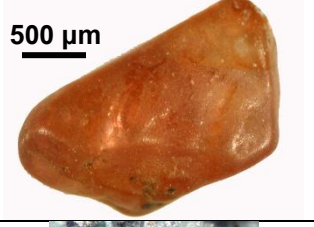

| Sample | Label | Color | Localities | Investigation by | | | |
|---|---------|------------|---------------------------|------------------|-----------|----------|------------|
| | | | | EMPA | LA-ICP-MS | OAS+FTIR | Raman + PL |
|  | 800801 | Dark blue | Catanzaro, Italy | ✓ | ✓ | ✓ | ✓ |
|  | 881694a | Magenta | Ceylon, India | ✓ | | ✓ | ✓ |
|  | 881694c | Orange | Ceylon, India | ✓ | ✓ | ✓ | ✓ |
|  | 881728 | Blue-green | Charlemont, Massachusetts | ✓ | ✓ | ✓ | ✓ |

Table 3.1. Continued.



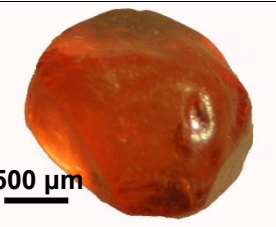

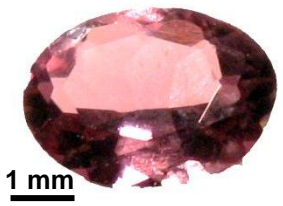
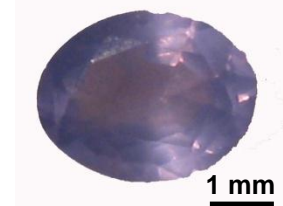


| Sample | Label | Color | Localities | Investigation by | | | |
|---|---------|------------|-------------------------|------------------|---|--------------|---------------|
| | | | | EMPA | | OAS+ FTIR | Raman + PL |
|  | 890290 | Blue-green | Sodermanland, Sweden | | ✓ | ✓ | ✓ |
|  | 890292b | Magenta | Burma, Myanmar | ✓ | ✓ | ✓ | ✓ |
|  | 890292c | Orange | Burma, Myanmar | | ✓ | ✓ | ✓ |
|  | 890292d | Red | Burma, Myanmar | ✓ | ✓ | ✓ | ✓ |

Table 3.1. Continued.

| Sample | Label | Color | Localities | Investigation by | | | |
|---|-------|--------------|-------------------|----------------------------------|----------------------------------|----------------------------------|-------------------------|
| | | | | EMPA | LA-ICP-MS | OAS+FTIR | Raman + PL |
|  | Nat.1 | Light Purple | Tunduru, Tanzania | ✓ The equivalent rough sample | ✓ The equivalent rough sample | ✓ The equivalent rough sample | ✓ The gem-cut sample |
|  | Nat.2 | Light blue | Tunduru, Tanzania | ✓ The equivalent rough sample | ✓ The equivalent rough sample | ✓ The equivalent rough sample | ✓ The gem-cut sample |
|  | Nat.3 | Purple | Tunduru, Tanzania | ✓ The equivalent rough sample | ✓ The equivalent rough sample | ✓ The equivalent rough sample | ✓ The gem-cut sample |
|  | Nat.4 | Blue-green | Tunduru, Tanzania | ✓ The equivalent rough sample | ✓ The equivalent rough sample | ✓ The equivalent rough sample | ✓ The gem-cut sample |

3.2. Synthesis by Flux growth method

Flux growth is the process of crystal growth from molten salt solvents at high temperatures. A high temperature solvent is called flux because it permits growth to proceed at temperatures well below the melting point of the growing phase.

Major techniques for the crystal growth are the Verneuil, the Czochralski, the hydrothermal and the flux methods. Melt growth (Verneuil and Czochralski) are commercially the most important methods of crystal growth because the rate of growth is normally much higher than that possible by other methods. However the melt methods require sophisticated and expensive equipment, steep temperature gradient and involve high concentration of defects such as vacancies and dislocation in crystals. Hydrothermal growth, although requiring expensive and sophisticated equipment, provides high quality, defect-free crystals. Flux growth is the method by which a wide range of good quality crystals may be obtained with less sophisticated equipment.

The main advantages of this technique compared to growth from the pure melt are:

- ✓ Lower temperatures. In fact, often the melting point of some materials is too high for apparatus available. The material melts incongruently or exhibits, at some lower temperature, a phase change which leads to severe stress or fracture;
- ✓ Better quality crystals. In fact, crystals grown from melts may be not well formed and non-stoichiometric due to the high vapor pressure of one or more of the constituents.

Simple metals (Ni, Fe), oxides (B_2O_3 , Bi_2O_3), hydroxides ((KOH, NaOH), salts (BaO, PbO, PbF_2) can be used as solvents. However, eutectics, found in binary (PbO/B_2O_3 , PbO/PbF_2 , BaO/B_2O_3 , Li_2O/MoO_3) or ternary ($PbO/PbF_2/B_2O_3$, $BaO/Bi_2O_3/B_2O_3$) diagrams, are generally preferred as a reason of their low temperature and their low viscosity.

In the present spinel synthetic samples belonging to the $\text{MgAl}_2\text{O}_4\text{-CoAl}_2\text{O}_4$ solid-solution series were produced at the Department of Earth Sciences, Sapienza University of Rome (Fig. 3.1).



Fig. 3.1. Experimental Mineralogy laboratory at the Department of Earth Sciences, Sapienza University of Rome.

The equipment consists in:

- ✓ an ENTECH vertical furnace that may operate at maximum temperature of 1400 °C, equipped with a multi-step temperature controller. Heating elements are at half height of the vertical and guarantee a homogeneous temperature zone of 30 cm.
- ✓ a mass-flow controller that allow a continuous flow of mixed gas composed from pure CO₂ and H₂. These two gases are disposed to enter into the furnace for reduced atmosphere thermal runs.
- ✓ an oxygen-fugacity sensor to measure the oxygen content of the atmosphere inside the furnace.
- ✓ a computer for temperature and oxygen fugacity record through thermocouples and oxygen sensor.

In the present study, flux growth method was used and experimental conditions were optimized to obtain high-quality single crystals of spinel belonging to the MgAl₂O₄ (spinel sensu stricto) - CoAl₂O₄ (cobalt spinel) solid solution.

3.2.1. Experimental conditions

The growth of single crystals with the investigated compositions using the flux growth method depends on some experimental factors:

1. cooling temperature range,
2. cooling rate,
3. flux content with respect to the total amount of nutrients,
4. molar oxide proportions content in the starting mixture. Every element enters the growing spinel phase according to its melt/crystal partition coefficient,
5. Flux/Nutrient ratio (F/N)

Ten experiments were carried out along MgAl_2O_4 (spinel sensu stricto) - CoAl_2O_4 (cobalt spinel) solid solution, following the procedure described by Andreozzi, (1999). In the first experiment, **CoAl05**, the cooling rate of 4 °C/h was kept equal to those of Andreozzi (1999), whereas the cooling temperature range of 1200-900 °C was changed modifying the lower temperature from 900 °C to 800 °C in order to improve the size and shape of crystal. Results were not completely satisfactory in terms of crystal quality, so that in the other nine runs also the cooling rate of 4 °C/h was reduced to 2 °C/h in order to promote an increase of crystal quality (Table 3.2).

The best flux/nutrients ratio of each composition was determined by trial and error as no literature data were found. It was observed that this ratio must be decreased in order to grow spinels with increasing contents of transition element oxides (Andreozzi, 1999). The F/N ratio of the crystals spinel synthesized in the present study changed from 1.50 to 1.40 (Table 3.2).

Regarding the molar oxide proportions of the starting material, Andreozzi (1999) observed that crystals improve in both size and quality when some MgO excess over the stoichiometric ratio is added to the starting mixture, so an excess of MgO ranging from 0.10 (for Co-rich spinels) to 0.20 (for Co-poor spinels) was taken.

The starting materials consisted of analytical MgO, Al_2O_3 , and CoO powders (molar proportions used are reported in Table 3.2), which were dehydrated and dried at 1000 °C for 12 h, before being mixed with $\text{Na}_2\text{B}_4\text{O}_7$, used as flux compound.

Table 3.2. Flux grown spinels of the MgAl_2O_4 - CoAl_2O_4 series: molar proportions of starting oxide mixture, flux to nutrient ratio (F/N), and experimental conditions. Sample name is referred to the percentage of CoAl_2O_4 end member that would be expected from oxide proportions.

| Run | CoAl0.5 | CoAl1 | CoAl10 | CoAl14 | CoAl20 | CoAl34 | CoAl45 | CoAl50 | CoAl67 | CoAl100 |
|---|--------------|--------------|--------------|--------------|--------------|--------------|--------------|---------------|--------------|--------------|
| MgO | 1.20 | 1.20 | 1.15 | 0.96 | 0.95 | 0.76 | 0.65 | 0.60 | 0.43 | - |
| CoO | 0.05 | 0.01 | 0.10 | 0.14 | 0.20 | 0.34 | 0.45 | 0.50 | 0.67 | 1.00 |
| Al_2O_3 | 1.00 | 1.00 | 1.00 | 1.00 | 1.00 | 1.00 | 1.00 | 1.00 | 1.00 | 1.00 |
| F/N | 1.50 | 1.50 | 1.50 | 1.50 | 1.50 | 1.45 | 1.45 | 1.45 | 1.45 | 1.40 |
| T range (°C) | 1200- 800 | 1200- 800 | 1200- 800 | 1200- 800 | 1200- 800 | 1200- 800 | 1200- 800 | 1200- 800* | 1200- 800 | 1200- 800 |
| Cooling range (°C/h) | 4°C/h | 2°C/h | 2°C/h | 2°C/h | 2°C/h | 2°C/h | 2°C/h | 2°C/h | 2°C/h | 2°C/h |
| CO_2 : H_2 (cm_3 /min) | 100:4 | 100:4 | 100:4 | 100:4 | 100:4 | 100:4 | 100:4 | 100:4 | 100:4 | 100:4 |
| Yield (g) | 0.80 | 0.85 | 1.85 | 1.80 | 1.90 | ~1.80 | ~1.70 | 1.90 | ~1.20 | ~1.75 |
| Main size (μm) | 300 | 300 | 500 | 500 | 500 | 500 | 500 | 500 | 500 | 500 |

*accidental quenching happened before the end of the slow cooling path

$\text{Na}_2\text{B}_4\text{O}_7$ was chosen because of its low melting point (742.5 °C), the low-energy barriers to crystal growth in the borate flux and its absence of interaction with spinel compositions. About 5 g of starting material were thoroughly ground and mixed under acetone in an agate mortar and then transferred to a 10 mL yttrium-stabilized Pt/Au (5%) crucible, covered by a platinum lid (Fig. 3.2.).

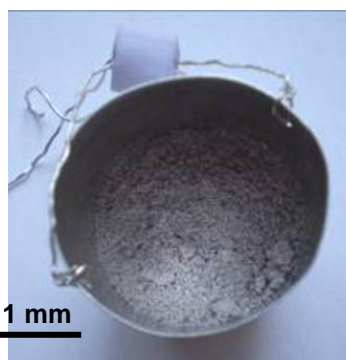


Fig. 3.2. Starting material in the yttrium-stabilized Pt/Au (5%) crucible.

Yttrium-stabilized Pt/Au (5%) crucible was used for their good resistance to chemicals at high temperatures in reducing conditions. The crucible was suspended inside an ENTECH vertical furnace equipped with a multi-step temperature controller and an oxygen fugacity control system, which uses a binary gas mixture (CO_2 - H_2).

Crystals were grown in a gas-controlled atmosphere, required for the reduction of Co^{3+} to Co^{2+} . The reducing atmosphere was created by a continuous flow of high-purity CO_2 and H_2 gases into the furnaces. The ratio CO_2/H_2 was maintained by gas-flow controllers and was kept constant in the ratio of 100:4 (cm^3/min). Oxygen fugacity ranged from 10^{-8} to 10^{-15} when temperature is decreased from 1200 to 800°C, respectively.

The linear temperature profile of cooling was chosen with respect to the saw-tooth one, according to previous works in which crystal quality and size have seen to improve (Andreozzi, 1999). Thermal runs, schematized in Fig. 3.3, consisted of a rather steep increment in temperature up to 1200 °C, after which the temperature was kept constant for 24 h (for complete dissolution and homogenization of the oxide mixture) and subsequently decreased slowly to 800 °C at 2 °C/h cooling rate (with exception of the $\text{CoAl}_{0.5}$ run that was cooled down at 4 °C/h). Shutting off the power to the heating elements ended thermal runs, and the material was rapidly cooled down to room temperature.

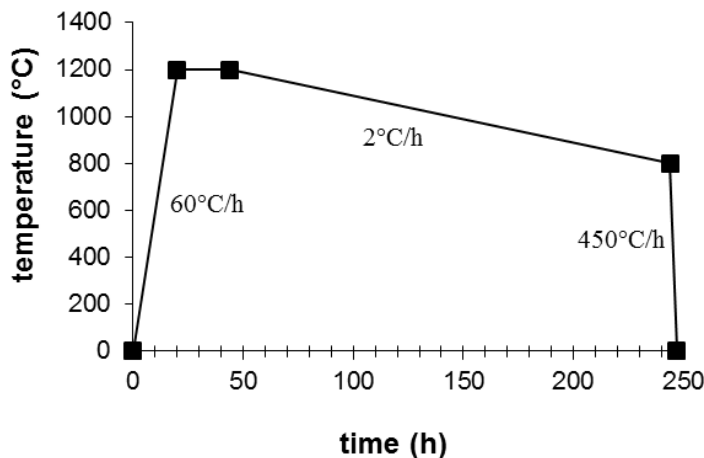


Fig. 3.3. Thermal run expressed as time versus temperature.

The products of each of the 10 experiments consisted of an intergrowth network of elongated, prismatic cobalt-magnesium borate crystals and octahedral spinel crystals embedded in minor sodium borate glass. The spinel crystals nucleate not only on the walls of the crucible and the surface of the melt but also in the bulk of material (Fig. 3.4).

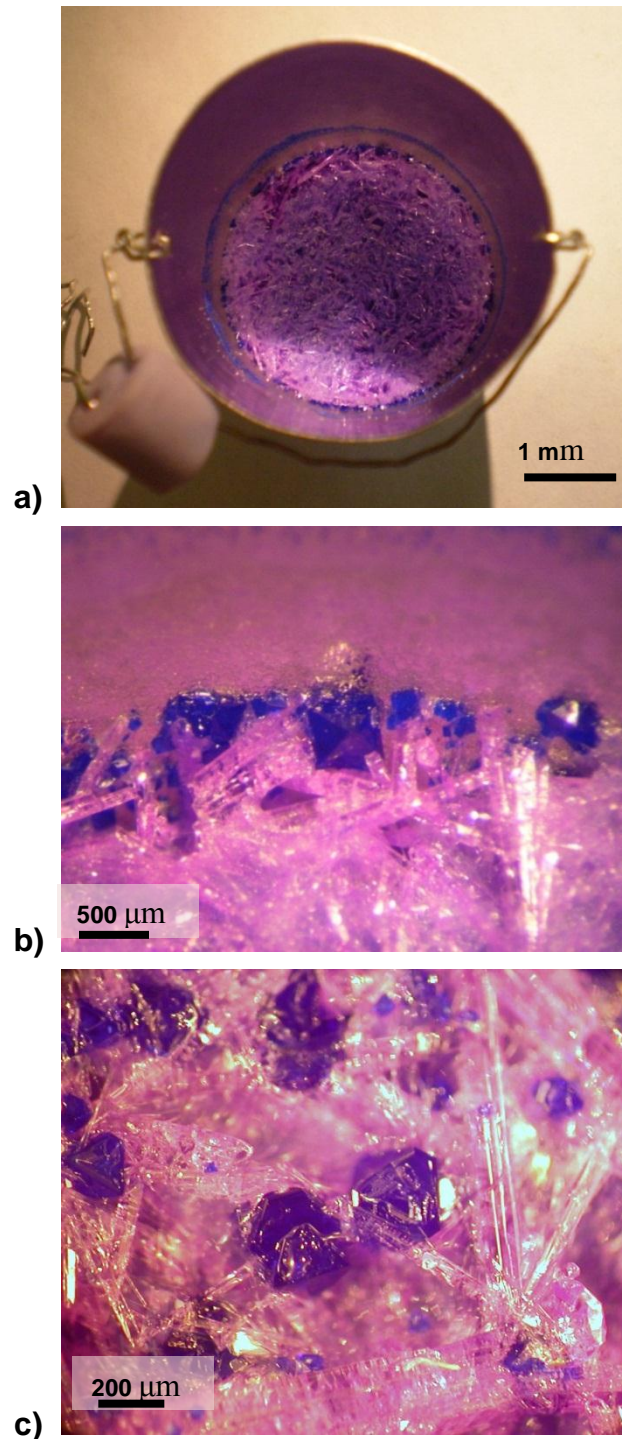


Fig. 3.4. Intergrowth of octahedral spinels and elongated, prismatic borate crystals at increasing magnification a) in the yttrium-stabilized Pt/Au (5%) crucible b) on the walls of the crucible and c) on the surface of the melt and in the bulk of material.

By dissolving the glass phase and most of the borate crystals in warm and dilute HCl (10%) solution, the run products were reduced to euhedral and/or subhedral

octahedra of spinels of various sizes (Table 3.2). Ten single crystals of synthetic spinel belonging to the $\text{MgAl}_2\text{O}_4\text{-CoAl}_2\text{O}_4$ series, representative for different compositions, were chosen for the single crystal analyses on basis of quality in terms of size and shape (checked by binocular microscope) and crystallinity (checked by X-ray single crystal diffractometer). The same crystals were used then for the following chemical electron-microanalysis, UV-VIS-NIR spectroscopy and Raman investigation.

3.3. Single-Crystal X-Ray Diffraction

Single-crystal X-ray Diffraction is an analytical technique which provides detailed information about the lattice parameters of crystalline substances, including unit cell dimensions, bond-lengths, bond-angles, and details of site-ordering. Directly related is structural refinement, where the data generated from the X-ray analysis are interpreted and refined to obtain the crystal structure.

X-ray diffraction measurements were performed at the Earth Sciences Department, Sapienza University of Rome, with a Bruker KAPPA APEX-II single-crystal diffractometer, equipped with CCD area detector ($6.2 \times 6.2 \text{ cm}^2$ active detection area, 512×512 pixels) and a graphite crystal monochromator, using $\text{MoK}\alpha$ radiation from a fine-focus sealed X-ray tube (Fig. 3.5). The sample-to-detector distance was 4 cm. A total of about 1600 exposures for the natural samples and about 5000 exposures per the synthetic samples (step = 0.2° , time/step = 10 s) covering a full reciprocal sphere were collected.



Fig. 3.5. Bruker KAPPA APEX-II single-crystal diffractometer of the Earth Sciences Department, Sapienza University of Rome.

The orientation of the crystal lattice was determined from 500 to 1000 strong reflections ($I > 100 \sigma_I$) evenly distributed in the reciprocal space, and used for subsequent integration of all recorded intensities. Final unit-cell parameters were refined by means of the Bruker AXS SAINT program from ca. 800 (natural spinels) and ca. 2300 (synthetic spinels) recorded reflections with $I > 10 \sigma_I$ in the range $8^\circ < 2\theta < 90^\circ$. The intensity data were processed and corrected for Lorentz, polarization, and background effects with APEX2 software program of Bruker AXS. The data were corrected for absorption using multi-scan method (SADABS). The absorption correction led to a significant improvement in R_{int} . No violation of $Fd\bar{3}m$ symmetry was noted. Sporadic appearance of forbidden space-group reflections was recognized as double reflections by their anomalously narrow reflection profiles.

Structural parameters of chosen single crystals were obtained by X-ray single crystal diffraction analysis combined with the structural refinement. Structural refinements were carried out with the SHELXL-PC program (Sheldrick, 2008). Setting the origin at $3m$, initial atomic positions for oxygen atoms were taken from the structure of spinel

(Princivalle et al., 1989). Variable parameters were: scale factor, secondary extinction coefficient, oxygen positional parameter (u), Mg and Al occupancy in T and M sites, respectively, site-scattering values expressed as mean atomic number (m.a.n.), and atomic displacement parameters $U(O)$, $U(M)$, and $U(T)$. No chemical constraint was applied during the refinement. To obtain the best values of statistical indexes ($R1$ and $wR2$) the oxygen site was modeled with neutral vs. full, ionized oxygen scattering curves, while neutral curves were used for the cation sites. In detail, the T site was modeled considering the presence of Mg and Co scattering factors, whereas the M site was modeled with the Al scattering factor. Three full-matrix refinement cycles with isotropic displacement parameters for all atoms were followed by anisotropic cycles until convergence was attained, that is, when the shifts in all refined parameters were less than their estimated standard deviation. No correlation over 0.7 between parameters was observed at the end of refinement. Table 3.3 summarizes the refinement details whereas the structural parameters will be described in next chapter (Table 4.6).

Table 3.3. X-ray diffraction data of the analyzed spinels single crystals along $(Mg_{1-x}Co_x)Al_2O_4$.

| Crystal | CoAl0.5 | CoAl1 | CoAl10 | CoAl14 | CoAl20 |
|--------------------------------------|----------------------|----------------------|----------------------|----------------------|----------------------|
| Crystal sizes (mm) | 0.20×0.20×0.12 | 0.22×0.21×0.18 | 0.22×0.20×0.15 | 0.20×0.20×0.16 | 0.20×0.20×0.20 |
| Reciprocal space range hkl | $-15 \leq h \leq 15$ | $-14 \leq h \leq 15$ | $-15 \leq h \leq 13$ | $-15 \leq h \leq 14$ | $-16 \leq h \leq 12$ |
| | $-15 \leq k \leq 14$ | $-15 \leq k \leq 15$ | $-15 \leq k \leq 15$ | $-16 \leq k \leq 16$ | $-16 \leq k \leq 16$ |
| | $-15 \leq l \leq 13$ | $-11 \leq l \leq 16$ | $-9 \leq l \leq 15$ | $-15 \leq l \leq 8$ | $-15 \leq l \leq 6$ |
| EXTI | 0.164(7) | 0.22(1) | 0.195(9) | 0.090(3) | 0.073(3) |
| Set of read reflections | 2552 | 2490 | 2452 | 2492 | 2465 |
| Unique reflections | 132 | 132 | 130 | 133 | 132 |
| R int. (%) | 2.57 | 2.08 | 1.46 | 2.26 | 1.87 |
| $R1$ (%) all reflections | 1.56 | 2.11 | 1.86 | 1.28 | 1.49 |
| $wR2$ (%) all reflections | 3.56 | 4.57 | 4.13 | 3.17 | 3.48 |
| GooF | 1.239 | 1.322 | 1.330 | 1.178 | 1.293 |
| Diff. Peaks ($\pm e/\text{\AA}^3$) | -0.36; 0.23 | -0.53; 0.49 | -0.50; 0.55 | -0.37; 0.23 | -0.36; 0.27 |

Notes: EXTI = extinction parameter; R int. = merging residual value; $R1$ = discrepancy index, calculated from F -data; $wR2$ = weighted discrepancy index, calculated from F^2 -data; GooF = goodness of fit; Diff. Peaks = maximum and minimum residual electron density. Radiation, Mo- $K\alpha$ = 0.71073 Å. Data collection temperature = 293 K. Total number of frames = 1500.

Table 3.3. *continued*

| Crystal | CoAl34 | CoAl45 | CoAl50 | CoAl67 | CoAl100 |
|--------------------------------------|----------------------|----------------------|----------------------|----------------------|----------------------|
| Crystal sizes (mm) | 0.30×0.25×0.20 | 0.20×0.20×0.20 | 0.16×0.16×0.10 | 0.16×0.14×0.09 | 0.19×0.19×0.12 |
| Reciprocal space range <i>hkl</i> | $-9 \leq h \leq 15$ | $-11 \leq h \leq 15$ | $-13 \leq h \leq 16$ | $-10 \leq h \leq 15$ | $-14 \leq h \leq 15$ |
| | $-14 \leq k \leq 10$ | $-15 \leq k \leq 16$ | $-14 \leq k \leq 11$ | $-16 \leq k \leq 16$ | $-15 \leq k \leq 15$ |
| | $-16 \leq l \leq 16$ | $-15 \leq l \leq 13$ | $-13 \leq l \leq 16$ | $-15 \leq l \leq 7$ | $-15 \leq l \leq 7$ |
| EXTI | 0.045(2) | 0.045(2) | 0.23(1) | 0.024(1) | 0.026(1) |
| Set of read reflections | 2471 | 2460 | 2567 | 2445 | 2484 |
| Unique reflections | 129 | 132 | 133 | 133 | 131 |
| <i>R</i> int. (%) | 2.58 | 4.49 | 1.86 | 1.55 | 2.40 |
| <i>R</i> 1 (%) all reflections | 1.49 | 1.36 | 1.98 | 1.06 | 1.11 |
| <i>wR</i> 2 (%) all reflections | 3.39 | 3.50 | 4.48 | 2.65 | 2.45 |
| GooF | 1.376 | 1.244 | 1.286 | 1.153 | 1.286 |
| Diff. Peaks ($\pm e/\text{\AA}^3$) | -0.56; 0.32 | -0.30; 0.30 | -0.70; 0.29 | -0.30; 0.25 | -0.28; 0.33 |

Notes: EXTI = extinction parameter; *R* int. = merging residual value; *R*1 = discrepancy index, calculated from *F*-data; *wR*2 = weighted discrepancy index, calculated from *F*²-data; GooF = goodness of fit; Diff. Peaks = maximum and minimum residual electron density. Radiation, Mo-*K* α = 0.71073 Å. Data collection temperature = 293 K. Total number of frames = 1500.

3.4. Electron microprobe analysis

Electron microprobe analysis was performed in order to obtain chemical composition of both synthetic and natural spinels crystals. For the synthetic spinels belonging to the MgAl₂O₄-CoAl₂O₄ series the analyses were carried out on the same crystals used for the structural refinements. Natural and synthetic single crystals were mounted in an epoxy disc, thinned, polished and carbon-coated for electron microprobe analysis (EMPA, wavelength dispersive mode) using a Cameca SX 50 instrument at the CNR-IGAG laboratory c/o Sapienza University of Rome, operating at an accelerating potential of 15 kV and a sample current of 15 nA, with an incident beam size of ~1 mm (Fig.3.6).



Fig. 3.6. Cameca SX 50 instrument at the CNR-IGAG laboratory c/o Sapienza University of Rome.

No less than 5 spot analyses for each sample were performed to obtain the average chemical composition and a preliminary estimation of the compositional homogeneity. Standards used for the synthetic samples (with a semi-known composition) were periclase (MgO), corundum (Al_2O_3), and metallic Co. A synthetic MgAl_2O_4 spinel single crystal, produced and fully characterized by Andreozzi et al. (2000), served as a reference material. For the natural samples the synthetic and natural standards used were corundum (Al), magnetite (Fe), wollastonite (Si), rutile (Ti), vanadinite (V), metallic Zn, Mn, Co and Ni, and synthetic MgAl_2O_4 (Mg) and MgCr_2O_4 (Cr) spinel single crystals, produced and fully characterized by Andreozzi et al. (2000) and Hålenius et al. (2010), respectively.

A PAPCAMECA program (Pouchou and Pichoir, 1984) was used to convert X-ray counts into weight percentages of the corresponding oxides.

3.5. X-ray mapping technique in SEM/EDS analysis

Compositional homogeneity of the synthetic crystals belonging to the MgAl_2O_4 - CoAl_2O_4 series was further investigated by SEM and demonstrated by image analysis coupled with energy-dispersive spectrometry (EDS) analysis using color coding to depict the 2D spatial distribution of the characteristic energy emission from respective

elements present in the samples. All the samples were carbon coated and analyzed at Earth Sciences Department, Sapienza University of Rome, by a SEM/EDS FEI Quanta 400 instrument operating at an accelerating voltage of 30 kV, a specimen tilt of 0°, a working distance of 9.7 mm and a magnification of 520× (Fig. 3.7).



Fig. 3.7. SEM/EDS FEI Quanta 400 instrument.

3.6 Cation distribution procedure

Several different procedures may be adopted to determine cation distribution, and very satisfactory results have been obtained by combining data from single-crystal X-ray structural refinements and electron microprobe analysis (Carbonin et al. 1996; Andreozzi et al., 2001a; Lavina et al. 2002; Bosi et al. 2004; Lenaz and Princivalle 2011). This approach simultaneously takes into account both structural and chemical data and reproduces the observed parameters by optimizing cation distributions. Differences between measured and calculated parameters are minimized by the “chi-square” function:

$$F(X_i) = \sum_{j=1}^n \left(\frac{O_j - C_j(X_i)}{\sigma_j} \right)^2 \quad (22)$$

where O_j is the observed quantity, σ_j its standard deviation, X_i the variables, i.e., cation fractions in T and M sites, and $C_j(X_i)$ the same quantity as O_j calculated by means of X_i parameters. The n C_j quantities taken into account were: unit-cell and oxygen parameter, m.a.n. of T and M sites, total atomic proportions given by microprobe analyses, and constraints imposed by crystal chemistry (total charges and occupancies of T and M sites). Several minimization cycles of Equation 21 up to convergence were performed using a home-developed calculation routine. $F(X_i)$ values ≈ 1 mean good agreement among calculated and observed data

The a_0 and u values were linked to the cation site fractions (X_i) considering that the T-O and M-O bond distances were calculated as the linear contribution of each cation multiplied by its specific site bond distance, the latter refined on the basis of analysis of more than 250 spinel structural data from the literature (Lavina et al. 2002). However, for the synthetic Co-spinels using the bond length of 1.972(2) Å reported for ${}^T\text{Co}^{2+}\text{-O}$ in Lavina et al. (2002), low values in the minimization function were obtained only for the Co-rich terms. Best fits for all examined crystals were obtained using variable ${}^T\text{Co}^{2+}\text{-O}$ bond lengths, ranging from 1.966 Å in the Co-poor terms to 1.972 Å in the Co-rich terms. The final cation distribution was obtained by using the average value of 1.969(3) Å for ${}^T\text{Co}_{2+}\text{-O}$ along the entire solid-solution series. For the natural spinels the bond length of 1.949(1) Å was used for ${}^T\text{Zn-O}$, following Bosi *et al.* (2011) who showed that the ${}^T\text{Zn-O}$ value varies as a function of the M site population, increasing from 1.949 Å (for ${}^M\text{Al}$) to 1.980 Å (for ${}^M\text{Fe}^{3+}$).

Final $F(X_i)$ values confirmed that all chemical and structural parameters were reproduced on average within $\pm 2\sigma$, and hence that the corresponding cation distributions are highly reliable.

3.7. LA-ICP-MS instrument

The analyses were carried out using an 193 nm ArF excimer laser ablation system (Lambda Physik, Göttingen Germany) coupled to an ICP-MS (DRC II +, Perkin Elmer, Norwalk, USA) (Ottinger et al. 2005). The samples were ablated for 40 s (10Hz, 60 μm crater diameter) and the operating conditions are summarized in Table 3.4. The

reference material NIST 610 was used as external calibration standard and Al was used as internal standard. Data reduction and concentration calculation was carried out using the protocol as described in Longerich et. al. (1996).

Table 3.4 Operating conditions of the measurement at LA-ICP-MS.

| Parameter | Value |
|---------------------------------------|-------------------------|
| Laser type | ArF excimer |
| Laser wavelength | 193 nm |
| Spot diameter (sample and standard) | 60 μ m |
| Repetition rate (sample and standard) | 10 Hz |
| Laser energy | 22 J/cm ² |
| He carrier gas flow rate | 1.2L min ⁻¹ |
| RF power | 1380 |
| Nebulizer gas flow rate | 0.85 |
| Auxiliary gas flow rate | 0.75 |
| Coolant gas flow rate | 17.5 |
| Dwell time | 10 ms |
| Detector mode | Dual (pulse and analog) |

3.8. Raman spectroscopy instruments

The Raman analyses were carried out on the same crystals used for the structural refinements and chemical investigation, after removing the carbon-coated layer. In addition, five gems of natural spinels and a synthetic spinel synthesized by flame fusion Verneuil method were analyzed in order to distinguish between natural and synthetic spinels.

Raman spectroscopy was performed on the single crystal sample using a Jobin-Yvon Horiba LabRam microRaman apparatus at the Physics and Earth Sciences Department “Macedonio Melloni”, Università degli Studi di Parma. (Fig. 3.8).

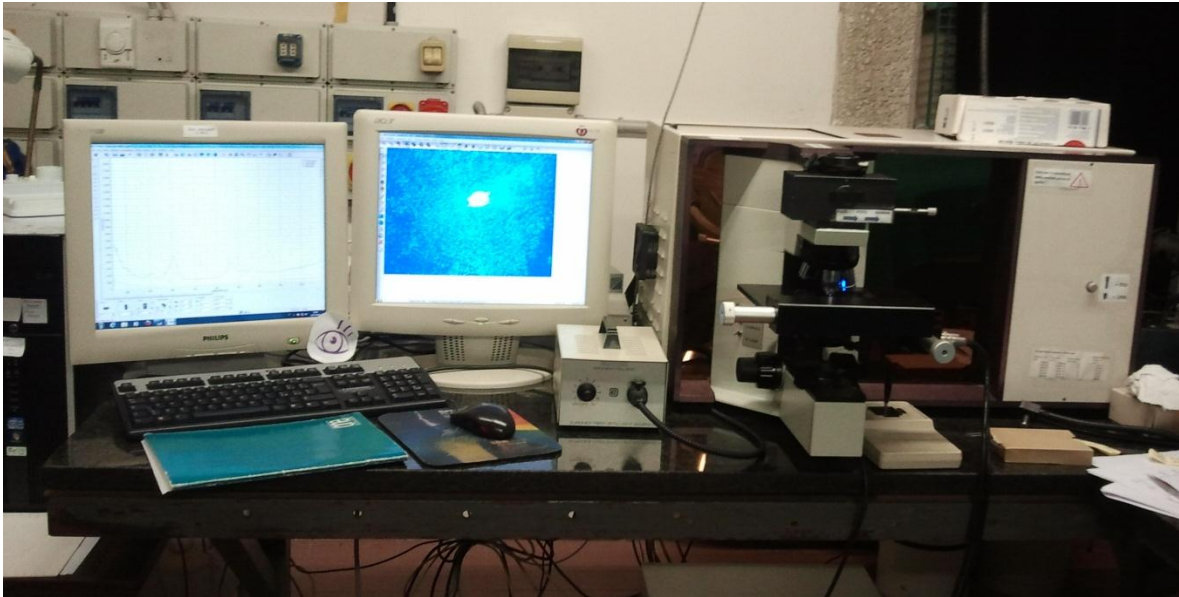


Fig.3.8. Jobin-Yvon Horiba LabRam microRaman apparatus.

The experiment in generally consist to light up the sample with a laser beam, then the light from the illuminated spot is collected with a lens and sent through a monochromator. Wavelengths close to the laser line due to elastic Rayleigh scattering are filtered out (through the Notch filter) while the rest of the collected light is dispersed onto a detector (CCD). In detail, several spectra were recorded using the excitation of both the red 632.8 nm line of a He-Ne laser and the blue 473.1 nm line of a solid state Nd:YAG laser. A filter wheel reduced the laser power to less than 1 mW on the sample. Laser power was controlled by means of a series of density filters in order to avoid heating effects. The system was calibrated using the 520.6 cm^{-1} Raman band of silicon before each experimental session. Spatial resolution was $\sim 1\text{ }\mu\text{m}$, whereas spectral resolution ranges between 2 and 3 cm^{-1} depending on the laser source. No attempt was done to measure oriented crystals. The peak positions were obtained from baseline-corrected spectra by least-squares spectral peak curve fitting using the computer program Labspec (Horiba). A Lorentzian profile was used in the peak profile analysis. At least 5 spectra were collected at different positions within the sample and the resulting spectra were found to be identical. The acquisition time ranges between 30 s to 180s. The typical Raman shift range for the spinel from 200

to 800 cm^{-1} was explored, but, in order to explore also the photoluminescence (PL) features, the analysis were carried up to 8000 cm^{-1} .

Raman and PL analysis were performed also with the GemmoRaman-532 instrument at the private laboratory of the gemologist Alberto Scarani (Fig. 3.9). Raman and PL spectra were recorded with the TEC-cooled 532nm DPSS laser (green) in the range $225\text{-}4700\text{ cm}^{-1}$. The acquisition time ranges between 200 s to 8000ms. Average acquisition number ranging between 6 and 50. Spectral resolution for the FWHM is 11 cm^{-1} .

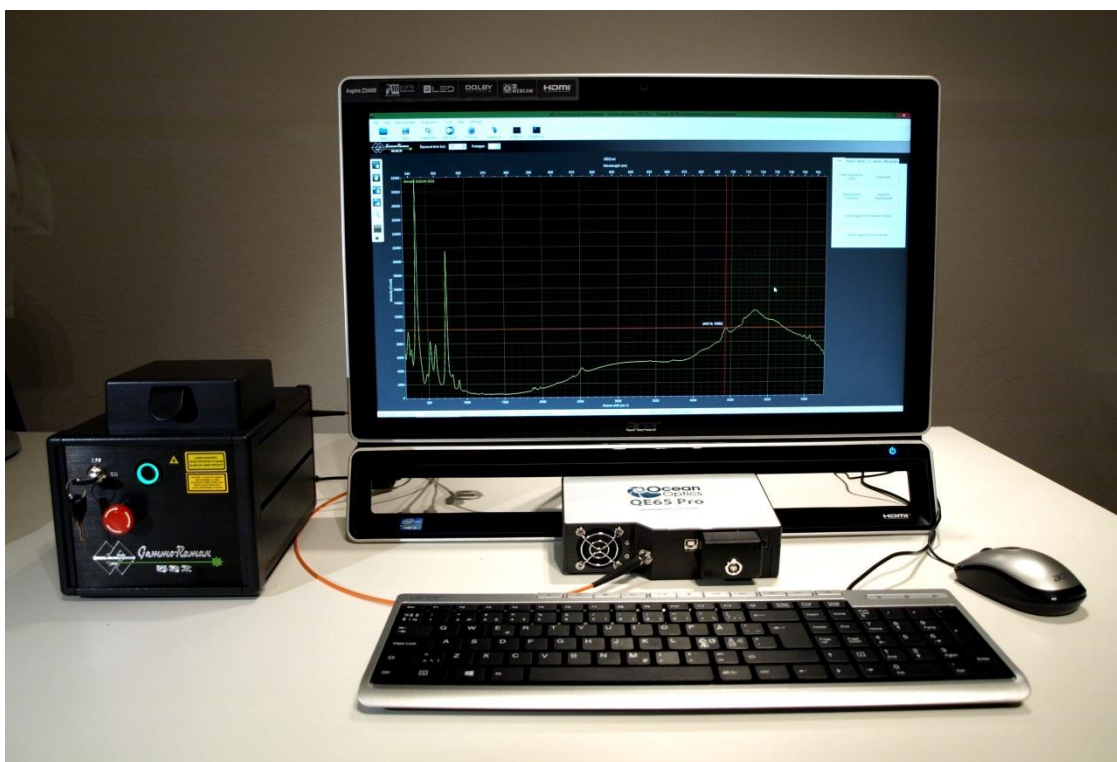


Fig. 3.9. GemmoRaman-532 instrument.

3.8.1. Polarized Raman spectra

In order to follow the shift and growth of each peak along the series, a polarized Raman study on single crystals was performed. In addition polarized Raman investigation represents a powerful tool for deducing the symmetry of vibrational modes. The assignment of Raman lines may be aided by measuring their intensity with a polarizing filter, first parallel and then perpendicular to the polarization of the

incident radiation. If the polarization of the scattered beam is the same as that of the incident beam (intense only in the parallel direction), then the Raman line is said to be *polarized*. If the scattered light is intense in both the parallel and perpendicular direction, then the Raman line is *depolarized*.

Unpolarized, polarized and depolarized Raman spectra were taken for all the synthetic spinel crystals. The corresponding polarizability tensors for the O_h cubic symmetry are:

$$A_{1g}: a \begin{pmatrix} 1 & 0 & 0 \\ 0 & 1 & 0 \\ 0 & 0 & 1 \end{pmatrix},$$

$$E_g: b \begin{pmatrix} 1 & 0 & 0 \\ 0 & 1 & 0 \\ 0 & 0 & -2 \end{pmatrix}, \quad b\sqrt{3} \begin{pmatrix} 1 & 0 & 0 \\ 0 & -1 & 0 \\ 0 & 0 & 0 \end{pmatrix},$$

$$F_{2g}: c \begin{pmatrix} 0 & 1 & 0 \\ 1 & 0 & 0 \\ 0 & 0 & 0 \end{pmatrix}, \quad c \begin{pmatrix} 0 & 0 & 1 \\ 0 & 0 & 0 \\ 1 & 0 & 0 \end{pmatrix}, \quad c \begin{pmatrix} 0 & 0 & 0 \\ 0 & 0 & 1 \\ 0 & 1 & 0 \end{pmatrix}$$

To describe the particular experimental configuration, the notation of Damen, Porto and Tell (1966) is used to describe the direction and polarization of the incident and scattered light. This notation consists of four letters, a(bc)d in general, expressing the direction of the propagation of the incident radiation (a), the polarization of the incident radiation (b), the polarization of the analyzed radiation (c) and the direction of propagation of the analyzed radiation (d). For example in the case of X(XY)Z, the term outside the parentheses refer to the direction of the incident and scattered beams, respectively, while inside they refer to the polarization directions. Only totally symmetric vibrations (a normal mode with all characters = 1 in the character table) give rise to polarized lines. Crossed polarizations of the incident and scattered light bring the modes about whose tensors contain the components out of the main diagonal. These are the F_{2g} modes. The A_{1g} and E_g modes can be observed when the incident and scattered beams are polarized in a parallel way. The analysis of the tensor components shows that the A_{1g} mode is the only one that remains extinct in a depolarized experiment regardless of the crystal orientation. This allows its

identification immediately. On the other hand, the intensities of the other modes will vary depending on the crystal orientation. For examples, to distinguish the E_g modes from the A_{1g} modes a rotation of the crystal by 45° in crossed polarization is required (Shebanova and Lazor, 2003)

Non-polarized micro-Raman spectra were obtained in nearly backscattered geometry with a Jobin-Yvon Horiba “Labram” apparatus, equipped with an Olympus microscope with $\times 10$, $\times 50$ and $\times 100$ objectives and a motorized x - y stage. The blue 473.1 nm line of a solid state Nd:YAG laser was used as excitation; laser power was controlled by means of a series of density filters in order to avoid heating effects. The polarized Raman investigation was made in synthetic spinels in the epoxidic resin and an orientation of the crystal is quite difficult. Only the $Z(XY)\bar{Z}$ and $Z(XX)\bar{Z}$ spectrum were taken and not in a specific crystallographic orientation.

3.9. Optical absorption spectroscopy instrument

3.9.1. Experimental conditions of synthetic spinels

Ten representative crystal fragments were selected along the $MgAl_2O_4$ - $CoAl_2O_4$ series. Nonpolarized room-temperature optical absorption spectra were recorded in the UV/VIS to NIR spectral range (330–2000 nm) on double-sided polished single crystals ranging in thickness from 13 to 390 μm with a Zeiss MPM800 microscope spectrometer equipped with Ultrafluar 10 \times objective and condensor lenses, Xenon arc 75W and Halogen 100 W light sources, blazed concave monochromators and photomultiplier and photoconductive PbS-cell detectors. The spectra were recorded at the Mineralogy Department, Naturhistoriska Riksmuseet, Stockholm, using a spot with a measured diameter of 40 μm during three cycles at a resolution of 1 and 5 nm in the UV/VIS (330–800 nm) and NIR (800–2000 nm) spectral regions, respectively. The accuracy of determined absorption band energies in the UV/VIS-NIR region is estimated on the basis of measured Ho_2O_3 -doped and Pr_2O_3/Nd_2O_3 -doped calibration standards (Hellma glass filters 666-F1 and 666-F7) to be better than 60 cm^{-1} . In the MIR range (2000–4000 nm) spectra were collected on the same single-crystal

absorbers as above during 128 cycles using a square-shaped $40 \times 40 \mu\text{m}$ aperture at a spectral resolution of 4 cm^{-1} with a Bruker Equinox 55S FTIR microscope spectrometer equipped with a glowbar source, KBr beamsplitter and a MCT-detector. Recorded spectra were fitted using the peak resolution program Jandel PeakFit 4.0 assuming Gaussian absorption bands.

3.9.2. Experimental conditions of natural spinels

Unpolarized room-temperature optical absorption spectra were recorded on single crystals in the spectral range 270-1100 nm ($37037\text{-}9091 \text{ cm}^{-1}$) at a spectral resolution of 1 nm using an AVASPEC-ULS2048X16 spectrometer attached via a $400 \mu\text{m}$ UV optical fiber to a Zeiss Axiotron UV-microscope (Fig. 3.10).



Fig. 3.10. Zeiss MPM800 single beam microscope-spectrometer.

The crystals studied by optical absorption spectroscopy are identical to the ones used for the EMP-analyses. These crystals were embedded in a thermoplastic resin, placed on a glass slide and polished on two parallel surfaces. The resulting thickness of each absorber was in the range 11–183 μm as determined by means of a digital micrometer. A 75 W Xenon arc lamp served as illuminating source, concave gratings served as monochromator, and a photomultiplier as detector. Spectra in the NIR spectral region from 1100 nm to 2000 nm ($9091\text{-}5000 \text{ cm}^{-1}$) were recorded on the

same crystal absorber with a Zeiss MPM800 single beam microscope-spectrometer using a 100 W halogen lamp as light source. Light detection was achieved by means of a photoconductive PbS-cell. The NIR-spectra were recorded at a spectral resolution of 5 nm. Zeiss Ultrafluar 10x lenses served as objective and condenser in all measurements. The size of the circular measure aperture ranged from 40 to 64 μm in diameter. The wavelength scale of the spectrometers was calibrated against Ho_2O_3 doped and $\text{Pr}_2\text{O}_3/\text{Nd}_2\text{O}_3$ doped standards (Hellma glass filters 666F1 and 666F7) with accuracy better than 15 cm^{-1} .

Spectroscopic data were also measured within the NIR-MIR range (2000–9000 nm) by means of a FTIR spectrometer (Bruker Equinox 55S) equipped with an IR microscope, equipped with a glowbar source, KBr beamsplitter and a MCT-detector (Fig. 3.11). Spectra were collected on the same single-crystal absorbers as above but with a thickness of 0.098 mm during 128 cycles using a square-shaped $40 \times 40\ \mu\text{m}$ aperture at a spectral resolution of 4 cm^{-1} .

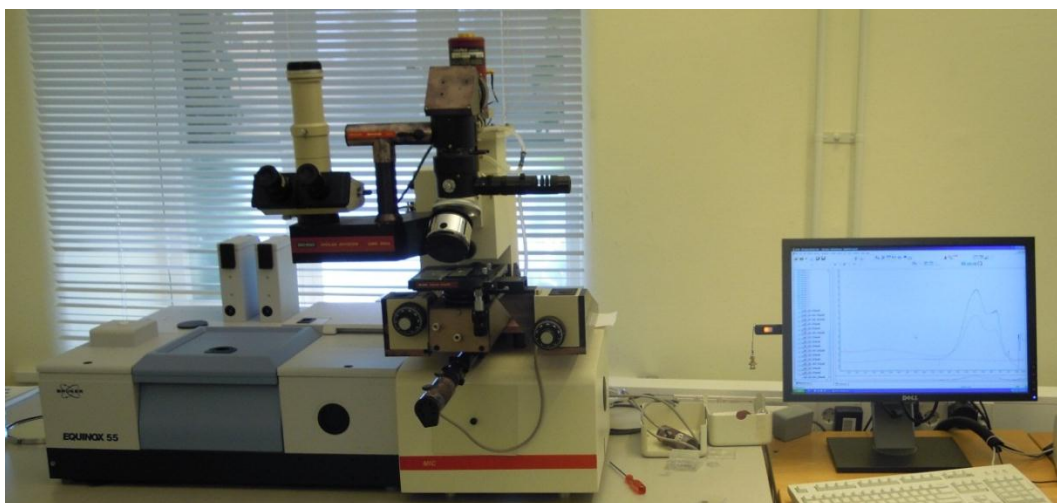


Fig. 3.11. Bruker Equinox 55S FTIR microscope instrument.

Recorded spectra in the UV-VIS-NIR-MIR range were deconvoluted using the peak resolution program Jandel PeakFit 4.12. In the deconvolution process all fitted bands were assumed to be of Gaussian shape. The recorded UV-absorption edges were also fitted with a Gaussian function. No other constraints were applied during the fitting procedure.

Chapter 4

RESULTS and DISCUSSION

4.1. Synthetic blue Co-spinels

Co-bearing spinels are very rare in nature, but are actively sought as gemstones due to their vivid, high-purity blue color that makes them more precious than sapphires. Previous studies evidenced small amounts of cobalt (CoO = 1 wt%) in natural gems of Sri Lanka (Shigley and Stockton, 1984) and in a sample from the island of Samos (Taran et al., 2009). Although the cobalt contents were very low, these natural Co-bearing spinel crystals showed light and fancy blue colors. Up to a few decades ago cobalt was considered a coloring agent only of synthetic blue spinel, whereas the blue color in natural spinel was attributed solely to iron. However, Shigley and Stockton (1984) demonstrated that both cobalt and iron are capable of producing blue colors in materials, and considerably less cobalt than iron is required to produce an equally intense blue. Besides the above mentioned natural Co-poor spinel crystals, the only reported natural occurrence of a Co-rich spinel (CoO \leq 22.8 wt%) is a very small crystal (\sim 200 μ m large) included in a gem-quality blue sapphire from Bo Phloi, Thailand (reported as Bo Ploi in gemological literature), occurring in alluvial/eluvial deposits near basaltic outcrops (Guo et al., 1994).

Synthetic CoAl_2O_4 spinel is a high-temperature oxide (melting point of 1955 $^{\circ}\text{C}$), and it is the most stable compound of a family of spinel-structured oxides obtained from Co_3O_4 at progressive increase of Al contents (Tielens et al., 2006, 2009). From an optical point of view, the increase of Al results in the transition from black Co_3O_4 to dark green Co_2AlO_4 , bright blue CoAl_2O_4 , and white $\text{Al}_{8/3}\text{O}_4$, that is, $\gamma\text{-Al}_2\text{O}_3$. These color changes are functions of both the oxidation states and the structural position of the cobalt cations. The black color is caused by total absorption of visible light due to the interactions between Co^{2+} and Co^{3+} (i.e., comparable to $\text{Fe}^{2+}\text{-Fe}^{3+}$ in magnetite), the dark green color is ascribed to electronic transitions in Co^{3+} in octahedral coordination, and the bright blue color results from electronic transitions in Co^{2+} in

tetrahedral coordination (Burns, 1993; Fernández and Pablo 2002; Tielens et al. 2006, 2009; Kurajica et al. 2011). Besides, when Co^{2+} is in octahedral coordination (as in pyroxene $\text{CaCoSi}_2\text{O}_6$) the hue becomes pink (Mantovani et al., 2012). From a coloring point of view, cobalt in tetrahedral coordination has a higher hiding power with respect to the octahedral coordination (Llusar et al., 2001). Cobalt aluminate was utilized since the Middle Ages under the pigment form of *smalt* (a potassium glass containing cobalt) and some authors also reported an uncommon use of cobalt aluminate pigment in ancient Egyptian ceramics (Bouchard and Gambardella, 2010). Except these few occurrences, the bright blue synthetic CoAl_2O_4 , commercially well known as Thenard's blue, has been extensively used, since the discovery of its industrial synthesis route in 1802, as a pigment (classified with the DCMA number 13-26-2) for the coloration of ceramics, glazes, porcelain enamels, glass, paint, fibers, paper, cement, rubber, plastics, and cosmetics. Cobalt-bearing pigments, commonly Co-spinel and Co-olivine, are the most efficient and widely used blue ceramic pigments, but the spinel is strongly preferred to olivine since a navy blue color can be obtained with strongly reduced CoO content (42 wt% in CoAl_2O_4 against 71 wt% in Co_2SiO_4), besides some differences in color saturation (Eppler and Eppler, 2000). In addition to pigment industry, cobalt-aluminate and iron-manganite spinels have been successfully used for heterogeneous catalysis such as NO_x reduction or the CO_2 reforming of methane (Hou and Yashima, 2004; Fierro et al., 2005).

Because of the chemical complexity frequently observed in natural spinel samples, a large number of crystal-chemical studies have been performed on synthetic materials of well-defined compositions, with the objective to model their physical properties. As for example, CoAl_2O_4 has been extensively synthesized by several methods: sol-gel method (Sales et al. 1997; Areán et al. 1999), coprecipitation method (Chokkaram et al. 1997; Rangappa et al. 2007), polymeric precursor method (Cho and Kakihana 1999; Gama et al. 2009), solid-state reactions (Chemlal et al. 2000; Melo et al. 2003; Suzuki et al. 2007), combustion synthesis (Mimani and Ghosh 2000; Li et al. 2003), hydrothermal synthesis (Chen et al. 2003), complexation method (Wang et al. 2006; Mindru et al. 2010) floating-zone technique (Maljuk et al. 2009). The solid solution

(Co,Mg)Al₂O₄ was explored by Angeletti et al. (1977), by calcination of alumina powder soaked in cobalt nitrate solution to 1200 °C. They obtained six compounds, mainly consisting of powder or nanosized particles of cobalt spinel.

The chemical composition of synthetic powder materials is difficult to characterize accurately, especially when transition elements with more than one oxidation state are present. An alternative approach is to synthesize large single crystals, which offer the potential for high-accuracy material characterization.

Despite the interest in CoAl₂O₄ (and Co-bearing materials with spinel structure) due to its physical properties, very little structural information is available in literature, and many aspects regarding electronic structure and cation distribution are not well understood or are even unknown. In this regard, the steric factors seem to be very important for the cation allocations in the structural sites as exemplified by, e.g., FeAl₂O₄, CuAl₂O₄, and CoAl₂O₄ spinels (Harrison et al., 1998; O'Neill, 1994; O'Neill et al., 2005), in which the small Al³⁺ cation prefers the larger octahedral coordination to the tetrahedral one. In these spinels, cation size and crystal field stabilization energy suggest that Fe²⁺, Cu²⁺, and Co²⁺ should prefer the octahedra, but the presence of Al obviously counteracts this behavior. The CoAl₂O₄ spinel is in fact an almost normal spinel with Co²⁺ ions ordered at the tetrahedrally coordinated (T) and Al³⁺ ions ordered at the octahedrally-coordinated sites (M) sites in the slightly distorted cubic close packed of oxygens. Previous studies on CoAl₂O₄ include investigations of electron density (Toriumi et al. 1978), crystal field transitions (e.g., Kuleshov et al., 1993) and cation distribution as a function of temperature (O'Neill 1994; Nakatsuka et al. 2003). In particular, the latter authors highlighted that at high temperatures, limited fractions of the Co²⁺ and Al³⁺ ions may interchange their structural positions. Nevertheless, systematic investigation of the structural variations all along the entire (Mg_{1-x}Co_x)Al₂O₄ solid-solution series is missing.

In the present study, a flux growth method was used and experimental conditions were optimized to obtain high-quality single crystals of spinel with compositions corresponding to the solid-solution series MgAl₂O₄-CoAl₂O₄. Then the materials

obtained have been investigated by a combined chemical, structural and spectroscopic approach via scanning electron microscope (SEM), electron microprobe (EMP), and X-ray diffraction (XRD), in order to reveal structural details and improve our understanding of the factors that affect cation distribution and influences some of the physical properties (e.g., color).

The following chemical, structural and spectroscopic characterizations have been published in the American Mineralogist (D'Ippolito et al., 2012; Bosi et al., 2012). Part of these data has been here rearranged, or implemented with further data for a more exhaustive description.

4.1.1 Synthesis and chemical characterization

Conditions adopted during flux growth proved to be well optimized as demonstrated by the large number of spinel single crystals obtained from every experimental run. Apart from the first tentative run (CoAl_{0.5}, see experimental section), all subsequent runs had the same thermal path and cooling rate. Crystals were formed in the range between 1200 and 800 °C, with an exception being sample CoAl₅₀, which by accident was quenched before the end of the slow cooling stage. The unintentional breaking of the wire that holds the crucible in the vertical furnace resulted in a rapid cooling of the crystals of this run in the middle of the growth process. In spite of this, good quality spinel crystals were retrieved and the quenching temperature was estimated to be approximately 1000 °C. Due to this difference in thermal history, it may be expected that the structural/physical properties of sample CoAl₅₀ will differ from the general trends identified for the majority of the other samples.

A large number of spinel single crystals were obtained from every experimental run. Crystals appear as inclusion-free, regular octahedra sized up to 1.2 mm in diameter, variable in color from light blue to intensely dark blue as a function of chemical composition (Table 3.2 in chapter 3). With rising total cobalt content the saturation of the vivid blue color increases but no shift in color hue is observed along the series (Fig. 4.1).

In contrast, distinct color shifts were observed by the naked eye (and confirmed by optical absorption spectroscopy) in Fe^{2+} - and Cr^{3+} -bearing spinel solid-solution series previously synthesized (Hålenius et al., 2002 2010).

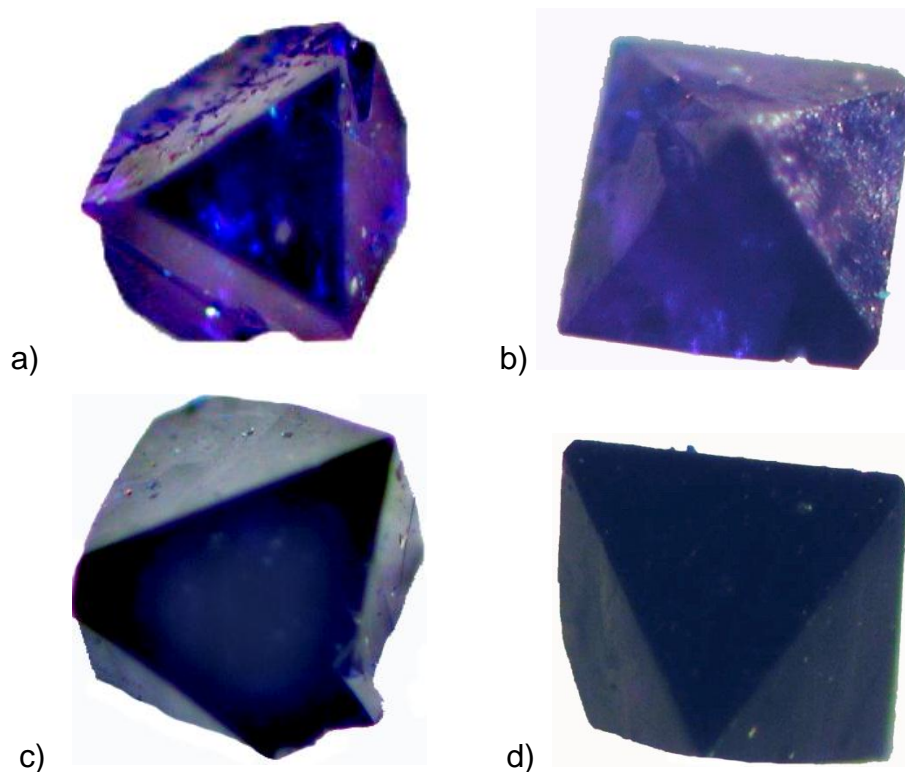


Fig. 4.1. Photomicrographs of selected synthetic spinel single crystals: (a) sample CoAl1; (b) CoAl10, (c) CoAl20, (d) CoAl100. Crystal size is approximately 300 μm .

Besides large single crystals, solid crusty aggregates and loose microcrystalline powder were also obtained from most of the experiments and usually retrieved from the bottom of the Pt-crucible. SEM inspection showed that both the crusts and the powder consist of smaller spinel crystals (probably second generation or influenced by the interaction with the crucible walls) with octahedral shape and sharp edges (Fig. 4.2).

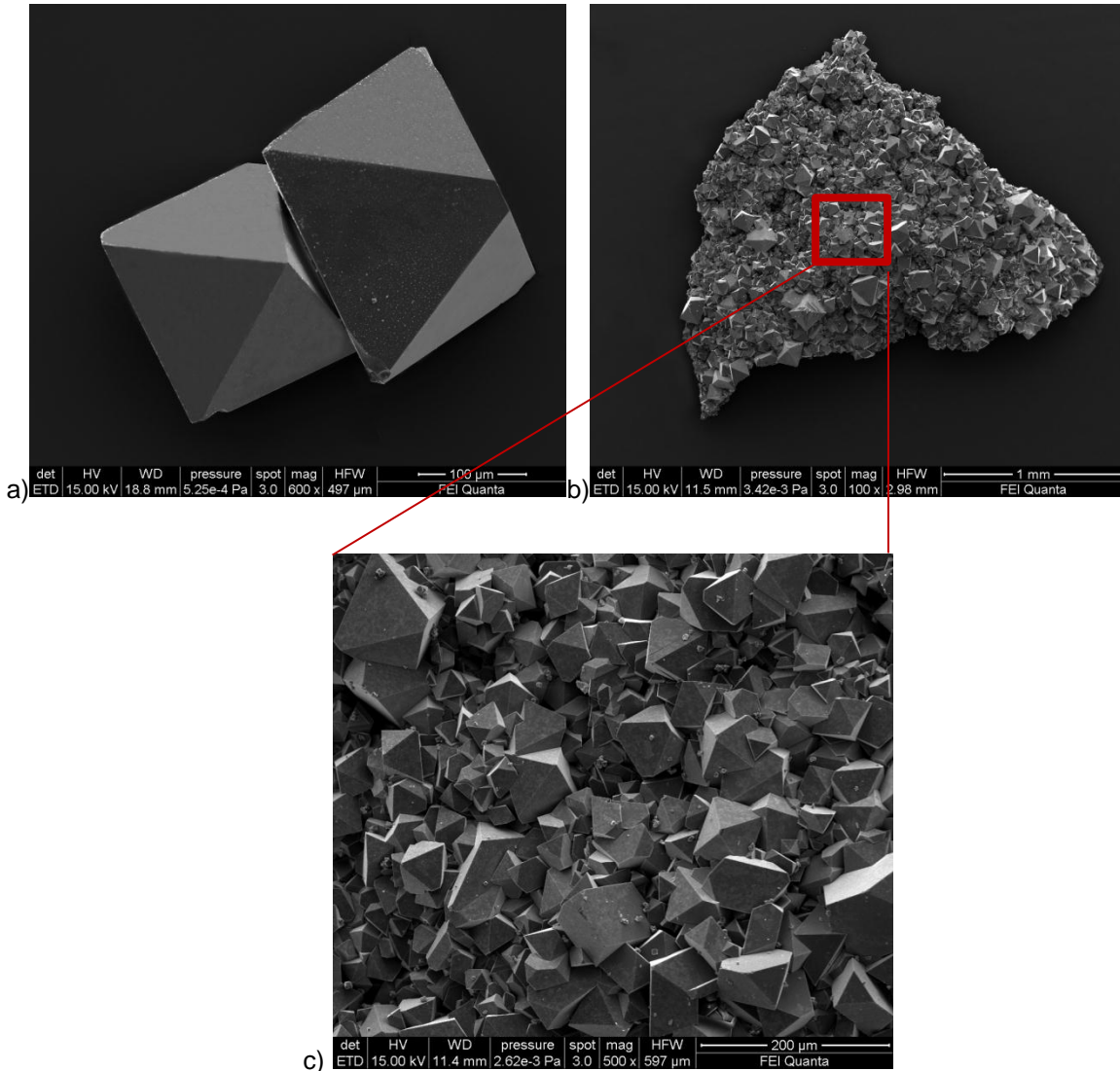


Fig. 4.2. SEM images of selected small spinel samples retrieved at the bottom of the Pt crucible: (a) single crystals (magnification 600×); (b) crusty aggregates (magnification 100×); (c) a detail of the crusty aggregates with single crystal from 10 to 100 μm ((magnification 500×).

Some samples showed a dendritic formation on the faces which exhibited the same chemical composition of the sample (Fig. 4.3). Despite the crystals are not subjected to quenching during the synthesis experiment, probably the samples felt the effect of the rapid cooling from 800°C to the room temperature. In fact, at slow rates of crystal growth, the interface between melt and solid remains planar, and growth occurs uniformly across the surface. At faster rates of crystal growth, instabilities are more likely to occur; this leads to the dendritic growth. These formations are up to 8 μm size and do not influence the analysis.

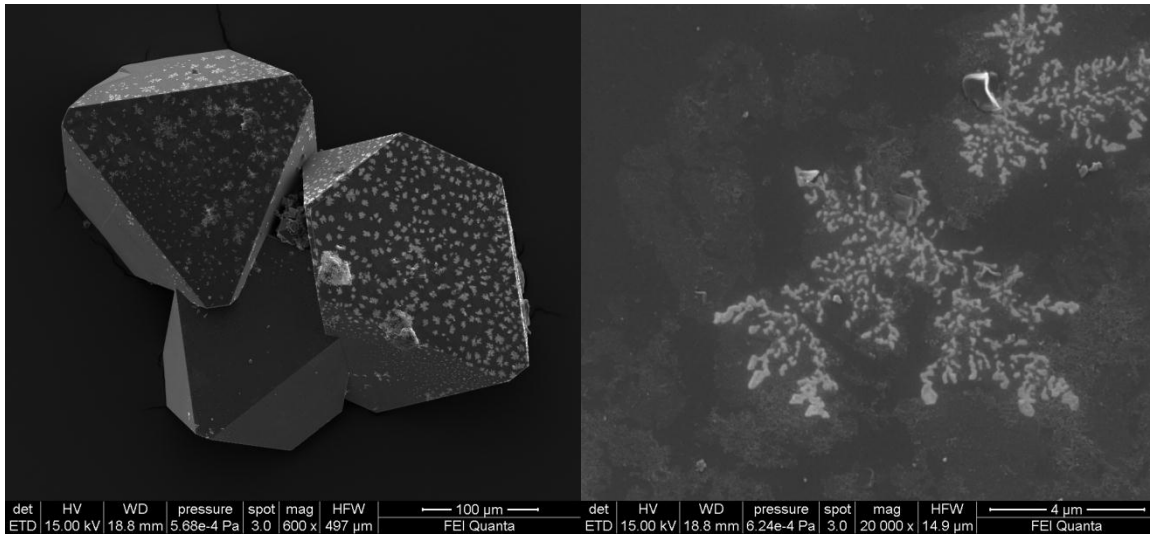


Fig. 4.3. Dendritic formation on the faces of the crystal spinel.

Chemical characterization via EMP confirmed that both large and small crystals belong to the $(\text{Mg},\text{Co})\text{Al}_2\text{O}_4$ spinel series, without evidence of other phases. This is an experimental confirmation of what was expected on the basis of ab initio calculations by Tielens et al. (2009), who showed the larger thermodynamic stability of the CoAl_2O_4 phase with respect to other $(\text{Co},\text{Al})_3\text{O}_4$ phases. These authors also predicted that the formation process of CoAl_2O_4 is largely exothermic and consequently this phase is highly stable with respect to decomposition. The present spinels satisfactorily represent the whole MgAl_2O_4 - CoAl_2O_4 solid solution as their CoAl_2O_4 component ranges from 7 to 100 mol% (Table 4.1).

Table 4.1. Average chemical composition and unit-cell parameter (*a*) of synthetic crystals belonging to the MgAl₂O₄-CoAl₂O₄ series.

| Sample | CoAl0.5 | CoAl1 | CoAl10 | CoAl14 | CoAl20 |
|--|----------------|---------------|---------------|---------------|----------------|
| MgO | 25.9(7) | 25.2(1) | 24.2(9) | 20.0(1) | 17.8(7) |
| CoO | 3.6(5) | 4.4(1) | 5.3(1) | 12.4(3) | 16.9(3) |
| Al ₂ O ₃ | 70.5(4) | 70.3(3) | 70.2(3) | 67.1(3) | 66.2(3) |
| Tot. | 100.0 | 99.9 | 99.7 | 99.5 | 100.9 |
| Cations on basis of 4 oxygen anions | | | | | |
| Mg | 0.929(4) | 0.908(3) | 0.878(4) | 0.753(4) | 0.676(4) |
| Co ²⁺ | 0.069(1) | 0.085(2) | 0.103(3) | 0.251(3) | 0.344(3) |
| Al | 2.002(4) | 2.005(4) | 2.012(5) | 1.997(5) | 1.986(4) |
| Tot. | 3.000 | 2.998 | 2.993 | 3.001 | 3.006 |
| Sample | CoAl34 | CoAl45 | CoAl50 | CoAl67 | CoAl100 |
| MgO | 13.1(5) | 10.5(4) | 9.1(1) | 6.0(1) | - |
| CoO | 22.4(5) | 27.2(6) | 29.0(2) | 34.0(1) | 43.1(3) |
| Al ₂ O ₃ | 63.8(2) | 62.3(3) | 62.0(2) | 59.3(6) | 57.3(2) |
| Tot. | 99.3 | 100.0 | 100.1 | 99.3 | 100.4 |
| Cations on basis of 4 oxygen anions | | | | | |
| Mg | 0.520(4) | 0.424(6) | 0.369(3) | 0.252(5) | - |
| Co ²⁺ | 0.478(4) | 0.590(14) | 0.635(4) | 0.768(4) | 1.017(5) |
| Al | 2.001(5) | 1.991(13) | 1.997(2) | 1.986(4) | 1.989(5) |
| Tot. | 2.999 | 3.005 | 3.001 | 3.006 | 3.006 |

Cation sums are in excellent agreement with the expected value required from spinel stoichiometry and this is a good indication against any presence of Co³⁺. The absence of Co³⁺ in our samples was expected due to the strongly reducing conditions imposed during crystal growth, and it has been also confirmed by UV-VIS-NIR spectroscopy and crystal structure refinements. Moreover, EMP spot analyses indicate compositional homogeneity within a single crystal, further evidenced by SEM/EDS X-ray mapping, which displays for all samples the lack of chemical zoning via uniform spatial distribution of Co (Fig. 4.4). In contrast, in Cr-bearing synthetic spinels previously produced a strong Cr enrichment was observed in the core region, especially in samples with low nominal Cr-contents (Hålenius et al. 2010).

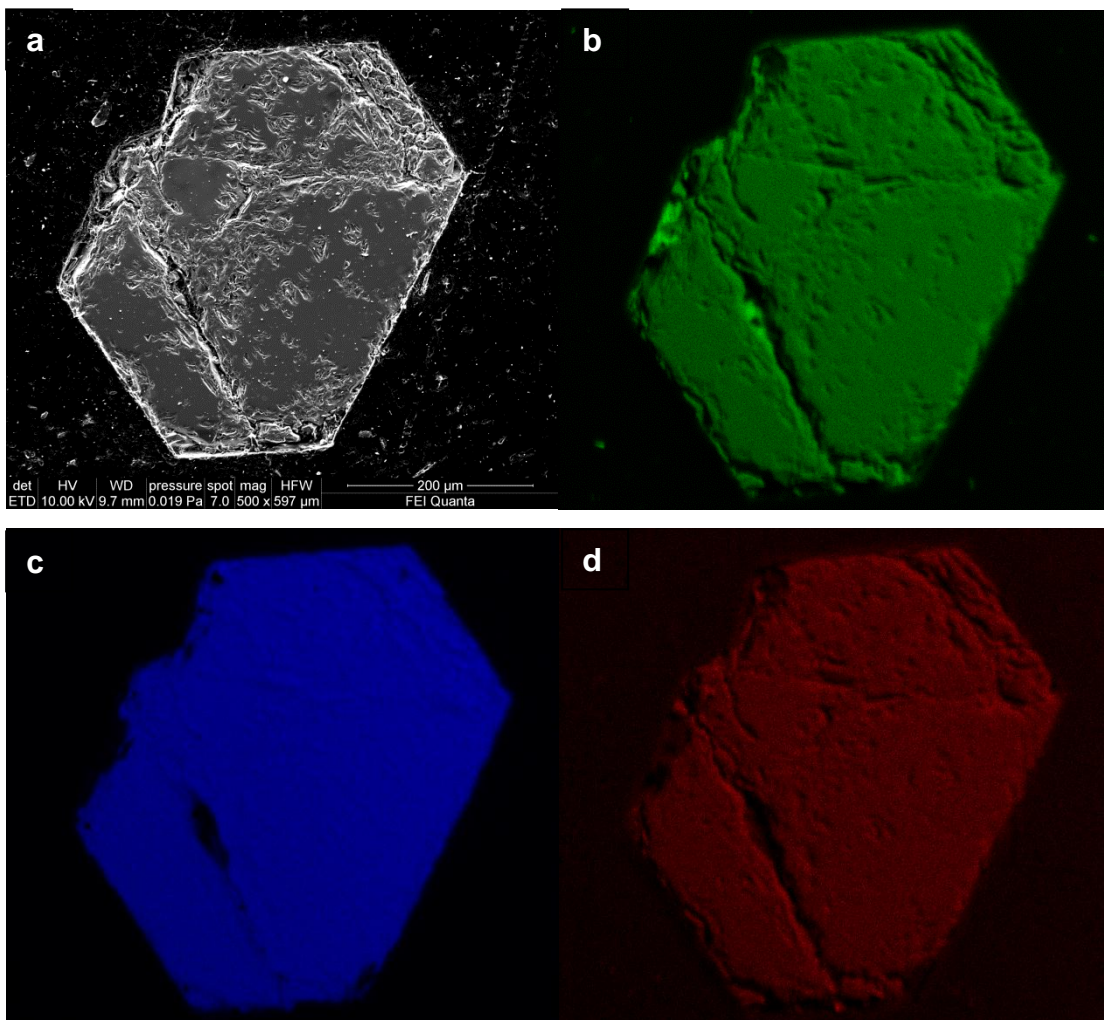


Fig. 4.4. SEM/EDS X-ray map of CoAl₆₇ sample: (a) SEM image of a polished crystal; (b) uniform spatial distribution of Al concentration (c) uniform spatial distribution of Co concentration (d) uniform spatial distribution of Mg concentration.

If a comparison between the composition of starting oxide mixture (reagents) and the composition of crystalline materials (products) is made, it is evident that the CoAl₂O₄ component of our products does not show a linear relationship with the analogous component of the reagents, but rather a distinct symmetrical deviation (Fig. 4.5). In particular, the difference between products and reagents is zero at the two end-members and reaches a maximum value of ca. 14% (in terms of CoAl₂O₄ component expressed in mol%) for the samples in the central part of the series (CoAl₃₄, CoAl₄₅, and CoAl₅₀), reflecting a concentration of cobalt into the crystalline phase. It is noteworthy that opposite behavior was observed in the previously synthesized

MgAl₂O₄-MgCr₂O₄, MgAl₂O₄-FeAl₂O₄ and MgAl₂O₄-MnAl₂O₄ solid-solution series (Andreozzi and Lucchesi, 2002; Hålenius et al., 2010, 2011). A plot of corresponding data for those two binary systems shows a marked depletion of their transition metal component in the crystal products with respect to the starting reagents. Notably, the first two series show a marked depletion of their component in the crystals with respect to the starting reagents. On the opposite, the third one shows a strong enrichment of the MgCr₂O₄ component in the crystals.

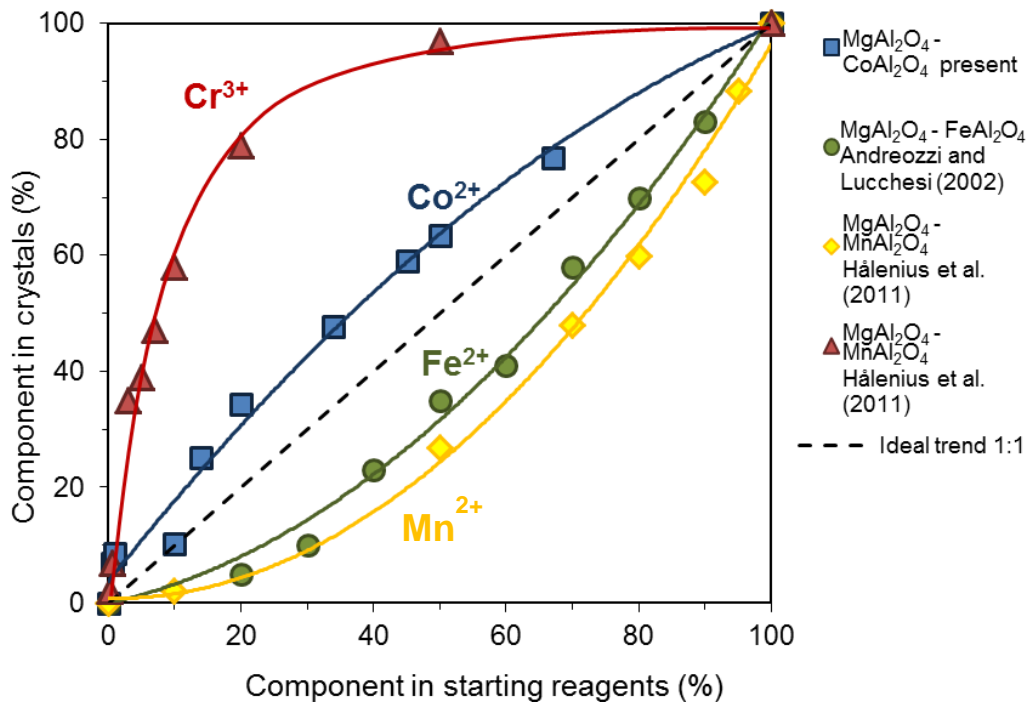


Fig. 4.5. Comparison (in terms of chemical components expressed in mol%) between crystal products and starting reagents along the solid-solution series MgAl₂O₄-AAl₂O₄ (with A = Co²⁺, Fe²⁺, and Mn²⁺) and MgAl₂O₄-MgCr₂O₄ series. Continuous lines = best fit to experimental data; dashed line = 1:1 ideal trend.

This behavior may be tentatively explained by considering that partitioning of transition element cations between minerals and coexisting melt is strongly influenced by Octahedral Site Preference Energy (OSPE) in crystal structures. The OSPE parameter is the difference between the crystal field energy of a cation in octahedral coordination (CFSE_o) and that in tetrahedral coordination (CFSE_t). As for example, in several silicate systems a relationship between OSPE and distribution coefficients

has been demonstrated for transition metal ions (Leeman and Scheidegger, 1977; Takahashi, 1978). The latter authors showed that the partition coefficient (toward crystals) between olivine and silicate groundmass follows the sequence $\text{Co} > \text{Fe} > \text{Mn}$, that is exactly what is predicted on the basis of CFSE and observed in Figure 4.5 for spinels. In addition Klemme et al., (2006) calculated the partitioning of trace elements between spinel crystals and silicate melts, and found that the distribution coefficient of Cr is considerably higher than that of Co, in agreement with high value of OSPE of Cr^{3+} (Table 4.2). This is particularly relevant because in borates and borate glass there are only availability of tetrahedral sites (Osipov and Osipova, 2009), so that during the crystal growth from borate system, as in our case, transition metal ions will enter in the spinel crystals according to their OSPE. However, CFSE contributes less than 10% to the total lattice energy (Burns, 1993), so that other factors must have a larger influence on cation partitioning.

According to Goldschmidt's rules, when two different ions occupy a particular position in a crystal structure, the ion with the higher ionic potential (namely charge/radius ratio) forms a stronger bond with anions. In this light the behavior observed in Figure 4.5 may be easily explained bearing in mind that the ionic potential is ranked $\text{Cr}^{3+} > \text{Co}^{2+} > \text{Fe}^{2+} > \text{Mn}^{2+}$ (Table 4.2).

Table 4.2. Ionic potential and OSPE for the different cation involved in the synthesis.

| Ion | Ionic potential | OSPE (kcal/mole) |
|------------------------|------------------------|-------------------------|
| Cation 2+ | | |
| Mn²⁺ | 3.049 | 0 |
| Fe²⁺ | 3.226 | 4.0 |
| Co²⁺ | 3.378 | 7.4 |
| Cation 3+ | | |
| Fe³⁺ | 4.651 | 0 |
| Cr³⁺ | 4.878 | 37.5 |

On the basis of both the above interpretations and results previously obtained (Hålenius et al. 2010, 2011; Bosi et al. 2011), it seems that, better than electronic interactions, steric factors (e.g., size of the ions) are central to determine the cation

intra-crystalline distribution in the aluminate spinel structure as well as inter-crystalline partitioning between aluminate spinels and other phases.

4.1.2 Structural and spectroscopic characterization (long and short range)

The recorded optical absorption spectra show two intense absorption bands at $\sim 17.000\text{ cm}^{-1}$ (ν_3) and $\sim 8.000\text{ cm}^{-1}$ (ν_2) in the visible and near infrared, and a weak and broad absorption bands at $\sim 4.500\text{ cm}^{-1}$ (ν_1) in the medium infrared (Figs. 4.6 and 4.7). Each of the three observed band regions is split in three absorption peaks due to first-order spin orbit coupling effects.

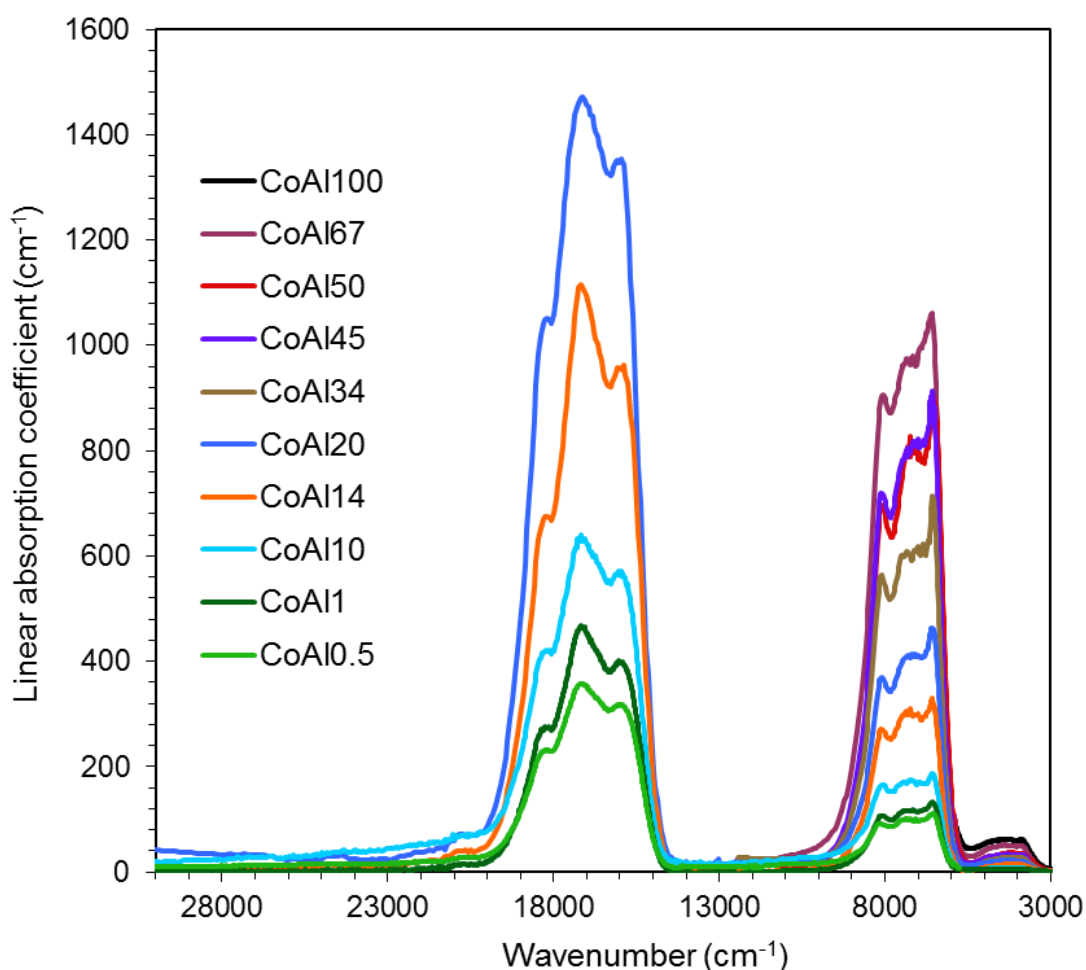


Fig. 4.6. Nonpolarized single-crystal absorption spectra of the $(\text{Mg}_{1-x}\text{Co}_x)\text{Al}_2\text{O}_4$ series. Complete spectra into the UV-region could not be recorded for the high-Co crystals CoAl34 to CoAl100 because of difficulties to prepare sufficiently thin absorbers ($\leq 8\ \mu\text{m}$).

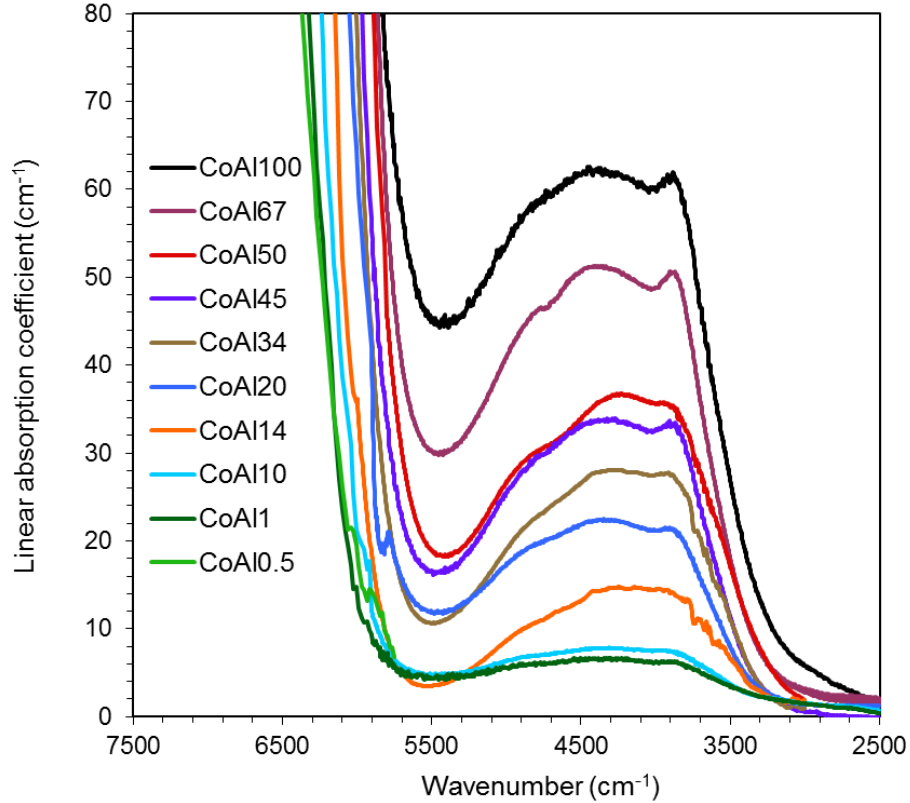


Fig. 4.7. Nonpolarized single-crystal absorption spectra of the split ${}^4A_2 \rightarrow {}^4T_2(F)$ transition in tetrahedrally coordinated Co^{2+} in the $(\text{Mg}_{1-x}\text{Co}_x)\text{Al}_2\text{O}_4$ spinel series. Low Co-content in combination with limited crystal size and low molar absorption coefficient precluded recordings of this transition in sample CoAl0.5.

These optical absorption spectra are in general agreement with published spectra of natural cobalt-bearing spinel (Taran et al. 2009) and in the spectrum of synthetic Co^{2+} bearing MgAl_2O_4 (Dereń et al. 1994). The two main absorption bands, which increase in intensity with increasing cobalt content, are assigned to the spin-allowed electronic transitions ${}^4A_2 \rightarrow {}^4T_1(P)$ and ${}^4A_2 \rightarrow {}^4T_1(F)$ of ${}^1\text{Co}^{2+}$, in accordance with Tanabe-Sugano diagram for the d^7 in tetrahedral crystal field. The third low-energy absorption band is due to spin-allowed transition ${}^4A_2 \rightarrow {}^4T_2(F)$ of tetrahedrally coordinated Co^{2+} . The absorbance in the three band regions vary greatly, with absorption caused by the split ${}^4A_2 \rightarrow {}^4T_1(P)$ transition displaying a linear absorption coefficient ca. 2 orders of magnitude stronger than for the ${}^4A_2 \rightarrow {}^4T_2(F)$ transition. The triple band in the visible range absorbs green, yellow-orange and red light, causing peculiar blue coloration of Co-bearing spinels. The reason for the observed low intensity for bands caused by

the latter transition is that they represent electric-dipole forbidden transitions. In spectra of the sample CoAl0.5 it was not possible to record bands caused by the ${}^4A_2 \rightarrow {}^4T_2(F)$ transition due to their low intensity in combination with low Co-concentration and small crystal sizes. On the contrary, in spectra of the sample CoAl100, corresponding to the end-member CoAl_2O_4 , it was impossible to observe peak positions of the strong bands caused by the split ${}^4A_2 \rightarrow {}^4T_1(F)$ transition due to very high absorption coefficients in combination with high Co-concentrations and difficulties to prepare sufficiently thin double-sided polished sections (thickness $\leq 8 \mu\text{m}$ would have been required). For the same reasons, peak positions of the extremely strong bands caused by the split ${}^4A_2 \rightarrow {}^4T_1(P)$ transition could not be determined from spectra of the samples spanning from CoAl34 to CoAl100.

Energies of the observed bands caused by the three split spin-allowed transitions as determined from the peak fitting procedure are summarized in Table 4.3.

Table 4.3. Energies (cm^{-1}) of absorption bands caused by spin orbit coupling split spin-allowed transitions in tetrahedrally coordinated Co^{2+} .

| Sample | CoAl0.5 | CoAl1 | CoAl10 | CoAl14 | CoAl20 | CoAl34 | CoAl45 | CoAl50 | CoAl67 | CoAl100 |
|---------------------------|---------|-------|--------|--------|--------|--------|--------|--------|--------|---------|
| Transition | | | | | | | | | | |
| ${}^4A_2(F) - {}^4T_2(F)$ | | 4927 | 4916 | 4962 | 4913 | 4989 | 4891 | 4865 | 4886 | 4959 |
| | | 4388 | 4360 | 4374 | 4344 | 4417 | 4346 | 4364 | 4320 | 4315 |
| | | 3842 | 3834 | 3807 | 3799 | 3838 | 3839 | 3857 | 3833 | 3812 |
| ${}^4A_2(F) - {}^4T_1(F)$ | 8196 | 8156 | 8153 | 8164 | 8149 | 8152 | 8161 | 8152 | 8103 | |
| | 7178 | 7170 | 7212 | 7179 | 7187 | 7151 | 7195 | 7163 | 7276 | |
| | 6512 | 6515 | 6509 | 6514 | 6512 | 6510 | 6524 | 6460 | 6579 | |
| ${}^4A_2(F) - {}^4T_1(P)$ | 17834 | 17802 | 17865 | 17813 | 17762 | | | | | |
| | 17315 | 17394 | 17337 | 17406 | 17314 | | | | | |
| | 16606 | 16782 | 16614 | 16743 | 16755 | | | | | |

Note: Estimated relative standard uncertainties in band energies are 0.5%.

The intensities of the absorption band vary linearly with the Co^{2+} content. A linear relationship ($R^2=0.98$) between the linear absorption coefficient values of the

maximum absorption band at $\sim 17000\text{ cm}^{-1}$ and the ${}^T\text{Co}^{2+}$ content (in apfu) is obtained (Fig. 4.8):

$$\alpha = 4176.5[{}^T\text{Co}^{2+}] \quad (23)$$

Hence, a cobalt content of 0.001 apfu may provoke a linear absorption coefficient equal to 4 that is strong enough to produce a color.

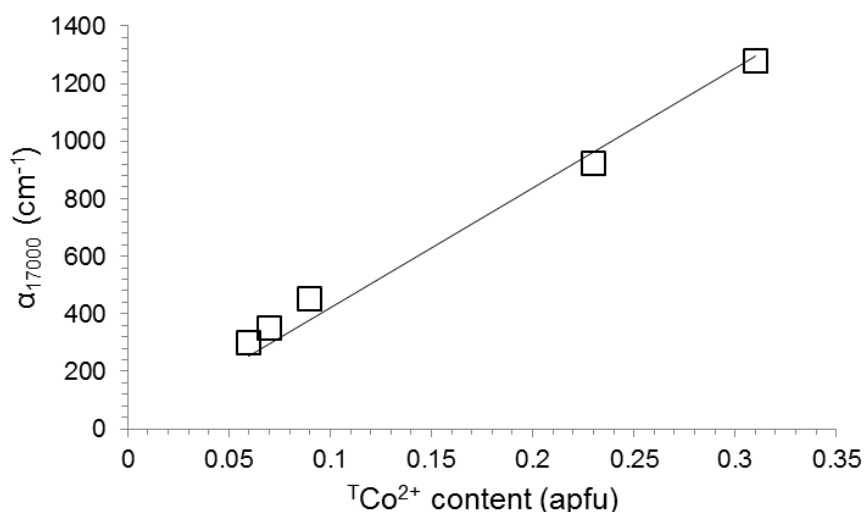


Fig. 4.8. Correlation plot between linear absorption coefficient of the absorption band at 17000 cm^{-1} and the ${}^T\text{Co}^{2+}$ content (apfu).

In addition it is evident from the peak positions of the fitted spectra that energies of all the observed main bands caused by electronic transitions in tetrahedrally coordinated Co^{2+} display only very marginal energy shifts with progressive Co^{2+} -Mg substitution at the T site (Fig. 4.9). The observed behavior has practical consequences because, together with the increase of absorption band intensity as a function of Co^{2+} content, it is the reason for both the absence of color shift and the perceived intensification of blue color of the crystals along the series. Notably, this is significantly different from what is observed in MgAl_2O_4 - FeAl_2O_4 and in MgAl_2O_4 - MgCr_2O_4 spinel solid-solution series, where a marked color shift (and absorption intensification) from pale lilac to dark green and from light red to dark green was observed as a function of Fe^{2+} and of Cr^{3+} content, respectively (Hålenius et al. 2002, 2010)

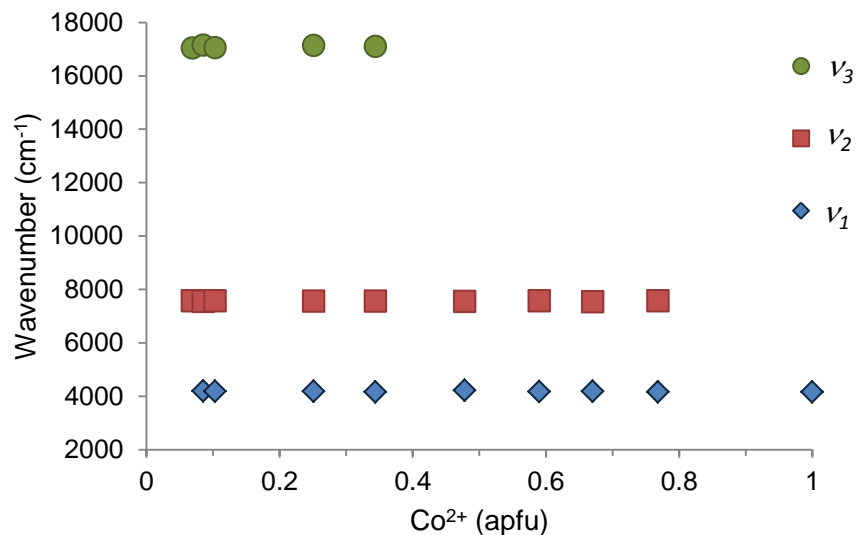


Fig. 4.9. Variation of the peak positions of the three absorption bands along the series.

The crystal field splitting parameter Dq , the Racah B -parameter and spin-orbit coupling λ -parameters for Co^{2+} at the T site may be calculated from the energies of the observed spin-allowed d-d transitions applying the Tanabe-Sugano equations (e.g. Oh et al., 2000; Pappalardo and Dietz, 1961):

$$\begin{aligned}
 {}^4A_2(F) \rightarrow {}^4T_2(F) (\nu_1): & \quad 10Dq + 5/2 |\lambda_0| \\
 & \quad 10Dq + |\lambda_0| \\
 & \quad 10Dq - 3/2 |\lambda_0| \\
 {}^4A_2(F) \rightarrow {}^4T_1(F) (\nu_2): & \quad 18Dq + 9/4 |\lambda_1| \\
 & \quad 18Dq - 6/4 |\lambda_1| \\
 & \quad 18Dq - 15/4 |\lambda_1| \\
 {}^4A_2(F) \rightarrow {}^4T_1(P) (\nu_3): & \quad 15B + 12Dq + 5/2 |\lambda_2| \\
 & \quad 15B + 12Dq + |\lambda_2| \\
 & \quad 15B + 12Dq - 3/2 |\lambda_2|
 \end{aligned}$$

Table 4.4 summarizes the parameters resulting from best fits of the energies of the spin-allowed transitions observed in our spectra for tetrahedrally coordinated Co^{2+} .

Table 4.4. Energies (cm⁻¹) of spin-allowed ^TCo²⁺-bands and crystal field splitting, repulsion and spin orbit coupling parameters.

| Sample | *V _{1soc} | *V _{2soc} | *V _{3soc} | Dq | B | λ ₀ | λ ₁ | λ ₂ |
|----------------|--------------------|--------------------|--------------------|-----|-----|----------------|----------------|----------------|
| CoAl0.5 | | 7578 | 17044 | 421 | 799 | | -283 | -312 |
| CoAl1 | 4197 | 7556 | 17154 | 420 | 808 | -283 | -276 | -257 |
| CoAl10 | 4181 | 7570 | 17060 | 419 | 802 | -284 | -279 | -318 |
| CoAl14 | 4179 | 7563 | 17142 | 419 | 808 | -303 | -278 | -268 |
| CoAl20 | 4157 | 7559 | 17105 | 418 | 806 | -292 | -276 | -258 |
| CoAl34 | 4215 | 7546 | <i>no</i> | 420 | | -300 | -275 | |
| CoAl45 | 4174 | 7570 | <i>no</i> | 419 | | -276 | -276 | |
| CoAl50 | 4187 | 7544 | <i>no</i> | 419 | | -263 | -286 | |
| CoAl67 | 4161 | 7581 | <i>no</i> | 419 | | -278 | -261 | |
| CoAl100 | 4158 | <i>no</i> | <i>no</i> | 416 | | -306 | | |

*Energies (after spin orbit coupling reduction) of absorption bands caused by the ⁴A₂(F)-⁴T₂(F), ⁴A₂(F)-⁴T₁(F) and ⁴A₂(F)-⁴T₁(P) transitions, respectively. *no*= not observed.

The *Dq* values were calculated from the determined energies for bands caused by transitions to the ⁴T₁-states. The *Dq* values are very similar (416–421 cm⁻¹) and compare very well with the range of *Dq*-values between 370–420 cm⁻¹ that were determined by optical absorption spectroscopy for a large range of Co²⁺-doped spinel compounds by Hochu and Lenglet (1998) and those reported for low Co²⁺ contents in MgAl₂O₄ (400 cm⁻¹, Weakliem, 1962; Kuleshov et al., 1993) and in ZnGa₂O₄ (403 cm⁻¹, Abritta and Blak, 1991). Moreover, the *Dq* values compare very well with the value of 390 cm⁻¹ determined for CoAl₂O₄ from magnetic neutron scattering experiments by Winkler et al. (1997). The presently obtained values for the Racah *B*-parameter (799–808 cm⁻¹), though limited to low-Co samples due to the above mentioned spectra limitations, are very close to each other and compare very well with those (790–815 cm⁻¹) calculated by Hochu and Lenglet (1998) for a range of aluminate spinels. Finally, the presently calculated spin-orbit coupling parameters (257–318 cm⁻¹) are relatively high, a fact that has been frequently observed in spectral studies of several other Co-bearing compounds (e.g., Pappalardo and Dietz 1961) and also commented on (e.g., Wildner, 1996) but not been resolved. Pappalardo and Dietz (1961)

suggested that anomalously high λ -value for the ${}^4A_2(F)$ - ${}^4T_1(P)$ transition may be due to strong spin-orbit mixing with the doublet terms derived from the 2G-state.

The crystal field splitting parameter Dq shows only insignificant changes within the present spinel series. This behavior is significantly different from what was observed in $MgAl_2O_4$ - $FeAl_2O_4$, $MgAl_2O_4$ - $MnAl_2O_4$ and in $MgAl_2O_4$ - $MgCr_2O_4$ spinel solid-solution series (Fig. 4.10). In the these series, a change in the Dq values, and then a marked color shift (and absorption intensification), were observed as a function of Fe^{2+} , of Mn^{2+} and of Cr^{3+} content, respectively (Hålenius et al. 2002, 2010,2011).

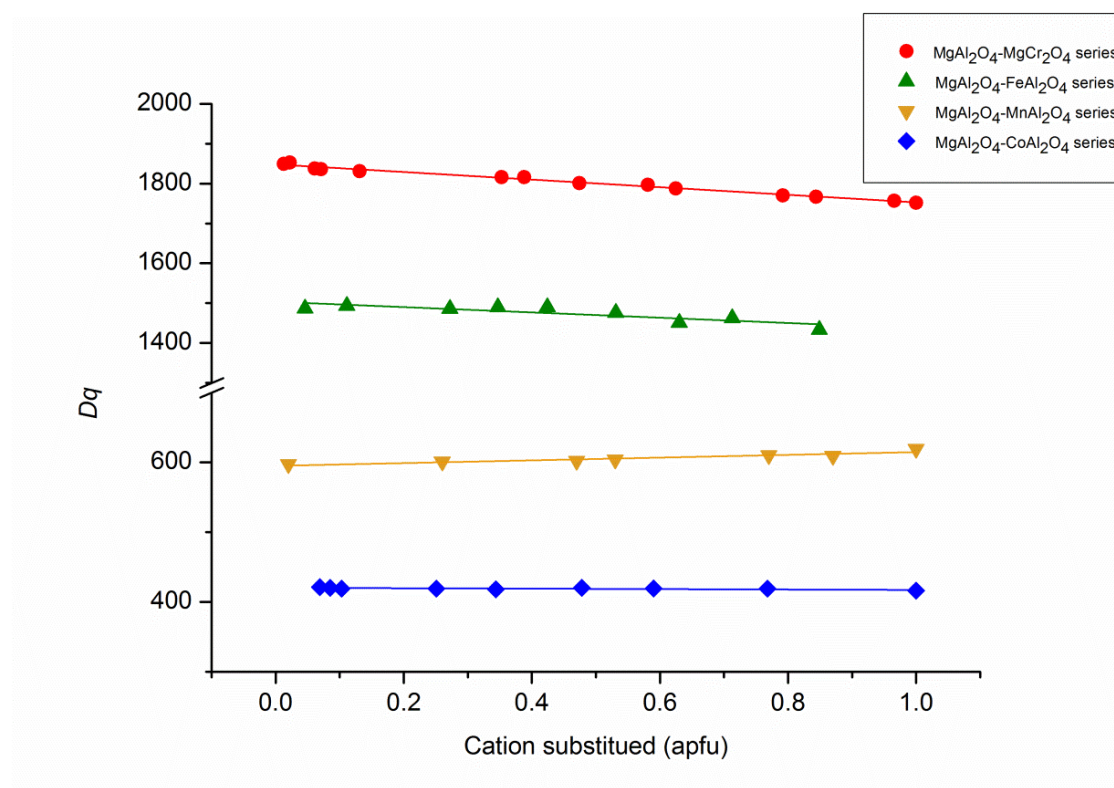


Fig. 4.10. Variation of the Dq value along the $MgAl_2O_4$ - $MgCr_2O_4$ (data taken from Hålenius et al., 2010); $MgAl_2O_4$ - $FeAl_2O_4$ (data taken from Hålenius et al., 2002); $MgAl_2O_4$ - $MnAl_2O_4$ (data taken from Hålenius et al., 2011) and $MgAl_2O_4$ - $CoAl_2O_4$ (data taken from this study).

Recalling the $Dq \approx 1/R^5$ ligand field relationship, this demonstrates that the local Co^{2+} -O bond distance at the T-site only marginally increases with increasing Co-content in the $MgAl_2O_4$ - $CoAl_2O_4$ series (Table 4.5). In addition, the almost constant Racah B -parameter for tetrahedrally coordinated Co^{2+} in this series suggests that any influence

of substitutional next nearest neighbor cations on the ionicity of Co^{2+} -O bonds at the T-site is very small. Constant Racah B -parameters for tetrahedrally coordinated Mn^{2+} and hence comparable insensitivity to next-nearest neighbor effects on bond ionicity were also observed for $^{\text{T}}\text{Mn}^{2+}$ -O bonds in the MgAl_2O_4 - MnAl_2O_4 spinel solid-solution series (Hålenius et al. 2011).

Table 4.5. Calculated local tetrahedral Co-O bond length.

| Sample | Dq (cm^{-1}) | $^{\text{T}}\text{Co-O}$ (Å) |
|----------------|--|--|
| CoAl0.5 | 421 | 1.967 |
| CoAl1 | 420 | 1.968 |
| CoAl10 | 419 | 1.969 |
| CoAl14 | 419 | 1.969 |
| CoAl20 | 418 | 1.970 |
| CoAl34 | 420 | 1.968 |
| CoAl45 | 419 | 1.969 |
| CoAl50 | 419 | 1.969 |
| CoAl67 | 419 | 1.969 |
| CoAl100 | 416 | 1.972 |

Structural parameters are summarized in the Table 4.6. The observed structural modifications are due to double causes:

1. Compositional changes with $^{\text{T}}\text{Co}^{2+} \rightarrow ^{\text{M}}\text{Mg}$ substitution;
2. Intracrystalline disorder, with a decrease of inversion, i.e., $^{\text{M}}\text{Al}$ content.

The site distributions of Mg, Co^{2+} and Al and degree of inversion were obtained by combining structural and chemical data by means of a minimization procedure (Table 4.7).

The site distribution shows that the M site is dominated by Al and the T site is mainly populated by Mg and Co^{2+} , with a marked preference of Co^{2+} for the tetrahedral coordination with respect to Mg (Fig. 4.11). Accordingly, the degree of cation inversion, expressed as the occurrence of Al at T sites, decreases from 0.24 to 0.13 with increasing Co^{2+} content.

Table 4.6. Selected X-ray diffraction data of the analyzed spinels single crystals along MgAl₂O₄-CoAl₂O₄ series.

| Crystal | CoAl0.5 | CoAl1 | CoAl10 | CoAl14 | CoAl20 |
|---|----------------|----------------|----------------|----------------|----------------|
| Crystal sizes (mm) | 0.20×0.20×0.12 | 0.22×0.21×0.18 | 0.22×0.20×0.15 | 0.20×0.20×0.16 | 0.20×0.20×0.20 |
| <i>a</i> (Å) | 8.0851(3) | 8.0848(4) | 8.0840(3) | 8.0875(4) | 8.0902(3) |
| <i>u</i> | 0.26209(4) | 0.26216(5) | 0.26216(5) | 0.26242(4) | 0.26249(5) |
| T-O (Å) | 1.9198(6) | 1.9207(7) | 1.9206(6) | 1.9250(6) | 1.9266(7) |
| M-O (Å) | 1.9285(3) | 1.9279(4) | 1.9277(3) | 1.9267(3) | 1.9268(4) |
| T-m.a.n. | 13.06(6) | 13.24(7) | 13.48(7) | 15.71(7) | 16.91(8) |
| M-m.a.n. | 12.82(4) | 12.86(5) | 12.89(4) | 13.03(4) | 13.17(4) |
| T- <i>U</i> ¹¹ (Å ²) | 0.0048(2) | 0.0046(2) | 0.0047(2) | 0.0049(1) | 0.0050(1) |
| M- <i>U</i> ¹¹ (Å ²) | 0.0045(1) | 0.0043(2) | 0.0045(1) | 0.0043(1) | 0.0043(1) |
| M- <i>U</i> ¹² (Å ²) | -0.00013(4) | -0.00013(4) | -0.00011(4) | -0.00016(4) | -0.00018(5) |
| O- <i>U</i> ¹¹ (Å ²) | 0.0078(1) | 0.0076(2) | 0.0076(2) | 0.0076(1) | 0.0076(1) |
| O- <i>U</i> ¹² (Å ²) | 0.00021(7) | 0.00017(8) | 0.00017(8) | 0.00015(8) | 0.0002(1) |

Notes: *a* = unit-cell parameter; *u* = oxygen fractional coordinate; T-O and M-O = tetrahedral and octahedral bond lengths, respectively; T- and M-m.a.n. = T- and M-mean atomic number; *U*¹¹ = atomic displacement parameter; *U*¹¹ = *U*²² = *U*³³ and *U*¹² = *U*¹³ = *U*²³ (= 0 for T-site due to symmetry reasons)

Table 4.6. continued

| Crystal | CoAl34 | CoAl45 | CoAl50 | CoAl67 | CoAl100 |
|---|----------------|----------------|----------------|----------------|----------------|
| Crystal sizes (mm) | 0.30×0.25×0.20 | 0.20×0.20×0.20 | 0.16×0.16×0.10 | 0.16×0.14×0.09 | 0.19×0.19×0.12 |
| <i>a</i> (Å) | 8.0914(4) | 8.0943(3) | 8.0957(3) | 8.1010(5) | 8.1047(4) |
| <i>u</i> | 0.26281(5) | 0.26308(5) | 0.26251(6) | 0.26321(4) | 0.26355(5) |
| T-O (Å) | 1.9314(7) | 1.9359(7) | 1.9282(9) | 1.9392(6) | 1.9449(7) |
| M-O (Å) | 1.9248(3) | 1.9235(3) | 1.9280(5) | 1.9242(3) | 1.9226(4) |
| T-m.a.n. | 18.91(9) | 20.34(10) | 20.11(12) | 22.10(11) | 25.28(8) |
| M-m.a.n. | 13.26(4) | 13.37(4) | 13.75(5) | 13.53(4) | 13.88(5) |
| T- <i>U</i> ¹¹ (Å ²) | 0.0052(1) | 0.0048(1) | 0.0056(2) | 0.00543(9) | 0.00524(8) |
| M- <i>U</i> ¹¹ (Å ²) | 0.0044(1) | 0.0039(1) | 0.0045(2) | 0.0045(1) | 0.0040(1) |
| M- <i>U</i> ¹² (Å ²) | -0.00021(5) | -0.00020(5) | -0.00021(6) | -0.00027(5) | -0.00028(6) |
| O- <i>U</i> ¹¹ (Å ²) | 0.0078(1) | 0.0071(1) | 0.0088(2) | 0.0078(1) | 0.0074(1) |
| O- <i>U</i> ¹² (Å ²) | 0.0002(1) | 0.0001(1) | 0.0002(1) | -0.00003(9) | -0.0002(1) |

Notes: *a* = unit-cell parameter; *u* = oxygen fractional coordinate; T-O and M-O = tetrahedral and octahedral bond lengths, respectively; T- and M-m.a.n. = T- and M-mean atomic number; *U*¹¹ = atomic displacement parameter; *U*¹¹ = *U*²² = *U*³³ and *U*¹² = *U*¹³ = *U*²³ (= 0 for T-site due to symmetry reasons)

Table 4.7. Structural formulae of the analysed spinel single crystals along MgAl₂O₄-CoAl₂O₄ series.

| Sample | Formula |
|---------|---|
| CoAl0.5 | ^T (Co _{0.06} Mg _{0.70} Al _{0.24}) ^M (Co _{0.01} Mg _{0.23} Al _{1.76})O ₄ |
| CoAl1 | ^T (Co _{0.07} Mg _{0.69} Al _{0.23}) ^M (Co _{0.01} Mg _{0.22} Al _{1.77})O ₄ |
| CoAl10 | ^T (Co _{0.09} Mg _{0.68} Al _{0.23}) ^M (Co _{0.02} Mg _{0.21} Al _{1.77})O ₄ |
| CoAl14 | ^T (Co _{0.23} Mg _{0.55} Al _{0.22}) ^M (Co _{0.02} Mg _{0.20} Al _{1.78})O ₄ |
| CoAl20 | ^T (Co _{0.31} Mg _{0.48} Al _{0.21}) ^M (Co _{0.03} Mg _{0.18} Al _{1.79})O ₄ |
| CoAl34 | ^T (Co _{0.44} Mg _{0.37} Al _{0.19}) ^M (Co _{0.04} Mg _{0.15} Al _{1.81})O ₄ |
| CoAl45 | ^T (Co _{0.54} Mg _{0.30} Al _{0.17}) ^M (Co _{0.05} Mg _{0.11} Al _{1.83})O ₄ |
| CoAl50 | ^T (Co _{0.52} Mg _{0.27} Al _{0.21}) ^M (Co _{0.11} Mg _{0.10} Al _{1.79})O ₄ |
| CoAl67 | ^T (Co _{0.67} Mg _{0.17} Al _{0.16}) ^M (Co _{0.09} Mg _{0.08} Al _{1.84})O ₄ |
| CoAl100 | ^T (Co _{0.87} Mg _{0.00} Al _{0.13}) ^M (Co _{0.13} Mg _{0.00} Al _{1.87})O ₄ |

Notes: T = tetrahedrally coordinated site; M = octahedrally coordinated site

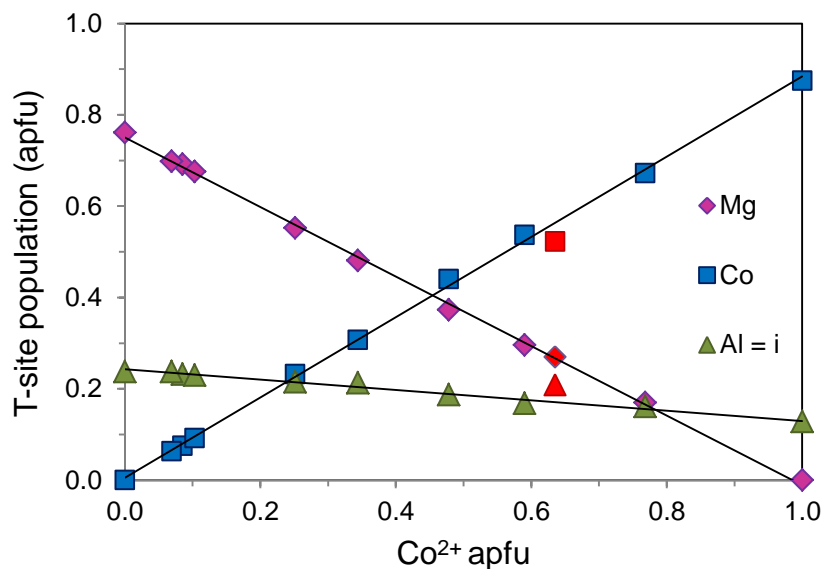


Fig. 4.11. Cation distribution in the T site along the MgAl₂O₄-CoAl₂O₄ series. Red symbols are used for the sample CoAl50.

The unit-cell parameter a of the $(\text{Mg},\text{Co})\text{Al}_2\text{O}_4$ synthetic spinel crystals increases from 8.084 to 8.105 Å along the solid-solution series. In literature there are many X-ray powder diffraction investigations on the end-member CoAl_2O_4 (JCPDS file no. 44-0160), all of them with an a -value close to 8.105 Å (Fig. 4.12). Only Angeletti et al. (1977) addressed the entire MgAl_2O_4 - CoAl_2O_4 series, and the values of the unit-cell parameter they obtained are in line with those measured here. As it is well known, the structural changes in spinels may depend on both chemical composition and inversion parameter, which in turn is a function of thermal history (O'Neill and Navrotsky 1984; O'Neill and Dollase 1994; Harrison et al. 1998; Andreozzi et al. 2000, 2001a; Andreozzi and Lucchesi 2002).

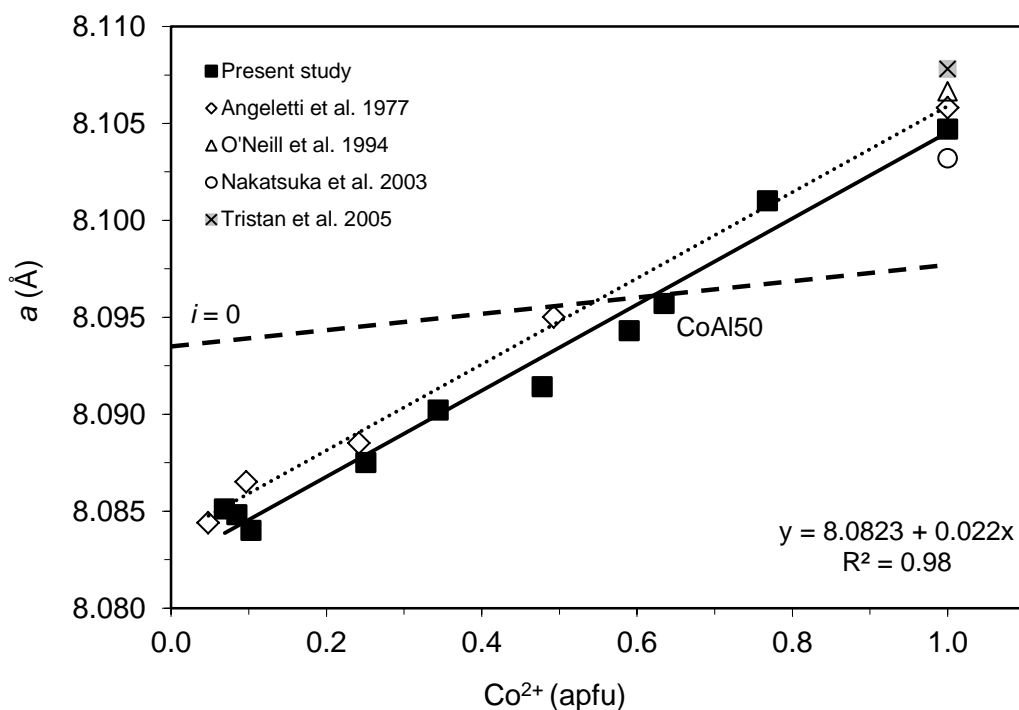


Fig. 4.12. Unit-cell parameter a against Co^{2+} content in MgAl_2O_4 - CoAl_2O_4 solid-solution series. Size of the symbols used is equal to or larger than standard uncertainties. Solid line = best fit to our data; dotted line = best fit to Angeletti et al. (1977) data: the two trends are parallel with the same slope (0.022). Dashed line = a values calculated for the MgAl_2O_4 - CoAl_2O_4 solid-solution series at inversion zero.

The values of unit-cell parameter for the $\text{MgAl}_2\text{O}_4\text{-CoAl}_2\text{O}_4$ series at $i = 0$ were calculated from cation-to-oxygen distances refined, which are consistent with those reported in Lavina et al. (2002). Results show that the contribution of the inversion degree strongly affects the unit-cell parameter, which at $i = 0$ is quite insensitive to the substitution of Co for Mg (Fig. 4.12). The trend obtained for the present samples (which experienced a closure temperature of ca. 800 °C) and the trend calculated for $i = 0$ cross each other close to the composition of 60% CoAl_2O_4 , that is almost coincident with the sample CoAl50, and this intercept is expected to be temperature-invariant. This coincidence explains why the sample CoAl50 (which experienced a closure temperature distinctly higher than the others) shows a unit-cell parameter in line with the general trend.

The observed variation of the unit-cell parameter a is mainly related to the strong variations in the tetrahedral bond length from 1.920 to 1.945 Å rather than to the considerably more limited variations in the octahedral bond length from 1.923 to 1.929 Å (Fig. 4.13).

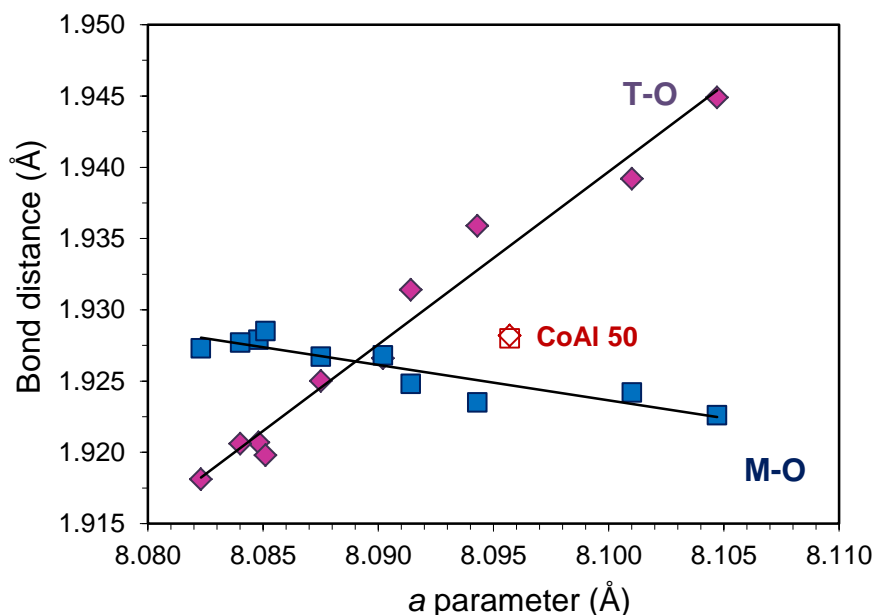


Fig. 4.13. Relationship between unit-cell parameter (a) and tetrahedral and octahedral bond distances in the synthesized crystals. The linear fit and the determination coefficient ($r^2 = 0.97$ and 0.83 for T-O and M-O, respectively) are calculated by using all points except for that of sample CoAl50. Symbol size is proportional to the analytical error.

In fact, the substitution $\text{Co}^{2+} \rightarrow \text{Mg}$ at the T site is not expected to cause any T-O bond distance change because the two cations have been shown to have very similar cation radii: as mentioned before, the optimized value for ${}^{\text{T}}\text{Co}^{2+}\text{-O}$ distance equals 1.969(3) Å compared to 1.966(1) Å for ${}^{\text{T}}\text{Mg}^{2+}\text{-O}$ (reported by Lavina et al. 2002). Consequently, any increase in T-O distance with increased incorporation of Co in the structure must be mainly ascribed to a decrease in Al content at the T site (Fig. 4.14). In this case, the CoAl50 sample agrees with the other sample.

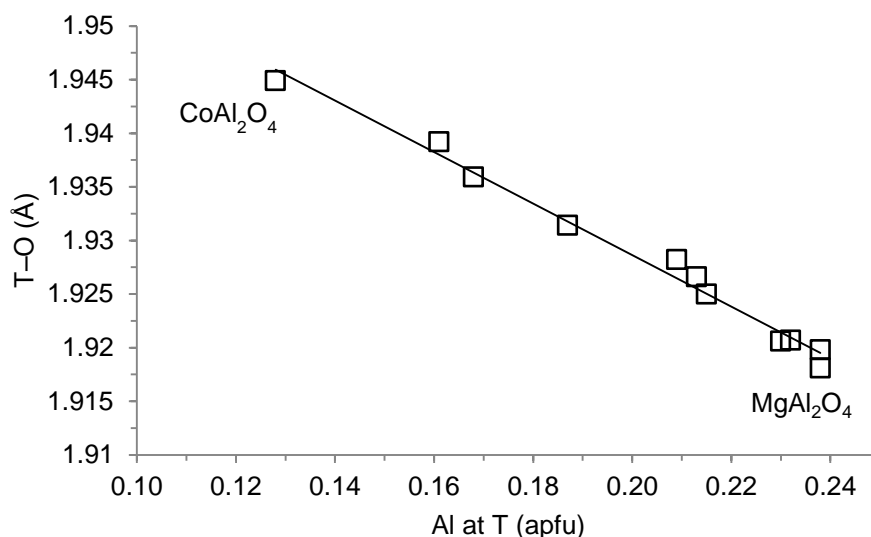


Fig. 4.14. Variation in tetrahedral bond length (T-O) as a function of Al content at the T site. Symbol size is proportional to the analytical error.

Since the studied spinels contain only two types of divalent cations (Mg and Co^{2+}) and only one type of trivalent cation (Al) and the size of Mg and Co^{2+} at the T site is very similar, the only steric effect that may account for variations in Al ordering must be related to the cation occupancy of the M site.

Hence, the small variation in ${}^{\text{T}}\text{Co}^{2+}\text{-O}$ from 1.966 to 1.972 Å derived from optical spectra and optimization of site occupancies of cations appears to be inversely related to M-O: i.e., ${}^{\text{T}}\text{Co}^{2+}\text{-O}$ increases with decreasing M-O. This behavior is in contrast with the variation in ${}^{\text{T}}\text{Co}^{2+}\text{-O}$ shown to occur in the normal spinel of the binary join $\text{Co}^{2+}(\text{Co}^{3+}_{2-x}\text{Cr}_x)\text{O}_4$ by O'Neill (2003). In this series, the ${}^{\text{T}}\text{Co}^{2+}\text{-O}$ increases, from

~1.93 Å in Co_3O_4 to ~1.97 Å in CoCr_2O_4 , with increasing M-O from ~1.92 to ~1.99 Å. This dual behavior of $\text{TCo}^{2+}\text{-O}$ could be explained by considering that the series $\text{Co}^{2+}(\text{Co}^{3+}_{2-x}\text{Cr}_x)\text{O}_4$ is characterized by a high degree of covalent bonding and Co^{3+} in the low-spin state, whereas the series $(\text{Mg}_{1-x}\text{Co}_x)\text{Al}_2\text{O}_4$ is ionically bonded with all cations in their high-spin states.

4.2. Natural multicolor spinels

Minerals belonging to the spinel group occur in a wide range of colors, e.g. pink, red, orange, purple, blue and green, depending on the trace elements present. As already handled in the Chapter 2, there are at least fifteen causes of color. In the spinels the different colors can be caused by simply a particular transition metal cation in a specific crystallographic site (crystal field theory), by an intervalence charge transfer, by a combination of two or more trace element absorptions and can be influenced also by a more complex mechanisms such as the structural relaxation (Hålenius et al., 2010). A detailed study on the causes of colors in the spinels is lacking. With the exception of Schmetzer et al. (1989), all the works present in literature are based on the investigation of a small number of samples, and, for most of these papers colors due to only one metal transition element were examined (Dickson and Smith, 1976; Shigley and Stockton, 1984; Taran et al., 2005, 2009; Malsy et al., 2012). However, it will be shown that two or more trace elements are often responsible for the great number of individual colors in natural spinels. In addition, Schmetzer et al. (1989) studied in detail the causes of several colors in many natural spinels, but, among the analyzed samples, the pink, lilac, violet and magenta spinels were missing. Many studies were performed on synthetic spinels but often the absorption spectra of these spinels differ from those of natural spinels because of the higher degree of disorder and a more complex composition of the former (Hålenius et al., 2002, 2010, Jouini et al., 2006; Fregola et al., 2011; Aramburu et al., 2013). Thus, the interpretation of the optical spectra and the band assignment for the same absorption peaks are not always homogeneous.

In this study a large number of natural spinels having absorption spectra and colors well representative for the entire variability of color were explored by Electron Microprobe Analysis and UV-VIS-NIR-MIR spectroscopy, in order to obtain a systematic examination of the color causes in natural spinels.

4.2.1 Chemical characterization

Electron microprobe analyses were performed on the same portions of crystals characterized by spectroscopic analyses and revealed that the chemical composition of the natural spinel crystals investigated is almost homogeneous within each crystal. No color zoning was observed, but some red spinels, such as the sample 890292d, showed a chemical zoning of the Cr^{3+} . The results of the chemical analysis are summarized in Table 4.8, whereas, for a better understanding, the crystal chemical formulae of the studied spinels are given in Table 4.9. They show that all the analyzed crystals contain Al as major trivalent component, and Mg or Zn as major divalent component. Thus the crystals show a prevalent spinel s.s. (MgAl_2O_4) or gahnite (ZnAl_2O_4) end-member component. The remaining composition is primarily dominated by Fe^{2+} , which is present in all the samples, and also by Fe^{3+} (especially in the blue-green and violet samples) and Cr^{3+} (especially in the red and orange samples). The amount of Fe^{3+} was calculated on the basis of charge-balance requirements and the spinel stoichiometry (3 cations per 4 anions). Of course, the real amount and distribution of Fe^{2+} and Fe^{3+} in the samples can not be sure on the basis of only microprobe composition. A Mössbauer analysis can help to distinguish between Fe^{2+} and Fe^{3+} and their distribution in the T and M sites. However, because of the small sizes and concentrations of Fe_{tot} in the sample, a Mössbauer analysis is hardly achievable. Only minor contents of Mn, ranging between 0.001(1) and 0.019(1) apfu, and V, between 0.001(1) and 0.032(2) apfu, were also found for the blue-green and the red-orange samples, respectively.

Table 4.8. Chemical composition of the examined natural colored spinels.

| Sample | Nat.1 | Nat.2 | Nat.3 | Nat.4 | ST | SX | 2366 |
|--|--------------|--------------|--------------|--------------|-----------|-----------|-------------|
| SiO₂ | 0.02(1) | 0.02(1) | 0.08(13) | 0.01(2) | 0.00 | 0.01(1) | 0.01(1) |
| TiO₂ | 0.01(1) | 0.00 | 0.020(1) | 0.01(1) | 0.01(1) | 0.01(1) | 0.01(1) |
| Al₂O₃ | 71.10(92) | 70.14(81) | 70.28(93) | 70.52(57) | 69.71(30) | 70.38(20) | 55.35(37) |
| V₂O₃ | 0.05(2) | 0.01(1) | 0.01(1) | 0.08(2) | 0.14(3) | 0.03(2) | 0.01(1) |
| Cr₂O₃ | 0.02(2) | 0.01(2) | 0.01(2) | 0.02(1) | 0.40(5) | 0.02(1) | 0.01(1) |
| FeO_{tot} | 0.35(4) | 1.83(9) | 0.52(3) | 1.47(3) | 0.21(3) | 1.58(10) | 5.85(8) |
| MgO | 28.20(26) | 27.18(25) | 27.55(39) | 27.76(29) | 27.60(8) | 27.37(14) | 0.01(1) |
| ZnO | 0.012(3) | 0.21(6) | 0.32(5) | 0.13(9) | 0.95(7) | 0.26(4) | 39.71(38) |
| MnO | 0.02(2) | 0.04(4) | 0.03(3) | 0.01(2) | 0.00 | 0.08(2) | 0.54(5) |
| CoO | 0.01(2) | 0.03(3) | 0.01(2) | 0.01(1) | 0.01(1) | 0.01(1) | 0.02(3) |
| NiO | 0.02(3) | 0.01(2) | 0.000 | 0.01(2) | 0.02(3) | 0.01(1) | 0.01(1) |
| Total | 99.81 | 99.50 | 98.94 | 100.03 | 99.05 | 99.76 | 101.53 |
| Cations on the basis of 4 oxygens | | | | | | | |
| Si | 0.000 | 0.000 | 0.002(3) | 0.000 | 0.000 | 0.000 | 0.000 |
| Ti | 0.000 | 0.000 | 0.000 | 0.000 | 0.000 | 0.000 | 0.000 |
| Al | 1.993(4) | 1.985(2) | 1.992(6) | 1.980(9) | 1.980(2) | 1.984(3) | 1.959(4) |
| V | 0.001(1) | 0.000 | 0.000 | 0.002(1) | 0.003(1) | 0.001(1) | 0.000 |
| Cr | 0.000 | 0.000 | 0.000 | 0.000 | 0.008(1) | 0.000 | 0.000 |
| Fe³⁺ | 0.004(1) | 0.015(2) | 0.005(1) | 0.017(1) | 0.003(1) | 0.015(2) | 0.041(2) |
| Fe²⁺ | 0.002(1) | 0.022(2) | 0.006(1) | 0.012(1) | 0.001(1) | 0.017(2) | 0.106(2) |
| Mg | 0.999(4) | 0.972(2) | 0.988(8) | 0.986(12) | 0.990(2) | 0.976(4) | 0.000 |
| Zn | 0.000 | 0.004(1) | 0.006(1) | 0.002(2) | 0.015(1) | 0.005(1) | 0.880(9) |
| Mn | 0.000 | 0.001(1) | 0.001(1) | 0.000 | 0.000 | 0.002(1) | 0.014(1) |
| Co | 0.000 | 0.001(1) | 0.000 | 0.000 | 0.000 | 0.000 | 0.001(1) |
| Ni | 0.000 | 0.000 | 0.000 | 0.000 | 0.000 | 0.000 | 0.000 |
| Total | 2.999 | 3.000 | 3.000 | 2.999 | 3.000 | 3.000 | 3.000 |

Table 4.8. *Continued.*

| Sample | 30070 | 31081 | 330763 | 330764 | 420491 | 440238 | 440243 |
|--|--------------|--------------|---------------|---------------|---------------|---------------|---------------|
| SiO₂ | 0.15(4) | 0.02(2) | 0.03(3) | 0.01(1) | 0.03(1) | 0.03(2) | 0.02(1) |
| TiO₂ | 0.03(4) | 0.00 | 0.01(2) | 0.02(2) | 0.06(2) | 0.00 | 0.03(3) |
| Al₂O₃ | 53.91(15) | 52.86(21) | 70.23(45) | 69.20(43) | 70.69(24) | 69.80(60) | 70.21(45) |
| V₂O₃ | 0.02(2) | 0.02(3) | 0.00 | 0.01(1) | 0.29(5) | 0.01(1) | 0.02(2) |
| Cr₂O₃ | 0.03(4) | 0.01(1) | 0.00 | 0.00 | 0.26(6) | 0.01(1) | 0.02(1) |
| FeO_{tot} | 1.82(1) | 2.62(15) | 3.54(8) | 5.51(12) | 0.13(3) | 2.51(14) | 2.52(5) |
| MgO | 0.08(3) | 1.06(2) | 26.05(33) | 24.71(27) | 27.81(26) | 26.71(45) | 26.66(25) |
| ZnO | 42.97(1.3) | 43.57(26) | 0.25(7) | 0.54(9) | 0.30(9) | 0.57(13) | 0.51(11) |
| MnO | 0.02(2) | 0.75(5) | 0.12(5) | 0.07(2) | 0.00 | 0.17(4) | 0.14(5) |
| CoO | 0.01(2) | 0.02(4) | 0.00 | 0.02(2) | 0.02(1) | 0.01(2) | 0.01(1) |
| NiO | 0.00 | 0.01(1) | 0.00 | 0.01(1) | 0.01(3) | 0.01(1) | 0.01(1) |
| Total | 99.04 | 100.94 | 100.26 | 100.1 | 99.60 | 99.83 | 100.15 |
| Cations on the basis of 4 oxygens | | | | | | | |
| Si | 0.005(2) | 0.001(1) | 0.001(1) | 0.000 | 0.001(1) | 0.001(1) | 0.000 |
| Ti | 0.001(1) | 0.000 | 0.000 | 0.000 | 0.001(1) | 0.000 | 0.001(1) |
| Al | 1.962(14) | 1.915(6) | 1.988(8) | 1.982(8) | 1.988(4) | 1.975(15) | 1.983(4) |
| V | 0.001(1) | 0.000 | 0.000 | 0.000 | 0.006(1) | 0.000 | 0.000 |
| Cr | 0.001(1) | 0.000 | 0.000 | 0.000 | 0.005(1) | 0.000 | 0.000 |
| Fe³⁺ | 0.017(1) | 0.067(4) | 0.011(1) | 0.018(3) | 0.001(1) | 0.015(2) | 0.016(1) |
| Fe²⁺ | 0.030(2) | 0.000 | 0.060(1) | 0.094(3) | 0.002(1) | 0.036(2) | 0.035(1) |
| Mg | 0.004(1) | 0.048(1) | 0.933(12) | 0.895(10) | 0.990(7) | 0.952(11) | 0.952(6) |
| Zn | 0.980(14) | 0.969(6) | 0.004(1) | 0.010(2) | 0.005(2) | 0.010(2) | 0.009(2) |
| Mn | 0.000 | 0.020(1) | 0.003(1) | 0.001(1) | 0.000 | 0.003(1) | 0.003(1) |
| Co | 0.000 | 0.001(1) | 0.000 | 0.000 | 0.000 | 0.000 | 0.000 |
| Ni | 0.000 | 0.000 | 0.000 | 0.000 | 0.000 | 0.000 | 0.000 |
| Total | 3.011 | 3.027 | 3.000 | 3.000 | 2.999 | 2.993 | 3.000 |

Table 4.8. *Continued.*

| Sample | 510941 | 510942 | 630250 | 670275 | 800801 | 881694a |
|--|---------------|---------------|---------------|---------------|---------------|----------------|
| SiO₂ | 0.03(2) | 0.01(1) | 0.02(1) | 0.08(9) | 0.05(3) | 0.01 (1) |
| TiO₂ | 0.01(1) | 0.00 | 0.02(1) | 0.04(3) | 0.00 | 0.03(1) |
| Al₂O₃ | 55.99(32) | 56.62(19) | 69.32(47) | 67.71(90) | 68.49(84) | 69.97(62) |
| V₂O₃ | 0.03(2) | 0.01(1) | 0.12(2) | 0.01(1) | 0.00 | 0.09(3) |
| Cr₂O₃ | 0.02(2) | 0.01(1) | 0.21(3) | 0.01(1) | 0.02(3) | 0.22(3) |
| FeO_{tot} | 4.34(13) | 6.71(48) | 3.52(4) | 4.16(12) | 3.15(13) | 0.63(4) |
| MgO | 2.38(14) | 1.49(6) | 24.21(27) | 26.26(44) | 23.41(25) | 28.13(30) |
| ZnO | 37.58(63) | 36.32(57) | 2.70(8) | 0.35(10) | 5.17(34) | 0.24(9) |
| MnO | 0.17(6) | 0.19(5) | 0.07(2) | 0.20(2) | 0.43(5) | 0.02(2) |
| CoO | 0.01(2) | 0.03(1) | 0.00 | 0.01(1) | 0.07(2) | 0.02(2) |
| NiO | 0.03(3) | 0.02(3) | 0.02(3) | 0.03(3) | 0.03(3) | 0.03(4) |
| Total | 100.59 | 101.41 | 100.21 | 98.85 | 100.82 | 99.39 |
| Cations on the basis of 4 oxygens | | | | | | |
| Si | 0.001(1) | 0.000 | 0.000 | 0.002(2) | 0.001(1) | 0.000 |
| Ti | 0.000 | 0.000 | 0.000 | 0.001(1) | 0.000 | 0.001(1) |
| Al | 1.957(2) | 1.970(3) | 1.991(7) | 1.947(11) | 1.977(7) | 1.977(4) |
| V | 0.001(1) | 0.000 | 0.002(1) | 0.000 | 0.000 | 0.002(1) |
| Cr | 0.000 | 0.000 | 0.004(1) | 0.000 | 0.000 | 0.004(1) |
| Fe³⁺ | 0.041(3) | 0.030(5) | 0.003(1) | 0.050(3) | 0.022(3) | 0.012(1) |
| Fe²⁺ | 0.067(3) | 0.136(6) | 0.069(1) | 0.036(3) | 0.043(3) | 0.001(1) |
| Mg | 0.105(6) | 0.066(3) | 0.880(9) | 0.955(14) | 0.854(6) | 0.998(6) |
| Zn | 0.823(11) | 0.792(13) | 0.049(1) | 0.006(2) | 0.093(7) | 0.004(2) |
| Mn | 0.004(2) | 0.005(1) | 0.002(1) | 0.004(1) | 0.009(1) | 0.000 |
| Co | 0.000 | 0.001 | 0.000 | 0.000 | 0.001(1) | 0.000 |
| Ni | 0.001(1) | 0.000 | 0.000 | 0.000 | 0.000 | 0.001(1) |
| Total | 3.000 | 2.999 | 3.000 | 3.004 | 3.000 | 2.999 |

Table 4.8. *Continued.*

| Sample | 881694c | 881728 | 890290 | 890292b | 890292c | 890292d |
|--|----------------|---------------|---------------|----------------|----------------|----------------|
| SiO₂ | 0.02(2) | 0.02(1) | 0.07(4) | 0.02(2) | 0.03(1) | 0.01(1) |
| TiO₂ | 0.08(3) | 0.01(1) | 0.01(1) | 0.23(4) | 0.01(1) | 0.06(2) |
| Al₂O₃ | 70.26(72) | 56.09(78) | 69.49(58) | 69.45(40) | 69.04(66) | 66.92(60) |
| V₂O₃ | 0.23(3) | 0.07(3) | 0.00 | 0.07(2) | 1.68(13) | 0.05(2) |
| Cr₂O₃ | 0.46(18) | 0.02(2) | 0.01(1) | 1.04(13) | 0.37(1) | 4.25(75) |
| FeO_{tot} | 0.10(2) | 5.10(11) | 3.58(7) | 0.13(1) | 0.52(7) | 0.15(3) |
| MgO | 27.92(17) | 1.52(2) | 26.00(17) | 27.76(30) | 27.97(27) | 27.75(33) |
| ZnO | 0.33(3) | 38.77(50) | 0.23(4) | 0.03(5) | 0.27(5) | 0.08(5) |
| MnO | 0.02(2) | 0.12(3) | 0.13(3) | 0.00 | 0.02(2) | 0.00 |
| CoO | 0.01(1) | 0.00 | 0.01(1) | 0.02(2) | 0.01(1) | 0.01(1) |
| NiO | 0.01(2) | 0.02(2) | 0.03(3) | 0.00 | 0.01(1) | 0.01(1) |
| Total | 99.44 | 101.72 | 99.56 | 98.75 | 99.93 | 99.29 |
| Cations on the basis of 4 oxygens | | | | | | |
| Si | 0.001(1) | 0.001(1) | 0.002(1) | 0.000 | 0.001(1) | 0.000 |
| Ti | 0.001(1) | 0.000 | 0.000 | 0.004(1) | 0.000 | 0.001(1) |
| Al | 1.981(5) | 1.955(9) | 1.981(1) | 1.972(5) | 1.95(2) | 1.914(16) |
| V | 0.005(1) | 0.002(1) | 0.000 | 0.001(1) | 0.032 | 0.001(1) |
| Cr | 0.009(4) | 0.000 | 0.000 | 0.020(2) | 0.007 | 0.081(14) |
| Fe³⁺ | 0.001(1) | 0.042(3) | 0.018(1) | 0.001(1) | 0.010 | 0.002(1) |
| Fe²⁺ | 0.001(1) | 0.084(3) | 0.056(1) | 0.002(1) | 0.001 | 0.001(1) |
| Mg | 0.994(4) | 0.067(1) | 0.937(5) | 0.997(5) | 0.997 | 0.999(5) |
| Zn | 0.005(1) | 0.846(13) | 0.004(1) | 0.001(1) | 0.004 | 0.001(1) |
| Mn | 0.000 | 0.003(1) | 0.002(1) | 0.000 | 0.000 | 0.000 |
| Co | 0.000 | 0.000 | 0.000 | 0.000 | 0.000 | 0.000 |
| Ni | 0.000 | 0.000 | 0.001(1) | 0.000 | 0.000 | 0.000 |
| Total | 2.997 | 2.999 | 3.001 | 2.998 | 3.002 | 3.000 |

Table 4.9. Crystal-chemical formula of the natural spinels investigated. The dominant endmember component is written in red. Label cell is colored as the color of the sample.

| | |
|----------------|--|
| Nat.1 | $(\text{Mg}_{0.999}\text{Fe}^{2+}_{0.002})_{1.001}(\text{Al}_{1.993}\text{Fe}^{3+}_{0.004}\text{V}_{0.001})_{1.999}\text{O}_4$ |
| Nat.2 | $(\text{Mg}_{0.972}\text{Zn}_{0.004}\text{Fe}^{2+}_{0.022}\text{Mn}_{0.001}\text{Co}_{0.001})_1(\text{Al}_{1.985}\text{Fe}^{3+}_{0.015})_2\text{O}_4$ |
| Nat.3 | $(\text{Mg}_{0.988}\text{Zn}_{0.006}\text{Fe}^{2+}_{0.006}\text{Mn}_{0.001})_1(\text{Al}_{1.992}\text{Fe}^{3+}_{0.005}\text{Si}_{0.002})_{1.999}\text{O}_4$ |
| Nat.4 | $(\text{Mg}_{0.986}\text{Zn}_{0.002}\text{Fe}^{2+}_{0.012})_1(\text{Al}_{1.980}\text{Fe}^{3+}_{0.018}\text{V}_{0.001})_{1.999}\text{O}_4$ |
| Ni8967d | $(\text{Mg}_{0.002}\text{Zn}_{0.931}\text{Fe}^{2+}_{0.064}\text{Mn}_{0.001}\text{Co}_{0.001}\text{Ni}_{0.001})_{1.01}(\text{Al}_{1.994}\text{Fe}^{3+}_{0.005}\text{Si}_{0.001})_2\text{O}_4$ |
| ST | $(\text{Mg}_{0.990}\text{Zn}_{0.015}\text{Fe}^{2+}_{0.001})_{1.06}(\text{Al}_{1.980}\text{Cr}_{0.008}\text{Fe}^{3+}_{0.003}\text{V}_{0.003})_{1.994}\text{O}_4$ |
| SX | $(\text{Mg}_{0.976}\text{Zn}_{0.005}\text{Fe}^{2+}_{0.017}\text{Mn}_{0.002})_1(\text{Al}_{1.984}\text{Fe}^{3+}_{0.015}\text{V}_{0.001})_2\text{O}_4$ |
| 2366 | $(\text{Zn}_{0.880}\text{Fe}^{2+}_{0.106}\text{Mn}_{0.014}\text{Co}_{0.001})_{1.001}(\text{Al}_{1.959}\text{Fe}^{3+}_{0.041})_2\text{O}_4$ |
| 30070 | $(\text{Mg}_{0.004}\text{Zn}_{0.980}\text{Fe}^{2+}_{0.017})_{1.001}(\text{Al}_{1.962}\text{Fe}^{3+}_{0.030}\text{Cr}_{0.001}\text{V}_{0.001}\text{Si}_{0.005}\text{Ti}_{0.001})_2\text{O}_4$ |
| 31081 | $(\text{Mg}_{0.048}\text{Zn}_{0.969})_{1.017}(\text{Al}_{1.915}\text{Fe}^{3+}_{0.067}\text{Mn}^{3+}_{0.020})_{2.02}\text{O}_4$ |
| 330763 | $(\text{Mg}_{0.933}\text{Zn}_{0.004}\text{Fe}^{2+}_{0.060}\text{Mn}_{0.003})_1(\text{Al}_{1.988}\text{Fe}^{3+}_{0.011}\text{Si}_{0.001})_2\text{O}_4$ |
| 330764 | $(\text{Mg}_{0.895}\text{Zn}_{0.010}\text{Fe}^{2+}_{0.094}\text{Mn}_{0.001})_1(\text{Al}_{1.982}\text{Fe}^{3+}_{0.018})_2\text{O}_4$ |
| 420491 | $(\text{Mg}_{0.990}\text{Zn}_{0.005}\text{Fe}^{2+}_{0.002})_{0.997}(\text{Al}_{1.988}\text{Fe}^{3+}_{0.001}\text{Cr}_{0.005}\text{V}_{0.006}\text{Si}_{0.001}\text{Ti}_{0.001})_{2.002}\text{O}_4$ |
| 440238 | $(\text{Mg}_{0.952}\text{Zn}_{0.010}\text{Fe}^{2+}_{0.036}\text{Mn}_{0.003})_{1.001}(\text{Al}_{1.975}\text{Fe}^{3+}_{0.015}\text{Si}_{0.001})_{2.001}\text{O}_4$ |
| 440243 | $(\text{Mg}_{0.952}\text{Zn}_{0.009}\text{Fe}^{2+}_{0.035}\text{Mn}_{0.003})_1(\text{Al}_{1.983}\text{Fe}^{3+}_{0.016}\text{Ti}_{0.001})_2\text{O}_4$ |
| 510941 | $(\text{Mg}_{0.105}\text{Zn}_{0.823}\text{Fe}^{2+}_{0.067}\text{Mn}_{0.004}\text{Ni}_{0.001})_1(\text{Al}_{1.957}\text{Fe}^{3+}_{0.041}\text{V}_{0.001}\text{Si}_{0.001})_2\text{O}_4$ |

Table 4.9. Continued.

| | |
|----------------|--|
| 510942 | $(\text{Mg}_{0.066}\text{Zn}_{0.792}\text{Fe}^{2+}_{0.136}\text{Mn}_{0.005}\text{Co}_{0.001})_1(\text{Al}_{1.970}\text{Fe}^{3+}_{0.030})_2\text{O}_4$ |
| 670275 | $(\text{Mg}_{0.955}\text{Zn}_{0.006}\text{Fe}^{2+}_{0.036}\text{Mn}_{0.004})_{1.001}(\text{Al}_{1.947}\text{Fe}^{3+}_{0.050}\text{Si}_{0.002}\text{Ti}_{0.001})_2\text{O}_4$ |
| 800801 | $(\text{Mg}_{0.854}\text{Zn}_{0.093}\text{Fe}^{2+}_{0.043}\text{Mn}_{0.009}\text{Co}_{0.001})_1(\text{Al}_{1.977}\text{Fe}^{3+}_{0.022}\text{Si}_{0.001})_2\text{O}_4$ |
| 881694a | $(\text{Mg}_{0.998}\text{Zn}_{0.004}\text{Fe}^{2+}_{0.001}\text{Ni}_{0.001})_{1.003}(\text{Al}_{1.977}\text{Cr}_{0.004}\text{Fe}^{3+}_{0.012}\text{V}_{0.002}\text{Ti}_{0.001})_{1.996}\text{O}_4$ |
| 881694c | $(\text{Mg}_{0.994}\text{Zn}_{0.005}\text{Fe}^{2+}_{0.001})_1(\text{Al}_{1.981}\text{Cr}_{0.009}\text{Fe}^{3+}_{0.001}\text{V}_{0.005}\text{Si}_{0.001}\text{Ti}_{0.001})_{1.998}\text{O}_4$ |
| 881728 | $(\text{Mg}_{0.067}\text{Zn}_{0.846}\text{Fe}^{2+}_{0.084}\text{Mn}_{0.003})_1(\text{Al}_{1.955}\text{Fe}^{3+}_{0.042}\text{V}_{0.002}\text{Si}_{0.001})_2\text{O}_4$ |
| 890290 | $(\text{Mg}_{0.937}\text{Zn}_{0.004}\text{Fe}^{2+}_{0.056}\text{Mn}_{0.002}\text{Ni}_{0.001})_1(\text{Al}_{1.981}\text{Fe}^{3+}_{0.018}\text{Si}_{0.002})_{2.001}\text{O}_4$ |
| 890292b | $(\text{Mg}_{0.997}\text{Zn}_{0.001}\text{Fe}^{2+}_{0.002})_1(\text{Al}_{1.972}\text{Cr}_{0.020}\text{Fe}^{3+}_{0.001}\text{V}_{0.001}\text{Ti}_{0.004})_{1.998}\text{O}_4$ |
| 890292c | $(\text{Mg}_{0.997}\text{Zn}_{0.004}\text{Fe}^{2+}_{0.001})_{1.002}(\text{Al}_{1.950}\text{Cr}_{0.007}\text{Fe}^{3+}_{0.0010}\text{V}_{0.032}\text{Si}_{0.001})_2\text{O}_4$ |
| 890292d | $(\text{Mg}_{0.999}\text{Zn}_{0.001}\text{Fe}^{2+}_{0.001})_{1.001}(\text{Al}_{1.914}\text{Cr}_{0.081}\text{Fe}^{3+}_{0.002}\text{V}_{0.001}\text{Ti}_{0.001})_{1.999}\text{O}_4$ |

Minor and trace elements were measured through LA-ICP-MS. The minor elements are reported in terms of ppm of the cation in the Table 4.10, whereas the trace elements were not considered in this study.

Table 4.10. Minor elements measured by LA-ICP-MS reported in terms of ppm.

| Sample | Si | Ti | V | Cr | Mn | Fe | Co | Ni |
|----------------|-----------|-----------|----------|-----------|-----------|-----------|-----------|-----------|
| SX | 496 | 58 | 183 | 378 | 214 | 7626 | 14.7 | 30.1 |
| ST | 346 | 51 | 684 | 2300 | 12 | 1418 | 1.4 | 5.3 |
| Nat.1 | 357 | 68 | 170 | 420 | 90 | 6128 | 2.6 | 15 |
| Nat.2 | 337 | 4.8 | 5.1 | 4 | 140 | 13060 | 13.3 | 23.4 |
| Nat.3 | 358 | 52 | 15 | 4 | 68 | 3698 | 6.2 | 5.68 |
| Nat.4 | 242 | 71 | 162 | 322 | 60 | 10700 | 13.9 | 40.3 |
| 2366 | 247 | 3 | 0.25 | 2.6 | 3623 | 40525 | 1.7 | 0.3 |
| 30070 | 902 | 48 | 77.3 | 4.8 | 168 | 12650 | 1.4 | 3.1 |
| 31081 | 200 | 6 | 0.4 | 59 | 3808 | 14920 | 6.7 | 1.9 |
| 330764 | 339 | 103 | 21.4 | 10.8 | 537 | 40420 | 12.3 | 3.61 |
| 420491 | 334 | 386 | 1912 | 1902 | 23 | 1022 | 0.4 | 1 |
| 440243 | 418 | 181 | 51.5 | 21.1 | 1162 | 18840 | 7.7 | 4.5 |
| 510942 | 264 | 11 | 227 | 4.5 | 1308 | 47517 | 107 | 30.1 |
| 670275 | 337 | 58 | 14.2 | 20 | 1148 | 28900 | 10.3 | 11.3 |
| 800801 | 648 | 2.5 | 3.8 | 2.8 | 2746 | 22680 | 611 | 80 |
| 881694c | 428 | 301 | 1376 | 3430 | 59 | 716 | 0.3 | 0.7 |
| 881728 | 258 | 2.7 | 426 | 2.3 | 668 | 35160 | 2 | 1.1 |
| 890292b | 362 | 1276 | 448 | 7436 | 64.5 | 953 | 0.2 | 0.6 |
| 890292d | 348 | 350 | 250 | 27780 | 18.1 | 1312 | 0.25 | 1 |

A preliminary inspection of sample colors as a function of chemical composition was tried reporting the molar percentages of gahnite (ZnAl_2O_4), hercynite (FeAl_2O_4), and spinel s.s. (MgAl_2O_4) components of the analyzed samples in a triangular diagram (Fig. 4.15). This diagram highlights that the different colors do not depend on the end-member composition. In fact, while the samples having a gahnitic composition show colors close to the blue hue, the samples having a spinel s.s. composition show all kind of colors.

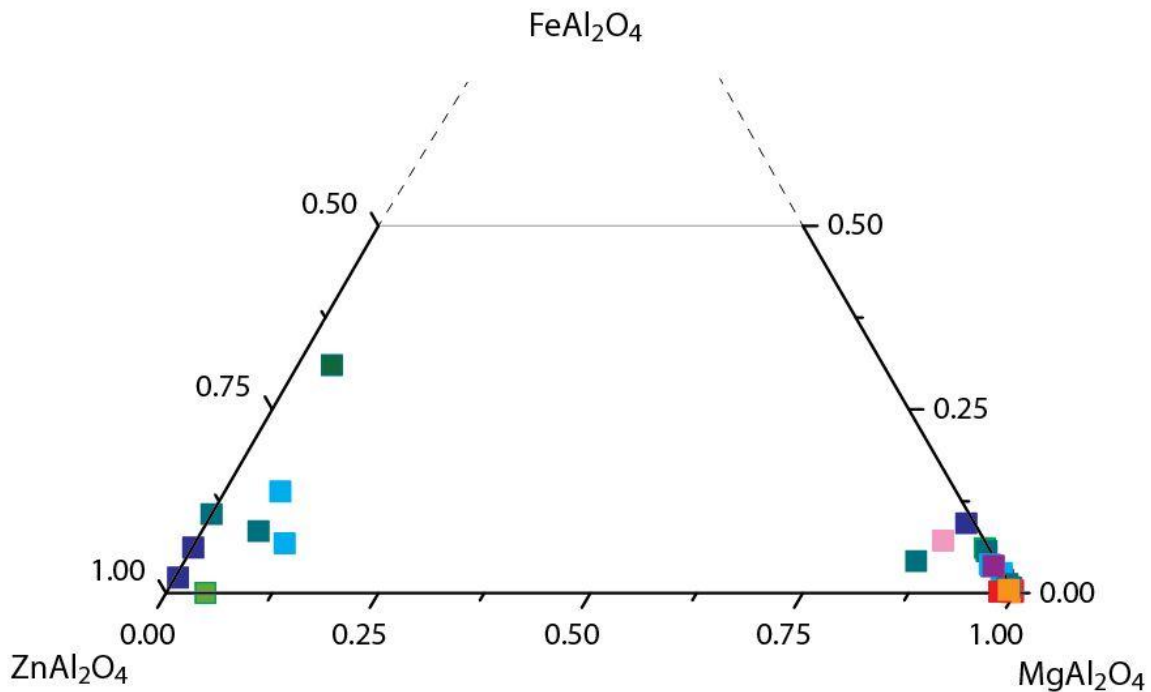


Fig. 4.15. Chemical composition of the analyzed natural samples in a triangular plot in terms of gahnite, hercynite and spinel s.s. components. The colors of the square represent the color exhibited from the samples.

This behavior is better underlined in a graph spinel s.s versus gahnite end-member where only the portions approaching to the end-member are plotted (Fig. 4.16). Thus, discrimination among the different colors on the strength of the principal component is not possible, especially for the spinel s.s.

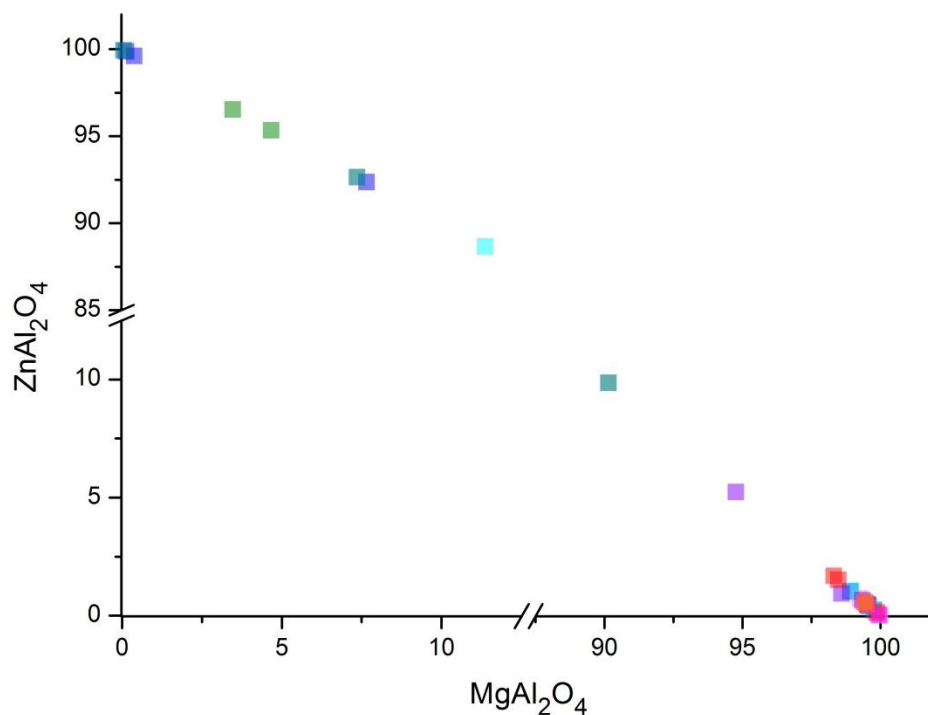


Fig. 4.16. Chemical composition of the analyzed natural samples in terms of gahnite and spinel s.s. components. The colors of the square represent the color exhibited from the samples.

Hence, the difference in colors is due to the minor transition metal cations. In order to highlight the role of the different transition metal elements on the colors, ternary diagrams were made. According to the dominant combination of minor elements, the pink, lilac, purple, violet, magenta, red and orange colored samples were studied in terms of the relative concentrations of FeO_{tot} , Cr_2O_3 and V_2O_3 weight per cent (Fig. 4.17a). The light blue, blue, blue-green, and green colored samples were studied in terms of the relative concentrations of FeO_{tot} , CoO and MnO weight per cent (Fig. 4.17b).

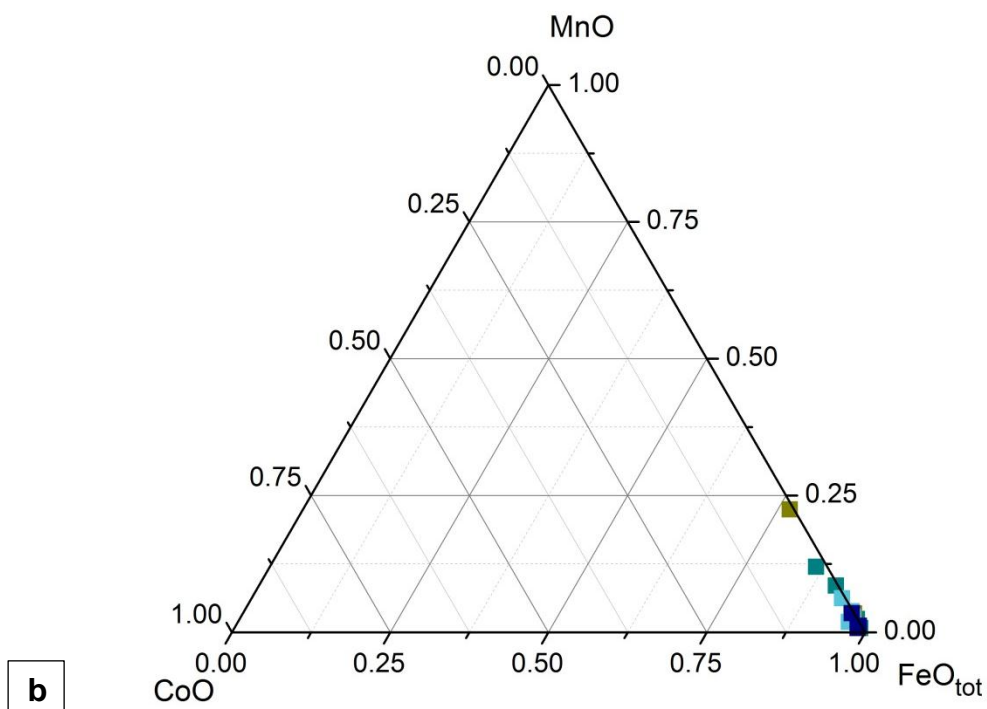
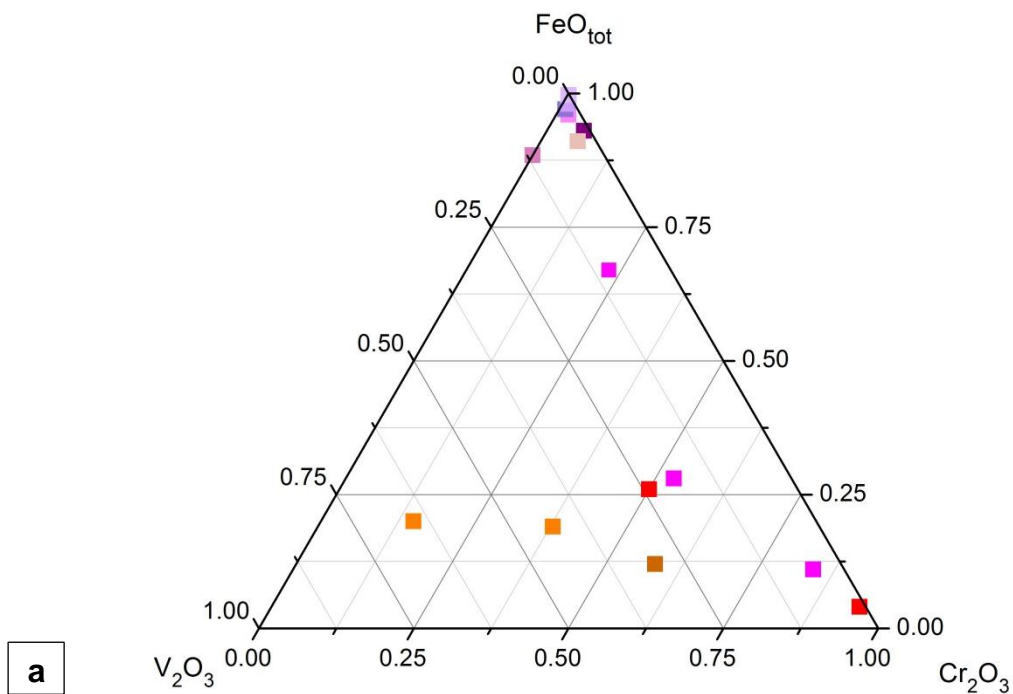


Fig. 4.17. Chemical composition of the natural spinels expressed in terms of their minor trace element: a) Pink, violet, magenta, red and orange colored spinels expressed in terms of the normalized concentrations of FeO_{tot} , and Cr_2O_3 and V_2O_3 weight per cent; b) Light blue, blue, blue-green and green colored spinels in terms of the normalized concentrations of FeO_{tot} , CoO and MnO weight %. The colors of the square represent the color exhibited from the samples.

The color of the spinels with magenta, intense red or orange coloration is caused mainly by a combination of Cr and V in the trivalent state. The Fe (both Fe^{2+} and Fe^{3+}) has a secondary role in the coloration of these samples. In addition, when the amounts of Cr exceed the amounts of V, the spinels show an intense red and magenta color. On the contrary, when the amounts of V exceed the amounts of Cr, the spinels show an orange color. The other samples with a pink, violet, or blue and blue-green coloration show a strong influence of Fe_{tot} . The latter samples were put in a ternary diagram plotting their contents of Fe_2O_3 , FeO and MnO (for the blue and green shade) or Cr_2O_3 (for the pink and violet shade) in order to discriminate the influence of Fe^{2+} and Fe^{3+} (Fig. 4.18).

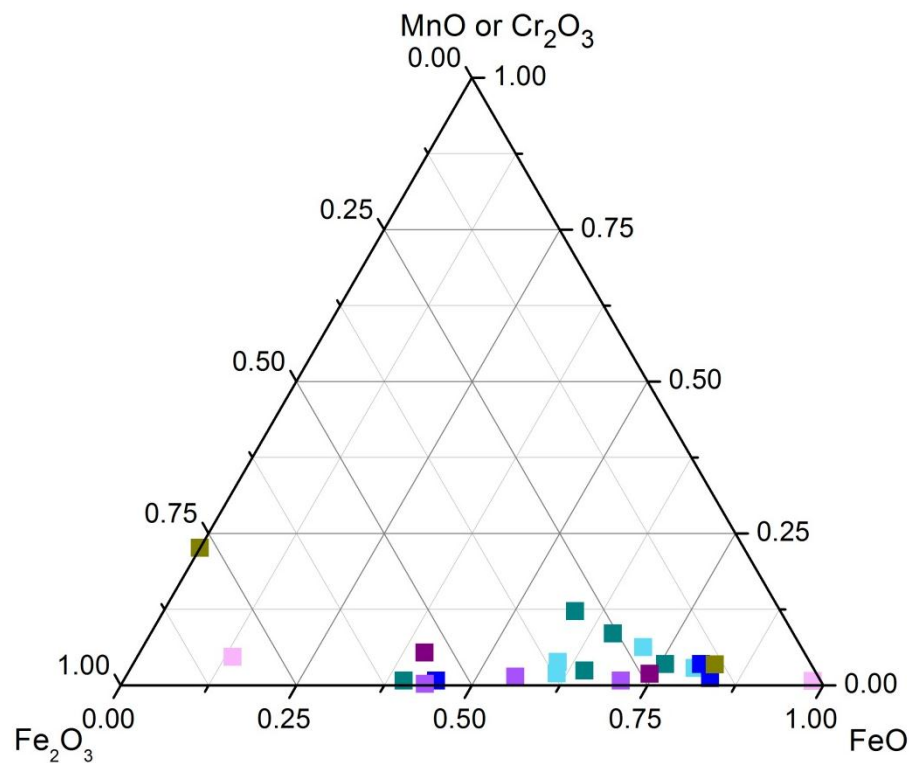


Fig. 4.18. Chemical composition of the natural spinels expressed in terms of Fe_2O_3 , FeO and MnO (for the blue and green shade) or Cr_2O_3 (for the pink and violet shade) weight per cent.

The ternary diagram in Figure 4.18 does not show any correlation between the kind of tone and the amount of Fe^{2+} or Fe^{3+} . Bearing in mind that the Fe^{2+} and Fe^{3+} were calculated from the charge-balance and stoichiometry, the absence of any correlation

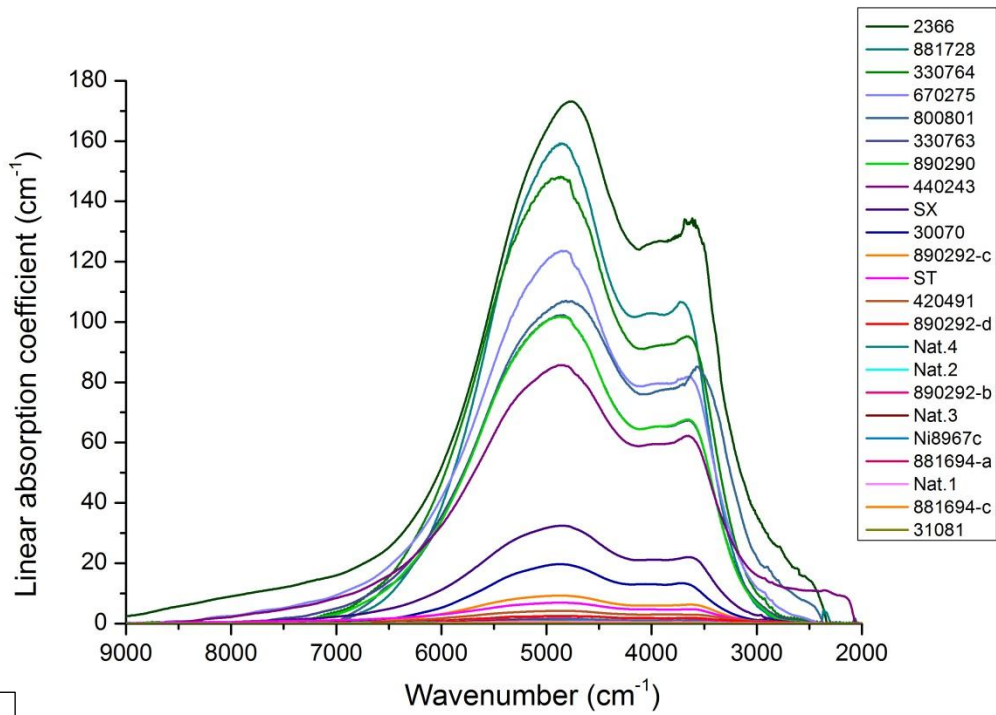
can be due to a lack of accuracy. The yellowish-green sample 31081 only contains Fe^{3+} and a fairly high amount of Mn.

4.2.2 Spectroscopic characterization

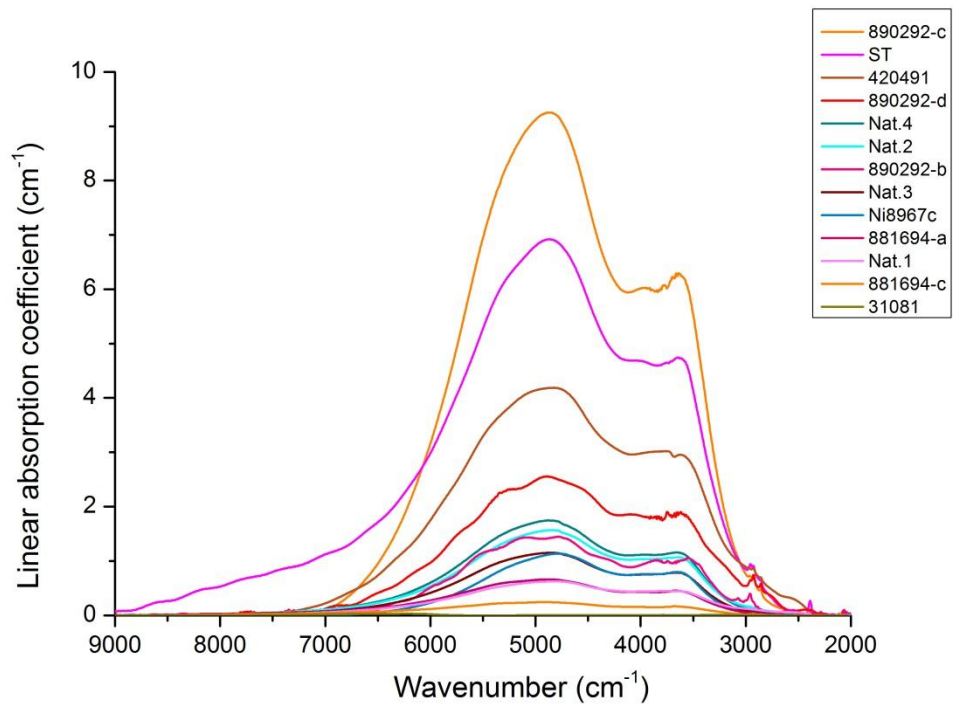
➤ *Fourier transform infrared spectroscopy*

The spectra of all the natural samples were acquired in the NIR and MIR spectral ranges (2000-9000) and are reported in Figure 4.19 a.

All natural spinels, with the exception of the 31081 sample, show a very intense absorption band in the NIR range centered at $\sim 5000 \text{ cm}^{-1}$ which is assigned, in agreement with previous studies, to spin allowed $d-d$ transitions ${}^5\text{E} \rightarrow {}^5\text{T}_2$ in Fe^{2+} located at the T sites. The strong band is split into four sub-bands, which cause a distinct shoulder at $\sim 3500 \text{ cm}^{-1}$, because of the dynamic Jahn-Teller effect of ${}^{\text{T}}\text{Fe}^{2+}$ in the spinel structure (Skogby and Hålenius, 2003; Taran et al. 2005). The intensity of such band increases with the increasing of the Fe^{2+} content in the natural samples. The spectra with a linear absorption coefficient higher than 10 cm^{-1} belong to the dark blue, blue-green and lilac-violet colored spinels, whereas the spectra with a linear absorption coefficient lower than 10 cm^{-1} belong to the red, orange, magenta, pink and light blue colored spinels (Fig. 4.19b). Besides, the 31081 sample does not show the absorption band of the ${}^{\text{T}}\text{Fe}^{2+}$, thus its yellowish-green color is surely not caused by the Fe^{2+} in the tetrahedrally coordinated sites but is probably influenced by the high Mn content.



a



b

Fig. 4.19. Single-crystal spectra of the natural spinels in the NIR-MIR range (9000-2000 cm^{-1}): a) the spectra of all the natural samples; b) the spectra of the samples with a linear absorption coefficient lower than 10 cm^{-1} .

The best fitting model of the ${}^{\text{T}}\text{Fe}^{2+}$ absorption envelope in the interval $2000\text{-}9000\text{ cm}^{-1}$ was obtained by applying a four-band model proposed by Skogby and Hålenius, 2003 using the peak resolution program Jandel PeakFit 4.12 and assuming a Gaussian shape for the bands (Fig. 4.20). The parameters obtained through curve-fitting are summarized in Table 4.11.

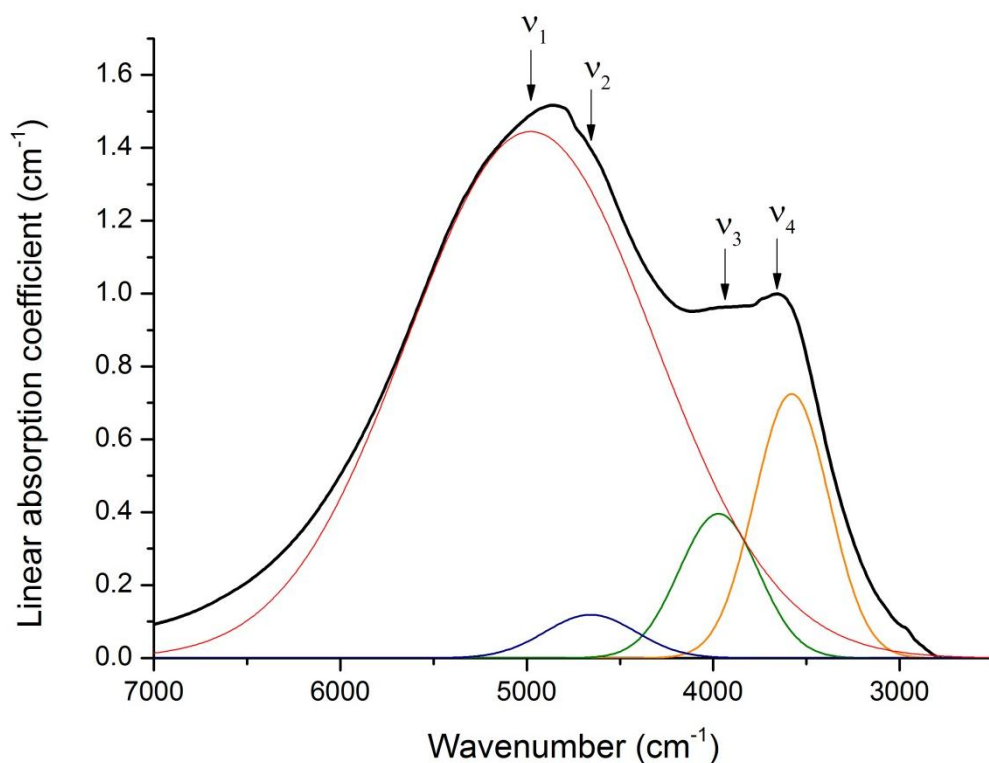


Fig. 4.20. Example of a fitted spectrum (sample Nat.4) showing the four band components (v_1 , v_2 , v_3 , and v_4) of the split spin-allowed electronic $d-d$ transitions ${}^5\text{E} \rightarrow {}^5\text{T}_2$ in tetrahedrally coordinated Fe^{2+} . The thick black line represents experimental data; the colored lines represent the fitted Gaussian shaped bands.

Table 4.11. Curve fitting results of the four absorption bands of ${}^1\text{Fe}^{2+}$ in the NIR and MIR. The parameter ν is the energy (cm^{-1}) α is the linear absorption coefficient (cm^{-1}), FWHM is the full width at the half maximum and A is the integral absorption coefficient (cm^{-2}).

| | Nat.1 | Nat.2 | Nat.3 | Nat.4 | ST | SX | 2366 | 30070 | 330763 | 330764 | 420491 | 440243 |
|---|--------------|--------------|--------------|--------------|-----------|-----------|-------------|--------------|---------------|---------------|---------------|---------------|
| Thickness (μm) | 832 | 279 | 583 | 429 | 545 | 364 | 56 | 245 | 163 | 113 | 690 | 157 |
| ν_1 | 4969 | 4973 | 5011 | 4989 | 5004 | 4992 | 4946 | 4949 | 5004 | 4994 | 5021 | 4953 |
| α_1 | 0.60 | 1.49 | 1.09 | 1.65 | 6.56 | 30.69 | 162.67 | 18.8 | 141.17 | 141.98 | 4.03 | 82.39 |
| FWHM | 1701 | 1550 | 1576 | 1495 | 1733 | 1584 | 1538 | 1426 | 1483 | 1497 | 1746 | 1717 |
| A_1 | 1087 | 2459 | 1831 | 2630 | 12096 | 51734 | 266340 | 28550 | 222870 | 226270 | 7487 | 150620 |
| ν_2 | 4675 | 4617 | 4629 | 4564 | 4616 | 4644 | 4614 | 4641 | 4611 | 4616 | 4666 | 4660 |
| α_2 | 0.05 | 0.14 | 0.13 | 0.20 | 0.67 | 3.27 | 16.94 | 1.49 | 15.12 | 13.09 | 0.39 | 4.84 |
| FWHM | 454 | 597 | 575 | 658 | 649 | 565 | 596 | 481 | 606 | 591 | 495 | 2930 |
| A_2 | 24 | 89 | 79 | 138 | 466 | 1967 | 10740 | 764 | 9756 | 8241 | 204 | 568 |
| ν_3 | 3935 | 4081 | 3993 | 4022 | 4036 | 3969 | 4044 | 4067 | 3975 | 3960 | 3859 | 4082 |
| α_3 | 0.17 | 0.23 | 0.32 | 0.40 | 1.25 | 9.29 | 45.56 | 4.89 | 42.26 | 42.76 | 1.48 | 7.73 |
| FWHM | 603 | 401 | 500 | 426 | 403 | 513 | 449 | 438 | 529 | 528 | 722 | 349 |
| A_3 | 111 | 97 | 169 | 180 | 535 | 5068 | 21754 | 2281 | 23780 | 24037 | 1139 | 2873 |
| ν_4 | 3535 | 3624 | 3597 | 3610 | 3591 | 3579 | 3612 | 3651 | 3576 | 3579 | 3482 | 3618 |
| α_4 | 0.28 | 0.86 | 0.56 | 0.93 | 3.55 | 15.24 | 106.17 | 10.61 | 69.41 | 63.65 | 1.45 | 44.66 |
| FWHM | 520 | 622 | 475 | 522 | 560 | 459 | 5299 | 504 | 494 | 470 | 513 | 649 |
| A_4 | 153 | 573 | 282 | 518 | 2118 | 7444 | 59784 | 5694 | 36473 | 31842 | 793 | 30840 |
| A_{sum} | 1375 | 3218 | 2361 | 3466 | 15214 | 66212 | 358618 | 37289 | 292878 | 290390 | 9623 | 187264 |

Table 4.11. Continued.

| | 510941 | 510942 | 670275 | 800801 | 881694a | 881694c | 881728 | 890290 | 890292b | 890292c | 890292d |
|---|---------------|---------------|---------------|---------------|----------------|----------------|---------------|---------------|----------------|----------------|----------------|
| Thickness (μm) | 76 | 70 | 128 | 126 | 445 | 789 | 89 | 130 | 649 | 323 | 315 |
| v₁ | 4957 | 5123 | 4960 | 5080 | 5081 | 5162 | 4991 | 5029 | 5030 | 5028 | 5106 |
| α_1 | 79.71 | 127.15 | 117.32 | 97.98 | 0.62 | 0.23 | 147.99 | 95.89 | 1.38 | 8.82 | 2.33 |
| FWHM | 1720 | 1632 | 1572 | 1561 | 1644 | 1487 | 1412 | 1481 | 1513 | 1582 | 1422 |
| A₁ | 145950 | 220910 | 196260 | 162750 | 1091 | 359 | 222400 | 151210 | 2231 | 14854 | 3528 |
| v₂ | 4533 | 4445 | 4683 | 4485 | 4619 | 4566 | 4642 | 4615 | 4526 | 4602 | 4562 |
| α_2 | 9.65 | 40.91 | 9.12 | 25.09 | 0.1 | 0.06 | 20.4 | 14.25 | 0.19 | 1.14 | 0.7 |
| FWHM | 565 | 708 | 544 | 809 | 607 | 676 | 581 | 593 | 632 | 593 | 615 |
| A₂ | 5804 | 308500 | 5280 | 21616 | 63 | 45 | 12617 | 8985 | 129 | 718 | 459 |
| v₃ | 4084 | 4086 | 3967 | 4002 | 3929 | 3994 | 4015 | 3939 | 3933 | 4012 | 4103 |
| α_3 | 17.83 | 26.117 | 31.508 | 29.07 | 0.24 | 0.09 | 52.541 | 37.14 | 0.5 | 2.353 | 0.67 |
| FWHM | 423 | 416 | 503 | 436 | 580 | 523 | 496 | 591 | 506 | 463 | 484 |
| A₃ | 8035 | 11556 | 16862 | 13482 | 146 | 52 | 27752 | 23377 | 266 | 1159 | 344 |
| v₄ | 3622 | 3635 | 3588 | 3579 | 3562 | 3592 | 3636 | 3562 | 3516 | 3579 | 3609 |
| α_4 | 55.71 | 106.12 | 51.94 | 66.37 | 0.28 | 0.13 | 77.832 | 43.07 | 0.83 | 5.006 | 1.68 |
| FWHM | 614 | 678 | 462 | 541 | 406 | 429 | 437 | 447 | 498 | 526 | 706 |
| A₄ | 36461 | 76610 | 25567 | 38250 | 123 | 57 | 36201 | 20499 | 442 | 2801 | 1261 |
| A_{sum} | 196250 | 339926 | 243969 | 236097 | 1423 | 514 | 298971 | 204071 | 3068 | 19532 | 5593 |

Hålenius et al. (2002) showed an excellent linear correlation of the extinction coefficient of the 5000 cm^{-1} band (ν_1) with sample $^T\text{Fe}^{2+}$ concentration. Thus, an estimated Fe^{2+} content was calculated for the natural spinels here investigated, starting from the measured values of linear extinction coefficients and using the equation determined by Halenius et al. (2002). Good agreement between Fe^{2+} content calculated from OAS and Fe^{2+} content from microprobe analyses, were acquired, with exception of some samples for which the optical spectra results in an apparent overestimation of the $^T\text{Fe}^{2+}$ content (Fig. 4.21). This can be due to a chemical zoning of the sample. In fact, the Fe concentrations recorded by microprobe analyses reflect the chemistry at the sample surface, while the optical spectra reflect the average chemistry through the entire sample thickness.

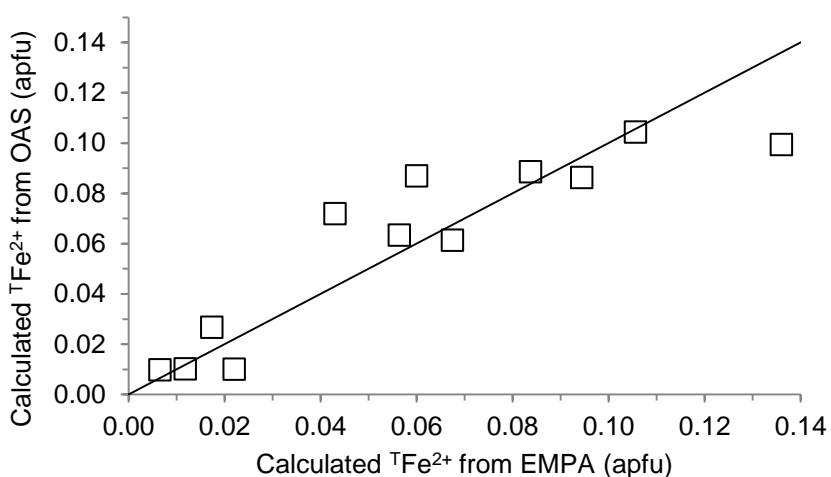


Fig. 4.21. Natural spinels: comparison between the Fe^{2+} content calculated from microprobe analyses and that one calculated from OAS, according to equation reported in Hålenius et al., (2002).

The position of the ν_1 band varies slightly in the colored samples ranging from 4946 cm^{-1} in a blue-green sample (2366) to 5162 cm^{-1} in an orange sample (881694c). The obtained values are in agreement with the values reported in literature (Lenaz et al., 2004, Skogby and Hålenius, 2003). A relationship between the color and the shift of the position in the natural samples can not be found. To investigate the causes of these variations a structural study is required in order to relate the shift position with the bond distance of the different sample.

➤ **UV-VIS-NIR spectroscopy**

The spectra of all the natural samples were acquired in the UV-VIS and NIR spectral ranges ($30000-9000\text{ cm}^{-1}$). According to the color, the optical absorption spectra and the predominant transition metal, the natural spinels studied can be subdivided into:

1. Spinel with dominant amount of Cr and V:
 - orange, red and magenta colored spinels;
2. Spinel with dominant amount of Fe:
 - pink, lilac and violet spinels;
 - light blue, and dark blue spinels;
 - blue-green and dark green spinels;
3. Spinel with dominant amount of Fe^{3+} and Mn:
 - A yellowish green spinel.

In the investigated natural samples, traces of all important transition metal ions such as Fe^{2+} , Fe^{3+} , Mn, Cr, V, Co are detected analytically and thus, the resulting absorption spectra of most natural samples are composed of absorption bands caused by two or even more transition metal ions. This is responsible for the great number of colors and hue in natural spinels.

1) Spinel with dominant amount of Cr and V

The red, orange and magenta colored spinels are gathered in a group because their absorption spectra show a similar shape, with two strong absorption bands at $\sim 25500\text{ cm}^{-1}$ (with a shoulder at $\sim 23900\text{ cm}^{-1}$) and at $\sim 18500\text{ cm}^{-1}$ in the blue violet and green regions of the visible spectrum (Fig. 4.22).

The absorption bands at $\sim 25500\text{ cm}^{-1}$ and at $\sim 18500\text{ cm}^{-1}$ are the principal responsible of the color in this group of spinel. Hålenius et al. (2010) stated that the position and intensity of these absorption bands largely determine a change in color from pale red to dark green with the increase of the Cr content along the MgAl_2O_4 -

MgCr₂O₄ series. This color variation is due to a shift of the spin-allowed Cr³⁺ *d-d* bands toward lower energies with increasing Cr contents.

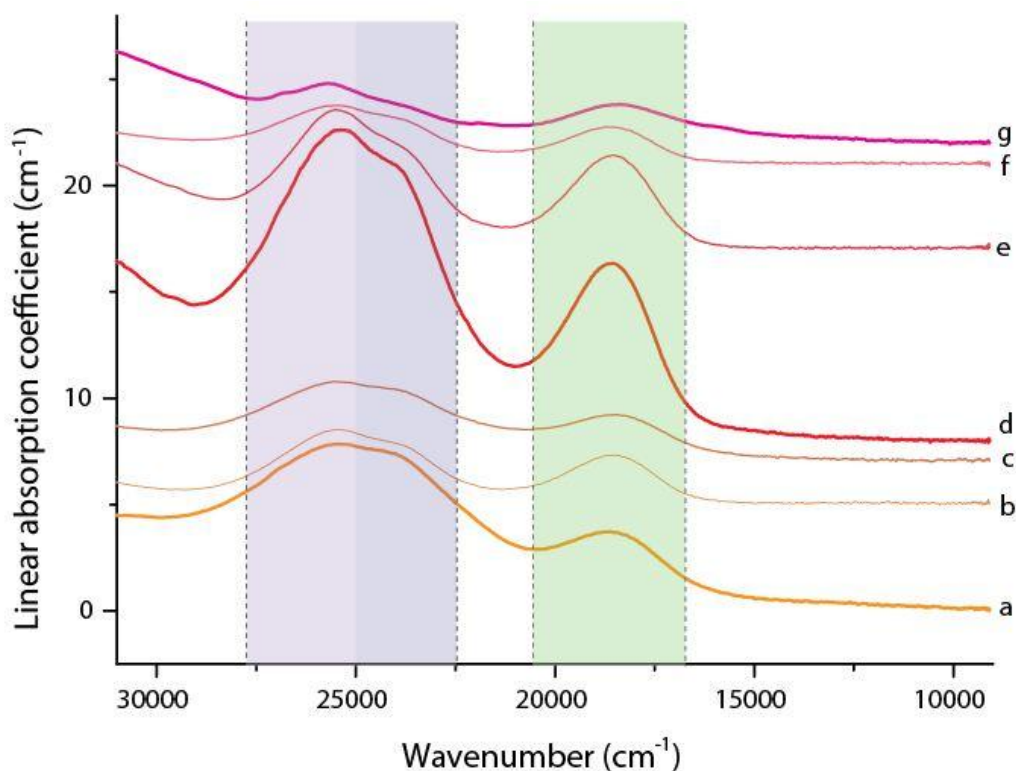


Fig. 4.22. Optical absorption spectra of the investigated natural spinels showing orange, red, magenta (and intermediate) colorations. a) OAS of an orange colored spinel (890292c); b) OAS of a dark orange colored spinel (881694c); c) OAS of a reddish orange colored spinel (420491); d) OAS of a red colored spinel (890292d); e) OAS of a magenta-red colored spinel (890292b); f) OAS of a reddish magenta colored spinel (ST); g) OAS of a magenta colored spinel (881694a). The colors of the spectra represent the color exhibited from the samples.

As already seen in the chemical characterization, the orange and red colored spinels contain both Cr³⁺ and V³⁺ as chromophore ions, which absorption bands are superimposed in the optical spectra. In agreement with previous studies (e.g., Schmetzer et al., 1989; Lenaz et al., 2004; Hålenius et al., 2010), each absorption band of the natural studied spinels was fitted with three sub-bands representing the spin-allowed transition of ^MCr³⁺ and ^MV³⁺ (Fig.4.23). The V³⁺-bearing spinels show two intense absorption bands (c and f) at ~18700 cm⁻¹ (ν₁) and at ~25000 cm⁻¹ (ν₂) related to the spin-allowed *d-d* transition ³T₁(F) → ³T₁(P) and ³T₁(F) → ³T₂(F), respectively, in V³⁺ at the M sites. Besides, the Cr³⁺-bearing spinels show two intense and broad

bands at $\sim 18600\text{ cm}^{-1}$ (ν_1) and at $\sim 25000\text{ cm}^{-1}$ (ν_2) caused by spin-allowed electronic $d-d$ transitions ${}^4A_{2g} \rightarrow {}^4T_{2g}(F)$ and ${}^4A_{2g} \rightarrow {}^4T_{1g}(F)$, respectively, in Cr^{3+} at the M sites. The point symmetry of the Cr^{3+} -bearing M site is lowered from O_h (ideal octahedron) to D_{3d} (trigonally distorted octahedron). As a consequence, the two excited spectroscopic states in Cr^{3+} are split into two spin-allowed $d-d$ transitions. Hence, the two absorption bands are fitted with four sub-bands: e and g and b and d , respectively.

Thus, after the fitting procedure, in the spinels with V concentration higher than Cr the bands c, f prevail on the bands b, d, e and g .

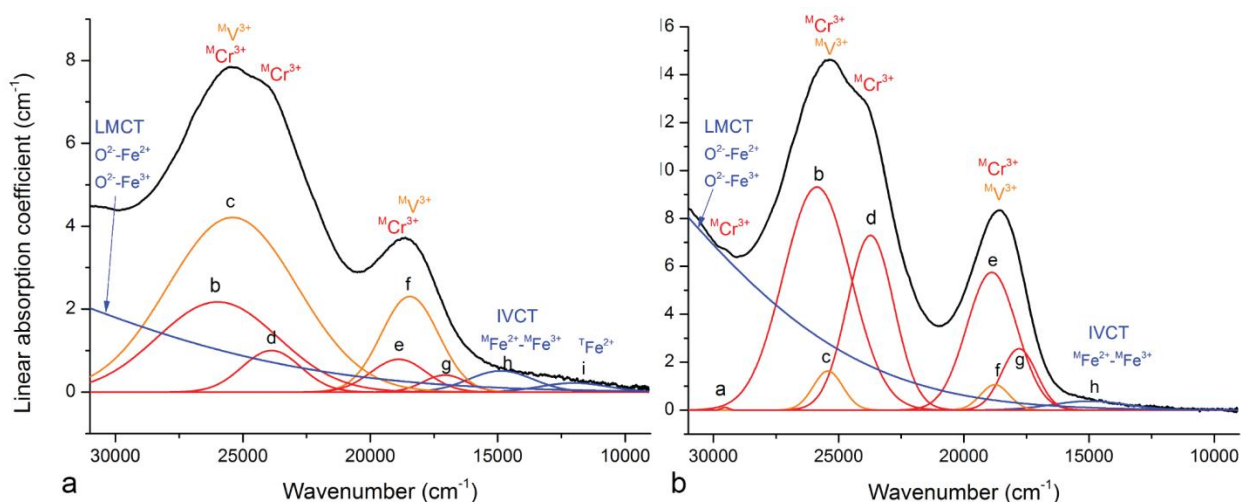


Fig. 4.23. Curve resolved spectrum in the spectral range $31000\text{--}9000\text{ cm}^{-1}$: a) fitting of an orange colored natural spinel (890292c); b) fitting of a red colored natural spinel (890292d). The red line in the UV-VIS range represent the low-energy wing of the UV absorption bands caused by oxygen to metal electronic charge transfer transition $\text{O}^{2-} \rightarrow \text{Fe}^{2+}$.

In the spinel with high Cr concentration a weak and narrow absorption band occur at $\sim 29000\text{ cm}^{-1}$ assigned to the spin-forbidden transition ${}^2A_{1g}({}^2G) \rightarrow {}^2T_{1g}({}^2G)$ of Cr^{3+} in octahedrally coordinated sites. Some spinels show an additional weak band at $\sim 15000\text{ cm}^{-1}$ attributable to the $\text{Fe}^{2+}\text{--Fe}^{3+}$ exchange interaction. In addition, all the spectra studied show the low-energy wing of the UV absorption bands caused by oxygen to metal electronic charge transfer transition $\text{O}^{2-} \rightarrow \text{Fe}^{2+}$ or $\text{O}^{2-} \rightarrow \text{Fe}^{3+}$. The results of the spectrum fits are summarized in Table 4.12.

Table 4.12. The observed energies (cm⁻¹) of the red, orange and magenta colored spinels.

| | ST | 420491 | 881694a | 881694c | 890292b | 890292c | 89292d | Assignment | Electronic transition |
|----------|-------|--------|---------|---------|---------|---------|--------|------------------------------------|--|
| a | – | 28808 | – | 28427 | – | – | – | ^M Cr ³⁺ | spin-forbidden transition ${}^2A_{1g}({}^2G) \rightarrow {}^2T_{1g}({}^2G)$ |
| b | 25757 | 25900 | 25670 | 25677 | 25865 | 25988 | 25865 | ^M Cr ³⁺ | spin-allowed electronic <i>d-d</i> transitions ${}^4A_{2g} \rightarrow {}^4T_{1g}(F)$ |
| c | 25560 | 25325 | 24875 | 25382 | 25590 | 25404 | 25424 | ^M V ³⁺ | spin-allowed <i>d-d</i> transition ${}^3T_1(F) \rightarrow {}^3T_1(P)$ |
| d | 23808 | 23674 | 23781 | 23515 | 23910 | 23876 | 23724 | ^M Cr ³⁺ | spin-allowed electronic <i>d-d</i> transitions ${}^4A_{2g} \rightarrow {}^4T_{1g}(F)$ |
| e | 18803 | 18649 | 18670 | 18905 | 18886 | 18887 | 18887 | ^M Cr ³⁺ | spin-allowed electronic <i>d-d</i> transitions ${}^4A_{2g} \rightarrow {}^4T_{2g}(F)$ |
| f | 18051 | 18393 | 18523 | 18471 | 18725 | 18449 | 18758 | ^M V ³⁺ | spin-allowed <i>d-d</i> transition ${}^3T_1(F) \rightarrow {}^3T_2(F)$ |
| g | 17202 | 17325 | 17253 | 18128 | 17914 | 17076 | 17797 | ^M Cr ³⁺ | spin-allowed electronic <i>d-d</i> transitions ${}^4A_{2g} \rightarrow {}^4T_{2g}(F)$ |
| h | 15014 | 14977 | 14582 | – | 15438 | 14876 | 14977 | Fe ²⁺ -Fe ³⁺ | Fe ²⁺ -Fe ³⁺ exchange interaction |
| i | 11483 | 12348 | 12594 | 12323 | 12950 | 12011 | – | ^M Fe ²⁺ | spin-allowed <i>d-d</i> transition ${}^5T_{2g} \rightarrow {}^5E_g$ |

The differences among the absorption spectrum of orange, red and magenta colored spinels are very slight (Fig. 4.24). The orange and red spinel spectra have the same absorption bands but, since the orange spinels have a significant amount of V, the absorption band centered at $\sim 25500\text{ cm}^{-1}$ is wider in the spectra of the orange spinels than that in the red ones. A greater width of the bands causes a greater absorption of the violet and blue to green regions of the visible spectrum and thus a transmission of the orange region.

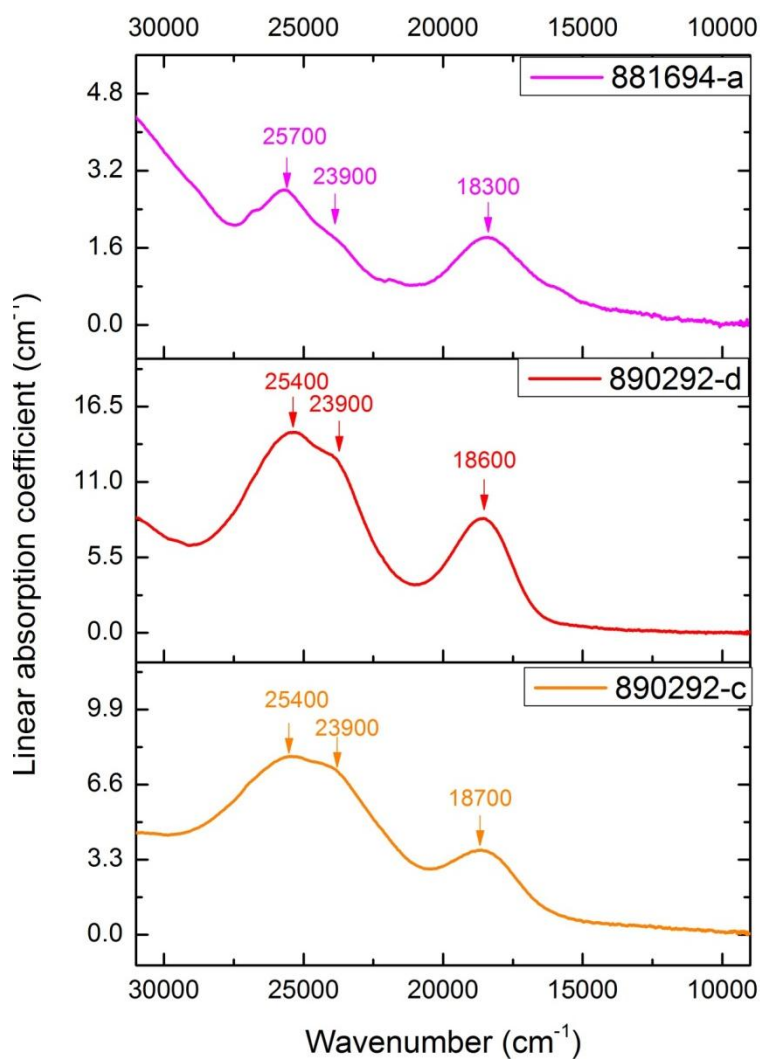


Fig. 4.24. Optical absorption spectra of orange, red and magenta colored spinels. The center positions are reported for the principal bands.

Regarding the magenta colored spinels, they have considerable amount of Cr and secondary amount of Fe. In fact, magenta spinels show an absorption spectrum similar to that of red spinels but with some absorption bands attributable to the iron cation. With respect to the absorption spectrum of the red spinel, the band of the magenta spinels at $\sim 25500\text{ cm}^{-1}$ is less intense and the band at $\sim 18000\text{ cm}^{-1}$ undergoes a red shift. In addition, the magenta spinels show an intense low-energy wing of the UV absorption band due to LMCT $\text{O}^{2-} \rightarrow \text{Fe}^{2+}$. Consequently, magenta spinels exhibit a larger window in the blue region of the visible spectrum and their color is obtained combining equal amounts of red and blue light transmitted.

2) Spinel with dominant amount of Fe

As already seen in the paragraph 4.2.1 dealing with chemical characterization, iron is the main transition metal component causing various colors with different tone like pink, violet, blue and dark green in the natural spinels. The absorption spectra of these colored spinels are very similar but they differ in some small features which are revealed only with a detailed and careful investigation. Typical spectra of Fe-bearing spinels consist of a high energy absorption edge and a series of absorption bands superimposed on it. The results of the curve-fitting of pink, blue and green colored spinels are shown in the Figure 4.25 and the values of energy are summarized in Table 4.13.

At least ten Gaussian curves are necessary for the fit of the pink spinels whereas in the case of the light blue and dark green spinels, twelve Gaussian curves are necessary for a satisfactory fit. For clearness a common labelling was taking for the same component bands in the different spectra. Most of the absorption bands are similar but others have different position, shape and intensity. The differences in the absorption spectra are caused by different total iron content, different amount of Fe^{2+} and Fe^{3+} and their distribution in the structural sites.

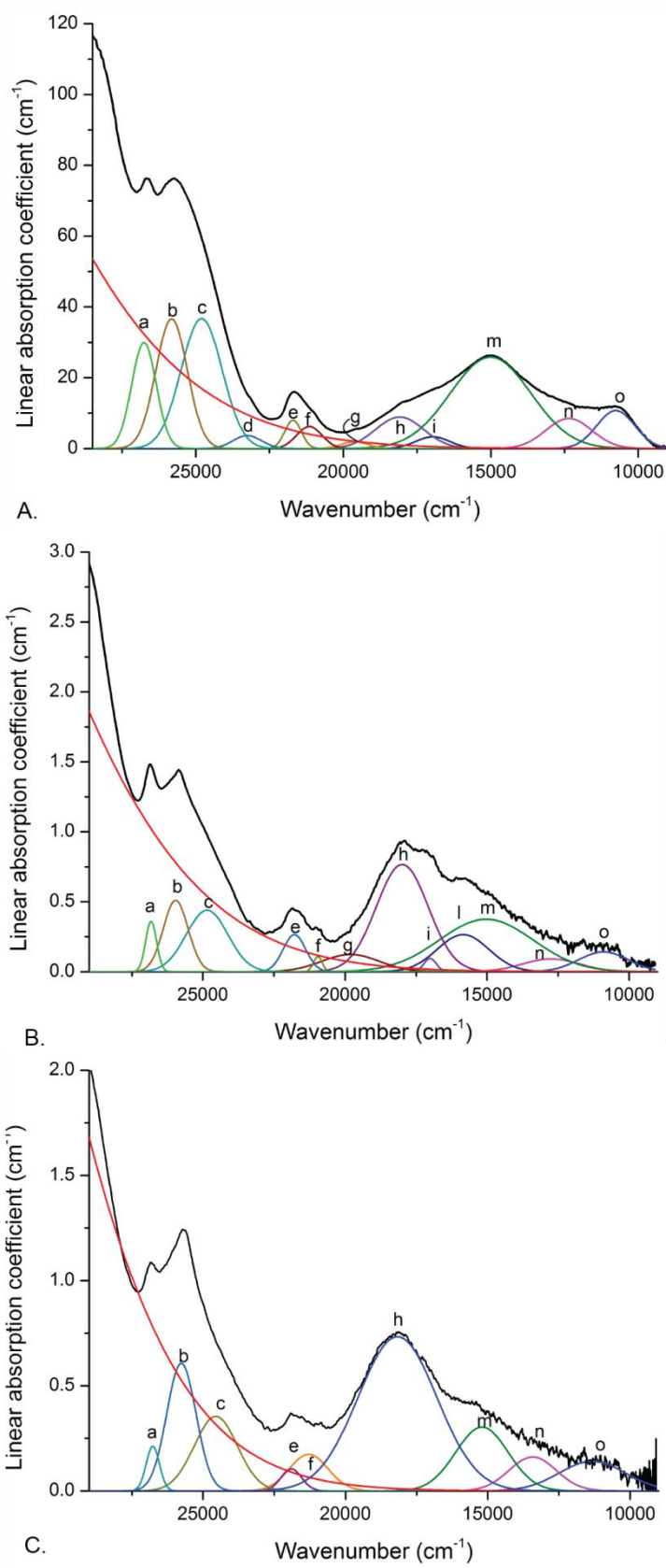


Fig. 4.25. Curve resolved spectra of pink , blue and green colored spinels (from base to top).

Table 4.13. Observed energies of the pink, blue and green colored spinels. The assignment of the absorption bands to the different transitions was made in agreement with previous studies (Schmetzer *et al.* 1989; Hålenius *et al.*, 2002; Lenaz *et al.* 2004; Taran *et al.*, 2005).

| | Nat.1 | Nat.2 | Nat.3 | Nat.4 | 2366 | 30070 | 330763 | 330764 | Assignment |
|---|-------|-------|-------|-------|-------|-------|--------|--------|--|
| a | 26797 | 26825 | 26830 | 26867 | 26697 | 26640 | 26822 | 26824 | spin-forbidden transitions ${}^5E \rightarrow {}^3E$ of TFe^{2+} |
| b | 25801 | 25956 | 25819 | 25972 | 25709 | 25730 | 25943 | 25862 | spin-forbidden transitions ${}^5E \rightarrow {}^3T_2, {}^3T_1$ of TFe^{2+} |
| c | 24285 | 24852 | — | 24675 | 24521 | 24870 | 24839 | 24692 | spin-forbidden transitions ${}^6A_{1g} \rightarrow {}^4E_g$ (4D) of ${}^MFe^{3+}$ |
| d | — | — | 23779 | — | 23101 | — | 23595 | — | |
| e | 21879 | 21775 | 21679 | 21789 | 21693 | 21656 | 21722 | 21739 | ${}^6A_{1g} \rightarrow {}^4A_{1g}, {}^4E_g$ transition of ${}^MFe^{3+}$ |
| f | 21533 | 20955 | 20406 | 21025 | 21056 | 21112 | 20936 | 21112 | spin-forbidden transitions ${}^5E \rightarrow {}^3T_2, {}^3T_1, {}^3E$ of TFe^{2+} |
| g | — | — | — | — | — | — | 19861 | 19426 | |
| h | 18269 | 17986 | 17920 | 17921 | 17927 | 17943 | 18046 | 17905 | spin-forbidden transitions ${}^5E \rightarrow {}^3T_2$ of TFe^{2+} |
| i | — | 17004 | — | 17335 | 17099 | 16932 | 16901 | 17020 | spin-forbidden transitions ${}^5E \rightarrow {}^3T_1$ of TFe^{2+} |
| l | — | 15843 | — | — | — | 16063 | — | — | spin-allowed transitions ${}^4A_2(F) \rightarrow {}^4T_1(P)$ of TCo^{2+} |
| m | 14992 | 15028 | — | 15617 | 14958 | 14842 | 15301 | 15147 | ${}^MFe^{2+} \leftrightarrow {}^MFe^{3+}$ IVCT |
| n | — | 12748 | 12899 | 12921 | 11921 | — | 12255 | 12065 | spin-forbidden transitions ${}^5E \rightarrow {}^3T_1$ of TFe^{2+} |
| o | — | 10904 | — | — | 10479 | 10629 | 10881 | 10716 | spin-allowed $d-d$ transition ${}^5T_{2g} \rightarrow {}^5E_g$ in ${}^MFe^{2+}$ |

Table 4.13. Continued.

| | 440243 | 510941 | 510942 | 670275 | 800801 | 881728 | 890290 | Assignment |
|---|--------|--------|--------|--------|--------|--------|--------|---|
| a | 26794 | 26670 | 26624 | 26850 | 26775 | 26758 | 25906 | spin-forbidden transitions ${}^5E \rightarrow {}^3E$ of ${}^TFe^{2+}$ |
| b | 25910 | 25874 | 25813 | 25860 | 25945 | 25821 | 25906 | spin-forbidden transitions ${}^5E \rightarrow {}^3T_2, {}^3T_1$ of ${}^1Fe^{2+}$ |
| c | 24854 | 25032 | 24787 | 24455 | 24740 | 24803 | 24809 | spin-forbidden transitions ${}^6A_{1g} \rightarrow {}^4E_g$ (4D) of ${}^MFe^{3+}$ |
| d | — | — | — | — | 23053 | 23255 | 23511 | spin-forbidden electronic $d-d$ transition ${}^6A_1(S) \rightarrow {}^4E_g, {}^4A_{1g}(G)$ in ${}^TMn^{2+}$ |
| e | 21820 | 21705 | 21685 | 21853 | 21766 | 21703 | 21751 | ${}^6A_{1g} \rightarrow {}^4A_{1g}, {}^4E_g$ transition of ${}^MFe^{3+}$ |
| f | 20994 | 21123 | 20926 | 20910 | 21179 | 21148 | 21265 | spin-forbidden transitions ${}^5E \rightarrow {}^3T_2, {}^3T_1, {}^3E$ of ${}^TFe^{2+}$ |
| g | — | — | — | — | 19157 | 19617 | | |
| h | 17935 | 17826 | 17831 | 17861 | 18314 | 18089 | 18135 | spin-forbidden transitions ${}^5E \rightarrow {}^3T_2$ of ${}^TFe^{2+}$ |
| i | — | 16973 | 16757 | — | 17021 | 16969 | 17115 | spin-forbidden transitions ${}^5E \rightarrow {}^3T_1$ of ${}^TFe^{2+}$ |
| l | — | 16048 | 15894 | — | 15809 | — | — | spin-allowed transitions ${}^4A_2(F) \rightarrow {}^4T_1(P)$ of ${}^TCo^{2+}$ |
| m | 14943 | 14741 | 14849 | 15128 | 14945 | 15006 | 15139 | ${}^MFe^{2+} \leftrightarrow {}^MFe^{3+}$ IVCT |
| n | 13325 | 11559 | 12619 | — | 12797 | 12350 | 12300 | spin-forbidden transitions ${}^5E \rightarrow {}^3T_1$ of ${}^TFe^{2+}$ |
| o | 11458 | 10204 | 10544 | — | 10848 | 10758 | 10822 | spin-allowed $d-d$ transition ${}^5T_{2g} \rightarrow {}^5E_g$ in ${}^MFe^{2+}$ |

The spectra of the all the colored spinels show a strong UV-edge absorption at energy $\gg 30000 \text{ cm}^{-1}$ which is due to $\text{O}^{2-} \rightarrow \text{Fe}^{2+}$ and $\text{O}^{2-} \rightarrow \text{Fe}^{3+}$ charge transfer transitions and causes a strong absorption of the violet and blue component of the visible light (red line in the Fig.4. 25). The bands close to the UV-absorption edge at ~ 26800 , 25800 and 24500 cm^{-1} (labelled *a*, *b* and *c*, respectively) are common to all spectra and could be assigned to spin-forbidden transitions ${}^5\text{E}(\text{D}) \rightarrow {}^3\text{E}(\text{D})$, for the *a* band, and ${}^5\text{E}(\text{D}) \rightarrow {}^3\text{T}_2(\text{G})$, ${}^3\text{T}_1(\text{G})$, for the *b* and *c* band, of isolated ${}^{\text{T}}\text{Fe}^{2+}$ ions. The position of these bands is almost the same for all crystals, with exception of a very slight shift of the *b* band to 25700 cm^{-1} for the dark green specimen. In addition, the height of the bands increases with the total iron content. In all the spectra, a sharp band at $\sim 21800 \text{ cm}^{-1}$ (labelled *e*) is also present with a split component at $\sim 20800 \text{ cm}^{-1}$ (labelled *f*). Similar optical absorption bands were observed in natural spinels by Schmetzer et al. (1989) and Taran et al. (2005) and in synthetic spinel-magnesioferrite crystals by Andreozzi et al. (2001b). Schmetzer et al. (1989) assigned these bands to spin forbidden transitions ${}^5\text{E}(\text{D}) \rightarrow {}^3\text{E}(\text{G})$, ${}^3\text{T}_2(\text{F})$, ${}^3\text{T}_1(\text{F})$ of ${}^{\text{T}}\text{Fe}^{2+}$, whereas the other authors assigned them to spin-forbidden ${}^6\text{A}_{1\text{g}} \rightarrow {}^4\text{A}_{1\text{g}}$, ${}^4\text{E}_{\text{g}}$ transitions of isolated ${}^{\text{M}}\text{Fe}^{3+}$ ions (Taran et al. 2005), and to exchange-coupled interaction (ECP) ${}^6\text{A}_{1\text{g}} \rightarrow {}^4\text{A}_{1\text{g}}$, ${}^4\text{E}_{\text{g}}$ in ${}^{\text{T}}\text{Fe}^{3+} - {}^{\text{M}}\text{Fe}^{3+}$ clusters (Andreozzi et al., 2001b). Since the bands *e* and *f* are present in the spectrum of the yellowish-green sample 31081, which not show evidence of ${}^{\text{T}}\text{Fe}^{2+}$, the assignment to only spin forbidden transitions ${}^5\text{E}(\text{D}) \rightarrow {}^3\text{E}(\text{G})$, ${}^3\text{T}_2(\text{F})$, ${}^3\text{T}_1(\text{F})$ of ${}^{\text{T}}\text{Fe}^{2+}$ is not correct. Raman spectra in the paragraph 4.4 (Fig. 4.60) show that only some natural spinels are disordered. On the basis of these evidence, the absorption bands *e* and *f* of the investigated natural spinels are caused mainly by spin-forbidden ${}^6\text{A}_{1\text{g}} \rightarrow {}^4\text{A}_{1\text{g}}$, ${}^4\text{E}_{\text{g}}$ transitions of isolated ${}^{\text{M}}\text{Fe}^{3+}$ ions but it is not excluded that it may be intensified by exchange-coupled interaction and by spin-forbidden transition of ${}^{\text{T}}\text{Fe}^{2+}$, above all in spinels with low Fe^{3+} content.

The largest discrepancy among the absorption spectra of pink, blue and green colored spinels stands between 20000 cm^{-1} and 10000 cm^{-1} . The origin of the band system occurring in this range is not quite clear. It is very likely that some of them may be caused by spin-forbidden transitions of Fe^{2+} . The absorption band at

$\sim 18000 \text{ cm}^{-1}$ (labelled *h*) is dominant in the pink, lilac and violet colored spinels and could be caused by spin forbidden transition ${}^5\text{E}(\text{D}) \rightarrow {}^3\text{T}_2(\text{H})$ of ${}^{\text{T}}\text{Fe}^{2+}$ (Schmetzer et al. 1989; Taran et al. 2005). In the light blue and blue spinels, with the increase of the Fe content, an absorption band at $\sim 17000 \text{ cm}^{-1}$ (labelled *i*) becomes noticeable. Following Schmetzer et al. (1989) and Taran et al. (2005), this band could be due to spin forbidden transitions ${}^5\text{E}(\text{D}) \rightarrow {}^3\text{E}(\text{H})$ of isolated ${}^{\text{T}}\text{Fe}^{2+}$ ions but it could be intensified by the presence of trace amount of Co^{2+} (as it will be proposed forward). In the blue-green and dark green colored spinels the previous bands become less intense and a dominant peak develops at $\sim 15500 \text{ cm}^{-1}$ (labelled *m*). In the green spinels the total Fe content as well as the Fe^{3+} content increase. A band in similar position was assigned to ${}^6\text{A}_{1\text{g}} \rightarrow {}^4\text{T}_{2\text{g}}$ transition of ${}^{\text{M}}\text{Fe}^{3+}$ intensified by antiferromagnetic exchange interaction in ${}^{\text{M}}\text{Fe}^{3+}-{}^{\text{T}}\text{Fe}^{2+}$ by Taran et al. (2005). But a relationship between the Fe^{3+} content and the intensity of the band *m* was not found in the studied spinels and the amounts of Fe^{3+} can not be responsible for the comparatively high intensity of this band. The $\text{Fe}^{2+}-\text{Fe}^{3+}$ IVCT processes in oxygen-based structures are restricted to clusters of cations located in edge- or face-sharing polyhedra (Mattson and Rossman, 1987b; Hålenius et al., 2002), thus the ${}^{\text{M}}\text{Fe}^{3+}-{}^{\text{T}}\text{Fe}^{2+}$ IVCT is not possible. On the other hand, exchange-coupled pairs in which the participating ions are located in polyhedra that share faces, edges, or just corners can act in spinel structures (Hålenius et al., 2002). The large widths displayed by the absorption band at $\sim 15500 \text{ cm}^{-1}$ as well as their nonlinear dependence on Fe content indicate a cooperative electronic processes between Fe^{2+} and Fe^{3+} . Hence, in agreement with Schmetzer et al. (1989) and Hålenius et al. (2002), the *m* band is assigned to ${}^{\text{M}}\text{Fe}^{2+} - {}^{\text{M}}\text{Fe}^{3+}$ IVCT and/or ${}^{\text{M}}\text{Fe}^{2+} - {}^{\text{T}}\text{Fe}^{3+}$ ECP interaction. This assignment is also well supported by the presence of the *o* band at $\sim 10800 \text{ cm}^{-1}$ attributed to a spin-allowed transition (${}^5\text{T}_{2\text{g}} \rightarrow {}^5\text{E}_{\text{g}}$) in octahedrally coordinated ${}^{\text{M}}\text{Fe}^{2+}$, in agreement with literature (Schmetzer et al., 1989; Hålenius et al., 2002).

The three subgroups (pink, blue and green colored spinels) are discriminated by the intensity and the width of the absorption bands (Fig. 4.26).

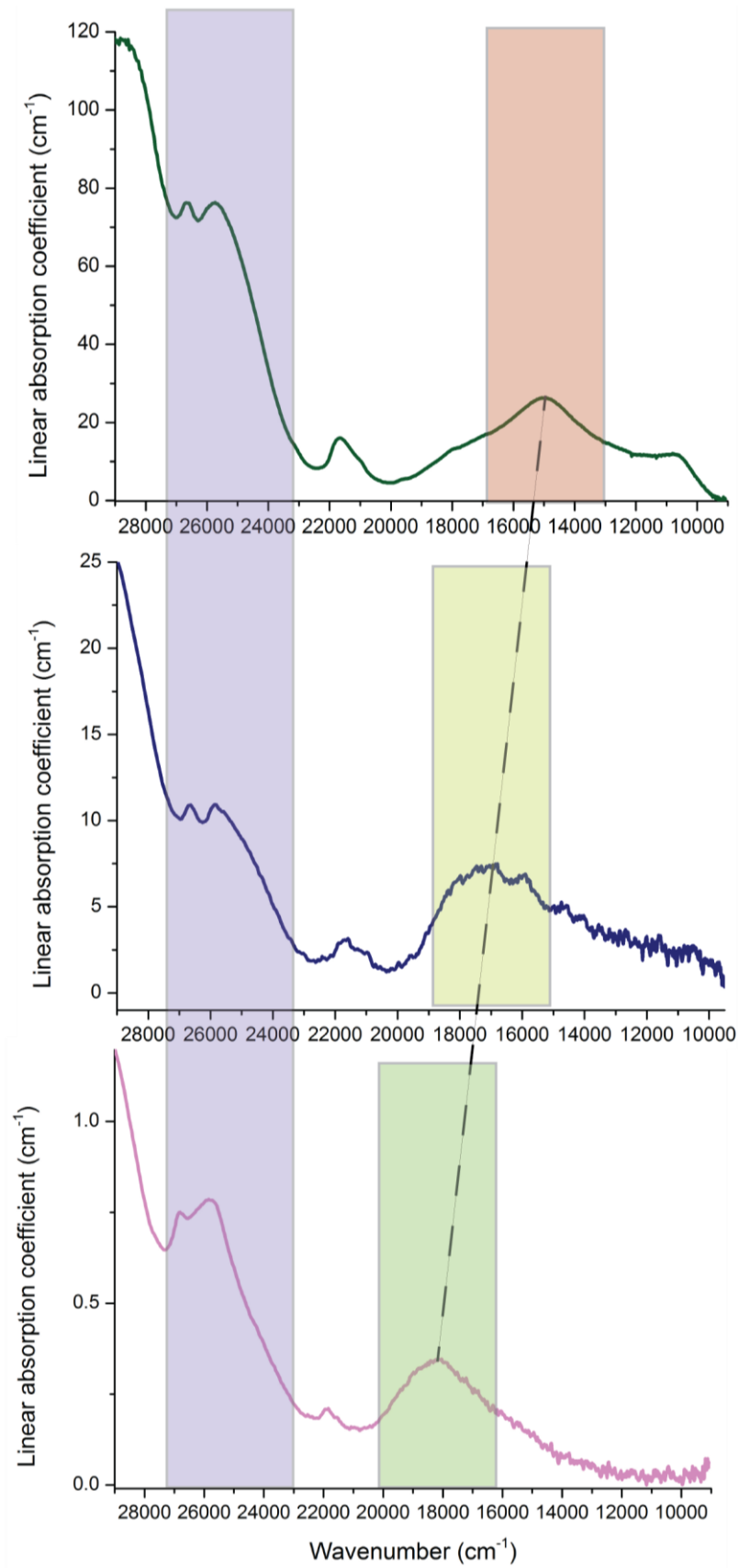


Fig. 4.26. Optical absorption spectra of pink, blue and green colored spinels (from base to top). The portions of the light absorbed are shown. The dash line indicates the shift of the maximum absorption in the 20000-10000 cm^{-1} range.

The component Gaussian bands in the pink, lilac and violet spinels are much broader than in the other subgroups. The intensity of some absorption bands increases with the total iron content: from pink to the green spinels. The most visible differences are shown between 20000 and 10000 cm^{-1} . In this range the most intense absorption bands shift from 18000 cm^{-1} for the pink spinels to 15500 cm^{-1} for the green spinels, whereas the blue spinels show an intermediate situation. This shift of the main absorption band causes obviously a shift in the absorption of the light from green for the pink spinels to red for the green spinels, originating the different colors. In addition, moving from pink to green spinels, the total amount of iron increases as well as the intensity of the strong UV-edge absorption at energy $\gg 30000 \text{ cm}^{-1}$ causing a strong absorption of the violet and blue component of the visible light.

The linear absorption coefficients of the main bands in the range 20000-10000 cm^{-1} were normalized and represented in the triangular diagram (Fig. 4.27). This figure shows as the pink spinels are characterized mainly by the absorption band at $\sim 18000 \text{ cm}^{-1}$, the green samples are characterized mainly by the absorption band at $\sim 15500 \text{ cm}^{-1}$, whereas the blue spinels have the 18000 cm^{-1} band as the main component but an important role may be played also by the absorption band at $\sim 17000 \text{ cm}^{-1}$.

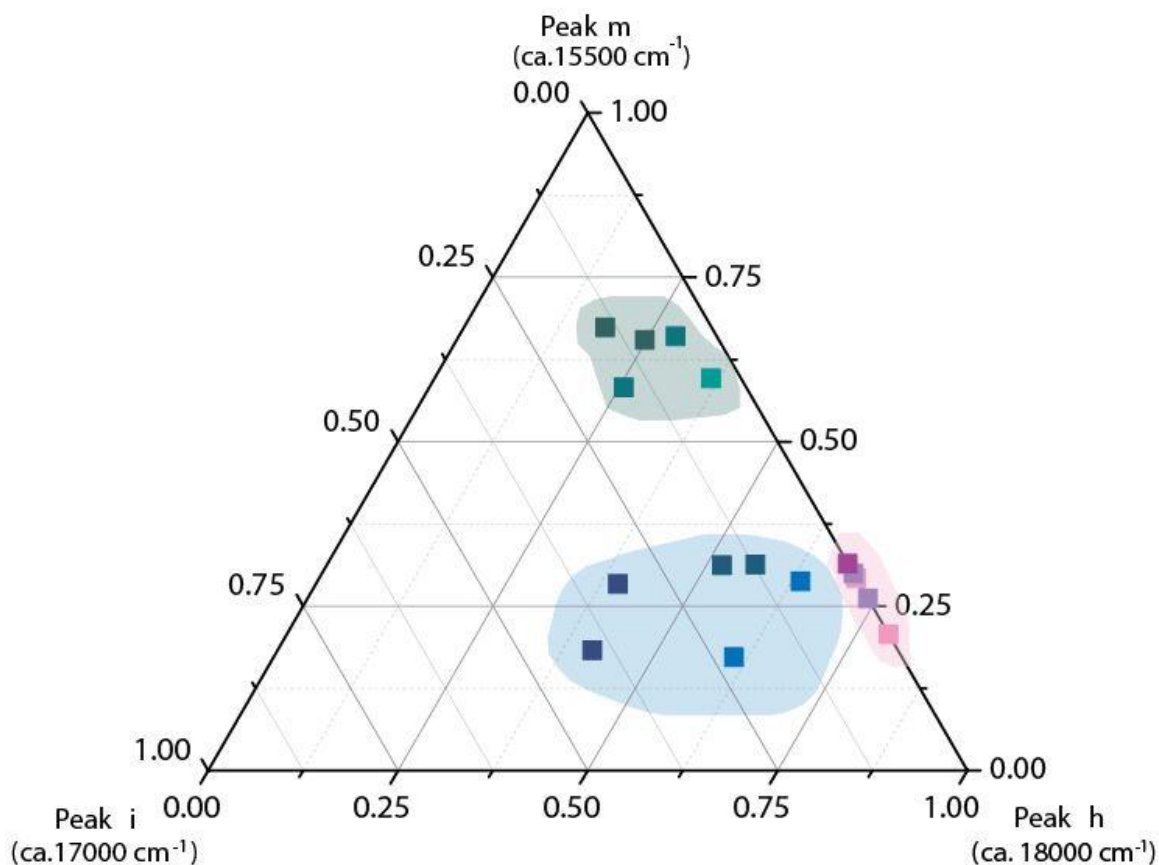


Fig. 4.27. Ternary diagram expressed in terms of the normalized linear absorption coefficient of the main absorption bands in the 20000-10000 cm^{-1} region of the visible spectrum. The colors of the symbols represent the color exhibited from the samples.

A similar situation was observed by Hålenius et al. (2002) in the synthetic crystal belonging to the spinel s.s.-hercynite solid solution, which varied in color from pale lilac to sky blue, green and deep green with increasing total Fe content. This variation of color was explained with an increase of the absorption of the blue light and of the band at $\sim 14500 \text{ cm}^{-1}$. The intensity of the latter band increases in a parabolic way with increasing Fe content (Fig. 4.28a). The same trend was shown by the ${}^M\text{Fe}^{2+}$ and ${}^M\text{Fe}^{3+}$ with increasing Fe content (Fig. 4.28b and c). Taking these features into consideration the authors proposed that the absorption band at $\sim 14500 \text{ cm}^{-1}$ are caused by a ${}^M\text{Fe}^{2+} - {}^M\text{Fe}^{3+}$ IVCT process.

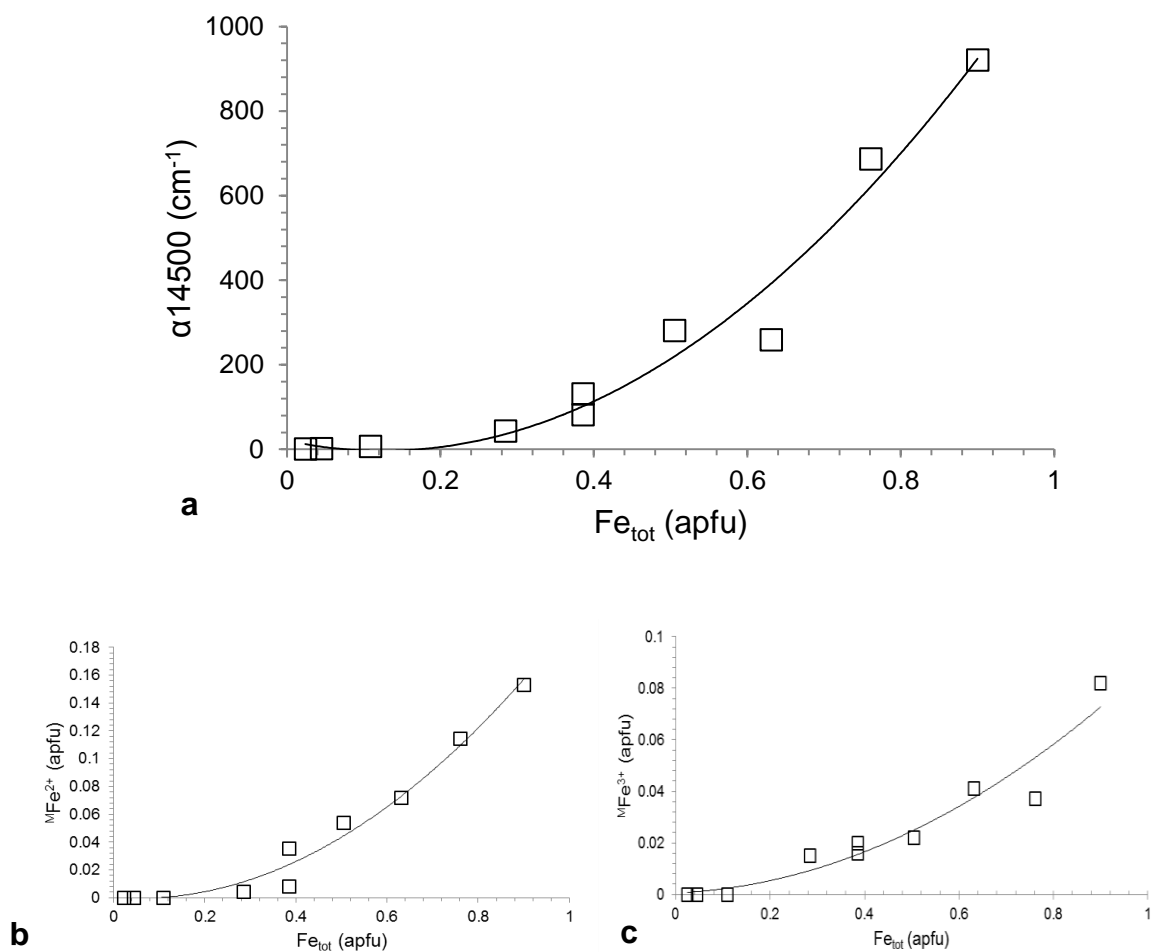


Fig. 4.28. Correlation plots of the linear absorption coefficients of the absorption band at $\sim 14500\text{ cm}^{-1}$ (a), the Fe^{2+} content in apfu in the octahedrally coordinated sites (b), and the Fe^{3+} content in apfu in the octahedrally coordinated sites (c) as a function of the iron total concentrations in apfu. Values taken from Hålenius et al., 2002.

In addition to the characteristic absorption bands of iron, spectra of some natural samples show minor absorption bands caused by electronic $d-d$ transitions in other cations. For example, in the spinel with rather amounts of Mn, such as the sample 2366, a small absorption band at $\sim 23500\text{ cm}^{-1}$ is observed (Fig. 4.29). This band shows very similar characteristic of the most intense absorption band shown by a synthetic spinel *sensu stricto* doped with low concentrations of Mn^{2+} (Jouini et al., 2006) and by a synthetic galaxite (Hålenius et al., 2007). This band was assigned in both the studies to the spin-forbidden electronic $d-d$ transition ${}^6A_1(S) \rightarrow {}^4E_g, {}^4A_{1g}(G)$ in $T Mn^{2+}$.

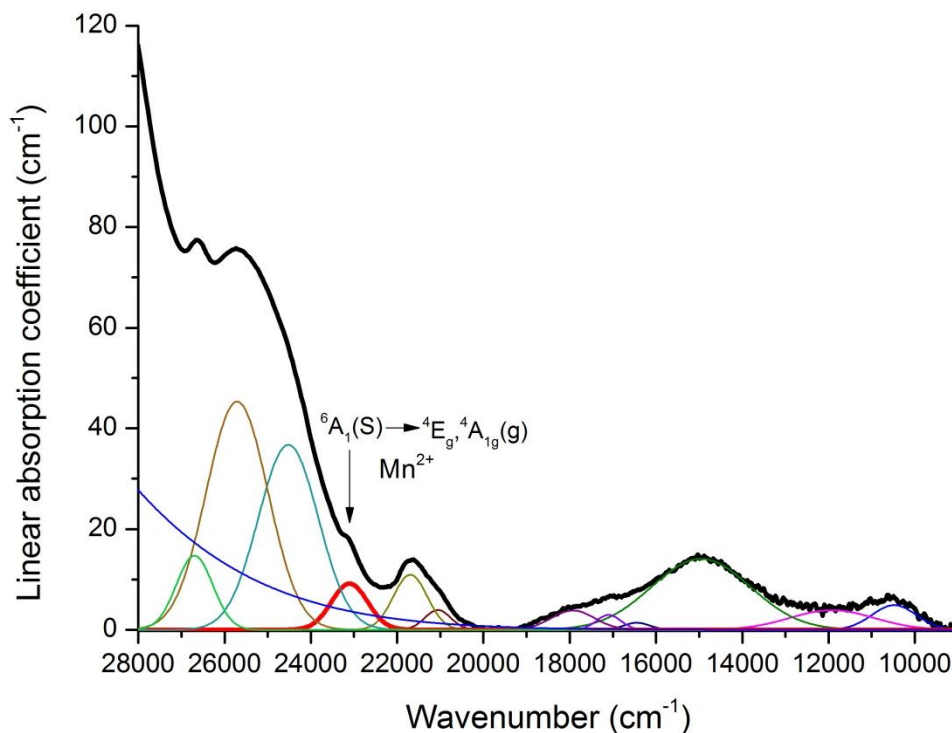


Fig. 4.29. Optical absorption spectra of a investigated natural sample 2366 containing significant amounts of Mn^{2+} .

In the recorded spectra only the most intense absorption band of the typical set of five was collected. In fact, the optical absorption intensities of the TMn^{2+} are quite low, because all transitions involving the ground state are parity- and spin-forbidden, being the ground state the sextet A_1 level whereas all the excited d-levels doublet or quartet states. Because the low intensity of the absorption band found in the recorded spectra, it could be assumed that the TMn^{2+} do not influence significantly the colors in the spinel wherein it occurs.

➤ ***The role of the Co^{2+} on the blue colored spinels***

The optical absorption bands in the range 20000-15000 cm^{-1} of the light blue, blue and blue-green colored spinels can be also intensified by the presence of Co^{2+} in tetrahedrally coordinated sites. Minor amounts of cobalt were detected in the investigated spinels. Because Co^{2+} occupies the tetrahedral position in the spinel structure which lacks a center of symmetry, TCo^{2+} is a strong absorber and its spin-allowed bands may be strong enough to appear in the spectra in spite of low

concentrations. Some natural spinels with Co concentrations between 0.001 and 0.05 wt.% of Co were found and studied in literature by (Shigley and Stockton, 1984; Harder, 1986; Schmetzer et al., 1989). Shigley and Stockton (1984) were the first authors who assumed that the cobalt is present in natural spinels in sufficient concentration to cause (or to help the Fe to cause) the blue color. Later Schmetzer et al. (1989) confirmed the hypothesis of Shigley and Stockton (1984) showing as extremely small amounts of cobalt in the range of 0.00X wt.% Co are sufficient to produce an intense blue coloration in spinels.

In the Figure 4.30 the absorption spectra of synthetic spinel s.s. containing the same concentrations of Co and Fe, respectively, were compare. It is evident as the two spectra show extremely different intensities of absorption.

This is due to the very strong intensity of the spin-allowed ${}^T\text{Co}^{2+}$ absorption, having the highest oscillator strength observed for 3d ions, which is one or two orders of magnitude greater for Co^{2+} than for the other ions such as Cr^{3+} , V^{3+} , Fe^{2+} and Fe^{3+} .

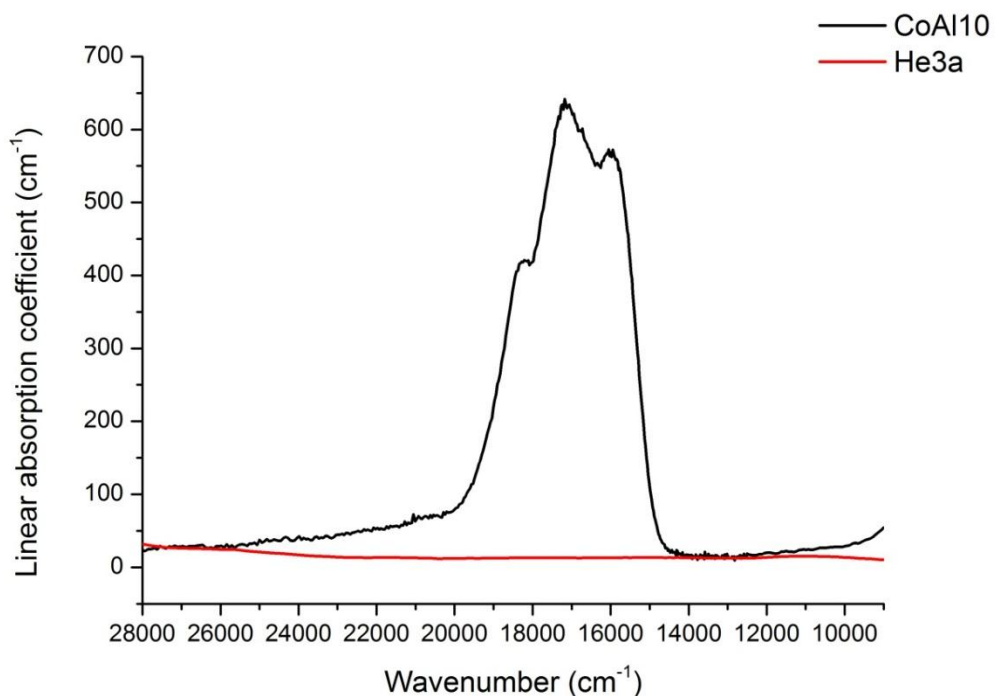


Fig. 4.30. Comparison between an absorption spectra of a synthetic spinel s.s. with a 11% of Fe^{2+} (red line: He3a from Hålenius et al., 2002) and a synthetic spinel s.s. with a 11% of Co^{2+} (black line: CoAl10).

As already described above, the absorption spectrum of Co-bearing spinel consists of a broad absorption band, which is split into three components with maxima at ~ 18000 , ~ 17000 and ~ 16000 cm^{-1} . In the blue and blue-green natural spinels investigated in the present work trace elements contents of Co were found in the range between 0.001 and 0.061 wt.%. Hence, in some cases, the Co concentration is very greater than those optically investigated in literature. The spectra of these samples show the three typical components of the Co-bearing spinels but they appears at energies very close to the bands assigned to the Fe and a discrepancy among them is quite difficult (Fig. 4.31). But the most characteristic feature of cobalt-bearing spinels is the presence of the absorption band at ~ 16000 cm^{-1} , which is not found in the Fe-bearing spinels.

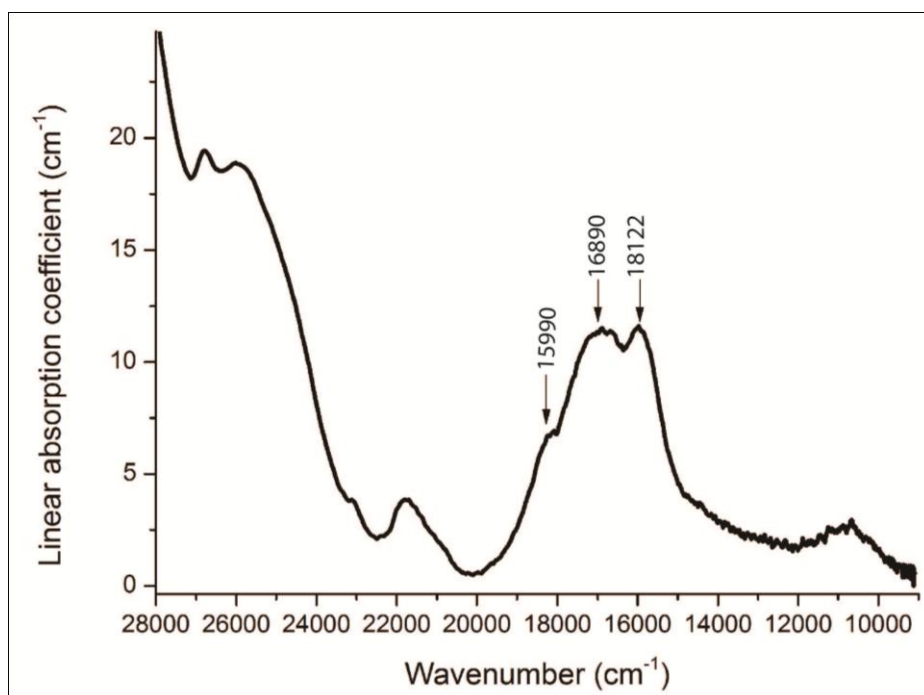


Fig. 4.31. Optical absorption spectrum of a blue colored spinel (800801) containing significant amount of Co. The three components of the typical band of $T\text{Co}^{2+}$ are shown.

In order to prove the role of cobalt in the blue coloration, the spectra of synthetic cobalt and iron spinels were compared in the right proportions to simulate the spectrum of the sample 800801 (Fig. 4.32). In spite of the very low amounts of cobalt (0.002 apfu), it is extremely evident that the cobalt influences the color more than iron in the central part of the VIS spectrum, that is in the range 20000-

15000 cm^{-1} . However the iron strongly contributes to reinforce the blue coloration of the spinels in the range 20000-26000 cm^{-1} with the intense absorption of the blue light due to the ligand-metal charge transfer.

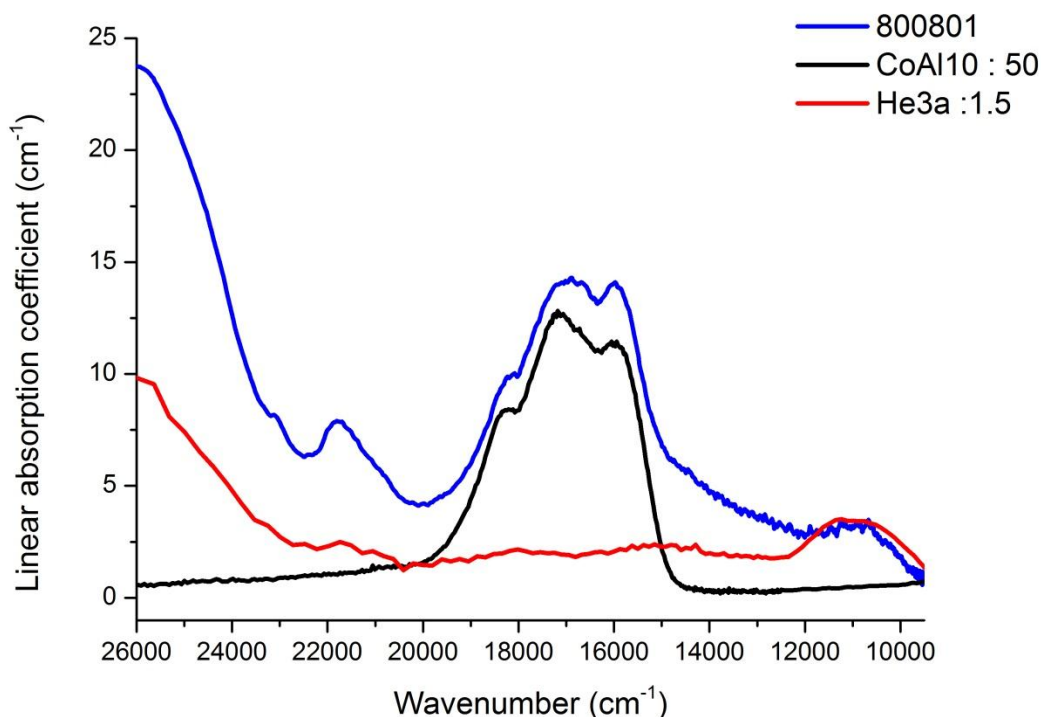


Fig. 4.32. Comparison among the natural intense blue sample 800801, a synthetic Co-bearing spinel CoAl10, and a synthetic Fe-bearing spinel He3a. The spectra of the synthetic spinels were divided by scaling factors (50 and 1.5, respectively) to simulate the spectrum of the sample 800801.

Taking the linear absorption coefficient of the sample 800801 from the equation 23 (paragraph 4.1.2), a calculated Co content of 0.0016 apfu is obtained, in agreement with the actual chemical concentration of 0.0018 apfu obtained by LA-ICP-MS analysis.

3) Spinel with dominant amount of Fe^{3+} and Mn

As already discussed in the chemical characterization paragraph, a yellowish green sample, labelled 31081, does not show evidence of Fe^{2+} in the NIR-MIR region. In addition, the sample displays relevant amounts of Mn, which by the charge balance results is supposed to be essentially in the oxidized form. Spinel with relevant amount of Mn are rare in nature and optical studies on Mn-bearing spinels are so scarce. The spectrum recorded between 30000 and 9000 cm^{-1} is

reported in Figure 4.33 and shows a strong UV absorption edge with a low-energy tail that rapidly falls off towards the visible range, an intense band at $\sim 25500 \text{ cm}^{-1}$ and a series of weak but prominent bands in the visible range. The band assignment is quite difficult because of lack of studies of this kind of spectra in literature. Since the absence of Fe^{2+} in the spectrum of sample 31081 it is possible to observe all the typical spin-forbidden of the Fe^{3+} , which are usually obscured by the spin-allowed transition of Fe^{2+} in natural spinels.

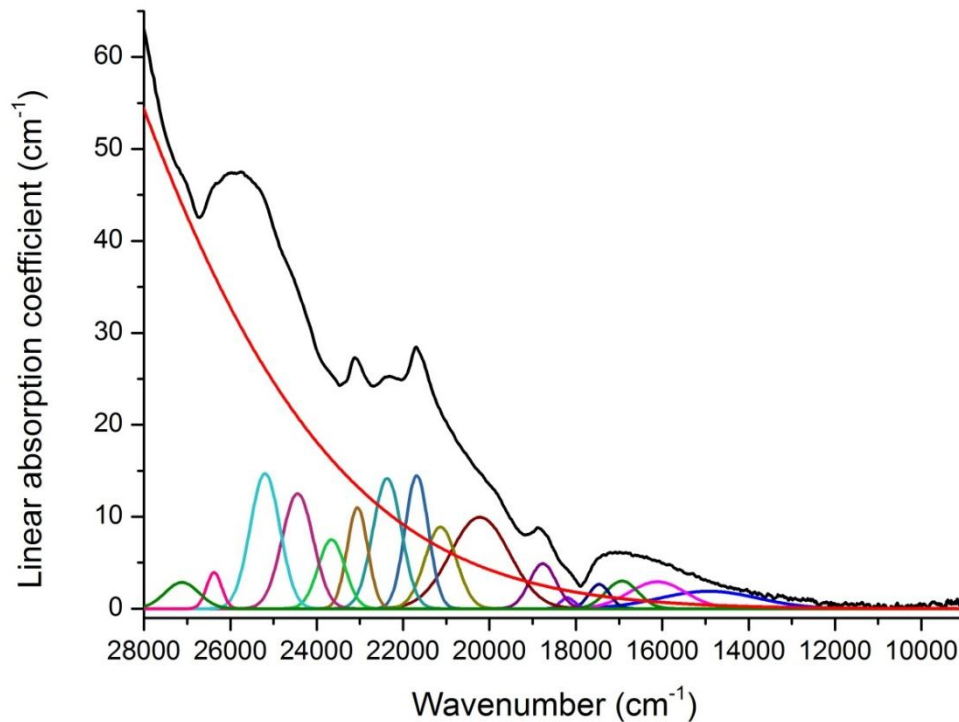


Fig. 4.33. Optical absorption spectrum and curve-fitting of the yellowish-green sample 31081.

The absorption edge is probably caused by ligand to metal charge-transfer transitions of $\text{O}^{2-} \rightarrow \text{Fe}^{3+}$ and $\text{O}^{2-} \rightarrow \text{Mn}^{3+}$ type. The band at $\sim 25500 \text{ cm}^{-1}$ has the characteristics of the spin-forbidden transition ${}^6A_{1g} \rightarrow {}^4E_g$ (4D) of Fe^{3+} in octahedrally coordinated sites. The band at $\sim 23000 \text{ cm}^{-1}$ was attributed to the spin-forbidden transition ${}^6A_{1g} \rightarrow {}^4T_{2g}$ (4D) by Taran et al. (2005), but it could be intensified by the spin-allowed ${}^5E_g \rightarrow {}^5T_{2g}$ transition in octahedrally coordinated Mn^{3+} . As already mentioned, the relatively narrow sharp band with maximum at $\sim 21700 \text{ cm}^{-1}$ can be assigned to the ${}^6A_{1g} \rightarrow {}^4A_{1g}, {}^4E_g$ transition of ${}^M\text{Fe}^{3+}$ in agreement with Taran et al. (2005) and Andreozzi et al. (2001b). The weak band at $\sim 21000 \text{ cm}^{-1}$ is, most probably, a split component of the ${}^6A_{1g} \rightarrow {}^4A_{1g}, {}^4E_g$

transition of ${}^M\text{Fe}^{3+}$. The very weak absorption at $\sim 22400\text{ cm}^{-1}$ could be assigned to the spin-forbidden transition of the tetrahedrally coordinated Fe^{3+} . In fact, as it will discuss in the paragraph 4.4, the Raman spectrum of the sample 31081 shows the characteristic peak at $\sim 705\text{ cm}^{-1}$ caused by the disorder. The spinels with Mn^{3+} in the tetrahedra show a strong and prominent band at $\sim 10800\text{ cm}^{-1}$ (Bosi et al., 2007). Since this band is not observed in the recorded spinel, the Mn^{3+} is assumed to be ordered at the M sites. The bands occurring at $< 19000\text{ cm}^{-1}$ are very difficult to assigned but they could be caused by the spin-forbidden transition ${}^6A_{1g} \rightarrow {}^4E_g$ (4G) and ${}^6A_{1g} \rightarrow {}^4T_{2g}$ (4G) of ${}^M\text{Fe}^{3+}$ and ${}^T\text{Fe}^{3+}$.

In addition to the absorption bands due to Fe^{3+} , some absorption bands of the spectrum of the sample 31081 could be intensified by small bands attributable to Mn^{3+} . The absorption bands at ~ 23700 , ~ 23050 and 21700 cm^{-1} can be affected also by broad bands due to the spin-forbidden transitions ${}^5E_g \rightarrow {}^3T_{1g}$, ${}^5E_g \rightarrow {}^3E_g$ and ${}^5E_g \rightarrow {}^5A_{1g}$ in the ${}^M\text{Mn}^{3+}$, in agreement with Bosi et al. (2007).

Moreover, the narrow absorption bands at ~ 27000 , 25200 , 23700 , 21700 , 21100 and 20200 cm^{-1} show a strong similarity with the absorption bands due to electron transitions in ${}^T\text{Mn}^{2+}$ - ${}^M\text{Mn}^{3+}$ pairs observed recently in a natural yellow spinel by Hålenius and Bosi (2014).

The absorption spectrum of the 31081 sample absorbs the light in almost all the portions of the spectrum and allows passing the light of narrow regions close to 18000 cm^{-1} (yellow-green light). A complete interpretation of the absorption spectrum of the sample 31081 needs further investigations.

Further and more detailed studies are necessary in order to confirm particular assignment of difficult interpretation. In particular, given the extreme efficiency of Fe ions for visible light absorption, a Mössbauer spectroscopic study could be useful to determine the real proportions of Fe^{2+} and Fe^{3+} . Furthermore, additional short-range sensitive techniques, as for example EXAFS spectroscopy, would be useful to know if differences in local bond distances may cause differences in colors.

4.3- Synthetic (Mg,Co,Fe)(Al,Cr)₂O₄ spinels: Raman study

As predicted by group theory for spinels (paragraph 2.2.3), a correlation of the site symmetries with the crystal symmetry enables one to identify the irreducible representations that describe the normal modes of vibration associated with each atomic species:

$$D_{3d} \text{ (T sites): } A_{2u} + E_u + 2F_{1u} + F_{2u}$$

$$T_d \text{ (M sites): } F_{1u} + F_{2g}$$

$$C_{3v} \text{ (O): } A_{1g} + A_{2u} + 2F_{2g} + 2F_{1u} + E_g + F_{1g} + E_u + F_{2u}$$

Thus, there are five Raman active modes ($A_{1g} + E_g + 3F_{2g}$) that might appear in the spectra. However, a breakdown in the Raman selection rules can occur due to various factors, such as the disordering, the presence of vacancies and general defects within the crystal structure which can affect the crystal symmetry. This can subsequently lead to an increase in the number of the Raman-active modes up to eight or nine.

Although there has been a large amount of experimental and theoretical work on spinel in literature, a systematic study of the variations of the Raman shift and/or their relative intensities along spinel solid solutions is lacking. The relationship between the vibrational modes and cation substitution is not straightforward. When two cations are exchanged in the spinel solid solution, the vibrational modes can vary differently. They can be described by an *one-mode behavior* when the phonons vary continuously from the frequency of one end member to the frequency of the other end member. Anyway, *two-mode behavior* is also possible, for which a mixed crystal system possesses two distinct vibrational modes, close to the frequency of both end members, with intensities proportional to the fraction of each pure member within the mixed system (Chang and Mitra, 1971; Preudhomme and Tarte, 1971). The Raman spectra of pure spinels are well known in the literature, but complete vibrational data is lacking for many of these mixed metal oxides.

In the present study three synthetic spinel series were investigated:

1. $\text{MgAl}_2\text{O}_4\text{-CoAl}_2\text{O}_4$ solid solution (10 samples);
2. $\text{MgAl}_2\text{O}_4\text{-FeAl}_2\text{O}_4$ solid solution (10 samples);
3. $\text{MgAl}_2\text{O}_4\text{-MgCr}_2\text{O}_4$ solid solution (12 samples).

These series were chosen in order to examine how substitution of the divalent cation (for the first two series) and trivalent cation (for the last series) affects the Raman modes.

In addition, chemical, structural and optical data of the three series are available (for $\text{MgAl}_2\text{O}_4\text{-CoAl}_2\text{O}_4$ series from this study; for $\text{MgAl}_2\text{O}_4\text{-FeAl}_2\text{O}_4$ from Andreozzi and Lucchesi, 2002 and Hålenius et al., 2002; for $\text{MgAl}_2\text{O}_4\text{-MgCr}_2\text{O}_4$ series from Hålenius et al., 2010). Moreover, the series have a common end-member (MgAl_2O_4) whose Raman spectrum is well known and examined in literature.

If systematic change in the Raman shift with the variation of the chemical composition was found, Raman spectroscopy could be used to obtain semi-quantitative chemical analyses when calibrated with suitable solid solution series. Furthermore, the method could also be used to detect cation order/disorder and possibly nonstoichiometry.

In order to follow the shift and growth of each peak along the series, unpolarized, polarized and depolarized Raman spectra were collected for all the synthetic spinel crystals.

4.3.1 The spinel s.s. (MgAl_2O_4) end-member

Before dealing with the different spinel solid solution, it is useful to make a detailed investigation of their common end-member. There has been a significant amount of work done on MgAl_2O_4 spinel by Raman spectroscopy because it is considered as the prototype of the large class of solid oxides of geological and technological interest. (O'Horo et al., 1973; Fraas et al., 1973; Chopelas and Hofmeister, 1991; de Wijs et al., 2002, Lazzeri and Thibaudeau, 2006; Caracas and Banigan, 2009). However, most of the studies are focused only on the additional bands due to disordering of the cations (Cynn et al., 1992; Cynn et al., 1993; Minh and Yang, 2004; Slotznick and Shim, 2008).

Unpolarized, polarized and depolarized Raman spectra of the synthetic spinel s.s. recorded are shown in Fig. 4.34a.

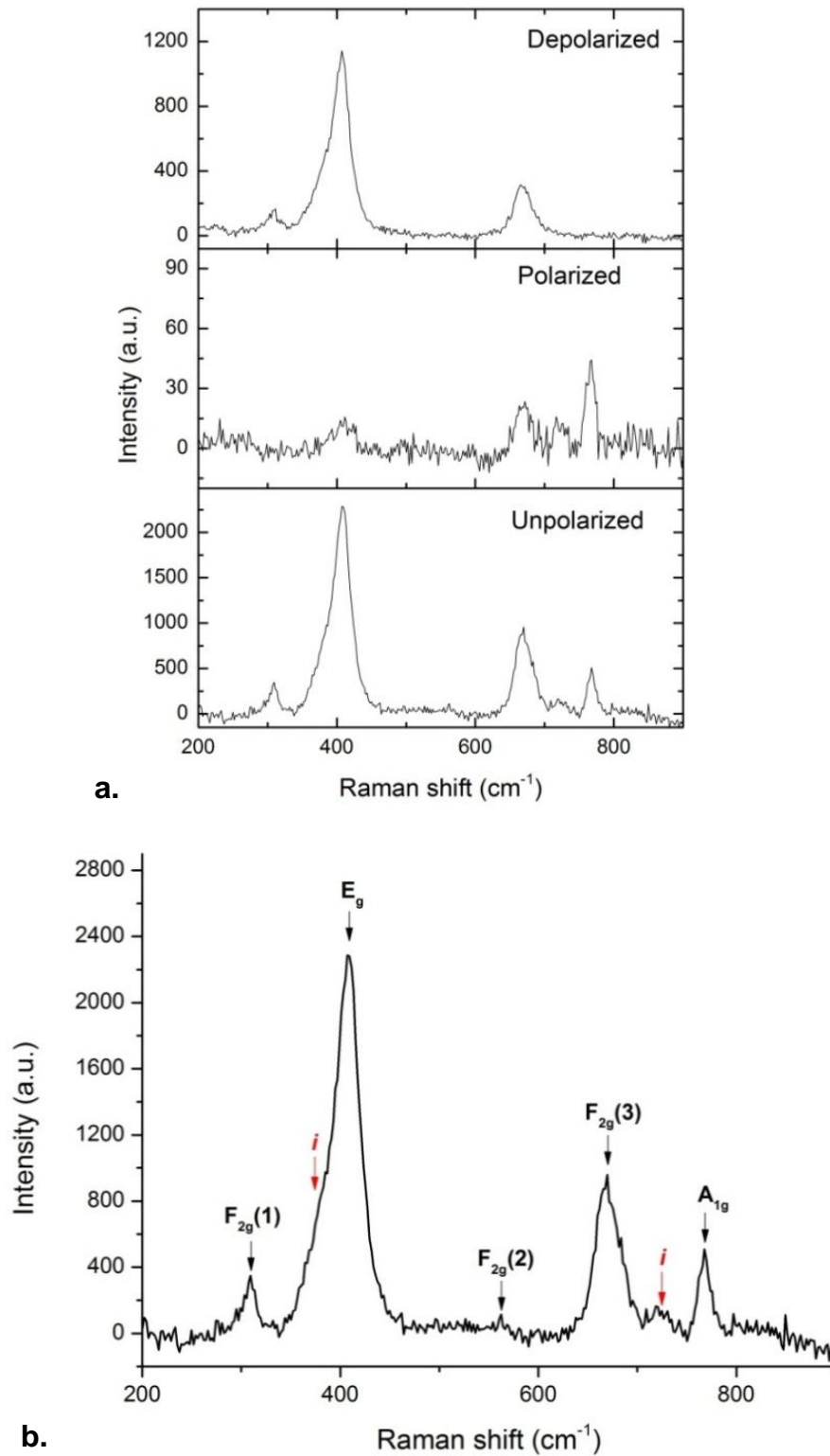


Fig. 4.34. Raman spectra of a synthetic spinel s.s. crystal: a) Raman spectrum taken with crossed polarization (on the top), parallel polarization (in the middle) and without polarization (on the bottom), b) Unpolarized Raman spectrum in detail.

Raman spectrum of MgAl_2O_4 exhibits four intense Raman active modes at 308, 409, 670 and 768 cm^{-1} . In agreement with the previous studies these bands are assigned to the $F_{2g}(1)$, E_g , $F_{2g}(3)$, and A_{1g} respectively (Fig. 4.34b and Table 4.14). In fact, the polarized Raman spectrum shows the peak at 768 cm^{-1} which does not appear in the depolarized spectrum, thus assigning it to the A_{1g} mode. The two F_{2g} modes are clearly visible in the polarized spectrum, and the E_g mode is present in all spectra and to distinguish it from the others a particular orientation of the crystal is required. The fifth Raman mode, $F_{2g}(2)$, was not observed in the experimental Raman spectra present in literature, but, in agreement with the calculated Raman spectra via *ab initio* calculation by de Wijs et al. (2002) and Lazzeri and Thibaudau (2006), it could be the small and weak peak at 562 cm^{-1} (Table 4.14). Since usually this peak is not observed in the experiment spectrum its assignment is not yet clear. The first $F_{2g}(1)$ mode has been assigned to the translation of the Mg cation in its tetrahedrally coordinated sites by Chopelas and Hofmeister (1991) and Slotznick and Shim (2008). Regarding the origin of the higher-frequency F_{2g} modes at $\sim 670 \text{ cm}^{-1}$, there is no consensus in literature. In general, some authors state that this Raman mode is related to antisymmetric stretching mode of the MgO_4 unit (O'Horo et al., 1973). Others, in contrast, claim that it is attributed to octahedral bending motion (Chopelas and Hofmeister, 1991; Slotznick and Shim, 2008 and Caracas and Banigan, 2009).

Table 4.14. Comparison between experimental and calculated frequencies (cm^{-1}) of the Raman modes in the cubic spinel structure of MgAl_2O_4 .

| Raman modes | This work | de Wijs et al. (2002) Calc. | Lazzeri & Thibaudau (2006) Calc. | O'Horo et al. (1973) Exp. | Fraas et al. (1973) Exp. | Chopelas & Hofmeister (1991) Exp. | Cynn et al. (1992) Exp. | Slotznick & Shim (2008) Exp. |
|-------------|-----------|-----------------------------|----------------------------------|---------------------------|--------------------------|-----------------------------------|-------------------------|------------------------------|
| $F_{2g}(1)$ | 308 | 319 | 317 | 311 | 305 | 312 | 311 | 309 |
| E_g | 409 | 426 | 408 | 410 | 405 | 407 | 409 | 410 |
| $F_{2g}(2)$ | 562 | 570 | 557 | – | – | – | – | – |
| $F_{2g}(3)$ | 670 | 682 | 667 | 671 | 663 | 666 | 670 | 670 |
| $A_{1g}(i)$ | 721 | – | – | 727 | 715 | – | 727 | 720 |
| A_{1g} | 768 | 776 | 762 | 772 | 770 | 767 | 770 | 768 |

The Raman-active A_{1g} mode was almost univocally assigned to the Mg-O symmetric stretching vibrations in literature. The synthetic spinel spectrum shows an additional peak at 721 cm^{-1} which has A_{1g} character. Cynn et al. (1992) observed that the position of this band is similar to those of Raman modes assigned as symmetric stretching vibration of AlO_4 in $\text{Ca}_3\text{Al}_2\text{O}_8$. Therefore, the 721 cm^{-1} mode was assigned to the symmetric Al-O stretching vibration of AlO_4 groups created by the cation disorder. In effect, XRD-SC and structural refinement have calculated an inversion degree of 0.24 apfu for the investigated spinel s.s (Andreozzi et al., 2000).

Another consequence of the cation disorder in the crystal is the appearance of a shoulder in the low-wavenumber part of the peak at 409 cm^{-1} . Given that the 409 cm^{-1} mode is assigned to the symmetric bending of Mg in the tetrahedra, its shoulder (at 385 cm^{-1}) can be attributed to the bending mode for Al ions in tetrahedral sites, in agreement with the previous studies (Cynn et al., 1992; Minh and Yang, 2004). As suggested by Minh and Yang (2004), the 410 cm^{-1} mode and its shoulder could be good indicator for the cation disorder suffered by the crystal.

4.3.2 The MgAl_2O_4 - CoAl_2O_4 spinel series

The systematic Raman study of the MgAl_2O_4 - CoAl_2O_4 series is not present in literature and it can be useful from a technological point of view and geological point of view. In fact, the only literature studies on the CoAl_2O_4 end-member are mainly focus on blue pigments, known to be used in China since the Tang dynasty (de Waal, 2004; Kock and de Waal, 2007).

The recorded spectra of the CoAl_2O_4 end-member (the CoAl100 sample described in the paragraph 4.1) are shown in the Figure 4.35a. Taking the polarized spectrum as a reference, in the depolarized spectrum the peaks at 708 and 775 cm^{-1} do not appear, and the peaks at 201 and 516 cm^{-1} are very intense. Thus, the former two have an A_{1g} character, while the latter ones have an F_{2g} character. As in the case of spinel s.s., the additional peak with the A_{1g} character at 708 cm^{-1} is caused by the cation disorder.

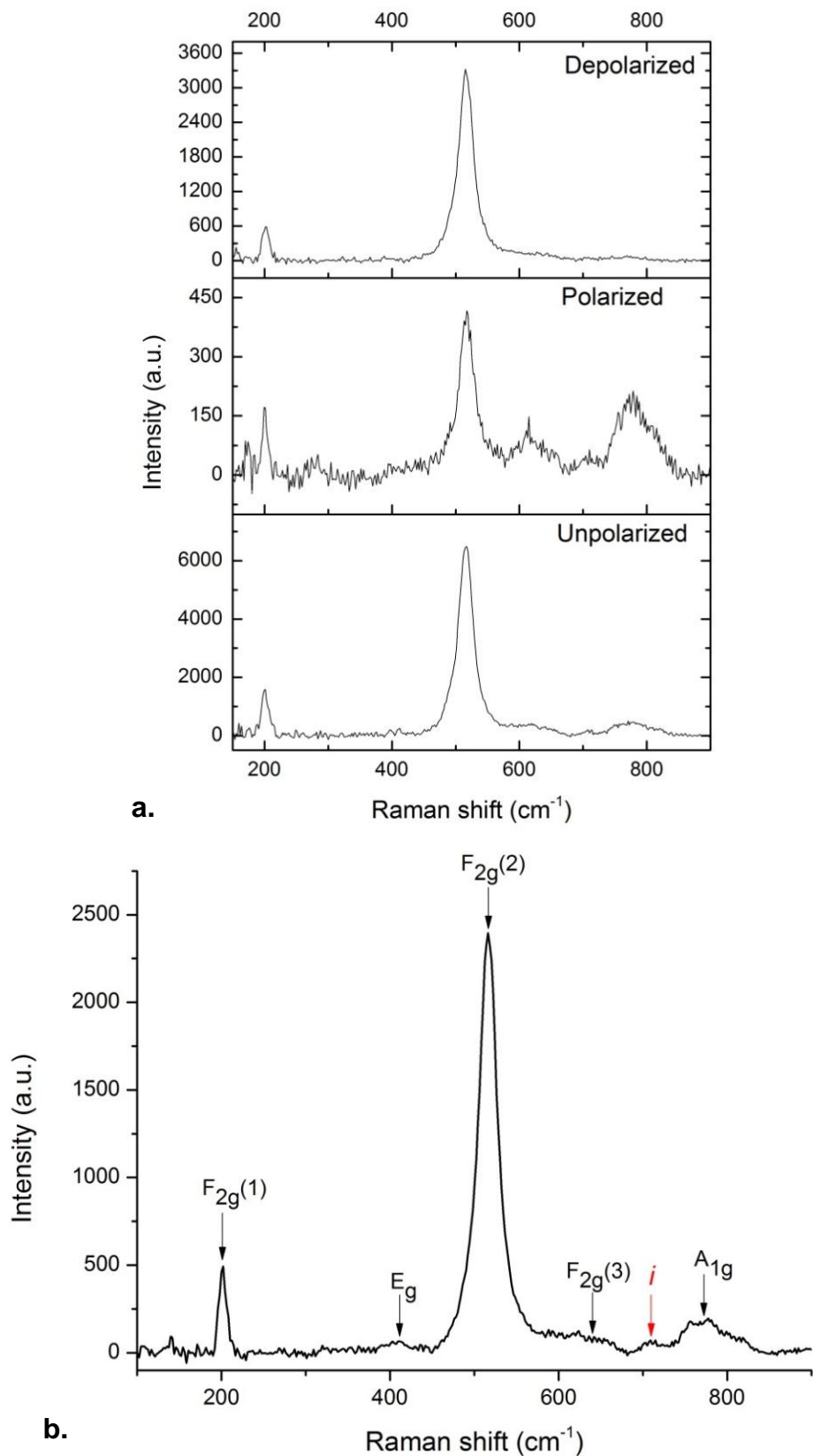


Fig. 4.35 Raman spectra of the synthetic CoAl_2O_4 crystal: a) spectrum taken with crossed polarization (on the top), parallel polarization (in the middle) and without polarization (on the bottom), b) Unpolarized Raman spectrum in detail.

The unpolarized spectrum shows all the five theoretically expected Raman active modes, two of which (at 201 and 516 cm^{-1}) more intense than the others. Both the measurements and the assignments of the peaks are in agreement with the values reported in literature (Fig. 4.35b and Table 4.15).

Table 4.15. Comparison between the wavenumber (cm^{-1}) of the Raman modes of CoAl_2O_4 from this work and those reported in literature.

| Raman modes | This work | Shirai et al. (1982) | Jongsomjit et al. (2001) | Kock and de Waal (2007) |
|-----------------------|-----------|----------------------|--------------------------|-------------------------|
| F_{2g} (1) | 201 | 201 | 198 | 201 |
| E_g | 411 | – | 412 | 408 |
| F_{2g} (2) | 516 | 516 | 519 | 509 |
| F_{2g} (3) | 619 | 615 | 619 | 617 |
| A_{1g} (<i>i</i>) | 709 | 705 | 690 | – |
| A_{1g} | 775 | 755 | 753 | 767 |

The polarized and unpolarized Raman spectra of the entire MgAl_2O_4 - CoAl_2O_4 series are shown in the Figure 4.36. The Raman study of a solid solution is complex because each spectrum is affected by the cation distribution. With the study of the polarized spectra it is possible to follow the shift of a peak along the series, allowing its assignment to a Raman active mode. The spectrum taken with the crossed polarization defines clearly the A_{1g} mode for the last peak at $\sim 775 \text{ cm}^{-1}$ and the additional peak at $\sim 720 \text{ cm}^{-1}$. The peaks at ~ 485 and $\sim 615 \text{ cm}^{-1}$ grow more markedly from the CoAl14 sample in the spectrum taken with the parallel polarization. In addition, these peaks show the same characteristics of the peaks at ~ 540 and $\sim 660 \text{ cm}^{-1}$, respectively. This behavior leads to assign these peaks to the $F_{2g}(2)$ and $F_{2g}(3)$ modes, respectively.

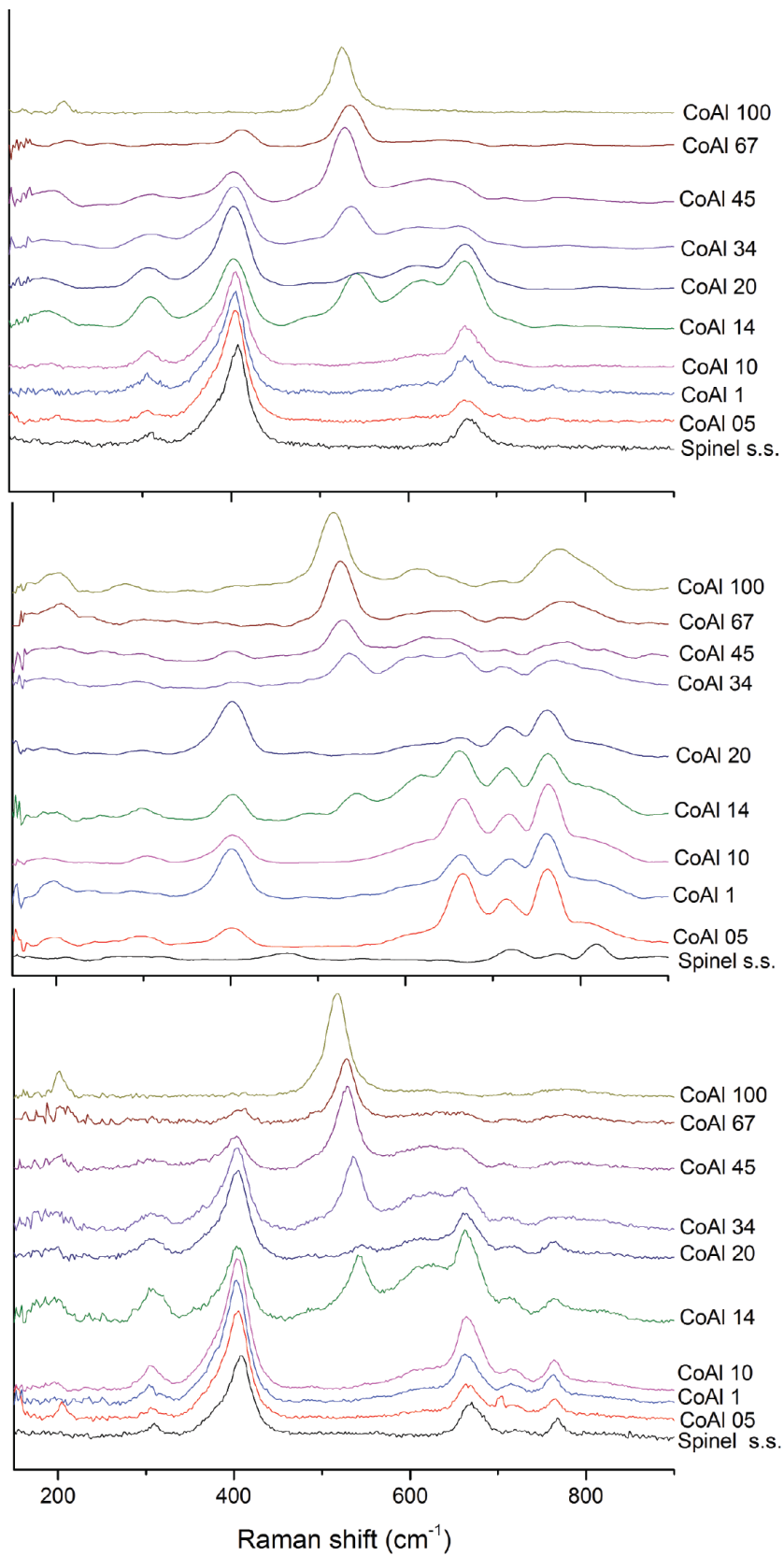


Fig. 4.36. Raman spectra of the MgAl_2O_4 - CoAl_2O_4 spinel series: spectra taken with crossed polarization (on the top), parallel polarization (in the middle) and without polarization (on the bottom).

The MgAl_2O_4 - CoAl_2O_4 series studied in this work is affected by the substitution of Mg by Co^{2+} but also by the decrease of the inversion degree from 0.24 to 0.13 along the series as already described in the paragraph 4.1.2. All the Raman-active modes are detected, although some modes are very weak and difficult to distinguish from background noise across the entire series (Fig. 4.37).

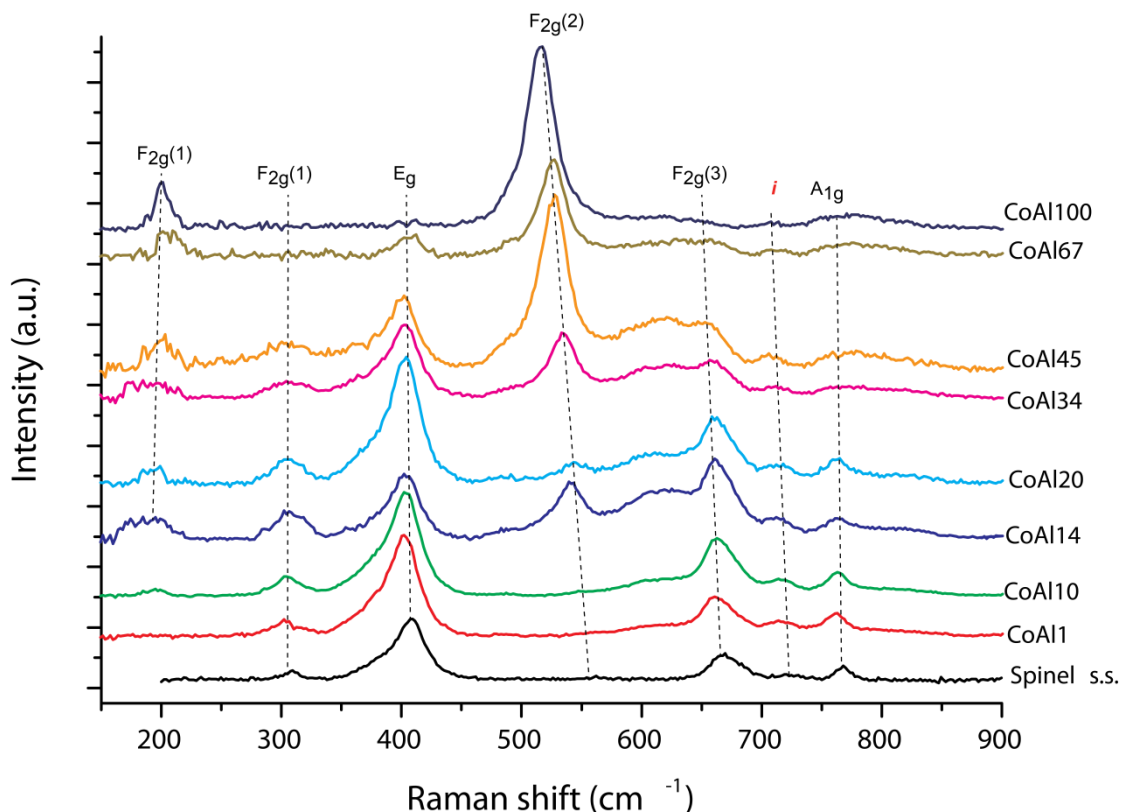


Fig. 4.37. Evolution of the unpolarized Raman spectra of synthetic spinels belonging to the MgAl_2O_4 - CoAl_2O_4 series.

Cobalt cation has a larger mass than the magnesium. Hence, from a simple mass on a spring model, the substitution $\text{Co}^{2+} \rightarrow \text{Mg}$ should lead to lower vibrational frequencies. In fact, a slightly decrease of the Raman shift can be perceived for all the peaks with the exception for the A_{1g} mode and the $F_{2g}(1)$ (Fig. 4.38). Another peak attributable to $F_{2g}(1)$ mode can be followed at $\sim 200 \text{ cm}^{-1}$ along the series but, with the exception for the CoAl_2O_4 end-member, its center position and intensity are uncertain. The Raman modes $< 300 \text{ cm}^{-1}$ are very complex because the vibration concerns the entire lattice. Unlike as reported by Slotznick and Shim (2008) for the vibrations of the MgO_4 and AlO_4 , the appearance in the recorded spectra of a new mode indicates that the vibrations of the MgO_4 and CoO_4

tetrahedra are not coupled each other, and thus, they can be treated as separated isolated vibrational units, showing a two-mode behavior.

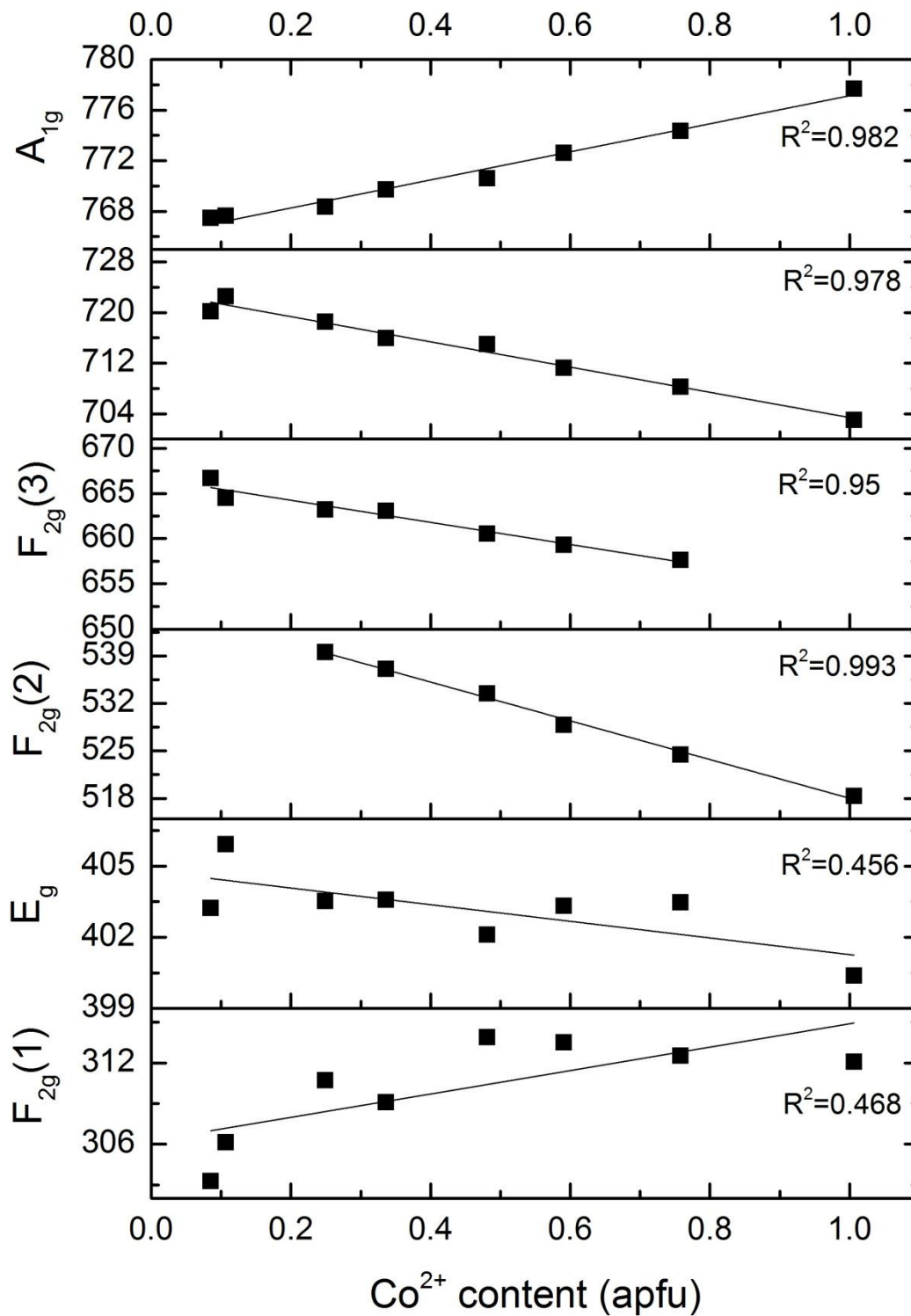


Fig. 4.38. Raman shift versus Co²⁺ content in MgAl₂O₄-CoAl₂O₄ spinels series.

The intermediate compositions exhibit more complex Raman spectrum because of the role of the cation substitution and the cation disorder. Up to the CoAl34 sample, the E_g mode is the strongest peak, then, when the Co becomes the main divalent component, the $F_{2g}(2)$ dominates the spectrum. In fact, this latter mode is linearly dependent on the Co^{2+} concentration and can be attributed to the Co-O stretching vibration in the tetrahedrally coordinated sites in agreement with Bouchard and Gambardella (2010). Besides, starting from the CoAl14 sample the appearance of a wide shoulder at $\sim 615\text{ cm}^{-1}$ of the $F_{2g}(3)$ mode is observed. This shoulder remains up to the $CoAl_2O_4$ end-member, whereas the peak at $\sim 670\text{ cm}^{-1}$ gradually disappears. From the literature the $F_{2g}(3)$ mode was attributed to vibration on either the tetrahedron or the octahedron, but the appearance of the shoulder from the CoAl14 sample might suggest a dependence on the octahedral cation. In fact, from the CoAl14 sample the Co^{2+} starts to occupy the octahedrally coordinated sites in a marked way (Fig. 4.39a). In addition the peak at 670 cm^{-1} has a good correlation with the amount of ${}^M Mg$ (Fig. 4.39b).

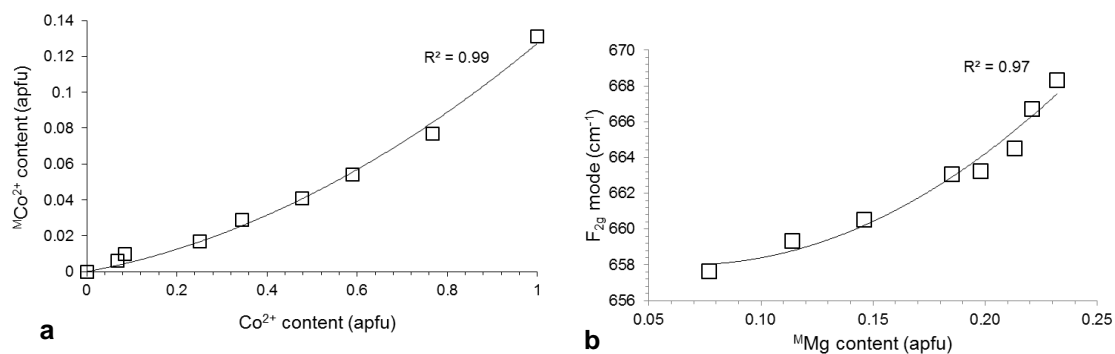


Fig. 4.39. Correlation of (a) the amount of ${}^M Co^{2+}$ versus the total amount of Co and (b) the amount of ${}^M Mg$ versus the position in Raman shift of the $F_{2g}(3)$ mode.

As already mentioned for the spinel s.s. end-member, the A_{1g} mode is assigned to the symmetric stretching of the MgO_4 tetrahedra within the spinel structure by many authors. However, as Preudhomme et al. (1971) have shown with extensive experimental data in their studies on spinels, the assumption that the higher-frequency vibrations depend solely upon the tetrahedral cations is incorrect. In many studies the A_{1g} mode shows a greater dependence upon the octahedral

trivalent cation than the tetrahedral divalent cation (Lenaz and Lughi, 2013, Bahlawane et al., 2009).

In the $\text{MgAl}_2\text{O}_4\text{-CoAl}_2\text{O}_4$ series a good correlation ($R^2=0.98$) between the unit cell parameter and the A_{1g} peak can be observed (Fig.4.40). Bearing in mind the equation 1 in chapter 1, this behavior validates the hypothesis that the A_{1g} mode is affected by both tetrahedral and octahedral cation.

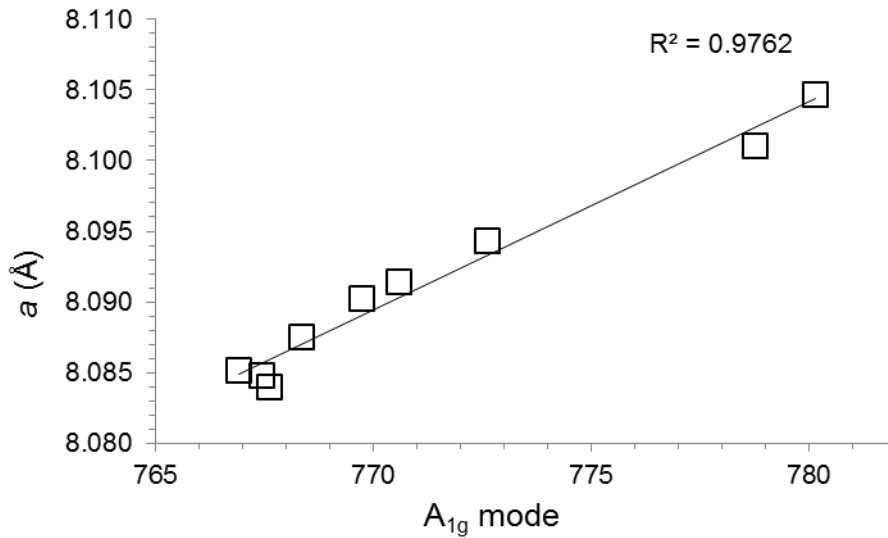


Fig. 4.40. Correlation between the unit cell parameter versus the A_{1g} mode.

Usually the E_g mode is attributed to the symmetric bending motion of the oxygen anions within the MgO_4 tetrahedra. The peak at $\sim 400 \text{ cm}^{-1}$ remains in almost in the same position along the series but a good correlation between the $^{\text{T}}\text{Mg}$ content and the Raman shift of this mode was not found.

In the CoAl_2O_4 end member the most characteristic peak at 516 cm^{-1} is attributable to the $F_{2g}(2)$ mode. This peak can be followed along the series from the CoAl14 sample and a relationship between the center position of the $F_{2g}(2)$ mode and the Co content (Co_{tot}) is obtained (Fig. 4.41):

$$F_{2g}(2) (\text{cm}^{-1}) = -28.58 [\text{Co}_{\text{tot}}] + 546.61 \quad (24)$$

Thanks to the equation 24, in the Co spinel it is possible to estimate the Co concentration by the Raman spectrum.

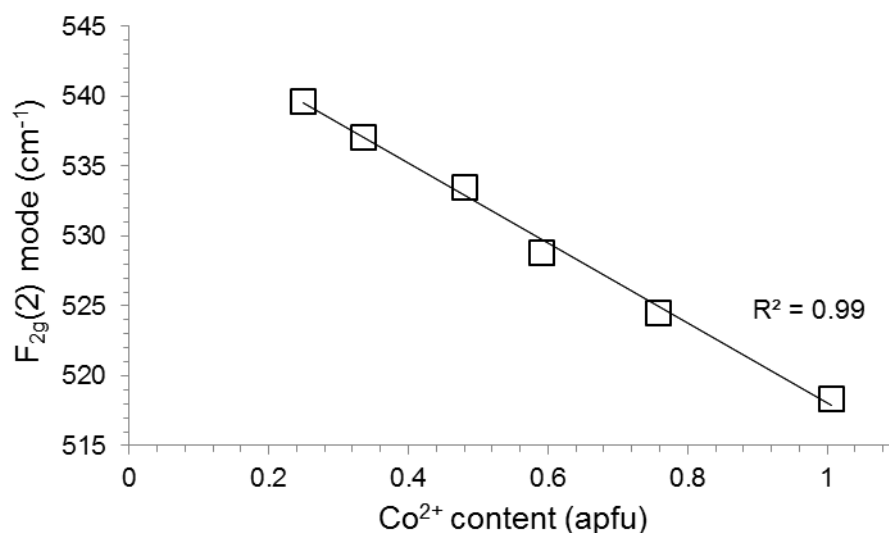


Fig. 4.41. Correlation between the center position of the $F_{2g}(2)$ mode and the Co content (apfu).

4.3.3 The $MgAl_2O_4$ - $FeAl_2O_4$ spinel series

Despite the hercynite is a mineral common in many terrestrial and extraterrestrial rocks, Raman studies on the $FeAl_2O_4$ end-member are lacking in literature. In fact, iron oxides are poor Raman scatterers and strongly absorb in the range of the wavelengths of typical excitation lasers, and high laser intensities are required to obtain an adequate signal (Bauer et al., 2011). Regarding the $FeAl_2O_4$ end-member there are very few studies in literature and all of them concern industrial material as pigment (Ospitali et al., 2005; Muralha et al., 2011). The $MgAl_2O_4$ - $FeAl_2O_4$ series was explored by Malézieux and Piriou (1988), but only three Mg-rich component were analyzed.

Polarized spectra of ten samples belonging to the $MgAl_2O_4$ - $FeAl_2O_4$ series were recorded and are shown in Figure 4.42. The trend of the spectra is very similar to those in the $MgAl_2O_4$ - $CoAl_2O_4$ series.

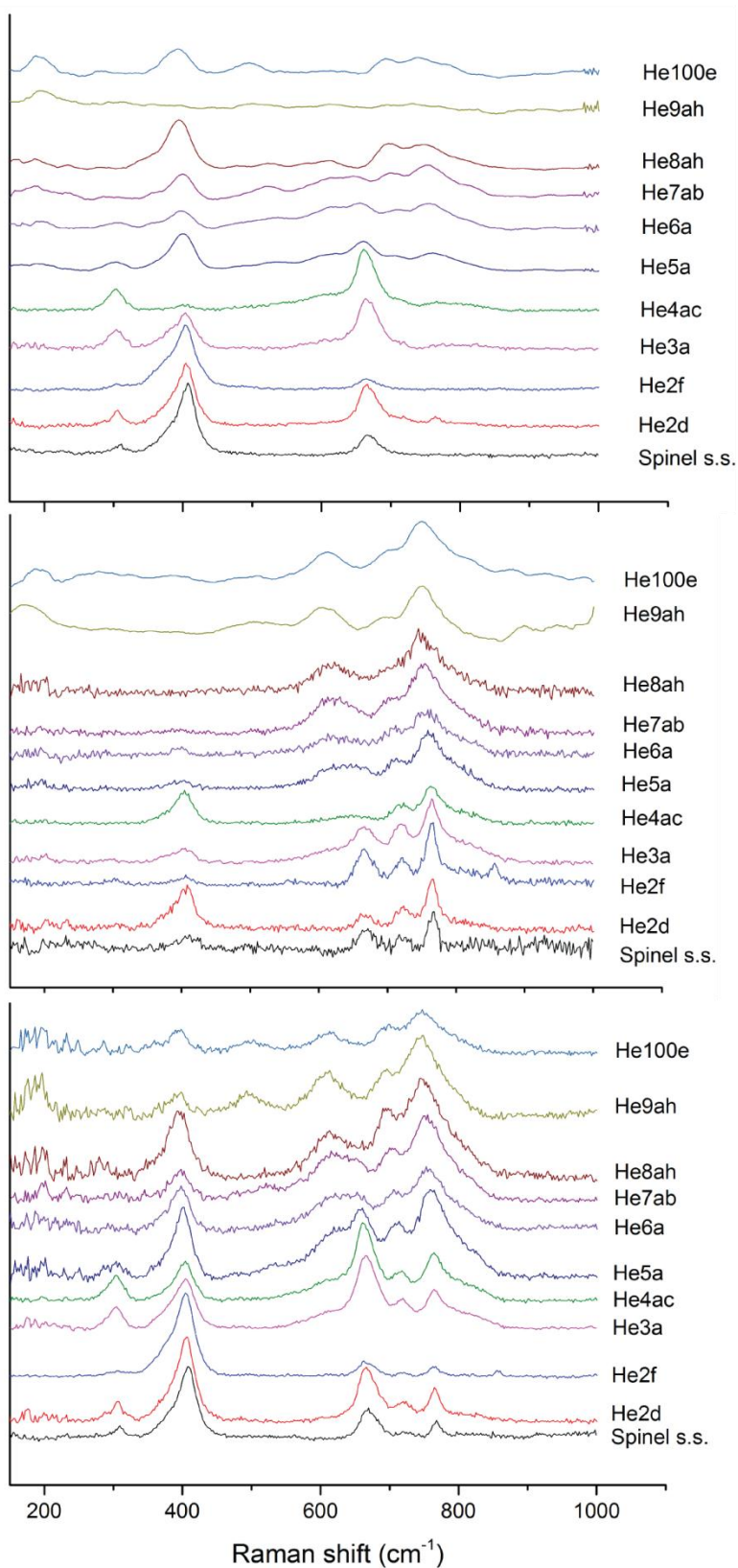


Fig. 4.42. Raman spectra of the MgAl₂O₄-FeAl₂O₄ spinel series: spectra taken with crossed polarization (on the top), parallel polarization (in the middle) and without polarization (on the bottom).

Even in this series only the spectra taken with parallel polarization exhibit the A_{1g} modes at ~ 700 and 750 cm^{-1} . The peak at $\sim 670\text{ cm}^{-1}$ seems to split in two contributions one more intense under parallel polarization and the other at $\sim 615\text{ cm}^{-1}$ under perpendicular polarization. Thus, the latter peak could be probably attributed to the E_g or A_{1g} mode caused by the entrance of the iron in the structure.

The detailed unpolarized spectrum of the hercynite end-member with the proposed peak assignment is shown in Figure 4.43.

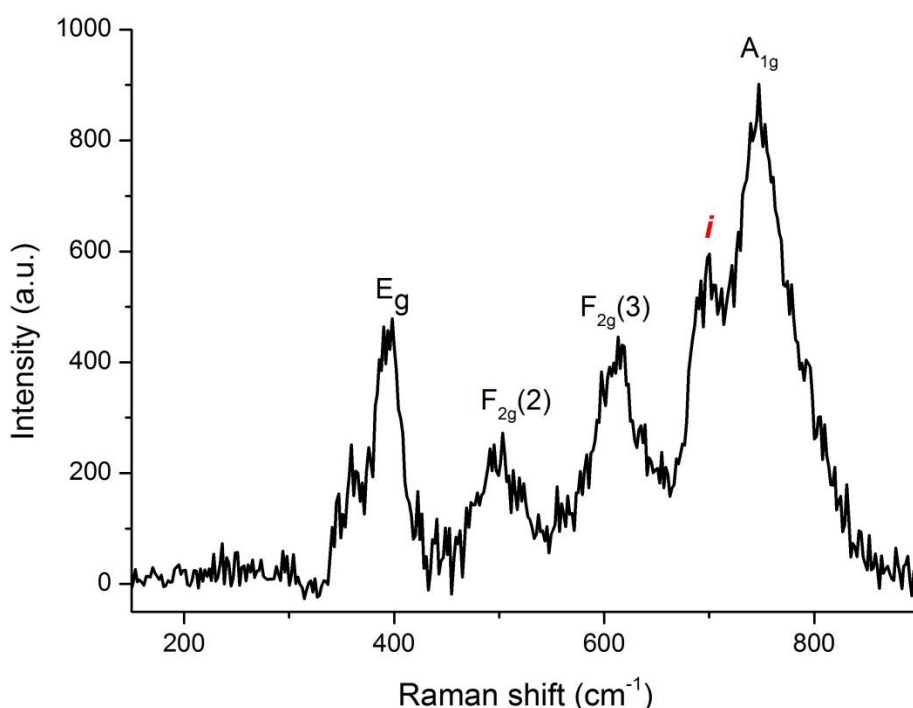


Fig. 4.43. Unpolarized Raman spectrum of the synthetic hercynite end-member with the proposed peak assignment.

The values of the frequencies and their assignments are reported in Table 4.16 and are compared with the only frequency values found in literature. Low-frequencies modes are not enough intense to be distinguished from the background noise. In the collected spectrum the E_g mode shows a small shoulder at 359 cm^{-1} .

Table 4.16. Comparison between the wavenumber (cm⁻¹) of the Raman modes of FeAl₂O₄ from this work and those reported in literature.

| Raman modes | This work | Ospitali et al. (2005) |
|---------------------|-----------|------------------------|
| F _{2g} (1) | – | 184 |
| E _g | 394 | – |
| F _{2g} (2) | 499 | – |
| F _{2g} (3) | 610 | 593 |
| A _{1g} (i) | 695 | 701 |
| A _{1g} | 750 | 753 |

The spinels belonging to the MgAl₂O₄-FeAl₂O₄ series were synthesized and then chemically and structurally characterized by Andreozzi and Lucchesi (2002). In order to investigate how the cation distribution influenced the Raman spectra, the structural formulae of the analyzed spinel crystals along the MgAl₂O₄-FeAl₂O₄ series are reported in Table 4.17.

Table 4.17. Structural formulae of the analyzed spinels along MgAl₂O₄-FeAl₂O₄ series.

| Sample | Formula |
|----------------|---|
| He2f | $T(Mg_{0.715}Fe^{2+}_{0.046}Al_{0.239})_1M(Mg_{0.239}Al_{1.761})_2O_4$ |
| He3a/b | $T(Mg_{0.640}Fe^{2+}_{0.111}Al_{0.249})_1M(Mg_{0.25}Al_{1.75})_2O_4$ |
| He4a/c | $T(Mg_{0.588}Fe^{2+}_{0.188}Al_{0.224})_1M(Mg_{0.227}Al_{1.766}Fe^{3+}_{0.007})_2O_4$ |
| He5a/a | $T(Mg_{0.434}Fe^{2+}_{0.347}Al_{0.219})_1M(Mg_{0.215}Fe^{2+}_{0.008}Al_{1.762}Fe^{3+}_{0.016})_{2.001}O_4$ |
| He6a/e | $T(Mg_{0.366}Fe^{2+}_{0.424}Al_{0.194}Fe^{3+}_{0.016})_1M(Mg_{0.178}Fe^{2+}_{0.035}Al_{1.768}Fe^{3+}_{0.020})_{2.001}O_4$ |
| He7a/b | $T(Mg_{0.267}Fe^{2+}_{0.531}Al_{0.192}Fe^{3+}_{0.010})_1M(Mg_{0.153}Fe^{2+}_{0.054}Al_{1.772}Fe^{3+}_{0.022})_{2.001}O_4$ |
| He8a/h | $T(Mg_{0.185}Fe^{2+}_{0.63}Al_{0.168}Fe^{3+}_{0.017})_1M(Mg_{0.118}Fe^{2+}_{0.072}Al_{1.770}Fe^{3+}_{0.041})_{2.001}O_4$ |
| He9a/h | $T(Mg_{0.101}Fe^{2+}_{0.713}Al_{0.152}Fe^{3+}_{0.034})_1M(Mg_{0.076}Fe^{2+}_{0.114}Al_{1.774}Fe^{3+}_{0.037})_{2.001}O_4$ |
| He100c* | $T(Fe^{2+}_{0.849}Al_{0.133}Fe^{3+}_{0.018})_1M(Fe^{2+}_{0.153}Al_{1.765}Fe^{3+}_{0.082})_2O_4$ |

*The sample studied by Raman spectroscopy is He100e, which contains less Fe³⁺ than He100c (see Halenius et al. 2002)

The evolution of the unpolarized Raman spectra along the MgAl₂O₄-FeAl₂O₄ series can be followed in Figure 4.44. As in the case of cobalt, being the iron heavier than the magnesium, substitution of the magnesium atoms with the iron

should lead to lower vibrational frequencies. In fact, a similar trend between the spinels of the $\text{MgAl}_2\text{O}_4\text{-CoAl}_2\text{O}_4$ series and of $\text{MgAl}_2\text{O}_4\text{-FeAl}_2\text{O}_4$ series can be observed. Also in the Raman spectra along the $\text{MgAl}_2\text{O}_4\text{-FeAl}_2\text{O}_4$ series, the intermediate compositions show more complex spectra. Unlike the $\text{MgAl}_2\text{O}_4\text{-CoAl}_2\text{O}_4$ series, in this series the spectra are affected not only by the substitution $\text{Fe}^{2+} \rightarrow \text{Mg}$ and the cation disorder, but also by the entrance of small amounts of Fe^{3+} in the spinel structure.

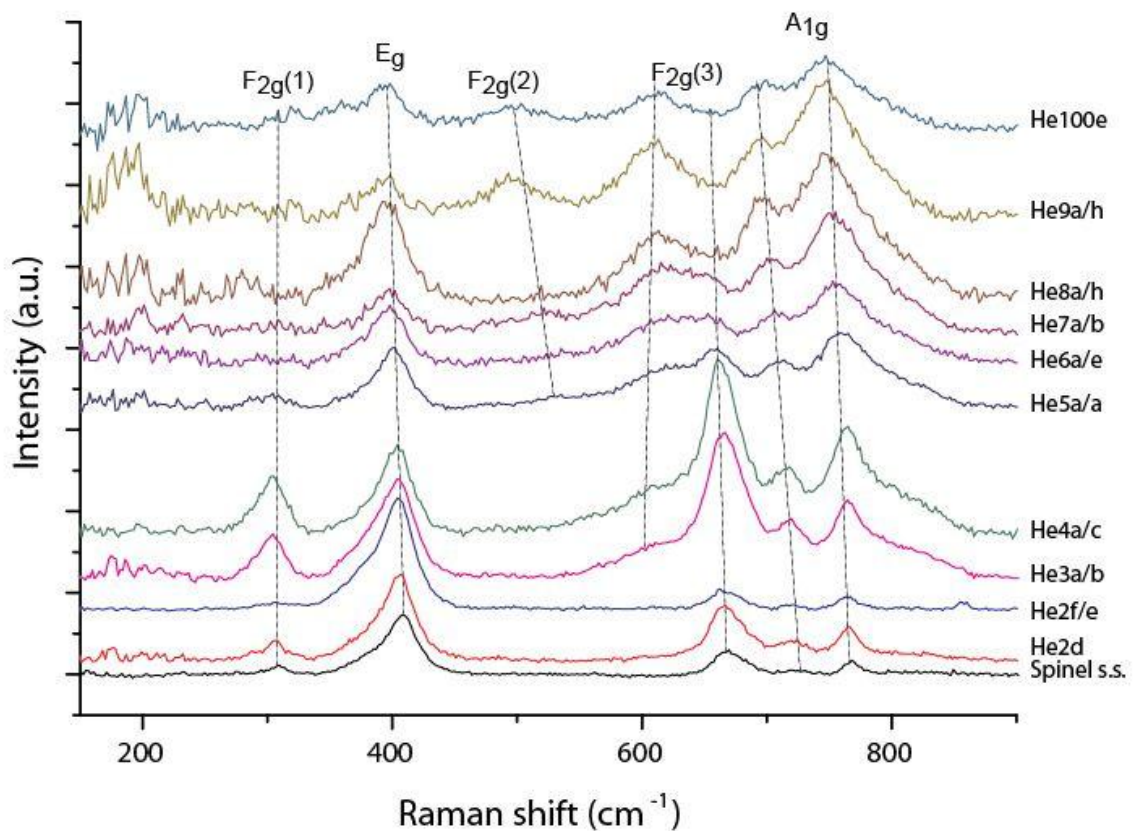


Fig. 4.44. Evolution of the unpolarized Raman spectra of synthetic spinels belonging to the $\text{MgAl}_2\text{O}_4\text{-FeAl}_2\text{O}_4$ series.

The wavenumber of all Raman-active modes of the spinels belonging to the $\text{MgAl}_2\text{O}_4\text{-FeAl}_2\text{O}_4$ series are plotted versus the iron composition in the Figure 4.45. At medium-to high Fe contents, all Raman-active modes display a decrease in wavenumber. On the contrary, at low Fe content up to the He4a/c sample (~20% of FeAl_2O_4 end-member), the E_g , $F_{2g}(3)$, and A_{1g} modes exhibit almost constant values. A similar trend was observed for Fe-poor samples by Malézieux and Piriou (1988).

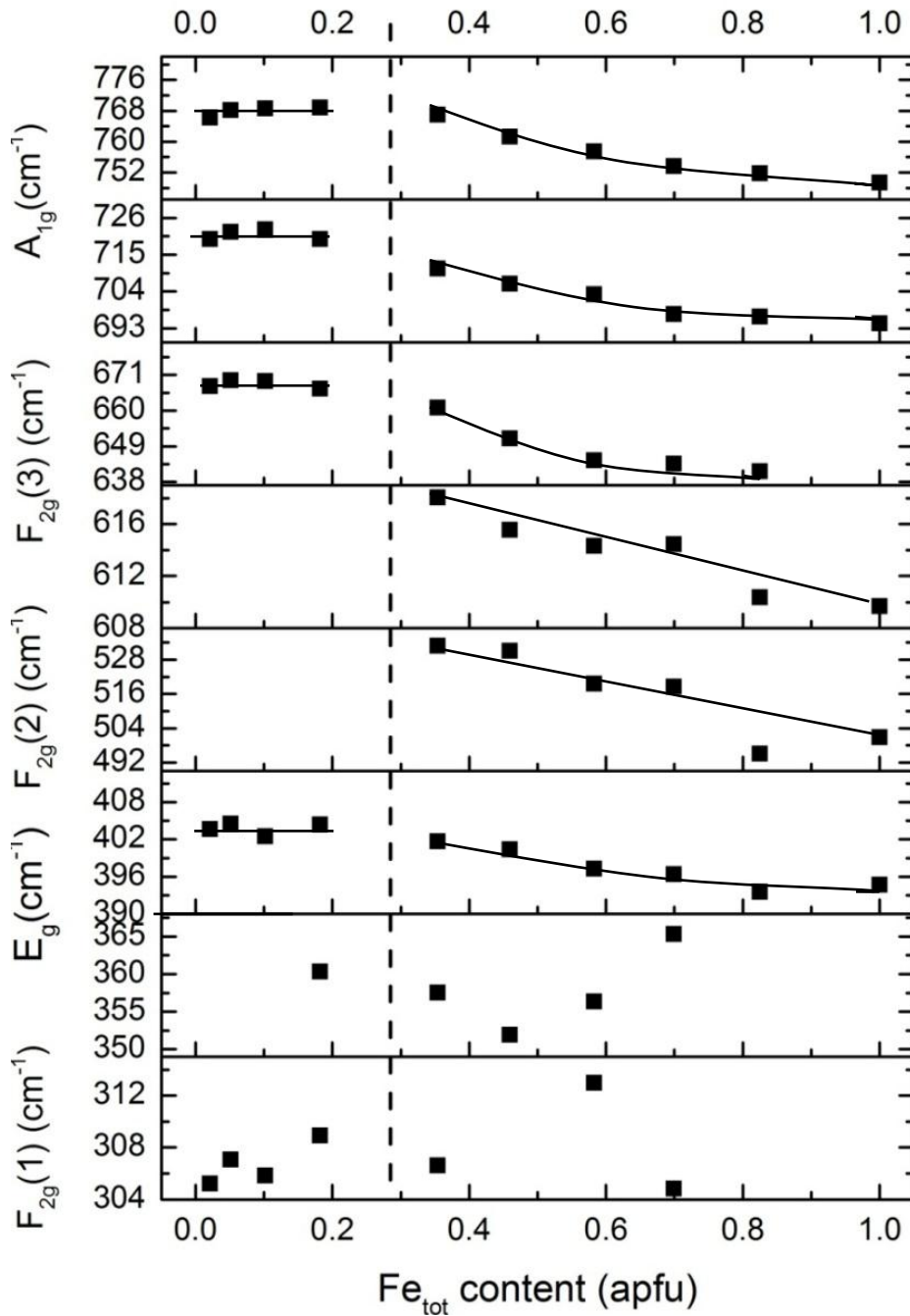


Fig. 4.45. Vibrational mode peak positions along the MgAl₂O₄-FeAl₂O₄ series.

After the 20% of the FeAl₂O₄ end-member a slowly polynomial decrease of wavenumber with the increase of iron content is observed. Crystal chemical data display that from the He5a/a sample Fe²⁺ starts to occupy the octahedrally coordinated sites and Fe³⁺ starts to occupy the tetrahedrally coordinated sites. Hence, the E_g, F_{2g}(3), and A_{1g} modes are affected by these exchanges more than the Fe²⁺→Mg substitution. In effect, the radius of Fe³⁺ in the tetrahedrally coordinated sites is smaller than that of Mg or Fe²⁺, thus, the entrance of Fe³⁺ in

the T site makes the T sites larger and consequently decreases the frequency of the vibrational sites. Analogous behavior of Fe^{3+} was described by Nakagomi et al. (2009) in the Raman spectra in the $\text{Mg}_x\text{Fe}_{3-x}\text{O}_4$ spinels.

As already mentioned, the A_{1g} mode is associated to the symmetric stretching of the oxygen in the tetrahedra. The Figure 4.46 shows as up to the Fe-composition of 0.20 apfu the A_{1g} mode does not change and then a rapid shift of the center position to lower frequency is observed. Since the Fe^{2+} starts to occupy the octahedrally coordinated site from Fe-composition greater than ~ 0.35 apfu (in the He5a/a), a strong effect of the presence of Fe^{2+} in the M site on the A_{1g} mode is shown.

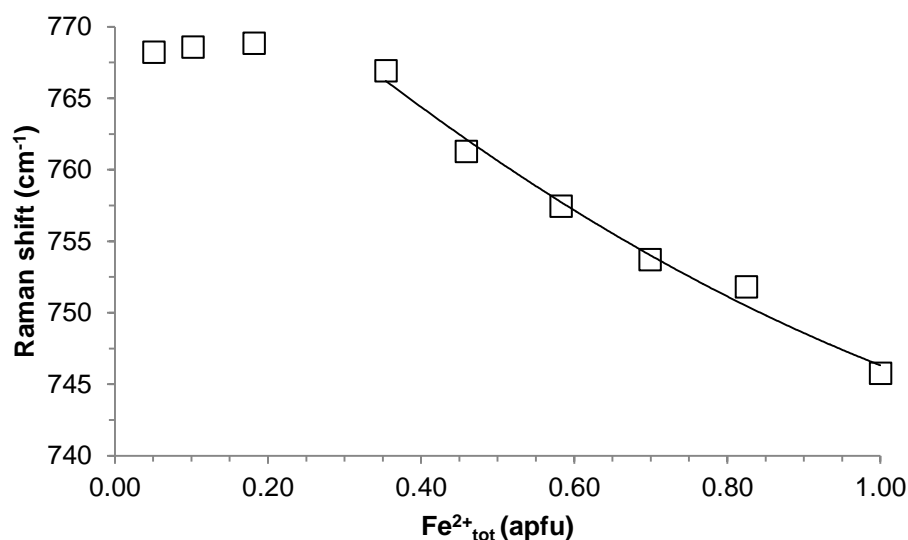


Fig. 4.46. Variation of the position of the A_{1g} mode (cm^{-1}) with the increase of the Fe^{2+} content along the MgAl_2O_4 - FeAl_2O_4 series.

A good correlation ($R^2=0.96$) between the position of the peak associated to the A_{1g} mode and the ratio $\text{Fe}/(\text{Fe}+\text{Mg})$ was found for the composition with the Fe concentration greater than 0.20 apfu (Fig. 4.47). The calculated equation can be used to know approximately the chemical composition of spinels belonging to the MgAl_2O_4 - FeAl_2O_4 series from the Raman spectra.

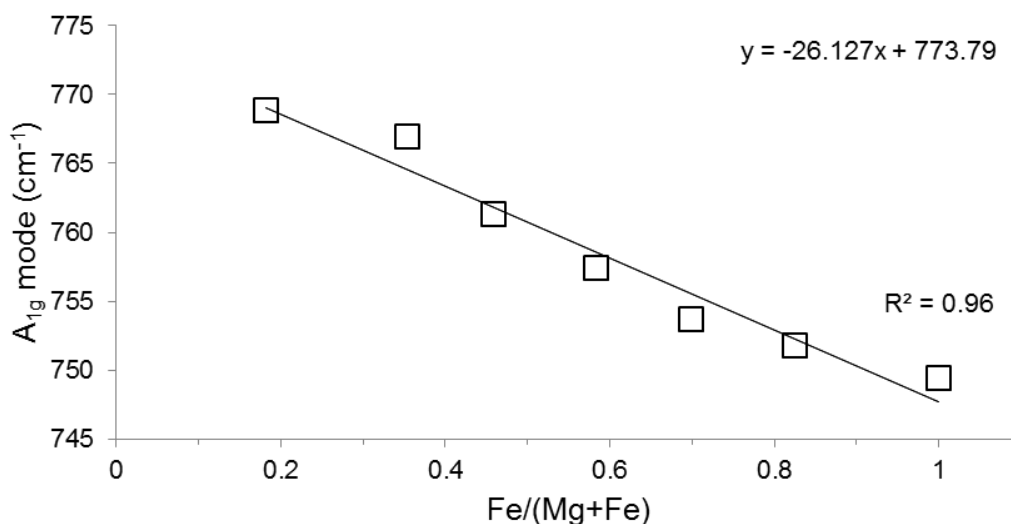


Fig. 4.47. Correlation between the position of the A_{1g} mode (cm^{-1}) and the ratio $\text{Fe}/(\text{Mg}+\text{Fe})$ along the MgAl_2O_4 - FeAl_2O_4 series.

The peak between 720 and 700 cm^{-1} with A_{1g} character is attributed to the cation inversion.

The $F_{2g}(3)$ mode at $\sim 670 \text{ cm}^{-1}$ is assigned to the asymmetric stretching of the oxygen in the MgO_4 from O'Horo et al. (1973) but, as in the case of A_{1g} , it is also affected by octahedral motion. A shoulder at $\sim 600 \text{ cm}^{-1}$ is observed, which increases in intensity to the detriment of the 670 cm^{-1} peak. Therefore, the shoulder at 600 cm^{-1} could be assigned to the asymmetric stretching of the oxygen in the FeO_4 .

As already mentioned, the E_g mode has a trend similar to the $F_{2g}(3)$ and the A_{1g} modes. This trend and its presence also in the hercynite end-member suggest that the Raman-active mode E_g at $\sim 400 \text{ cm}^{-1}$ can not assign only to the symmetric bending in MgO_4 .

4.3.4 The MgAl_2O_4 - MgCr_2O_4 spinel series

Magnesiocromite, MgCr_2O_4 , is an important component of spinel in upper mantle peridotites and it is widely considered to be an important petrogenetic indicators. In fact, MgCr_2O_4 , is thought to reflect primary crystallization from primitive mantle-derived magma (Barnes and Roeder, 2001). In addition, magnesiocromite is the only ore mineral of chromium and is a commercially important refractory material.

Several Raman investigations of pure MgCr_2O_4 are reported in literature (Wang et al., 2002a; Yong et al., 2012; Hosterman et al., 2013). Moreover, the MgAl_2O_4 - MgCr_2O_4 series was studied by Malézieux and Piriou (1988) but only few intermediate compositions were investigated. The MgAl_2O_4 - MgCr_2O_4 series provides a good opportunity to examine how substitution of the trivalent cation affects the Raman modes of this spinel system. In the present work twelve crystal spinels well representing of the entire series have been studied by polarized Raman spectra. The chemical and optical characterizations of these spinels are reported in Hålenius et al. (2010). Magnesiochromite has the Mg^{2+} and Cr^{3+} cations fully ordered in the tetrahedrally and octahedrally coordinated sites, respectively, because Cr^{3+} has a strong preference for the M site. Thus along the MgAl_2O_4 - MgCr_2O_4 series a rapid decrease of the inversion from 0.24 to 0 was observed.

The unpolarized Raman spectrum of the MgCr_2O_4 end-member shows well-defined peaks at 445, 539, 609, 682 cm^{-1} in agreement with the values reported in literature (Fig. 4.48 and Table 4.18).

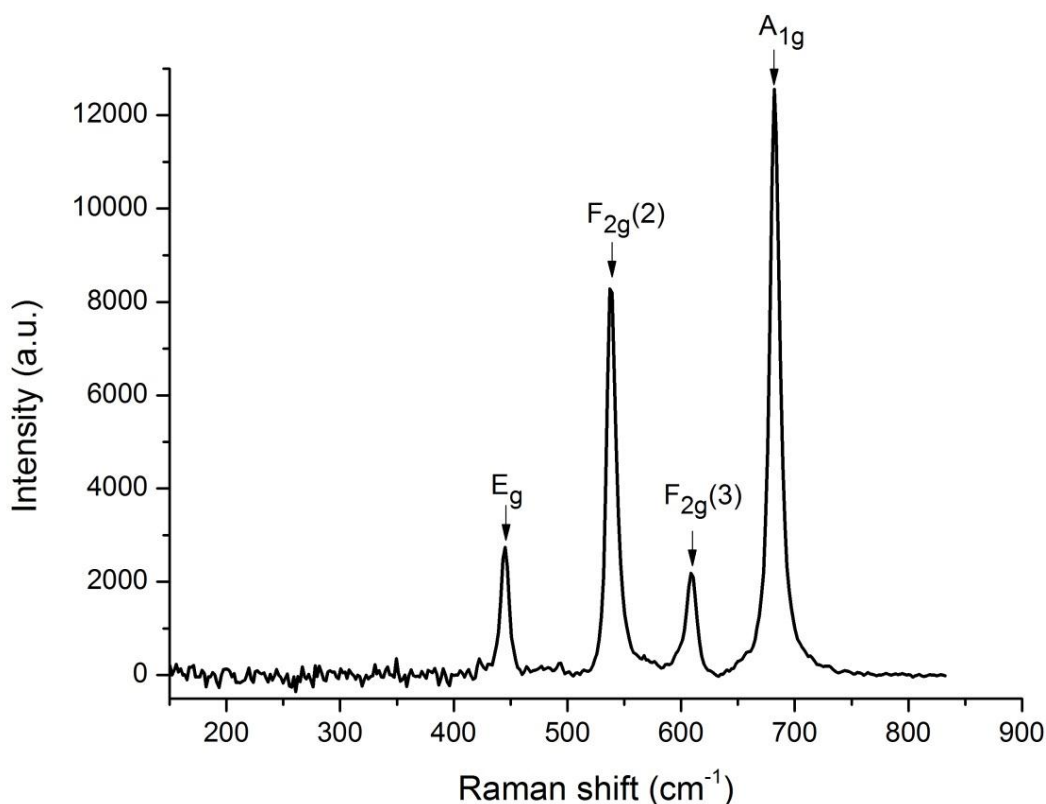


Fig. 4.48. Unpolarized Raman spectrum of the MgCr_2O_4 end-member, with the assignment of the four peaks.

Unlike the Raman spectra seen so far, the peaks of the MgCr_2O_4 are very sharp because of the absence of the cation disorder. Following the previous studies, the peaks can be assigned to E_g , $F_{2g}(2)$, $F_{2g}(3)$ and A_{1g} modes, respectively.

Table 4.18. Comparison among the peak wavenumber (cm^{-1}) observed in the present work for the MgCr_2O_4 end-member and those reported in literature.

| Raman modes | This work | Malézieux and Piriou (1988) | Wang et al. (2002a) | Yong et al. (2012) | Hosterman et al. (2013) | Lenaz and Lughì (2013) |
|-------------|-----------|-----------------------------|---------------------|--------------------|-------------------------|------------------------|
| $F_{2g}(1)$ | – | – | 227 | – | – | – |
| E_g | 445 | 448 | 447 | 447 | 446 | 445 |
| $F_{2g}(2)$ | 539 | 545 | 544 | 543 | 542 | 542 |
| $F_{2g}(3)$ | 609 | 615 | 614 | 612 | 612 | 611 |
| A_{1g} | 682 | 685 | 687 | 684 | 685 | 683 |

Polarized Raman spectra of the entire MgAl_2O_4 - MgCr_2O_4 series are shown in the Figure 4.49. The spectra collected with the perpendicular polarization show more intense the F_{2g} modes, whereas the spectra collected with parallel polarization show more intense the A_{1g} mode.

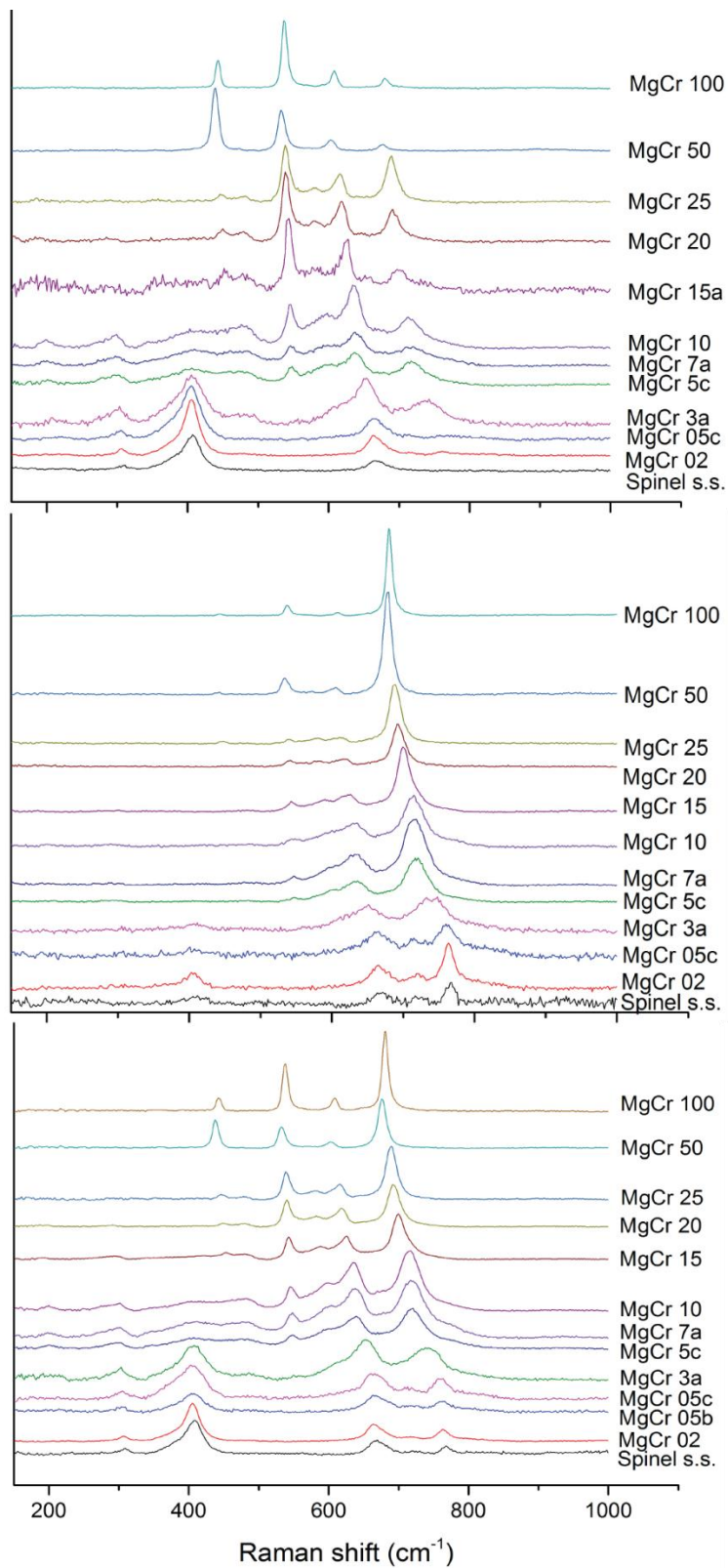


Fig. 4.49. Raman spectra of the $\text{MgAl}_2\text{O}_4\text{-MgCr}_2\text{O}_4$ spinel series: spectra taken with crossed polarization (on the top), parallel polarization (in the middle) and without polarization (on the bottom).

Unpolarized Raman spectra are shown in detailed in the Figure 4.50. The chromium atom has mass larger than that of the aluminium atom. Therefore, from a simple mass on a spring model, the substitution $\text{Cr}^{3+} \rightarrow \text{Al}^{3+}$ should lead to lower frequencies. In fact, a shift to low-frequency of the $F_{2g}(2)$, $F_{2g}(3)$ and A_{1g} modes is observed, more marked in the last mode than the others. The E_g mode seems to show a two-mode behavior with a gradually decrease of intensity of the peak at $\sim 400\text{cm}^{-1}$ and a gradually increase of a peak at $\sim 450\text{cm}^{-1}$ in the Cr-rich spinels.

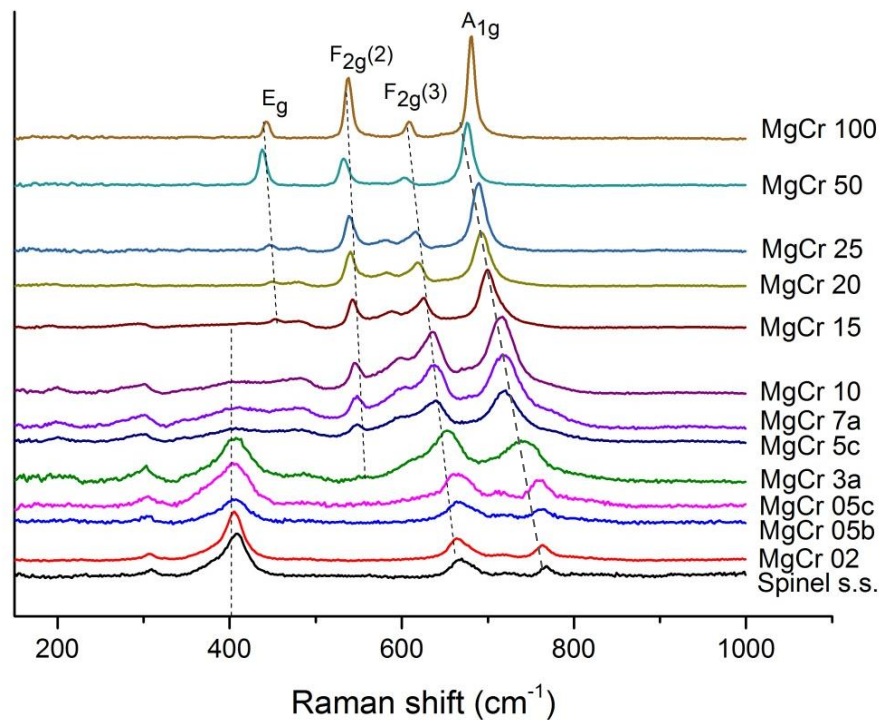


Figure 4.50. Evolution of the unpolarized Raman spectra of synthetic spinels belonging to the $\text{MgAl}_2\text{O}_4\text{-MgCr}_2\text{O}_4$ series.

Analysis of the Raman spectra shows that, as in the case of iron spinel, two trends can be observed for the A_{1g} and $F_{2g}(3)$ modes. Initially the spinels do not respond to the $\text{Cr}^{3+} \rightarrow \text{Al}^{3+}$ substitution and then a rapid decrease of the frequencies is perceived (Fig. 4.51).

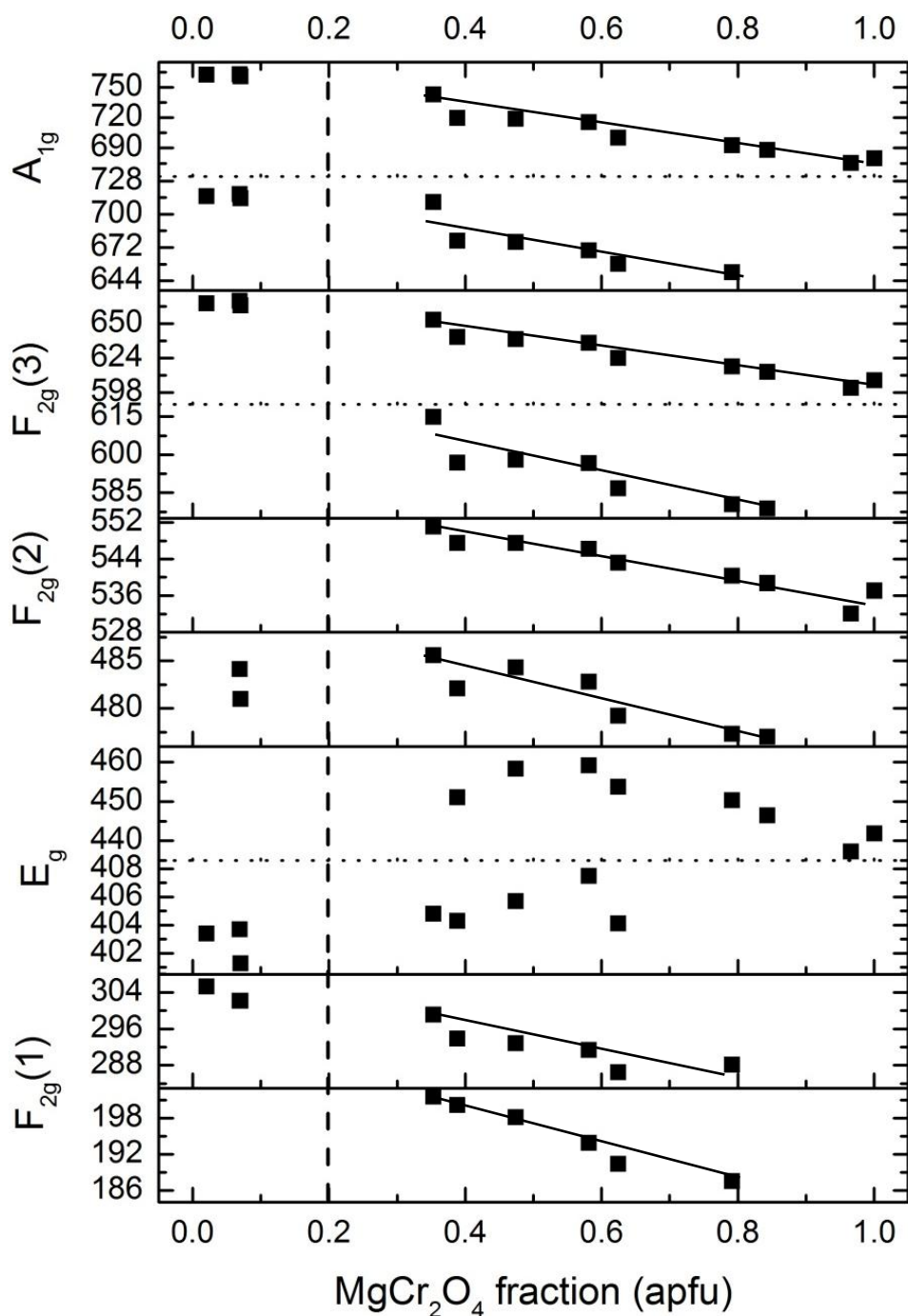


Fig. 4.51. Evolution of the vibrational mode peak positions along the MgAl_2O_4 - MgCr_2O_4 series.

The $F_{2g}(1)$ modes first weakens and then disappears along the series, showing a strong reliance on the Al in the tetrahedra. The E_g mode at 400cm^{-1} remains almost in the same position and disappears in spinel with more than 50% of chromite component. However, from chromite component near 50% an additional E_g mode starts to growth at $\sim 450\text{ cm}^{-1}$ (Fig. 4.52). Hence, the Raman-active E_g

mode can be assigned as a complex of vibration involving both Mg and Al or Cr atoms.

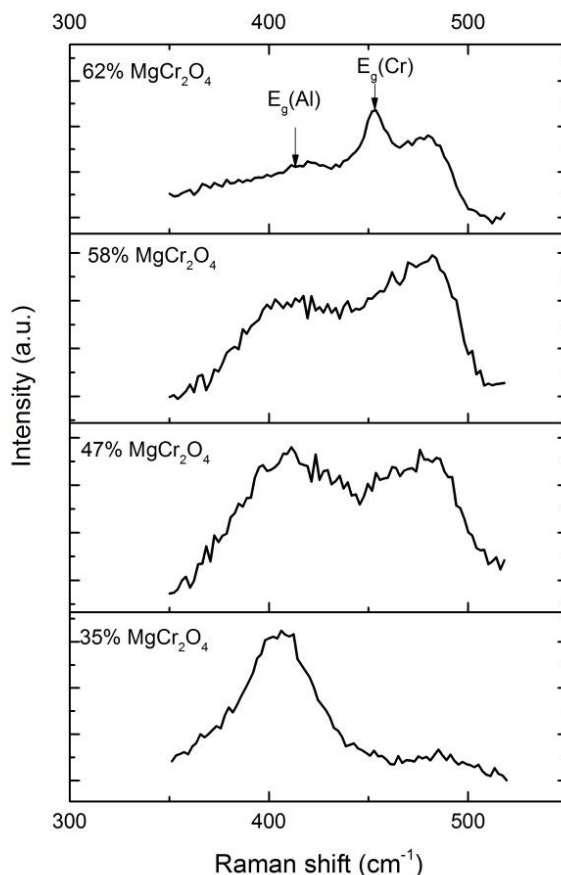


Fig. 4.52. E_g modes in the MgCr15aa, MgCr10, MgCr7a and MgCr3a samples from the top to the bottom. The characteristic E_g mode in the Al-rich spinels is labelled $E_g(\text{Al})$, while the characteristic E_g mode in the Cr-rich spinels is labelled $E_g(\text{Cr})$.

The $F_{2g}(2)$ mode intensifies with the increase of the Cr content. Its absence in the MgAl_2O_4 end-member can bring into question its attribution to the Mg-O motion in the tetrahedrally coordinated sites.

The $F_{2g}(3)$ mode can be followed along the series and shows a good correlation with the Cr content (Fig. 4.53). Its frequency decreases due to the substitution of the aluminium with a heavier chromium atom. This peak develops a lower wavenumber shoulder only in the intermediate compositions.

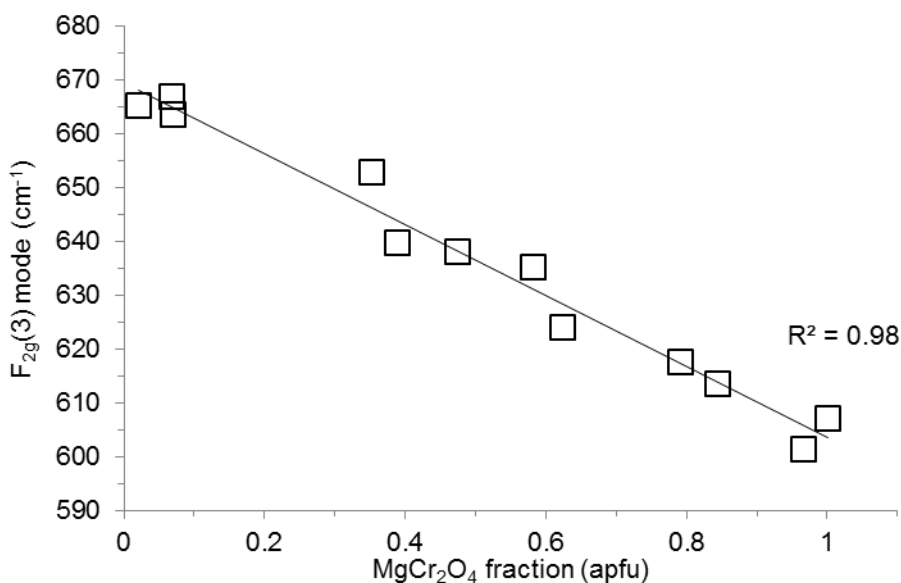


Fig. 4.53. Correlation between the wavenumber of the $F_{2g}(3)$ mode and the $MgCr_2O_4$ fraction.

Unlike the other studied series, the peak at $\sim 727\text{ cm}^{-1}$ with the A_{1g} mode character rapidly disappears, confirming the assignment to the symmetric stretching of the AlO_4 .

The A_{1g} mode becomes sharper and more intense along the series. As already mentioned, the A_{1g} mode is attributed to the stretching of the Mg-O, but it is subjected to a strong influence of the trivalent cations. In fact, during this mode the oxygen atoms move away from the tetrahedral cation along the direction of the bonds. Neither the tetrahedral nor octahedral cations are in motion during this vibration. Malézieux and Piriou (1988) argued that the frequencies of the A_{1g} mode are essentially conditioned by the valence force constants of the $^T A^{2+}\text{-O}$ bond distance and by the O-O repulsion. The trivalent cation in the M site intervenes only in a deformation of the $^M B^{3+}\text{-O}$ bond distance and thus as it conducts a bother on the A_{1g} mode.

A linear correlation between the Raman shift of the A_{1g} mode and $MgAl_2O_4$ or $MgCr_2O_4$ fraction is observed (Fig. 4.54). An increase of the $MgAl_2O_4$ fraction would lead to an increase of the Raman shift of the A_{1g} mode, while an increase of the $MgCr_2O_4$ fraction would lead to a decrease of the Raman shift. Following Malézieux et al. (1983), the equation obtained by a linear correlation between the frequency variations of the A_{1g} mode and the ratio $Cr/(Al+Cr)$ can give an estimated Cr and Al concentration in the spinel system (Fig. 4.55).

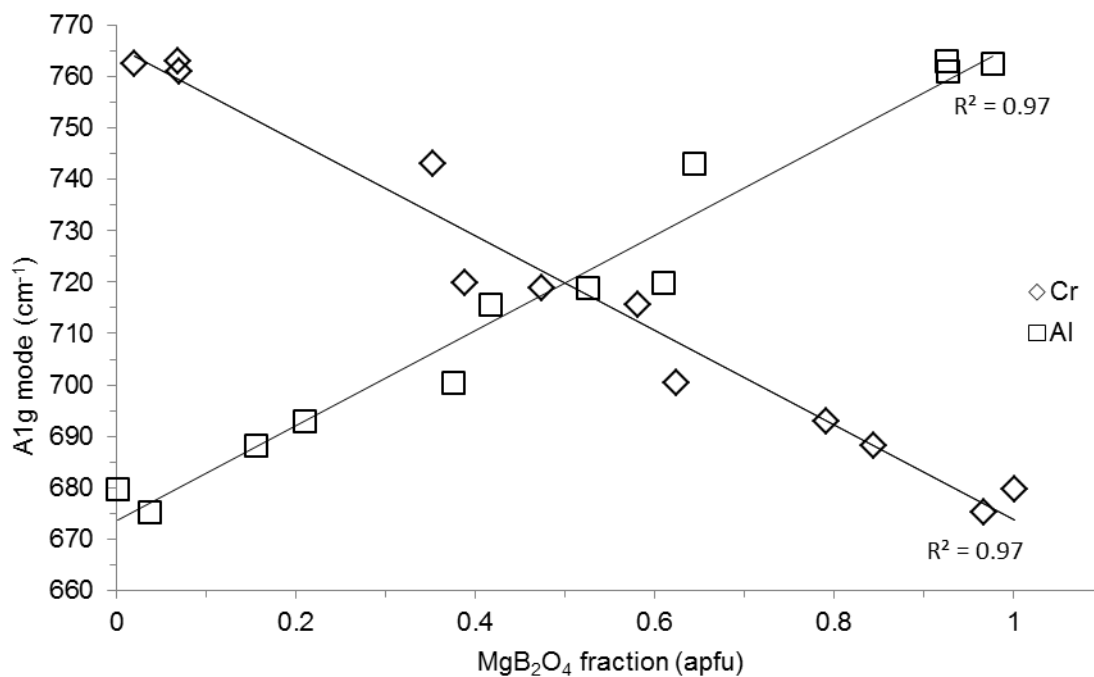


Fig. 4.54. Correlation between the Raman shift of the A_{1g} mode and the MgAl₂O₄ fraction (open square) or the MgCr₂O₄ fraction (open rhombus).

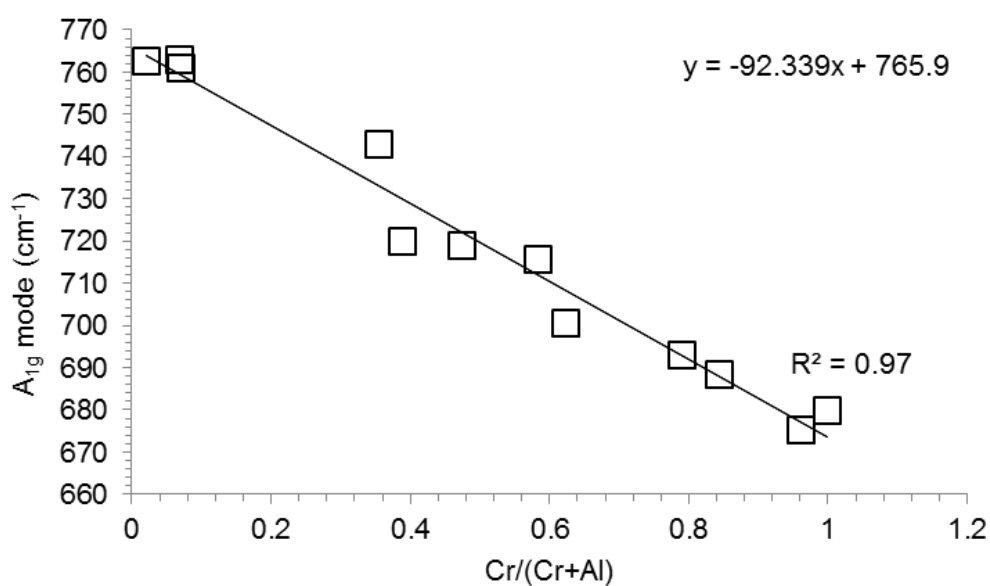


Fig. 4.55. Frequency variations of the A_{1g} mode as a function of the ratio Cr/(Cr+Al).

Moreover, an interesting correlation can be observed relating the variation of the A_{1g} mode and the local Cr-O bond distances in the M sites reported in Hålenius et

al. (2010) (Fig. 4.56). Hence, the frequency of the A_{1g} mode can also give information about the structural relaxation in the Cr-spinels.

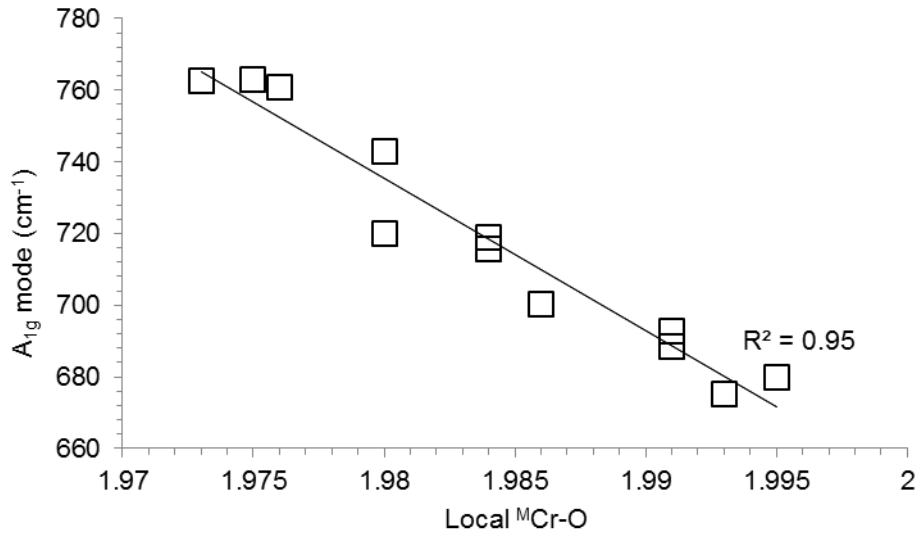


Fig. 4.56. Variations of the A_{1g} mode with the local Cr-O bond distances in the M sites.

➤ **ZnCr₂O₄ end-member**

In addition to the spinels belonging to the MgAl₂O₄-MgCr₂O₄ series, also the ZnCr₂O₄ end-member characterized by Hålenius et al. (2010) was investigated by the Raman spectroscopy. The Raman spectrum shows all the five Raman-active modes in the form of sharp peaks (Fig. 4.57).

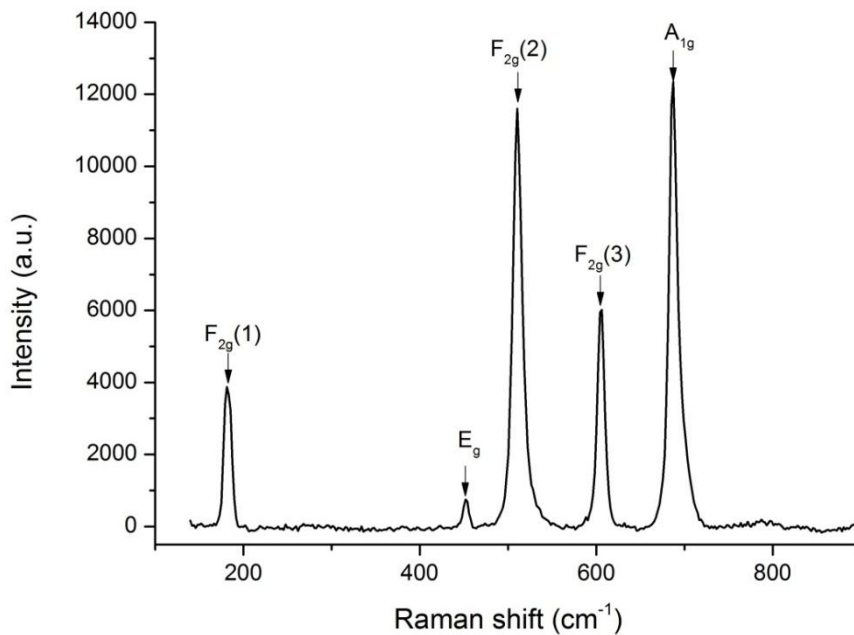


Fig. 4.57. Raman spectrum of a synthetic ZnCr₂O₄ spinel.

Given that the Zn has a strong preference for the tetrahedrally coordinate sites and Cr³⁺ has a strong preference for the octahedrally coordinated site, the ZnCr₂O₄ is almost fully ordered. In fact, the peak attributed to the cation disorder does not appear and all the peaks are very narrow. The values of the wavenumber are in good agreement with those reported in literature (Table 4.19).

Table 4.19. Comparison among the wavenumber (cm⁻¹) observed in the present work for the ZnCr₂O₄ end-member and those reported in literature.

| Raman modes | This work | Wang et al. (2002b) | Marinković Stanojević et al. (2007) | Gupta et al. (1993) | Himmrich, and Lutz (1991) |
|---------------------|-----------|---------------------|-------------------------------------|---------------------|---------------------------|
| F _{2g} (1) | 182 | 180 | 195 | 186 | 181 |
| E _g | 452 | 430 | 490 | 457 | 456 |
| F _{2g} (2) | 511 | 511 | 516 | 515 | 529 |
| F _{2g} (3) | 605 | 605 | 609 | 610 | 614 |
| A _{1g} | 687 | 687 | 690 | 692 | 690 |

The Raman spectra of the various end-members characterized above are compared in Figure 4.58. Notably, every end-member exhibits a characteristic fingerprint. As an immediate consequence, from the position of the peaks it is possible to distinguish if a spinel belongs to the spinel series (AAI₂O₄) or to the chromite series (ACr₂O₄). The biggest difference between the aluminates and the chromates is located in the A_{1g} mode. The chromates exhibit the A_{1g} mode at lower frequencies in agreement with their heavier atomic mass. In addition, a careful inspection of the Raman shift and the relative intensity of the peaks will allow the discrimination among the various end-members.

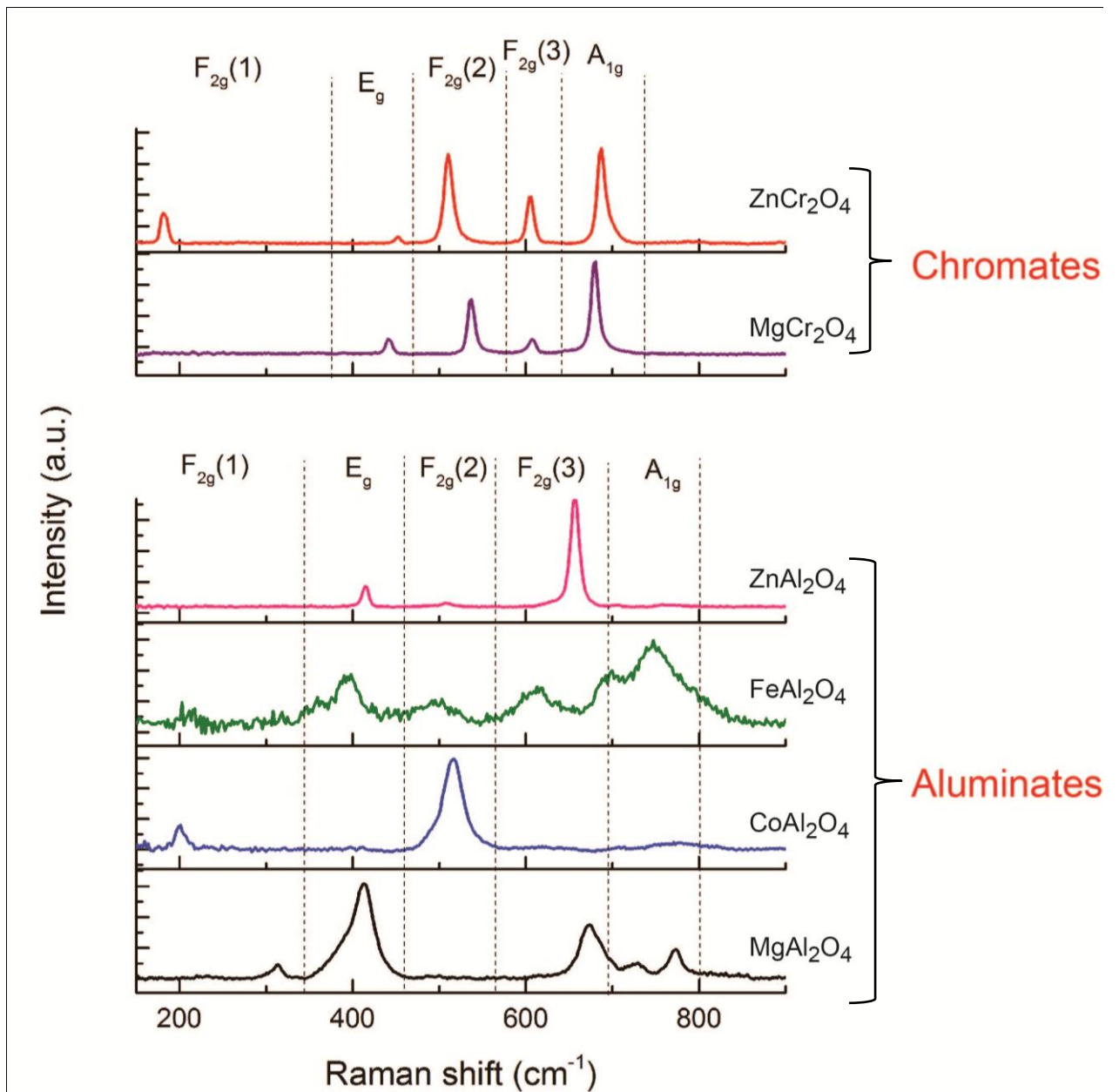


Fig. 4.58. Comparison among unpolarised Raman spectra of synthetic spinel end-members.

4.4 Raman spectra of natural spinels

As already mentioned in the Chapter 2, the Raman spectroscopy is a powerful tool for the identification of minerals and related phases but to do this a detailed database is necessary. Very few samples of natural spinels have been investigated by Raman spectroscopy because the presence of several cations within the structure has generated difficulties of interpretation of the Raman shifts, due to the possibility for several cations to enter the octahedral and tetrahedral

sites. In fact, many natural spinels have complex chemical composition being a mixture of different end-members. As seen above, the various spinel end-members show different fingerprint. The shift of the lines in the Raman spectrum gives the possibility to calculate the approximate chemical composition of the spinels using the positions of the lines.

In order to increase the database of Raman spectra of spinels a large amount of natural spinels was investigated. These natural spinels are the same spinel crystals analyzed by Electron MicroProbe and Optical Absorption Spectroscopy and discussed in the previous chapter. As already mentioned, these natural spinels exhibit a spinel s.s. (MgAl_2O_4) or gahnite (ZnAl_2O_4) composition. The Raman frequencies recorded for the 22 natural spinels investigated are shown in Table 4.20.

The Raman spectra of the studied natural spinels show two kind of fingerprint. Most of the samples with spinel s.s. composition exhibit four peaks at ~ 310 , 404, 663, and 765 cm^{-1} . Natural spinels with gahnite composition shows three of the five Raman-active modes at 415, 657 and 763 cm^{-1} attributed to the E_g , F_{2g} (3) and the A_{1g} modes, respectively.

Table 4.20. Frequencies recorded for the Raman modes of natural spinels. *sh*=shoulder.

| Samples | F_{2g}(1) | E_g | F_{2g}(2) | F_{2g}(3) | A_{1g} | A_{1g} |
|----------------|--------------------------|----------------------|--------------------------|--------------------------|-----------------------|-----------------------|
| Nat.1 | 312 | 406 | – | 665 | – | 766 |
| Nat.2 | – | 405 | – | 664 | – | 766 |
| Nat.3 | 314 | 408 | – | 667 | – | 768 |
| Nat.4 | 317 | 410 | – | 669 | – | 771 |
| ST | 313 | 408 | – | 667 | – | 768 |
| SX | 313 | 408 | – | 667 | – | 769 |
| 30070 | 357 | 419 442 <i>sh</i> | 501 526 <i>sh</i> | 656 624 <i>sh</i> | 705 | 755 |
| 31081 | – | 417 | 508 | 657 626 <i>sh</i> | 707 | 757 |
| 330763 | 312 | 406 | – | 664 | – | 766 |
| 330764 | 311 | 404 | – | 662 | – | 765 |
| 440243 | 311 | 406 | – | 665 650 <i>sh</i> | – | 766 |
| 510941 | – | 414 | – | 657 | – | – |
| 510942 | – | 415 | 508 | 657 | – | – |
| 670275 | 313 | 406 | – | 664 | – | 767 |
| 800801 | 313 | 406 | – | 662 | 709 | 764 |
| 881694a | 310 | 406 | – | 664 | – | 765 |
| 881694c | 312 | 406 | – | 665 | – | 766 |
| 881728 | 296 | 413 387 <i>sh</i> | – | 655 622 <i>sh</i> | 703 | 755 |
| 890290 | 310 | 405 | – | 664 | – | 766 |
| 890292b | 377 | 416 429 <i>sh</i> | 575 | 643 | – | 749 |
| 890292c | 312 | 406 | – | 665 | – | 765 |
| 890292d | 377 | 415 431 <i>sh</i> | 575 | 643 | – | 749 |

In the Figure 4.59 two Raman spectra of natural blue spinels with different composition were compared. Sample Nat.2 (spinel s.s.) has the E_g mode more intense than the F_{2g} mode, whereas the sample 510942 (gahnite) shows the contrary. In addition the gahnite sample shows the F_{2g} (2) mode at 508 cm^{-1} unlike the spinel sample.

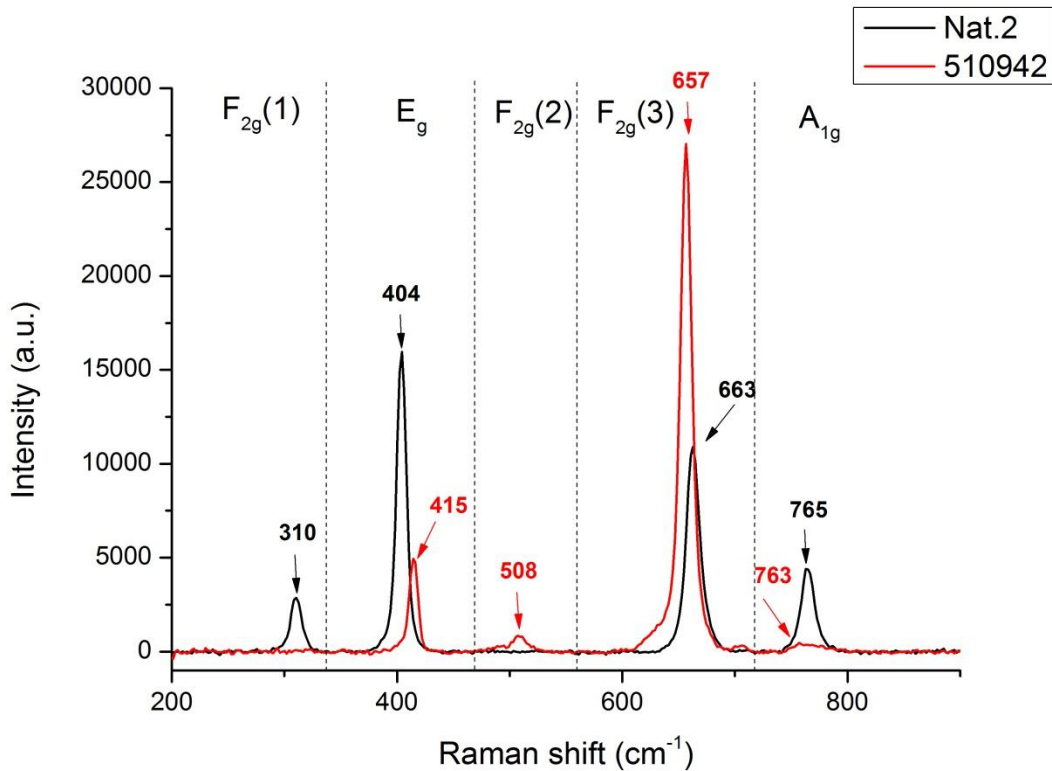


Fig. 4.59. Comparison of the Raman spectra of two natural spinels with different composition.

Consequently, in all the cases examined the discrimination among spinels with different principal component has been easily possible looking at the Raman shift and at the relative intensity of the peaks.

Some spinels show the appearance of the peak at $\sim 705\text{ cm}^{-1}$ attributed to the cation disorder (Fig. 4.60). In addition, with the appearance of the peak at $\sim 705\text{ cm}^{-1}$, often shoulders of the E_g , $F_{2g}(2)$ and $F_{2g}(3)$ modes are noticed. Hence, these shoulders could be assigned to the cations inverted.

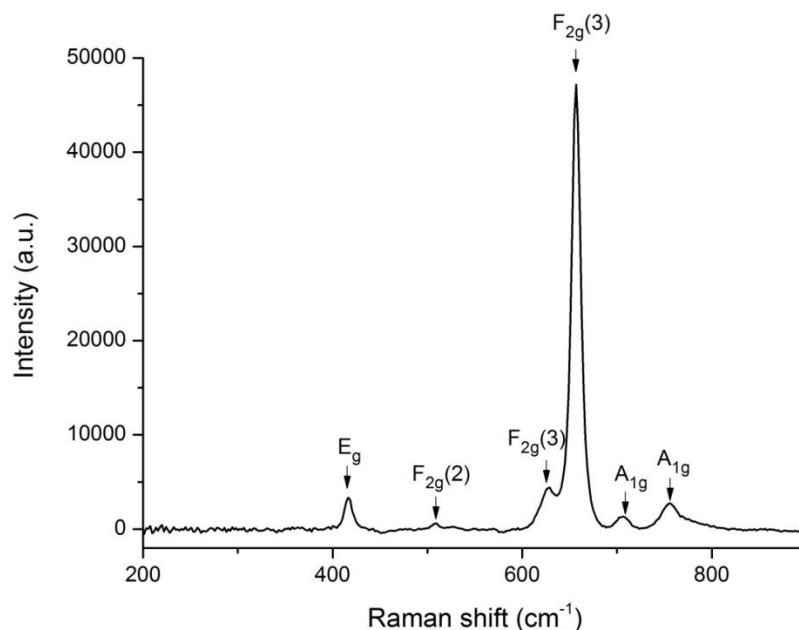


Fig. 4.60. Raman spectrum of the yellowish-green 31081 sample.

Taking into account the correlation found by Minh and Yang (2004) between the FWHM values of the $\sim 410 \text{ cm}^{-1}$ mode in the MgAl_2O_4 and the annealing temperature (reported in figure 4.61), information on the formation temperature can be extrapolated. In the natural spinels investigated the FWHM values of the $\sim 405 \text{ cm}^{-1}$ mode range from 9 to 12 cm^{-1} , thus their formation temperature is estimated to be below 750°C .

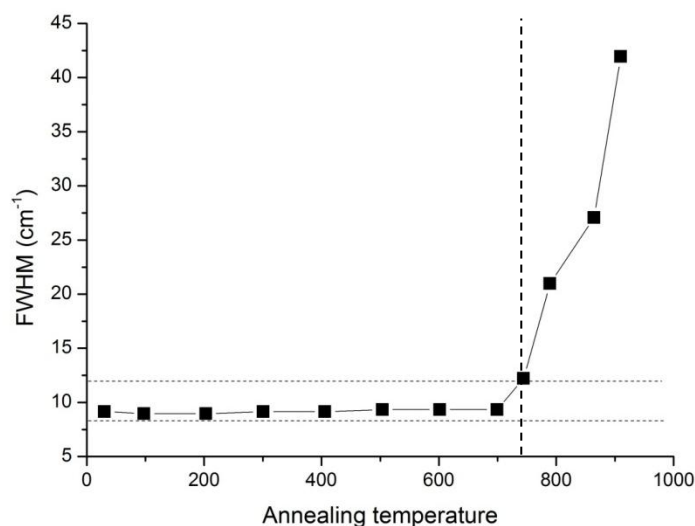


Fig. 4.61. The FWHM values of the E_g mode as a function of the annealing temperature as reported by Minh and Yang (2004). The dashed lines represent the range of values found in the spinels investigated in this work.

Spinel with the same principal component and different minor elements have been compared, and the conclusion is that they show the same fingerprint (Fig. 4.62). All the natural samples displayed in figure 4.62 have the spinel s.s. composition but different amount of chromophore ions like Fe^{2+} , Fe^{3+} , Cr and V, which cause the differences in colors. These features, however, do not create big change in the Raman fingerprint.

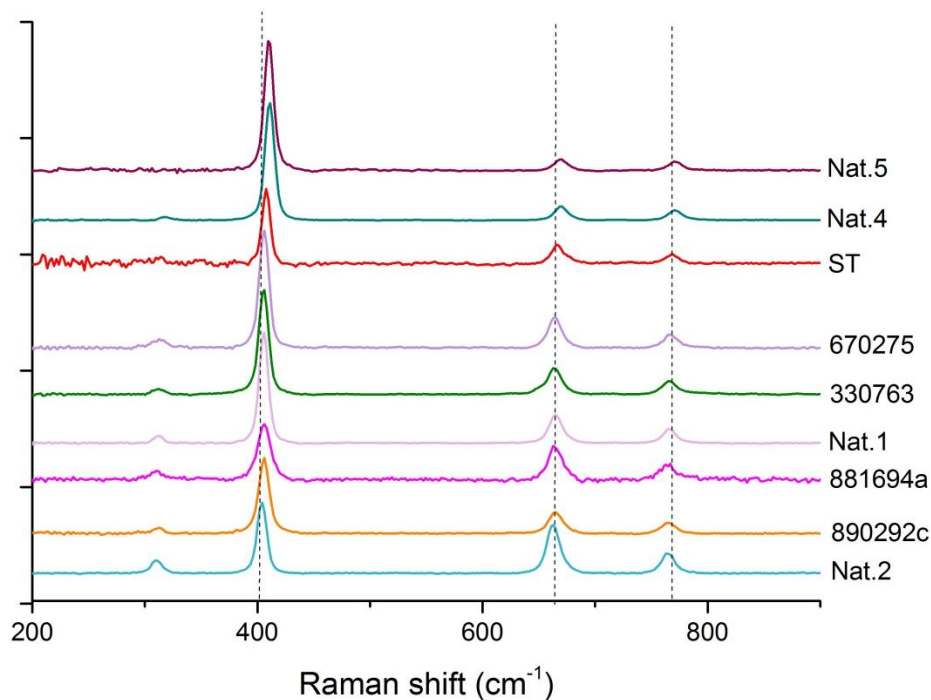


Fig. 4.62. Comparison of the Raman spectra of natural spinels with the same major elements and different minor elements. The spectra are colored as the color of the sample.

At highly meticulous inspection of Figure 4.62,, a small shift of the peaks can be perceived but a linear relationship between these changes and the chemical variation of the minor elements is not found. More detailed studies on the structural parameters are necessary.

4.4.1 Comparison between natural and synthetic spinels

Unlike natural spinel, the synthetic spinel frequently produces six to seven Raman peaks. A comparison of Raman spectra between a natural and a synthetic sample with similar composition is shown in the Figure 4.63.

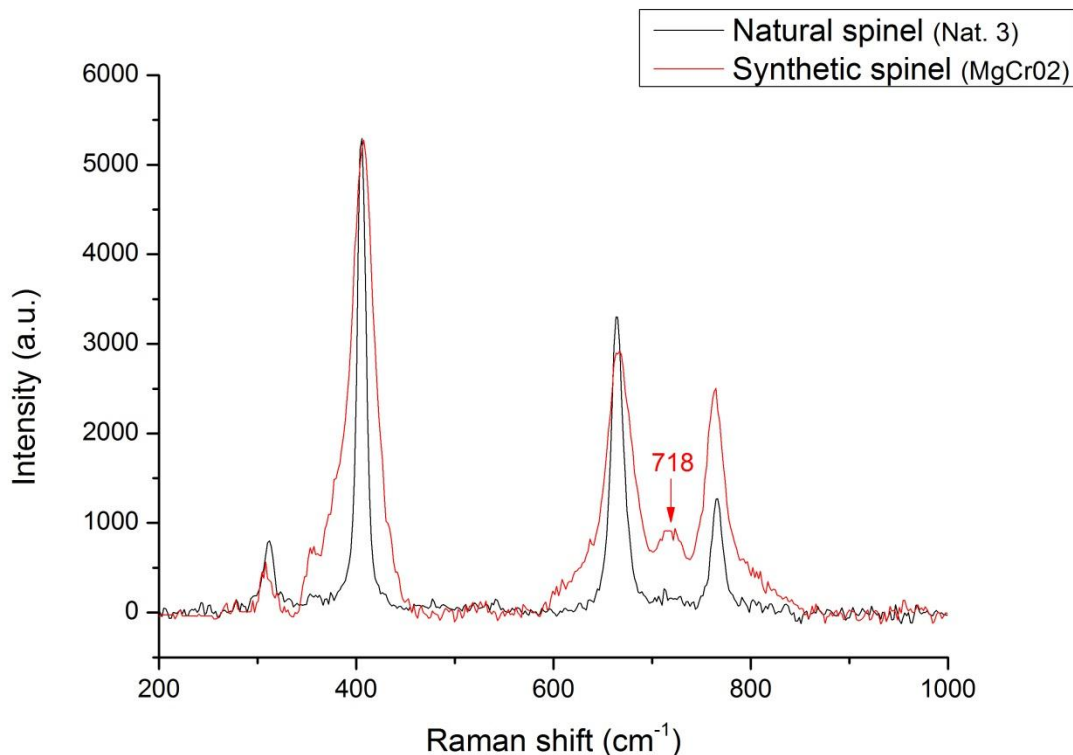


Fig. 4.63. Comparison of the Raman spectra of a natural and a synthetic spinels with similar composition.

The peaks in the synthetic and natural spinels show the same position of the Raman modes, but some systematically different features are observed. In the synthetic spinels an additional peak centered at 718 cm^{-1} is observed and it is attributed to the stretching vibration of AlO_4 groups created by the rearrangement of some Al ions from octahedral to tetrahedral sites (i.e., cation disorder), in agreement with Cynn et al. (1992). In addition, a broadening of all the peaks is perceived. In particular, the FWHM of the main band at $\sim 405\text{ cm}^{-1}$ increases from about 9 cm^{-1} in the natural spinel to 27 cm^{-1} in the synthetic spinel, and it becomes also asymmetric in the latter.

As a conclusion, distinguishing natural unheated spinel from a re-heated or a synthetic spinel is simply a matter of looking at the line width of the 405 cm^{-1} Raman peak and the presence of a peak at $\sim 720\text{ cm}^{-1}$. This information may be very useful in gemological field, to disclose spinel gemstones re-heated with the purpose to enhance the color.

More recently, fluorescence features attributed to chromophoric ions and trace elements have been observed in Raman spectra, revealing important information about crystal chemistry. Analysis and interpretation of these features may help distinguish between natural, treated, and synthetic materials.

In the field of gemology, both Raman and photoluminescence analyses have become extremely employed to verify the nature of the gemstones, and to detect synthetic and imitation stones.

To investigate the photoluminescence features, the Raman spectra were recorded in a wide range of Raman shift, from 100 to 8000 cm^{-1} with blue laser and from 200 to 4800 cm^{-1} with green laser (Fig. 4.64 and 4.65). To compare the spectra recorded with the two lasers and with those present in literature, the PL spectrum will be shown in terms of wavelength (nm).

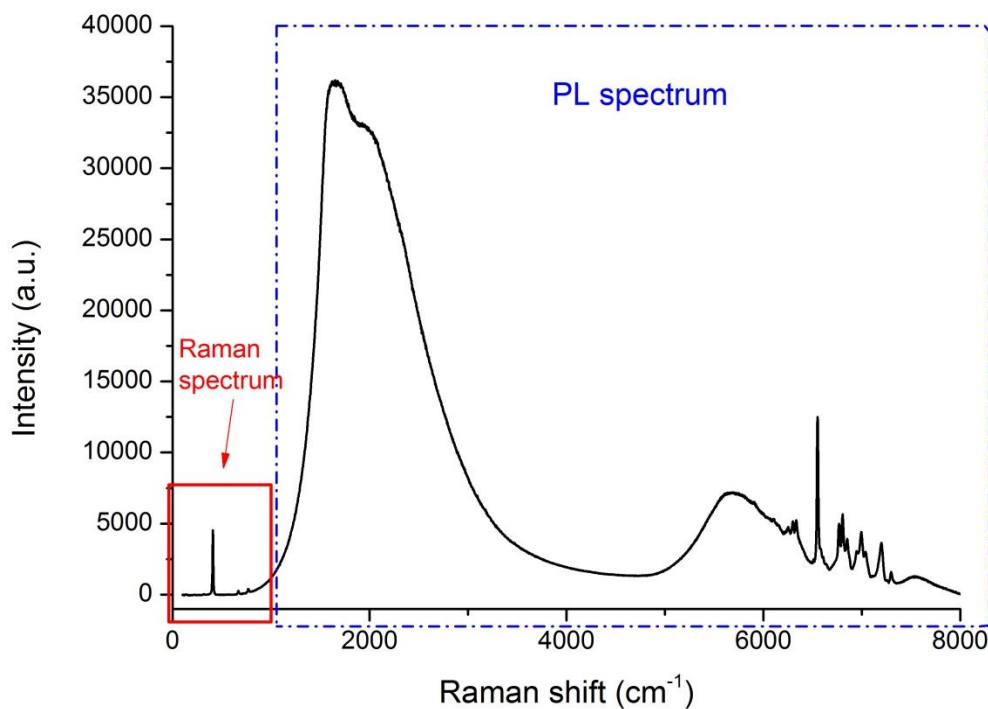


Fig. 4.64. Raman and photoluminescence spectrum of the Nat.2 sample taken with the blue laser (473.1 nm line of a solid state Nd:YAG).

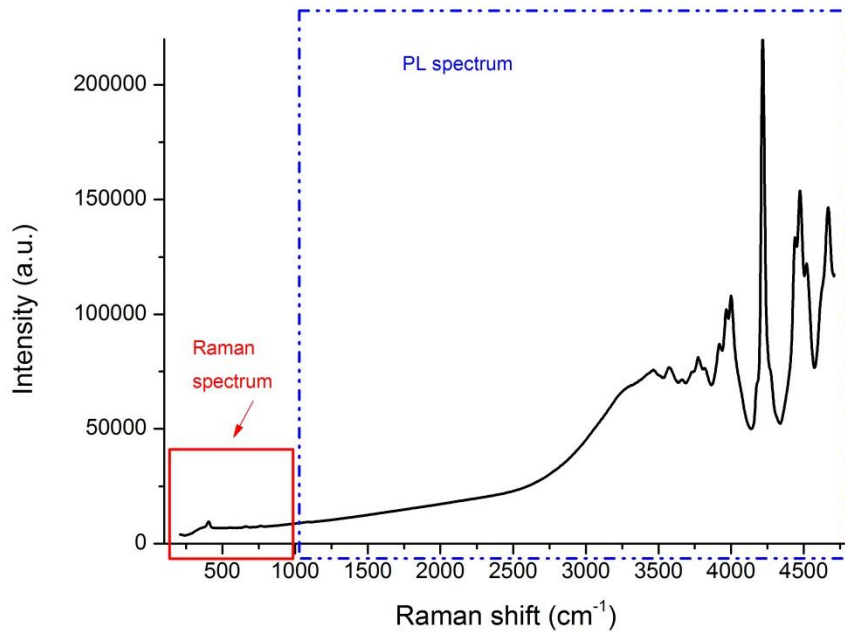


Fig. 4.65. Raman and photoluminescence spectrum of the 440243 sample taken with the green laser (TEC-cooled 532nm DPSS laser).

Despite of the low concentration, most of the PL spectra of natural spinels show the PL bands occurring in the range between 640 and 750 nm (5700-8000 cm^{-1}). These bands are known by gemologists as 'organ pipes', characteristic shape of the Cr photoluminescence bands (Fig. 4.66).

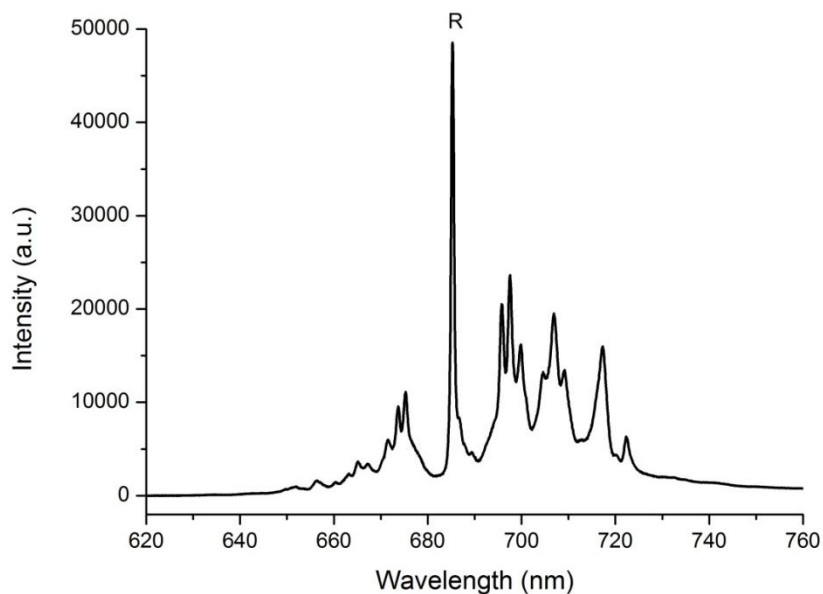


Fig. 4.66. Photoluminescence spectrum of a natural sample (Nat.1).

The complex is composed from a principal prominent peak and numerous less intense peaks, corresponding the zero phonon lines (R and N lines) and their

phonon sidebands, respectively. The sharp and dominant R line at 685 nm arises from the class of Cr^{3+} ions, which has an ideal short-range order due to the spin-forbidden transition ${}^2E_g \rightarrow {}^4A_{2g}$. The R line belongs to regular $16d$ site of spinel structure whereas the N lines are related to a coupling between the Cr^{3+} classes. The N lines can be interpreted as zero-phonon lines of different luminescence centers and are, therefore, spectroscopic analogues of the R line (Singh et al., 2011). The N-line can reflect the local perturbations of the lattice. An increase of the lattice defects and the lattice disorder increases the numbers of centers of all the corresponding Cr^{3+} class.

Natural samples showed narrow peaks, while the synthetic spinels showed broader and less resolved peaks (Fig. 4.67). The width of the PL-peaks is linked to the environment in which the Cr-ions are embedded. The disordering of the cations in the crystal structure changes this environment and thus causes a broadening (from 0.7 to 4.7 nm) and a shift of 3 nm towards IR of most intense peak in the synthetic spinels. In addition, the less intense bands are broadened and merged.

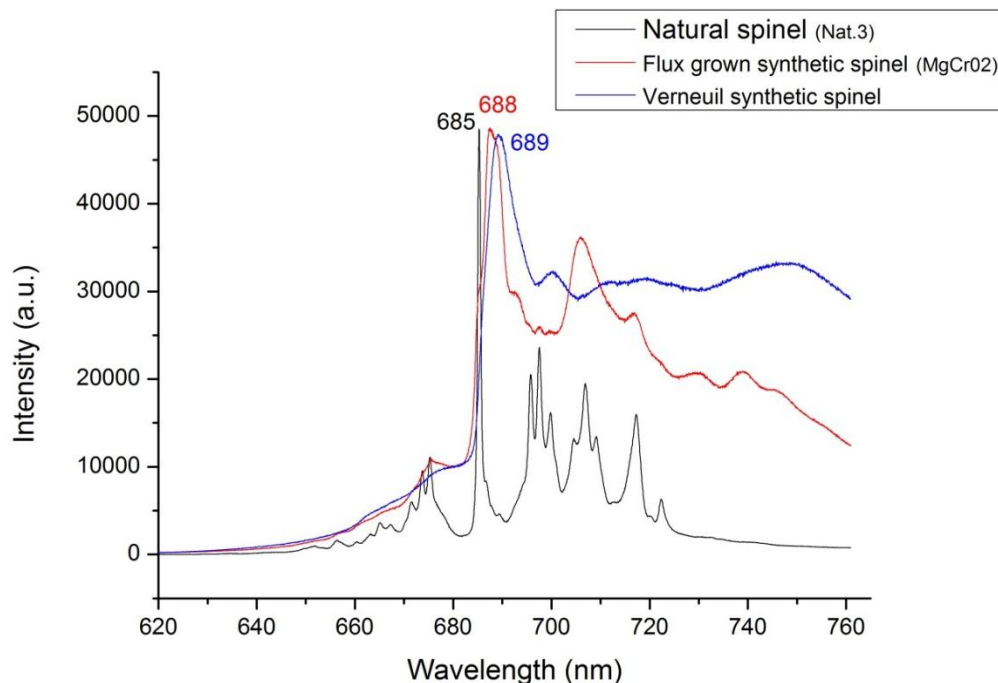


Fig. 4.67. Photoluminescence spectra of a natural (black line), flux grown (red line) and Verneuil (blue line) synthetic spinels.

In Verneuil synthetic spinels the broadening and shift are more marked due to the presence of irregularities and defects in their crystal lattice, such as an excess of Al. Similar observations in PL spectra have been reported for heat-treated spinels.

Different position of the R and N lines is shown by the samples with spinel s.s. and gahnite composition (Fig. 4.68). The R line of all the spinels with spinel s.s. composition appears at ~685.5 nm, whereas the R line of all the spinels with gahnite composition appears at ~686.7 nm. The shift in the position of the entire spectrum maybe is due to the differences in the spinel structure in terms of both cation disorder and chemical composition.

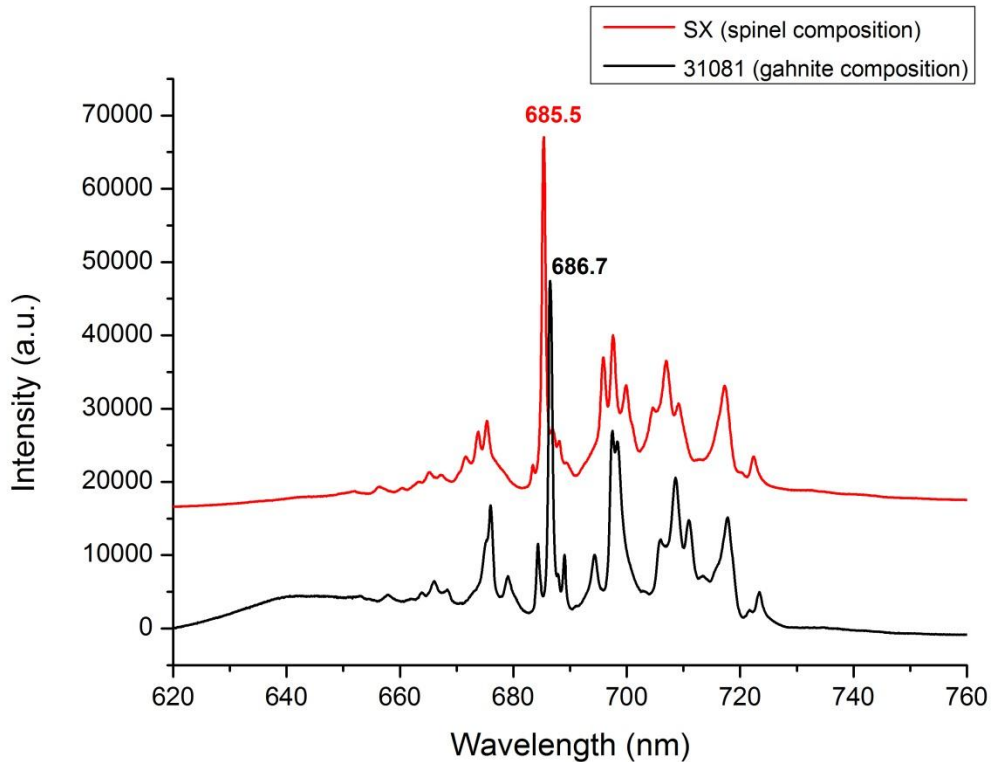


Fig. 4.68. PL spectra of Cr³⁺ in a natural spinel with a spinel s.s. composition (red line) and a natural spinel with a gahnite composition (black line).

4.5 A multi-analytical study of a natural blue gahnite (ZnAl_2O_4)

Gahnite, ideally ZnAl_2O_4 is generally assumed to be a normal spinel regardless of temperature, with Zn ordered at the T site and Al at the M site, due to the strong preference of Zn for the tetrahedral coordination. End-member gahnite has not been observed in nature so far. Several Zn-rich gahnite minerals approaching the ideal composition have been reported (ZnAl_2O_4 component 94.5% Hicks et al., 1985; 96.6% Yalçin et al., 1993; 98.7% Henry and Dutrow, 2001), but replacements by Fe^{2+} together with minor Mg^{2+} , Mn^{2+} , Fe^{3+} , Cr^{3+} commonly occur in natural samples (Spry and Scott, 1986a; Appel, 2000). Zincian spinel occurs as an accessory mineral in a large number of geologic settings like metamorphosed massive sulphide deposits (Spry, 1987; Sundblad, 1994; Heimann et al., 2005; Praveen and Ghosh, 2007), aluminous metasediments and metavolcanics (Frost, 1973; Spry and Scott, 1986b), granitic pegmatites and quartz veins (Gandhi, 1971; Jackson, 1982; Batchelor and Kinnaird, 1984; Morris et al., 1997), marbles and skarns (Novák et al., 1997), diasporites and metabauxites (Yalçin et al., 1993; Feenstra et al., 2003) and sulfide-bearing granulites (Visser et al., 1992).

Knowledge of the composition of zincian spinels is useful as an exploration guide to discriminate among a large variety of source environments. For example, Zn contents are high in spinels occurring in rocks that have experienced low-grade metamorphism and high oxygen and sulphur fugacity (f_{O_2} and f_{S_2}), whereas Zn contents are lowest in high-grade metamorphic rocks (Heimann et al., 2005). Transparent natural gahnite can be used as gemstone because of its attractive range of colors from colorless to grey, blue and green depending on its Fe-content, oxidation state and cation site occupancy (Schmetzer and Bank, 1985).

Synthetic zinc aluminate spinel is transparent for wavelengths greater than 320 nm, is highly reflective at wavelengths lower than 300 nm and possesses high thermal stability, low surface acidity, and high mechanical resistance. Due to its physical and optical properties, synthetic ZnAl_2O_4 has been widely used as wide-gap semiconductor (energy band gap ~ 3.8 eV), as catalysts in various chemical and petrochemical industries and in ultraviolet photoelectronic devices and reflective optical coatings in aerospace applications. It was proposed also as an important phosphor host material for applications in thin film electroluminescent

displays and stress imaging devices (Valenzuela et al., 1997; Sampath and Cordaro, 1998; Van der Laag et al., 2004).

In spite of the abundance of studies on the chemistry and petrogenesis of natural gahnite and on the physical properties of synthetic zinc aluminate spinel, a comprehensive, multianalytical characterization of a natural zincian spinel is very rarely found, especially for compositions approaching the gahnite end-member. In this study a natural gem-quality, inclusion free, single crystal of zinc aluminate spinel from the Jemaa district, Kaduna State (Nigeria), was studied. The sample, labelled Ni8967c, belongs to the mineral collection of the Museum of Earth Sciences, University of Bari. The crystal displays a pale blue-grey color, octahedral habitus and its dimensions are 2.5 mm x 2.7 mm x 2.3 mm (Fig. 4.69).



Fig. 4.69. The natural pale blue-grey single crystal gahnite (Ni8967c) from Jemaa, Nigeria.

Natural blue gahnite crystals from Jemaa (Nigeria) were previously described for gemological purposes by Jackson (1982), but they were not fully characterized.

The single crystal gahnite Ni8967c was fully characterized by electron microprobe, single-crystal X-ray diffraction, Raman and optical absorption spectroscopies and the results were published in the *Mineralogical Magazine* (D'Ippolito et al., 2013).

4.5.1 Chemical and structural characterization

The Nigerian gahnite Ni8967c is chemically homogenous and shows a composition very close to that of the end-member gahnite, with ~94 mol-% of the $ZnAl_2O_4$ component. The remaining composition is dominated by the hercynite

component (FeAl_2O_4), with very minor content of Mn^{2+} and Mg. On the basis of charge-balance requirements and the spinel stoichiometry (3 cations per 4 anions), a small amount of Fe^{3+} (0.012 apfu) was also calculated (Table 4.21).

Table 4.21. Chemical composition of the Nigerian gahnite obtained by electron microprobe. The FeO and Fe_2O_3 contents were calculated on the basis of charge-balance requirements.

| Sample | Ni8967c |
|---|----------------|
| Al_2O_3 | 55.5(4) |
| MnO | 0.11(3) |
| FeO_{tot} | 2.95(6) |
| FeO_{calc} | 2.43 |
| $\text{Fe}_2\text{O}_3_{\text{calc}}$ | 0.52 |
| ZnO | 41.7(4) |
| MgO | 0.03(1) |
| Total | 100.29 |
| Cations normalized to 4 oxygen atoms | |
| Al | 1.987(3) |
| Fe^{3+} | 0.012(1) |
| Fe^{2+} | 0.062(1) |
| Mn | 0.003(1) |
| Zn | 0.935(4) |
| Mg | 0.001(1) |
| Total | 3.000 |

Notes: digits in brackets are estimated uncertainties (1σ): for reported oxide concentrations, they represent standard deviations of several analyses on the crystal, while, for cations, they were calculated according to error propagation theory.

Silicon, Ti, V, Cr, Ni and Co were not detected. The Nigerian mineral gahnite Ni8967c is one of the Zn-richest spinel samples studied so far, as it is evident from a comparison with the other zincian spinels described in literature (Fig. 4.70).

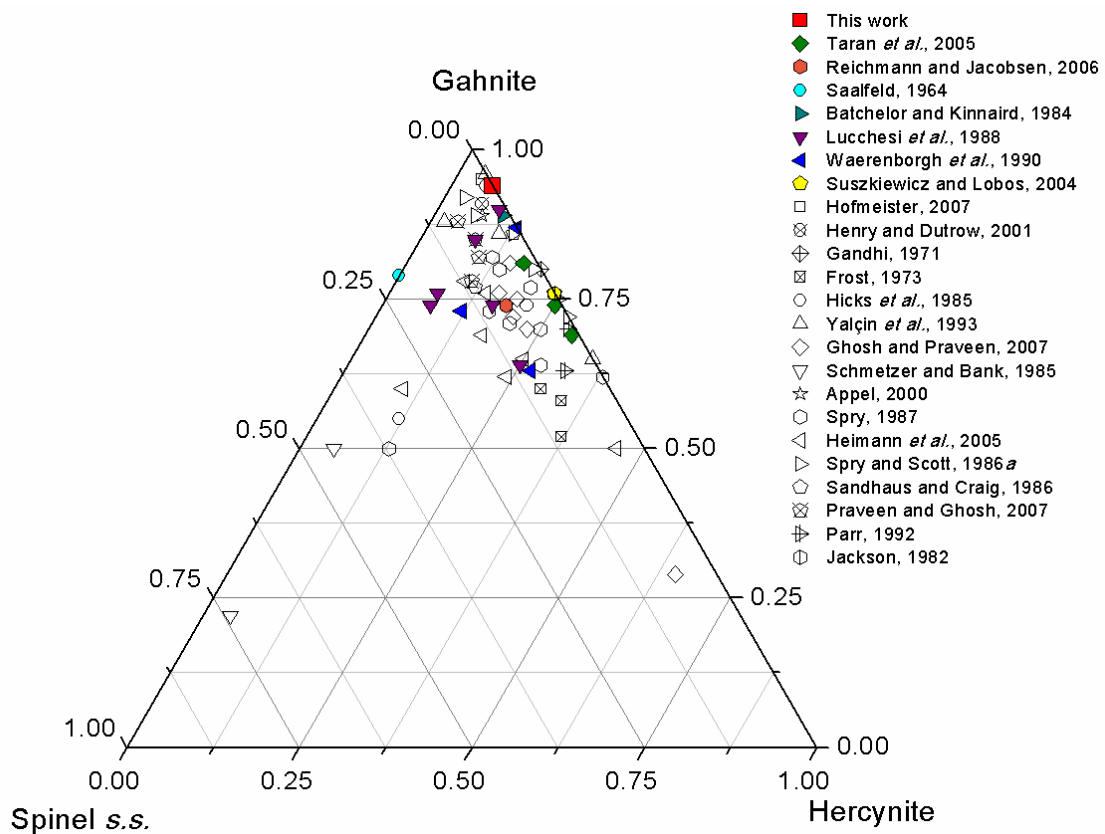


Fig. 4.70. Composition of the Nigerian gahnite Ni8967c and of zincian spinels reported in the literature: triangular plot in terms of gahnite, hercynite and spinel components. Red square: this work; color symbols: chemical composition of zincian spinel also characterized by structural and/or spectroscopic analyses.

In accordance with the division of the paragenetic regimes defined by Spry and Scott (1986b) and Heimann *et al.* (2005), the composition of the Nigerian gahnite falls within the field of granitic pegmatites and that of diasporites and metabauxites (Fig. 4.71). On the other hand, in agreement with Jackson (1982), the Ni8967c sample can be ascribed to the former field. In fact, the latter author reported that the gahnite samples from Jemaa (Nigeria) occur in a pegmatite complex 3.2 km NNW of Jemaa. The hypothesis that gem-quality gahnite occurred as an accessory phase disseminated in pegmatites and quartz-sillimanite veins of late Pan-African age (450-500 Ma) in central Nigeria was also proposed by Batchelor and Kinnaird (1984) for another blue-grey gem-quality gahnite.

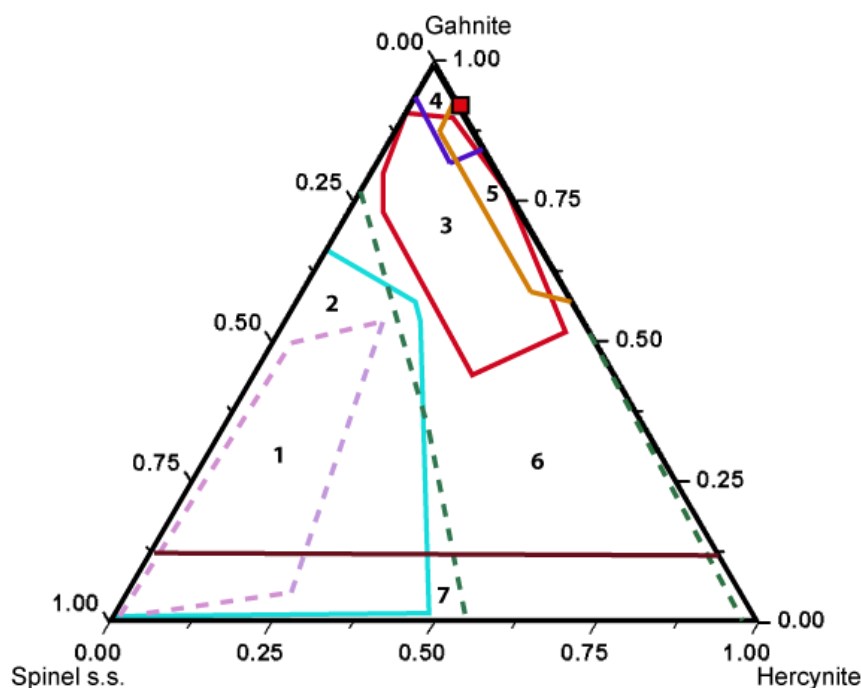
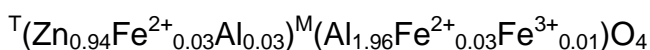


Fig. 4.71. Zincian spinel composition in relation to paragenesis (redrawn from Heimann et al., 2005): 1) Marbles; 2) Metamorphosed massive sulfide deposits and S-poor rocks in Mg-Ca Al alteration zones; 3) Metamorphosed massive sulfide deposits in Fe-Al metasedimentary and metavolcanic rocks; 4) Diasporites and metabauxites; 5) Granitic pegmatites; 6) Unaltered and hydrothermally altered Fe-Al-rich metasedimentary and metavolcanic rocks; 7) Al-rich granulites. Red filled square shows the chemical composition of the Nigerian gahnite Ni8967c.

The cation distribution at the T and M sites of the investigated Nigerian gahnite was optimized by using a least-squares program to minimize the residuals between calculated and observed data (e.g., m.a.n. and bond distances). Octahedral and tetrahedral bond lengths (M-O and T-O, respectively) were calculated as the linear contribution of each cation multiplied by its specific bond length, the latter refined on the basis of analysis of more than 250 spinel structural data from the literature (Lavina et al., 2002). However, the bond length of 1.949(1) Å was used for $^T\text{Zn-O}$, following Bosi et al., (2011) who showed that the $^T\text{Zn-O}$ value varies as a function of the M site population, increasing from 1.949 Å (for ^MAl) to 1.980 Å (for $^M\text{Fe}^{3+}$).

The empirical structural formula of the investigated Nigerian gahnite was optimized by constraining the small amounts of Fe^{3+} at M, in accord with the optical absorption spectroscopy results (see later), and the result is:



where very small amounts of Mg and Mn^{2+} (< 0.005 apfu) occur at T. Such a formula shows Zn and Al strongly ordered at T and M (respectively), and a very low degree of inversion (0.03) due to the cation exchange $Fe^{2+} \leftrightarrow Al$ of the hercynite component. The presence of elements other than Zn and Al in the gahnite structure is considered to possibly cause very small departures from a completely normal cation distribution (Waerenborgh et al., 1994; Lucchesi et al., 1998). In particular, the inversion of Fe^{2+} and Al in hercynite was proved to increase with temperature from 0.15 at 800 °C to 0.22 at 1150 °C for synthetic $FeAl_2O_4$ end-member (Harrison et al., 1998, Andreozzi and Lucchesi, 2002). On the contrary, the cation distribution of gahnite is very weakly dependent on temperature, as shown by Cooley and Reed (1972) and O'Neill and Dollase (1994) for synthetic $ZnAl_2O_4$ end-member, and by Andreozzi et al. (2001a) for synthetic $(Zn,Mg)Al_2O_4$: the inversion only increases from 0.00 at 800 °C to 0.06 at 1400 °C.

In summary, the cation distribution of the Nigerian gahnite Ni8967c is most likely due to its thermal history, but it was also modulated by its bulk composition.

The unit-cell parameter value of the Nigerian gahnite is 8.0850(3) Å. This value is lower than those of the natural spinels studied in literature and is very close to those reported for the synthetic end-member $ZnAl_2O_4$ (Fig. 4.72). Small deviations from the approximately linear, decreasing trend can be due to the variation in chemical composition as well as in inversion degree.

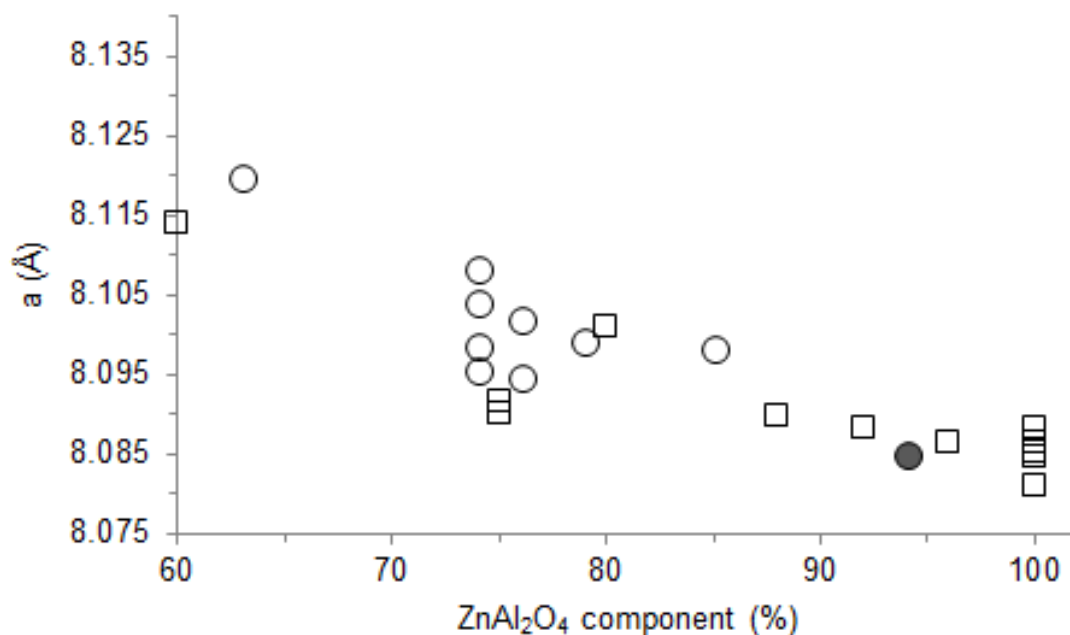


Fig. 4.72. Zn-rich spinels: *a* cell parameter vs ZnAl_2O_4 component. Full circle: the Nigerian gahnite Ni8967c; Open circles: natural samples from literature (Saalfeld, 1964; Batchelor and Kinnaird, 1984; Waerenborgh et al., 1990; Lucchesi et al., 1998; Suszkiewicz and Lobos, 2004; Reichmann and Jacobsen, 2006); Open squares: synthetic spinels reported in literature (O'Neill and Dollase, 1994; Waerenborgh et al., 1994; Gaudon et al., 2009; Popović et al., 2009; Ardit et al., 2012).

The unit-cell parameter depends on the tetrahedral and octahedral bond lengths according to the equation 1 in the Chapter 1.

The T-O and M-O distances obtained from Nigerian gahnite are 1.9485(6) and 1.9137(3) Å, respectively. Such distances are strictly related to cation radii at T and M sites. Natural gahnite samples studied in detail by structural investigation (Waerenborgh et al., 1990; Lucchesi et al., 1998) have Zn and Al contents lower than the present Nigerian sample, the former substituted by Mg, Fe^{2+} and Mn^{2+} , and the latter by Fe^{3+} . As a consequence of the difference among the ionic radii ($\text{Mn}^{2+} > \text{Fe}^{2+} > \text{Mg} > \text{Zn}$; $\text{Fe}^{3+} \gg \text{Al}$), those samples show larger T-O and M-O bond distances (and thus also higher unit-cell parameter values) than our sample. Furthermore, as reported above, Bosi et al. (2011) showed that $^{\text{T}}\text{Zn-O}$ bond-length value is strongly affected by the cation population at the M site, so that in natural gahnite samples $^{\text{T}}\text{Zn-O}$ increases with increasing substitution of Fe^{3+} for Al at M.

4.5.2 Spectroscopic characterization

According to group theory, gahnite should exhibit five Raman active modes: $A_{1g}(R) + E_g(R) + 3F_{2g}(R)$.

A strong fluorescence was observed, but in spite of this, of the five Raman-active modes of the gahnite the two most characteristic and intense were recorded with the blue laser (Fig. 4.73).

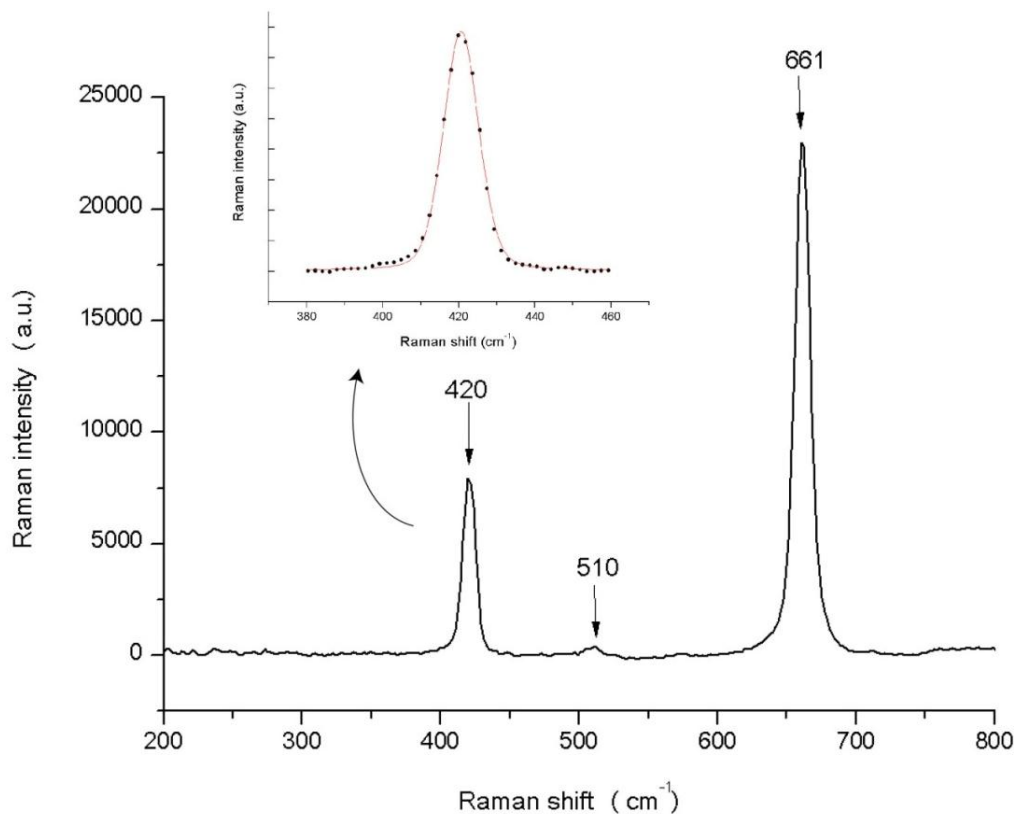


Fig. 4.73. Raman spectrum collected with the blue (473.1 nm) line of the Nd:YAG laser of the natural Nigerian gahnite sample Ni8967c and a detail of the 420 cm⁻¹ peak, symmetric Gauss-Lorentzian (pseudo-voigt) curve fitting.

The observed peaks are ascribable to the E_g mode at 420 cm⁻¹ and the high-frequency F_{2g} mode at 661 cm⁻¹. In addition, the small peak at 510 cm⁻¹ might be assigned to the medium-frequency F_{2g} mode. These modes are in agreement in frequency with the measurements on natural gahnite and the calculations made using different models reported in literature (Table 4.22).

Table 4.22. Comparison between experimental and calculated frequencies (cm^{-1}) of the Raman modes in the cubic spinel structure of ZnAl_2O_4 .

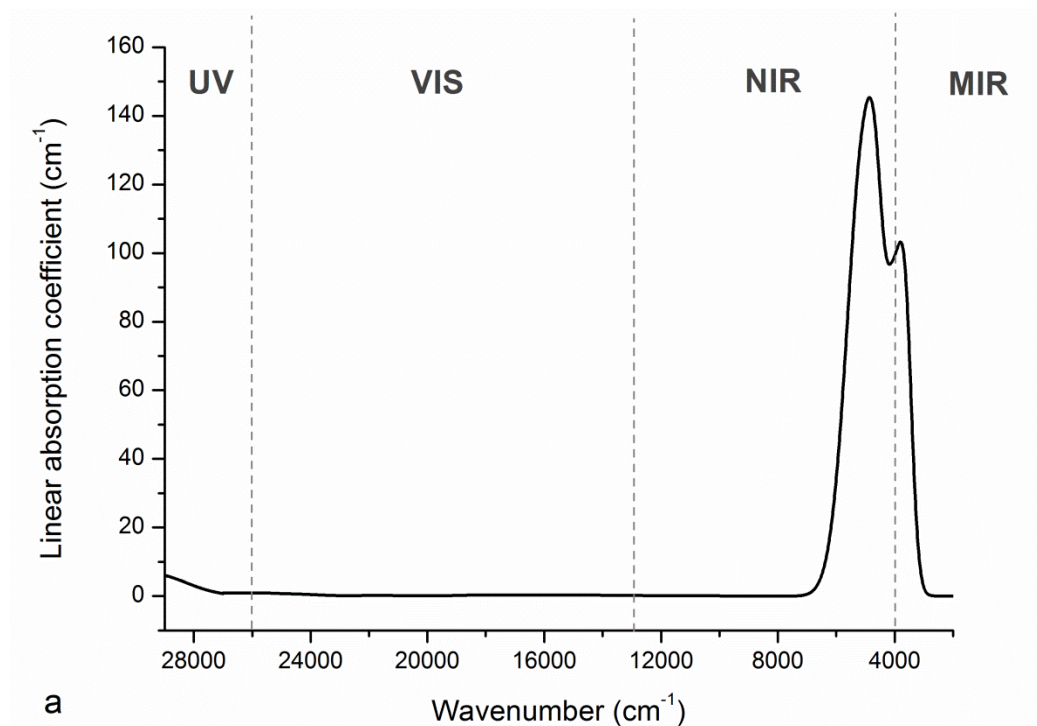
| Modes | This work | Chopelas and Hofmeister (1991) | Fang et al. (2002) | López-Moreno et al. (2011) |
|-------------|-----------|--------------------------------|--------------------|----------------------------|
| | Exp. | Exp. | Theory | Theory |
| $F_{2g}(1)$ | n.d. | 196 | 197 | 194 |
| E_g | 420 | 417 | 442 | 427 |
| $F_{2g}(2)$ | 510 | 509 | 520 | 513 |
| $F_{2g}(3)$ | 661 | 658 | 665 | 655 |
| A_{1g} | n.d. | 758 | 784 | 775 |

Note: n.d.- not detected

The partial Phonon Density of States of ZnAl_2O_4 calculated by Fang et al. (2002) and López-Moreno et al. (2011) shows that the low-frequency motions are mainly due to Zn ions ($< 250 \text{ cm}^{-1}$), while the phonon modes with frequencies over 250 cm^{-1} are due to O and Al, with a major contribution of O than Al. For example, the higher-frequency F_{2g} mode is due to the motions of oxygen atoms (breathing mode) inside the AlO_6 octahedra. No evidence was observed for the 727 cm^{-1} band assigned by Cynn et al. (1992) to the vibration of AlO_4 tetrahedra, and thus to the structural disorder; this is in agreement with the very low inversion degree obtained for the Nigerian gahnite. Indeed, also the E_g band at 420 cm^{-1} doesn't show the asymmetry typical of the disordered spinel. In fact the symmetric Gauss-Lorentzian (pseudo-voight) curve fitting of the 420 cm^{-1} peak shows an R^2 of 0.9983, indicating a negligible asymmetry (Fig. 4.73).

The recorded UV-VIS-NIR-MIR spectra show a very intense absorption band in the NIR range centered at $\sim 5000 \text{ cm}^{-1}$ (Fig. 4.74a). It has been assigned, as already described above, to spin allowed $d-d$ transitions ${}^5E \rightarrow {}^5T_2$ in Fe^{2+} located at the T sites. The best fitting model of the ${}^T\text{Fe}^{2+}$ -absorption envelope in the interval $2500\text{-}9000 \text{ cm}^{-1}$ was obtained by applying a four-band model, with the bands centred at 4952, 4742, 4095 and 3675 cm^{-1} (Fig. 4.74b). The ${}^T\text{Fe}^{2+}$ maximum

absorption band at 4952 cm^{-1} is shifted towards lower energies with respect to the analogous band observed at $\sim 5200\text{ cm}^{-1}$ in the spectra of spinel-hercynite series by Skogby and Hålenius (2003). Indeed, in the spectra of magnesiochromite-chromite series studied by Lenaz et al. (2004) the analogous band is shifted towards even lower energies, at $\sim 4700\text{ cm}^{-1}$. Notably, the observed band position is inversely correlated with the T-O bond distances, i.e., T-O is 1.949 \AA in the Nigerian gahnite and is 1.922 \AA and 1.966 \AA for the analogous synthetic spinels (containing 0.04 apfu of TFe^{2+}) in the $\text{MgAl}_2\text{O}_4\text{-FeAl}_2\text{O}_4$ and $\text{MgCr}_2\text{O}_4\text{-FeCr}_2\text{O}_4$ series, respectively. In addition, the population of the adjacent M sites and the role of the inversion cannot be ignored, as M is occupied by Al in the investigated gahnite, by Cr in the $\text{MgCr}_2\text{O}_4\text{-FeCr}_2\text{O}_4$ series and by a combination of (Al,Mg) in the $\text{MgAl}_2\text{O}_4\text{-FeAl}_2\text{O}_4$ series. This confirms the strong influence of the next-nearest neighbors on the optical absorption transitions.



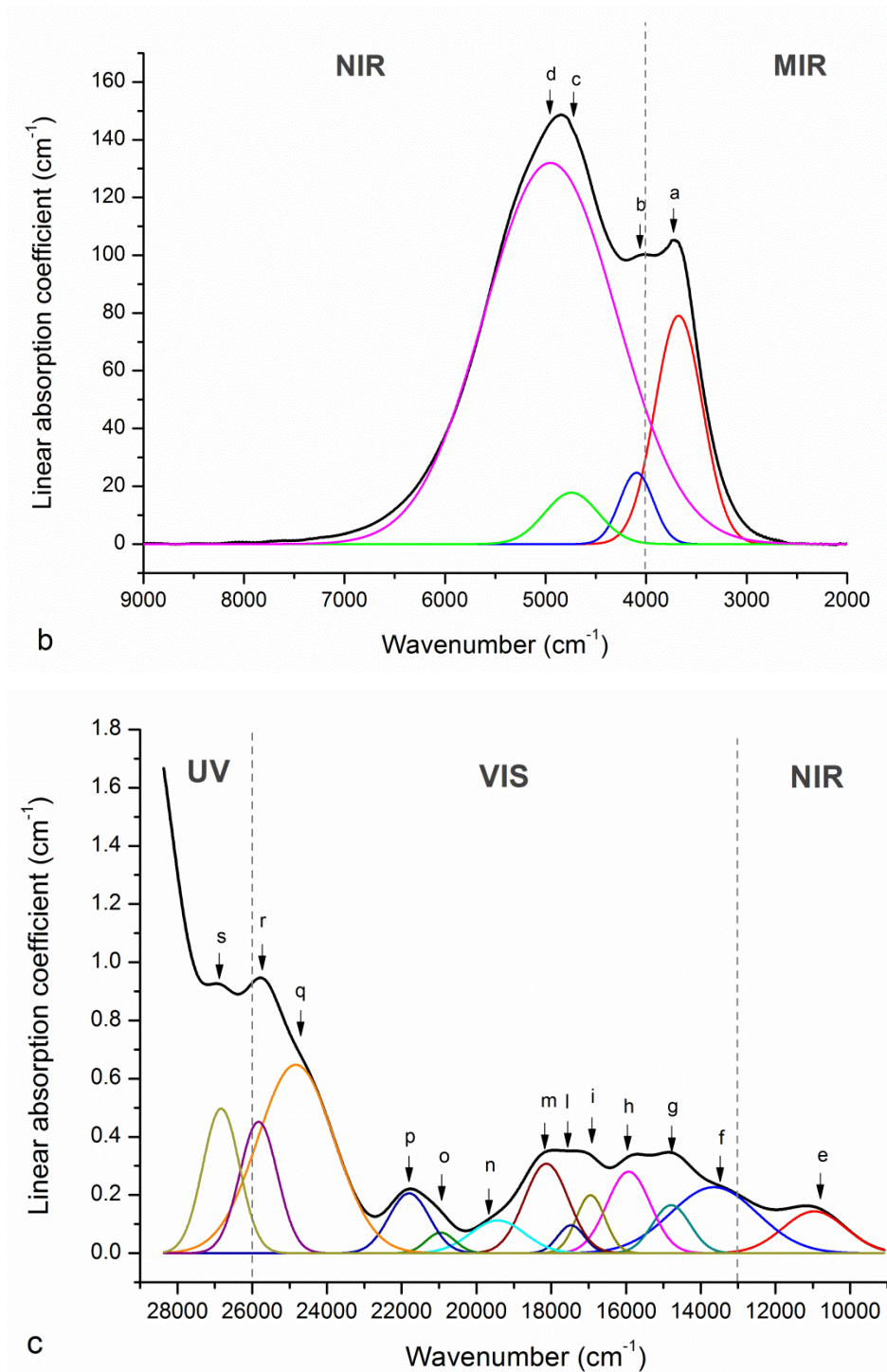


Fig. 4.74. Single-crystal spectra of the Nigerian gahnite Ni_{8967c} in the UV-VIS-NIR-MIR range: a) the entire spectrum from 29000 cm⁻¹ to 2000 cm⁻¹; b) curve resolved spectrum in the spectral range 9000-2000 cm⁻¹; c) curve resolved spectrum in the spectral range 29000-9000 cm⁻¹. Many small absorption bands, especially in the visible region, are hidden from the intense bands in the infrared region.

Between the UV-edge and the high-energy wing of the NIR-band, i.e., centered in the VIS range, a series of very weak absorption bands occurs. They are strongly

superimposed, and 13 Gaussian curves were necessary for a satisfactory fit (Fig. 4.74c). The origin of these bands has already been addressed above in the description of the blue spinels. Of the previously discussed absorption bands, those belonging to the VIS region (i.e., those named from *f* to *r* in Fig. 4.74c) are obviously responsible for the pale blue-grey color exhibited by the Nigerian gahnite. Accordingly, the blue-grey hue of the investigated Nigerian gahnite is mainly due to spin-forbidden electronic transitions in TFe^{2+} and to $MFe^{2+} \leftrightarrow MFe^{3+}$ IVCT, as also described by Schmetzer et al. (1989). Indeed the poor saturation of the color is due to the low concentration of both Fe^{2+} and Fe^{3+} . In general, the color of gahnite is highly sensitive to small variations in the Fe oxidation state. As for example, Jackson (1982) noted that on heating to 1000°C in an oxidizing atmosphere, a blue Nigerian gahnite changed to a permanent blue-green color, becoming olive green at 1400°C.

Chapter 5

CONCLUSIONS AND IMPLICATIONS

Natural and synthetic spinel single crystals were analyzed by a combined chemical, structural and spectroscopic approach in order to investigate the optical and vibrational properties.

5.1 Optical properties

An accurate characterization by EMPA, XRD-SC and OAS of synthetic spinels belonging to the MgAl_2O_4 - CoAl_2O_4 solid solution was made. The structural study shows a variation of the unit-cell parameter a from 8.084 to 8.105 Å mainly due to the variations in Al content at the T site. In fact, considering that the size of Mg and Co^{2+} at the T site is very similar, the only steric effect may account for variations in Al ordering. The optical study shows that Co-spinel strongly absorbs the light in the 18000-16000 cm^{-1} region of the visible spectrum. This absorption is due to Co^{2+} in the tetrahedrally coordinated sites and causes the typical blue coloration of the Co-spinel. A good correlation between the linear absorption coefficient value of the maximum absorption band at $\sim 17000 \text{ cm}^{-1}$ and the $^{\text{T}}\text{Co}^{2+}$ content is obtained. Even at very low concentrations of Co^{2+} the absorption is strong enough to cause a blue bright color. The absence of color shift and the perceived intensification of blue color of the crystals along the series is also underlined by the insignificant changes of the Dq parameter and the constancy of local Co^{2+} -O bond distances within the present spinel series. This behavior is explained by considering that the MgAl_2O_4 - CoAl_2O_4 series is characterized by the very similar size of Mg and Co^{2+} , the ionic bonding and the Co^{2+} in the high-spin state.

Optical properties of about thirty natural spinels coming from different geological environment were examined. These spinels show different chemical composition and color. From the chemical characterization most of them exhibit a prevalent spinel s.s. component (MgAl_2O_4), whereas the others show a prevalent gahnite (ZnAl_2O_4) component. The different colors do not depend on the main

composition. In fact, while the samples having a gahnitic composition show colors close to the blue hue, the samples having a spinel s.s. composition show all kind of colors from pink to orange to blue. The optical characterization show that the color of most of the natural spinels examined is caused by a combination of two or more minor elements such as Cr^{3+} , V^{3+} , Fe^{2+} , Fe^{3+} and Co^{2+} , occupying tetrahedrally (T) and/or octahedrally (M) coordinated sites in the spinel structure. The absorption bands related to every color were determined. Red, orange and magenta spinels owe their color mainly to the presence of Cr^{3+} and V^{3+} in the M sites which absorb the light in the violet-blue ($\sim 25500 \text{ cm}^{-1}$) and green regions ($\sim 18500 \text{ cm}^{-1}$) of the visible spectrum. The absorption sub-spectra of Cr^{3+} and V^{3+} are superimposed. When the contents of Cr^{3+} predominate on the contents of V^{3+} , the spinels appear as red. When the contents of V^{3+} predominate on the contents of Cr^{3+} , the band at $\sim 25500 \text{ cm}^{-1}$ broadens, this provoking a greater absorption of the violet and blue with respect to green regions of the visible spectrum and the spinels appear as orange. The magenta spinels have considerable content of Cr and secondary amount of Fe that shows a low-energy wing of the UV absorption band due to LMCT $\text{O}^{2-} \rightarrow \text{Fe}^{2+}$ and a red shift of the band at $\sim 18500 \text{ cm}^{-1}$.

All the pink, blue and dark green spinels, in spite of showing very different colors, have similar absorption spectra characterized by a strong UV-edge absorption at energy $\gg 30000 \text{ cm}^{-1}$ and series of weak absorption bands in the visible range. The strong UV-edge absorption is due to the $\text{O}^{2-} \rightarrow \text{Fe}^{2+}$ and $\text{O}^{2-} \rightarrow \text{Fe}^{3+}$ charge transfer transitions and causes a strong absorption of the violet and blue component of the visible light. The main differences among the spectra of the pink, blue and green spinels are: an increase of the intensity of the strong UV-edge absorption at energy $\gg 30000 \text{ cm}^{-1}$ from the pink to the green samples; a different position of the most intense peak occurring in the range 20000 and 10000 cm^{-1} . The peak of maximum absorption moves from 18000 cm^{-1} for the pink spinels to 15500 cm^{-1} for the green spinels, and the blue spinels show an intermediate situation. The variation is caused by the increase of the iron total content and thus also of the Fe^{3+} content. In fact, the band at 15500 cm^{-1} in the green samples is due to the Fe^{2+} - Fe^{3+} interaction.

LA-ICP-MS analysis has revealed that some natural blue spinels, especially with gahnite as the main component, show trace amounts of Co^{2+} . These spinels have the same absorption bands of the synthetic cobalt spinel and have an intensity of linear absorption coefficient comparable to that calculated from the linear regression obtained for the synthetic ones. Hence, cobalt, in spite of its very small concentrations (in the range of 0.002-0.001 apfu), is able to influence the color in natural spinels.

5.2 Vibrational properties

Vibrational properties of three synthetic solid solutions $(\text{Mg,Co})\text{Al}_2\text{O}_4$, $(\text{Mg,Fe})\text{Al}_2\text{O}_4$ and $(\text{Mg(Al,Cr)})_2\text{O}_4$ were investigated by Raman spectroscopy in order to determine relationships between the Raman active modes and spinel crystal chemistry. The collected polarized spectra and the advantage of having many Raman spectra along each series were useful to assign every Raman peak to one or more vibration in the spinel structure.

All the Raman spectra recorded show the predicted five Raman-active modes and an additional peak between the $F_{2g}(3)$ and A_{1g} modes which can be attributed to the cation disorder.

The Raman spectra of the spinel samples belonging to the MgAl_2O_4 - CoAl_2O_4 series show an one-mode behavior with the exception of the $F_{2g}(2)$ mode which shows a two-mode behavior. A continuous and monotonous shift of the Raman modes of the $F_{2g}(3)$ and the $F_{2g}(2)$, toward lower Raman shifts is observed with the increase of the cobalt content. The A_{1g} mode shows an increase of the Raman shift with the increase of the Co content, while all the remaining modes essentially maintain the same position. A good correlation between the $F_{2g}(2)$ mode shift and the Co content was found. Moreover, the A_{1g} mode is linearly related to the unit cell parameter and can be usefully exploited to obtain structural information.

The spinels belonging to the MgAl_2O_4 - FeAl_2O_4 series show two different behaviors. At the beginning of the Fe^{2+} -Mg substitution no spectral variations are observed; after the Fe component is higher than 20% a marked Raman shift

decrease is observed. A good correlation is found between the A_{1g} mode and the ratio $Fe/(Mg+Fe)$ for the iron composition higher than 20%.

The Raman spectra of the spinels belonging to the $MgAl_2O_4$ - $MgCr_2O_4$ series show an one-mode behavior for all the modes with exception of the E_g which shows a two-mode behavior. The relative intensity of the E_g mode at $\sim 400\text{ cm}^{-1}$ and $\sim 440\text{ cm}^{-1}$ can give information about the predominant Al or Cr end-member, respectively. Also for this series, initially the spinels do not respond to the $Cr^{3+} \rightarrow Al^{3+}$ substitution but then a rapid decrease of the frequencies is perceived. The A_{1g} mode can be related to the ratio $Cr/(Cr+Al)$ in order to obtain chemical information from the Raman spectra. In addition, the local Cr-O bond distance in the octahedrally coordinated sites proves information on the structural relaxation.

As a relevant conclusion, the relationships between Raman active modes and spinel principal component were established. This makes possible distinguishing each end-member from a characteristic fingerprint. In particular, from the position of the A_{1g} mode it is possible to distinguish between spinel chromates and aluminates. However, discrimination among spinels with the same principal component and different minor elements, which cause the difference in colors, is not straightforward and requests more studies.

Moreover, the detailed Raman study gave information about the cation disorder and then the genesis temperatures. Finally, a study of the fluorescence features attributed to chromophoric ions observed in the Raman spectra helped to distinguish between natural, thermally-treated, and synthetic materials.

5.3 Implications

The accurate spectroscopic study of the origin of color in materials with the spinel structure is crucial to improve the technological performance of existing ceramic pigments and/or to create new pigments. For example, no evidences of V-spinels exploited as pigments are found in literature and Cr and V spinel-based pigments could be patented.

Iron spinel is widely used in the ceramic pigment industry, and a detailed study of the change in the optical spectra will help to improve the synthesis conditions in order to obtain pink, blue or green pigments.

Cobalt spinel (CoAl_2O_4) is also widely used in ceramics industry, together with cobalt olivine (Co_2SiO_4). However, the increasing price and limited availability of cobalt raw materials have made important to minimize the Co content and to enhance its coloring performance and stability in a wide spectrum of ceramic glazes. In recent years, extensive research has been conducted to develop new pigments by doping white or colorless materials with efficient chromophores, in order to lower as much as possible the cobalt consumption. The gahnite (ZnAl_2O_4) and willemite (Zn_2SiO_4) structures have been pointed out as interesting host lattices, since nice and intense blue colors can be produced with very low Co doping. There are few studies in literature on blue pigments based on spinel s.s. (MgAl_2O_4) structure (Ahmed et al. 2009; Duan et al., 2004). The Co spinels studied in the present work prove that the spinel s.s. is an excellent host lattice, provoking an intense blue color with very low Co concentrations. In addition, the spinel s.s. has a high melting point (greater than gahnite) and is both thermally stable at high temperatures and chemically stable in molten glazes. Hence, Co doped spinels are candidate to be new blue pigments with very low Co content.

Furthermore, Co-rich natural spinels were already found in nature but none of these has yet been proposed to the IMA committee as new mineral. The complete and detailed characterization of the synthetic spinels belonging to the MgAl_2O_4 - CoAl_2O_4 series presented in this work will help recognizing the occurrence of Co spinel in nature by knowing in advance structural and spectroscopic features.

Concerning the vibrational properties, an original empirical approach for the assignment of the Raman modes in spinel spectra was defined. The application of this new approach has relevant consequences for both geological and analytical purposes, as for example study of inorganic pigments used in historical art. In fact, Raman spectroscopy has become a routine technique for identification of materials and minerals, without necessarily knowing the structural origin of the

individual spectral peaks. Hence, this detailed Raman characterization of spinel end-members is useful for identifying what kind of spinel a rock or a pigment contain. Notably, this can be done by using a simple portable and non-destructive Raman spectrometer. Moreover, the availability of miniaturized Raman devices, together with the expansion of the spinel Raman spectra database, is candidate to acquire increasing importance for the extraterrestrial exploration.

Raman spectral features are already used to discriminate untreated spinel gemstones from treated or synthetic ones in the gemological field, but they could be also useful to investigate *in situ* spinel inclusions in diamonds with the aim to extract information in situ on their crystallization environment and contribute to define mantle composition and physical properties.

Acknowledgments

First and foremost I would like to express my special appreciation and thanks to my supervisor, Prof. Giovanni B. Andreozzi. I would like to thank him for his support and dedication, for encouraging my research and for allowing me to grow as a research scientist through many interesting and fundamental experiences. I appreciate all his contributions of time, ideas, and funding to make my Ph.D. experience productive and stimulating.

I am also thankful to Dr. Ferdinando Bosi for his useful comments, remarks and suggestions during these years. In addition, I would like to thank him for recording all the XRD-SC and for helping me understand the results.

Thanks to the SYNTHESYS program (grant SE-TAF-2090) and to Prof. Ulf Hålenius for giving me the opportunity to study spinels coming from the Swedish Museum of Natural History, Stockholm. Moreover, I'm grateful to him and Prof. Henrik Skogby for their assistance and for giving me the opportunity to use their UV-VIS-NIR and NIR-MIR spectrometer.

I would like to express my gratitude to Marcello Serracino and Marco Albano to the kind assistance and support for the chemical analyses through the EMPA and SEM/EDS.

I would like to acknowledge Prof. Pier Paolo Lottici and Dr. Danilo Bersani for allowing the Raman measurements at the Physics and Earth Sciences department of the University of Parma. Thanks also to Danilo Bersani and Luciana Mantovani for their support during the Raman analysis and for teaching me the Raman basis. I would not have understood the instrument and grasped the concepts of vibrational spectroscopy as quickly as I did without their help.

Thanks and appreciation to Alberto Scarani for helping me in the interpretation of the PL spectra and for giving me the opportunity to use his innovative Raman spectrometer.

I express my gratitude also to Prof. Detlef Günther and Kathrin Hametner for the quickly recording of the LA-ICP-MS analysis despite their large amount of tasks.

Thanks and gratitude to Michele Macri and all the private gem collectors who allowed expanding my range of samples.

Finally, I gratefully acknowledge to Prof. Ulf Hålenius and Dr. Danilo Bersani for their brilliant comments and suggestions, greatly useful to make the final version of my PhD. Thesis more original.

References

- Abritta, T. and Blak, F.H. (1991) Luminescence study of $\text{ZnGa}_2\text{O}_4:\text{Co}^{2+}$. *Journal of Luminescence*, 48/49(2), 558–560.
- Ahmed, I.S., Shama, S.A., Moustafa, M.M., Dessouki, H.A., and Ali, A.A. (2009) Synthesis and spectral characterization of $\text{Co}_x\text{Mg}_{1-x}\text{Al}_2\text{O}_4$ as new nano-coloring agent of ceramic pigment. *Spectrochimica Acta Part A: Molecular and Biomolecular Spectroscopy*, 74(3), 665-672.
- Aizawa, H., Ohishi, N., Ogawa, S., Watanabe, E., Katsumata, T., Komuro, S., Morikawa, T., and Toba, E. (2002) Characteristics of chromium doped spinel crystals for a fiber-optic thermometer application. *Review of Scientific Instruments*, 73(8), 3089-3092.
- Allan, J.F., Sack, R.O., and Batiza, R. (1988) Cr-rich spinels as petrogenetic indicators; MORB-type lavas from the Lamont seamount chain, eastern Pacific. *American Mineralogist*, 73(7-8), 741-753.
- Andreozzi G.B. (1999) Synthetic spinels in the $(\text{Mg}, \text{Fe}^{2+}, \text{Zn}) (\text{Al}, \text{Fe}^{3+})\text{O}_4$ system: I. Flux growth of single crystals. *Periodico di Mineralogia*. 68 (1), 43-51.
- Andreozzi, G.B., and Lucchesi, S. (2002) Intersite distribution of Fe^{2+} and Mg in the spinel (sensu stricto)–hercynite series by single-crystal X-ray diffraction. *American Mineralogist*, 87(8-9), 1113-1120.
- Andreozzi, G.B., Lucchesi, S., Skogby, H., and Della Giusta, A. (2001a) Compositional dependence of cation distribution in some synthetic $(\text{Mg},\text{Zn})(\text{Al},\text{Fe}^{3+})_2\text{O}_4$ spinels. *European Journal of Mineralogy*, 13(2), 391-402.
- Andreozzi, G.B., Hålenius, U., and Skogby, H. (2001b) Spectroscopic active $^{\text{IV}}\text{Fe}^{3+}$ – $^{\text{VI}}\text{Fe}^{3+}$ clusters in spinel–magnesioferrite solid solution crystals: a potential monitor for ordering in oxide spinels. *Physics and Chemistry of Minerals*, 28(7), 435-444.
- Andreozzi, G.B., Princivalle, F., Skogby, H., and Della Giusta, A. (2000) Cation ordering and structural variations with temperature in MgAl_2O_4 spinel: An X-ray single-crystal study. *American Mineralogist*, 85(9), 1164-1171.

- Angeletti, C., Pepe, F., and Porta, P. (1977) Structure and Catalytic Activity of $\text{Co}_x\text{Mg}_{1-x}\text{Al}_2\text{O}_4$ spinel solid solutions. Part 1.—Cation distribution of Co^{2+} ions. *Journal of the Chemical Society, Faraday Transactions*, 1, 73, 1972–1982.
- Antretter, M., Fuller, M., Scott, E., Jackson, M., Moskowitz, B., and Solheid, P. (2003) Paleomagnetic record of Martian meteorite ALH84001. *Journal of Geophysical Research: Planets*, 108(E6), 5049.
- Appel, P.W.U. (2000) Gahnite in the ~3.75 Ga Isua Greenstone Belt, West Greenland. *Mineralogical Magazine*, 64(1), 121-124.
- Arai, T., Warren, P. H., Takeda, H. (1996) Four Lunar Mare Meteorites: Crystallization Trends of Pyroxenes and Spinel. *Meteoritics & Planetary Science*, 31(6), 877-892.
- Aramburu, J.A., García-Fernández, P., García-Lastra, J.M., Barriuso, M.T., and Moreno, M. (2013) Colour due to Cr^{3+} ions in oxides: a study of the model system $\text{MgO}:\text{Cr}^{3+}$. *Journal of Physics: Condensed Matter*, 25(17), 175501.
- Ardit, M., Cruciani, G., and Dondi, M. (2012) Structural relaxation in tetrahedrally coordinated Co^{2+} along the gahnite-Co-aluminate spinel solid solution. *American Mineralogist*, 97(8-9), 1394-1401.
- Areán, C.O., Mentrut, M.P., Platero, E.E., Xamena, F.X.L., and Parra, J.B. (1999) Sol–gel method for preparing high surface area CoAl_2O_4 and Al_2O_3 - CoAl_2O_4 spinels. *Materials Letters*, 39 (1), 22–27.
- Bahlawane, N., Ngamou, P.H.T., Vannier, V., Kottke, T., Heberle, J., and Kohse-Hoinghaus, K. (2009) Tailoring the properties and the reactivity of the spinel cobalt oxide. *Physical Chemistry Chemical Physics*, 11(40), 9224-9232.
- Ballhaus, C., Berry, R.F., and Green, D.H. (1991) High pressure experimental calibration of the olivine-orthopyroxene-spinel oxygen geobarometer: implications for the oxidation state of the upper mantle. *Contributions to Mineralogy and Petrology*, 107(1), 27-40.
- Barnes, S.J., and Roeder, P.L. (2001) The Range of Spinel Compositions in Terrestrial Mafic and Ultramafic Rocks. *Journal of Petrology*, 42(12), 2279-2302.
- Barpanda, P., Behera, S.K., Gupta, P.K., Pratihari, S.K., and Bhattacharya, S. (2006) Chemically induced order disorder transition in magnesium

- aluminium spinel. *Journal of the European Ceramic Society*, 26(13), 2603-2609.
- Batchelor, R.A. and Kinnard, J.A. (1984) Gahnite compositions compared. *Mineralogical Magazine*, 48(348), 425–429.
- Bauer, M., Davydovskaya, P., Janko, M., Kaliwoda, M., Petersen, N., Gilder, S., and Stark, R.W. (2011) Raman spectroscopy of laser-induced oxidation of titanomagnetites. *Journal of Raman Spectroscopy*, 42(6), 1413-1418.
- Bosi, F., Andreozzi, G.B., Hålenius, U., and Skogby, H. (2011) Zn-O tetrahedral bond length variations in normal spinel oxides. *American Mineralogist*, 96(4), 594-598.
- Bosi, F., Hålenius, U., and Skogby, H. (2009) Crystal chemistry of the magnetite-ulvöspinel series. *American Mineralogist*, 94(1), 181-189.
- Bosi, F., Hålenius, U., Andreozzi, G.B., Skogby, H., and Lucchesi, S. (2007) Structural refinement and crystal chemistry of Mn-doped spinel: A case for tetrahedrally coordinated Mn³⁺ in an oxygen-based structure. *American Mineralogist*, 92(1), 27-33.
- Bosi, F., Hålenius, U., D'Ippolito, V., and Andreozzi, G.B. (2012) Blue spinel crystals in the MgAl₂O₄-CoAl₂O₄ series: Part II. Cation ordering over short-range and long-range scales. *American Mineralogist*, 97(11-12), 1834-1840.
- Bosi, F., Lucchesi, S., and Giusta, A.D. (2002) Structural relationships in (Mn_{1-x}Zn_x)Mn₂O₄ (0 ≤ x ≤ 0.26): The “dragging effect”• of the tetrahedron on the octahedron. *American Mineralogist*, 87(8-9), 1121-1127.
- Bouchard, M., and Gambardella, A. (2010) Raman microscopy study of synthetic cobalt blue spinels used in the field of art. *Journal of Raman Spectroscopy*, 41 (11), 1477–1485.
- Burke, E.A.J. (2001) Raman microspectrometry of fluid inclusions. *Lithos*, 55(1–4), 139-158.
- Burns, R., 1993, *Mineralogical Applications of Crystal Field Theory*, Second Edition, Cambridge University Press, Cambridge, p 551.
- Caracas, R., and Banigan, E.J. (2009) Elasticity and Raman and infrared spectra of MgAl₂O₄ spinel from density functional perturbation theory. *Physics of the Earth and Planetary Interiors*, 174(1–4), 113-121.

- Carbonin, S., Martignago, F., Menegazzo, G., and Dal Negro, A. (2002) X-ray single-crystal study of spinels: in situ heating. *Physics and Chemistry of Minerals*, 29(8), 503-514.
- Carbonin, S., Russo, U., and Della Giusta, A. (1996) Cation distribution in some natural spinels from X-ray diffraction and Mössbauer spectroscopy. *Mineralogical Magazine*, 60 (399), 355–368.
- Chang, I.F., and Mitra, S.S. (1971) Long wavelength optical phonons in mixed crystals. *Advances in Physics*, 20(85), 359–404.
- Chemlal, S., Larbot, A., Persin, M., Sarrazin, J., Sghyar, M., and Rafiq, M. (2000) Cobalt spinel CoAl_2O_4 via sol-gel process: elaboration and surface properties. *Materials Research Bulletin*, 35 (14–15), 2515–2523.
- Chen, M., Shu, J., and Mao, H.-k. (2008) Xieite, a new mineral of high-pressure FeCr_2O_4 polymorph. *Chinese Science Bulletin*, 53(21), 3341-3345.
- Chen, Z.Z., Shi, E.W., Zheng, Y.Q., Xiao, B., and Zhuang, J.Y. (2003) Hydrothermal synthesis of nanosized CoAl_2O_4 on ZnAl_2O_4 seed crystallites. *Journal of the American Ceramic Society*, 86 (6), 1058–1060.
- Cho, W.S. and Kakihana, M.J. (1999) Crystallization of ceramic pigment CoAl_2O_4 nanocrystals from Co–Al metal organic precursor. *Alloys and Compounds*, 287 (1–2), 87–90.
- Chokkaram, S., Srinivasan, R., Milburn, D.R., and Davis, B.H. (1997) Conversion of 2-octanol over nickel-alumina, cobalt-alumina, and alumina catalysts. *Journal of Molecular Catalysis A: Chemical*, 121 (2–3), 157–169.
- Chopelas, A., and Hofmeister, A.M. (1991) Vibrational spectroscopy of aluminate spinels at 1 atm and of MgAl_2O_4 to over 200 kbar. *Physics and Chemistry of Minerals*, 18(5), 279-293.
- Cooley, R.F. and Reed, J.S. (1972) Equilibrium Cation Distribution in NiAl_2O_4 , CuAl_2O_4 and ZnAl_2O_4 Spinels. *Journal of the American Ceramic Society*, 55(8), 395-398.
- Cynn, H., Anderson, O., and Nicol, M. (1993) Effects of cation disordering in a natural MgAl_2O_4 spinel observed by rectangular parallelepiped ultrasonic resonance and Raman measurements. *Pure and Applied Geophysics*, 141(2-4), 415-444.

- Cynn, H., Sharma, S.K., Cooney, T.F., and Nicol, M. (1992) High-temperature Raman investigation of order-disorder behavior in the MgAl_2O_4 spinel. *Physical Review B*, 45(1), 500-502.
- Dal Maschio, R., Fabbri, B., and Fiori, C. (1988) Industrial applications of refractories containing magnesium aluminate spinel. *Industrial Ceramics* 8 (2) 121–126.
- D'Ippolito, V., Andreozzi, G.B., Bosi, F., and Hålenius, U. (2012) Blue spinel crystals in the MgAl_2O_4 - CoAl_2O_4 series: Part I. Flux growth and chemical characterization. *American Mineralogist*, 97(11-12), 1828-1833.
- D'Ippolito, V., Andreozzi, G.B., Bosi, F., Hålenius, U., Mantovani, L., Bersani, D., and Fregola, R.A. (2013) Crystallographic and spectroscopic characterization of a natural Zn-rich spinel approaching the endmember gahnite (ZnAl_2O_4) composition. *Mineralogical Magazine*, 77(7), 2941-2953.
- Damen, T.C., Porto, S.P.S., and Tell, B. (1966) Raman Effect in Zinc Oxide. *Physical Review*, 142(2), 570-574.
- de Waal, D. (2004) Raman investigation of ceramics from 16th and 17th century Portuguese shipwrecks. *Journal of Raman Spectroscopy*, 35(8-9), 646-649.
- de Wijs, G.A., Fang, C.M., Kresse, G., and de With, G. (2002) First-principles calculation of the phonon spectrum of MgAl_2O_4 spinel. *Physical Review B*, 65(9), 094305.
- Della Giusta, A., Carbonin, S., Ottonello, G. (1996) Temperature-dependent disorder in a natural Mg-Al- Fe^{2+} - Fe^{3+} spinel. *Mineralogical Magazine*, 60, 603-616.
- Della Giusta, A., Princivalle, F., and Carbonin, S. (1986) Crystal chemistry of a suite of natural Cr-bearing spinels with $0.15 < \text{Cr} < 1.07$. *Neues Jahrbuch für Mineralogie, Abhandlungen*, 155, 319-330.
- Dereñ, P.J., Streck, W., Oetliker, U., and Güdel, H.U. (1994) Spectroscopic properties of Co^{2+} ions in MgAl_2O_4 spinels. *Physica Status Solidi b*, 182 (1), 241- 251.
- Dick, H.B., and Bullen, T. (1984) Chromian spinel as a petrogenetic indicator in abyssal and alpine-type peridotites and spatially associated lavas. *Contributions to Mineralogy and Petrology*, 86(1), 54-76.

- Dickson, B.L., and Smith, G. (1976) Low-temperature optical absorption and Mössbauer spectra of staurolite and spinel. *The Canadian Mineralogist*, 14(2), 206-215.
- Duan, X.L., Yuan, D.R., Cheng, X.F., Wang, Z.M., Sun, Z.H., Luan, C.N., Xu, D., and Lv, M.K. (2004) Absorption and photoluminescence characteristics of Co^{2+} : MgAl_2O_4 nanocrystals embedded in sol-gel derived SiO_2 -based glass. *Optical Materials*, 25(1), 65-69.
- Durben, D.J. and Wolf, G.H. (1992) High-temperature behavior of metastable MgSiO_3 perovskite: a Raman spectroscopic study. *American Mineralogist*, 77 (7–8), 890.
- Economou-Eliopoulos, M. (1996) Platinum-group element distribution in chromite ores from ophiolite complexes: implications for their exploration. *Ore Geology Reviews*, 11(6), 363-381.
- Eppler, R. and Eppler, D. (2000) *Glazes and Glass Coating*. The American Ceramic Society, Westerville, Ohio.
- Etchepare, J., Merian, M., and Smetankine, L. (1974) Vibrational normal modes of SiO_2 . I. α and β quartz. *Journal of Chemical Physics*, 60 (5), 1873-1876.
- Fang, C.M., Loong, C.K., de Wijs, G.A., and de With, G. (2002) Phonon spectrum of ZnAl_2O_4 spinel from inelastic neutron scattering and first-principles calculations. *Physical Review B*, 66(14), 144301.
- Feenstra, A., Ockenga, E., Rhede, D., and Wiedenbeck, M. (2003) Li-rich zincstaurolite and its decompression-related breakdown products in a diaspore-bearing metabauxite from East Samos (Greece): An EMP and SIMS study. *American Mineralogist*, 88(5-6), 789-805.
- Fernandez, A.L. and De Pablo, L. (2002) Formation and the colour development in cobalt spinel pigments. *Pigment & Resin Technology* 31 (6), 350-356.
- Fierro, G., Jacono, M.L., Dragone, R., Ferraris, G., Andreozzi, G.B., and Graziani, G. (2005) Fe–Zn manganite spinels and their carbonate precursors: preparation, characterization and catalytic activity. *Applied Catalysis B: Environmental*, 57(3), 153-165.
- Fraas, L.M., Moore, J.E., and Salzberg, J.B. (1973) Raman characterization studies of synthetic and natural MgAl_2O_4 crystals. *The Journal of Chemical Physics*, 58(9), 3585-3592.

- Fregola, R.A., Bosi, F., and Skogby, H. (2011) A first report on anion vacancies in a defect MgAl_2O_4 natural spinel. *Periodico di Mineralogia*, 80 (1), 27-38.
- Fregola, R.A., Bosi, F., Skogby, H., and Hålenius, U. (2012) Cation ordering over short-range and long-range scales in the MgAl_2O_4 - CuAl_2O_4 series. *American Mineralogist*, 97(11-12), 1821-1827.
- Frezzotti, M.L., Tecce, F., and Casagli, A. Raman spectroscopy for fluid inclusion analysis. *Journal of Geochemical Exploration*, 112(0), 1-20.
- Fritsch, E., and Rossman, G.R. (1987) An update on color in gems. Part 1: introduction and colors caused by dispersed metal ions. *Gems and Gemology*, 23(3), 126-139.
- Fritsch, E., and Rossman, G.R. (1988) An update on color in gems. Part 2: colors involving multiple atoms and colors centers. *Gems and Gemology*, 24(1), 3-15.
- Frost, B.R. (1973) Ferroan gahnite from quartz-biotite-almandine schist, Wind River Mountains, Wyoming. *American Mineralogist*, 58(9-10), 831–834.
- Frost, R., Kloprogge, T., and Schmidt, J. (1999) Non-destructive identification of minerals by Raman microscopy. *Internet Journal of Vibrational Spectroscopy* [www.ijvs.com], 3, 4, 1.
- Galoisy, L. (1996) Local versus average structure around cations in minerals from spectroscopic and diffraction measurements. *Physics and Chemistry of Minerals*, 23(4-5), 217-225.
- Gama, L., Ribeiro, M.A., Barros, B.S., Kiminami, R.H.A., Weber, I.T., and Costa, A.C.F.M. (2009) Synthesis and characterization of the NiAl_2O_4 , CoAl_2O_4 and ZnAl_2O_4 spinels by the polymeric precursors method. *Journal of Alloys and Compounds*, 483 (1), 453–455.
- Gandhi, S.M. (1971) On the ferroan gahnite of Mamandur, Madras State, India. *Mineralogical Magazine*, 38(296), 528–529.
- Gaudon, M., Apeceixborde, A., Mel̄nel̄trier, M., Le Nestour, A., and Demourgues, A. (2009) Synthesis Temperature Effect on the Structural Features and Optical Absorption of $\text{Zn}_{1-x}\text{Co}_x\text{Al}_2\text{O}_4$ Oxides. *Inorganic Chemistry*, 48(19), 9085-9091.

- Gedam, N.N., Padole, P.R., Rithe, S.K., and Chaudhari, G.N. (2009) Ammonia gas sensor based on a spinel semiconductor, $\text{Co}_{0.8}\text{Ni}_{0.2}\text{Fe}_2\text{O}_4$ nanomaterial. *Journal of Sol-Gel Science and Technology*, 50(3), 296-300.
- Geiger, C.A., 2004 An introduction to spectroscopic methods in the mineral sciences and geochemistry. In: *European Notes in Mineralogy – Spectroscopic Methods in Mineralogy*, 6, Libowitzky, E. and Beran, A. (Eds), p. 1-42.
- Ghosh, A., Sarkar, R., Mukherjee, B., and Das, S.K. (2004) Effect of spinel content on the properties of magnesia–spinel composite refractory. *Journal of the European Ceramic Society*, 24(7), 2079-2085.
- Ghosh, B. and Praveen, M.N. (2007) Garnet–gahnite–staurolite relations and occurrence of ecandrewsite from the Koparpani base metal sulphide prospect, Betul Belt, Central India. *Neues Jahrbuch für Mineralogie*, 184/1, 105–111.
- Gillet, P. (2006) Applications of Vibrational Spectroscopy to Geology. *Handbook of Vibrational Spectroscopy*. John Wiley & Sons, Ltd.
- Goldman, D., and Rossman, G. (1979) Determination of quantitative cation distribution in orthopyroxenes from electronic absorption spectra. *Physics and Chemistry of Minerals*, 4(1), 43-53.
- Gross, J., and Treiman, A.H. (2011) Unique spinel-rich lithology in lunar meteorite ALHA 81005: Origin and possible connection to M3 observations of the farside highlands. *Journal of Geophysical Research: Planets*, 116(E10), E10009.
- Guo, J., Griffin, W.L., and O'Reilly, S.Y. (1994) A cobalt-rich spinel inclusion in a sapphire from Bo Ploi, Thailand. *Mineralogical Magazine*, 58 (391), 247–258.
- Gupta, H.C., Sinha, M.M., Balram, and Tripathi, B.B. (1993) Lattice Dynamics of Oxide-Spinel ZnCr_2O_4 . *Journal of Solid State Chemistry*, 102(2), 315-317.
- Gyngard, F., Zinner, E., Nittler, L.R., Morgand, A., Stadermann, F. J., and Mairin Hynes K. (2010) Automated NanoSIMS Measurements of Spinel Stardust from the Murray Meteorite. *Astrophysical Journal* 717 (1), 107-120.

- Haggerty, S.E. (1991) Oxide mineralogy of the upper mantle. In; Lindsley, D.H. (ed.) *Reviews in Mineralogy*, 25, Oxide Minerals: Petrological and Magnetic Significance. Mineralogical Society of America, Washington, DC, 355-416.
- Hålenius, U., and Bosi, F. (2014) Color of Mn-bearing gahnite: A first example of electronic transitions in heterovalent exchange coupled ${}^{\text{IV}}\text{Mn}^{2+}$ - ${}^{\text{VI}}\text{Mn}^{3+}$ pairs in minerals. In press, *American Mineralogist*.
- Hålenius, U., Andreozzi, G.B., and Skogby, H. (2010) Structural relaxation around Cr^{3+} and the red-green color change in the spinel (sensu stricto)-magnesiochromite (MgAl_2O_4 - MgCr_2O_4) and gahnite-zincochromite (ZnAl_2O_4 - ZnCr_2O_4) solid-solution series. *American Mineralogist*, 95(4), 456-462.
- Hålenius, U., Bosi, F., and Skogby, H. (2007) Galaxite, MnAl_2O_4 , a spectroscopic standard for tetrahedrally coordinated Mn^{2+} in oxygen-based mineral structures. *American Mineralogist*, 92(7), 1225-1231.
- Hålenius, U., Bosi, F., and Skogby, H. (2011) A first record of strong structural relaxation of TO_4 tetrahedra in a spinel solid solution. *American Mineralogist*, 96(4), 617-622.
- Hålenius, U., Skogby, H., and Andreozzi, G.B. (2002) Influence of cation distribution on the optical absorption spectra of Fe^{3+} -bearing spinel s.s.–hercynite crystals: evidence for electron transitions in ${}^{\text{VI}}\text{Fe}^{2+}$ - ${}^{\text{VI}}\text{Fe}^{3+}$ clusters. *Physics and Chemistry of Minerals*, 29(5), 319-330.
- Harder, H. (1986) Natürliche kobaltblau Spinelle von Ratnapura, Sri Lanka. *Neues Jahrbuch für Mineralogie*, 3, 97-100.
- Harrison, R.J., Redfern, S.A.T., and O'Neill, H.St.C. (1998) The temperature dependence of the cation distribution in synthetic hercynite (FeAl_2O_4) from in-situ neutron diffraction refinements. *American Mineralogist*, 83 (6), 1092–1099.
- Heimann, A., Spry, P.G., and Teale, G.S. (2005) Zincian spinel associated with metamorphosed proterozoic base-metal sulfide occurrences, Colorado: a re-evaluation of gahnite composition as a guide in exploration. *The Canadian Mineralogist*, 43(2), 601-622.
- Henry, D.J., and Dutrow, B.L. (2001) Compositional zoning and element partitioning in nickeloan tourmaline from a metamorphosed karstbauxite from Samos, Greece. *American Mineralogist*, 86(10), 1130-1142.

- Hicks, J.A., Moore, J.M., and Reid, A.M. (1985): The co-occurrence of green and blue gahnite in the Namaqualand Metamorphic Complex, South Africa. *Canadian Mineralogist*, 23(4), 535–542.
- Hill, R., Craig, J., and Gibbs, G.V. (1979) Systematics of the spinel structure type. *Physics and Chemistry of Minerals*, 4(4), 317-339.
- Himmrich, J., and Lutz, H.D. (1991) Normal coordinate analyses and lattice dynamical calculations of spinel-type ZnCr_2O_4 . *Solid State Communications*, 79(5), 447-452.
- Hiroi, T., Vilas, F., and Sunshine, J. M (1994) Possible spinel absorption bands in S-asteroid visible reflectance spectra. Lunar and Planetary Institute, The Twenty-Fifth Lunar and Planetary Science Conference. Part 2: 553-554.
- Hochu, F. and Lenglet, M. (1998) Co(II) optical absorption in spinels: Infrared and ligand-field spectroscopic study of the ionicity of the bond. Magnetic structure and Co^{2+} - Fe^{3+} MMCT in ferrites. Correlation with the magneto-optical properties. *Active and Passive Electronic Components*, 20(3), 169–187.
- Hofmeister, A.M. (2007) Thermal diffusivity of aluminous spinels and magnetite at elevated temperature with implications for heat transport in Earth's transition zone. *American Mineralogist*, 92(11-12), 1899-1911.
- Hosterman, B.D. (2011) Raman Spectroscopic Study of Solid Solution Spinel Oxides. PhD Thesis, University of Nevada, Las Vegas, p 144.
- Hosterman, B.D., Farley, J.W., and Johnson, A.L. (2013) Spectroscopic study of the vibrational modes of magnesium nickel chromite. *Journal of Physics and Chemistry of Solids*, 74(7), 985-990.
- Hou, Z. and Yashima, T. (2004) Supported Co catalysts for methane reforming with CO_2 . *Chemistry and Materials Science*, 81, 153–159.
- Irvine, T.N. (1965) Chromian spinel as a petrogenetic indicator: part 1. Theory. *Canadian Journal of Earth Sciences*, 2(6), 648-672.
- Irvine, T.N. (1967) Chromian spinel as a petrogenetic indicator: part 2. Petrologic applications. *Canadian Journal of Earth Sciences*, 4(1), 71-103.
- Jackson, B. (1982) Gem quality gahnite from Nigeria. *Journal of Gemmology*, 18(2), 265–276.

- Johnson, B.G., and Florián, J. (1995) The prediction of Raman spectra by density functional theory. Preliminary findings. *Chemical Physics Letters*, 247(1–2), 120-125.
- Jouini, A., Sato, H., Yoshikawa, A., Fukuda, T., Boulon, G., Kato, K., and Hanamura, E. (2006) Crystal growth and optical absorption of pure and Ti, Mn-doped MgAl_2O_4 spinel. *Journal of Crystal Growth*, 287(2), 313-317.
- Julien, C.M., and Massot, M. (2003) Lattice vibrations of materials for lithium rechargeable batteries I. Lithium manganese oxide spinel. *Materials Science and Engineering: B*, 97(3), 217-230.
- Kawakami, Y., Yamamoto, J., and Kagi, H. (2003) Micro-Raman Densimeter for CO_2 Inclusions in Mantle-Derived Minerals. *Applied Spectroscopy*, 57(11), 1333-1339.
- Keramidas, V.G., Deangelis, B.A., and White, W.B. (1975) Vibrational spectra of spinels with cation ordering on the octahedral sites. *Journal of Solid State Chemistry*, 15(3), 233-245.
- Klemme, S., Günther, D., Hametner, K., Prowatke, S., and Zack, T. (2006) The partitioning of trace elements between ilmenite, ulvospinel, armalcolite and silicate melts with implications for the early differentiation of the moon. *Chemical Geology*, 234(3–4), 251-263.
- Kock, L.D., and De Waal, D. (2007) Raman studies of the underglaze blue pigment on ceramic artefacts of the Ming dynasty and of unknown origins. *Journal of Raman Spectroscopy*, 38(11), 1480-1487.
- Kolitsch, U. (2003) Mg-rich wolfeite, $(\text{Fe}^{\text{II}}, \text{Mg})_2(\text{PO}_4)(\text{OH})$: structure refinement and Raman spectroscopic data. *Acta Crystallographica Section E*, 59(9), i125-i128.
- Kuleshov, N.V., Mikhailov, V.P., Scherbitsky, V.G., Prokoshin, P.V., and Yumashev, K.V. (1993) Absorption and luminescence of tetrahedral Co^{2+} ion in MgAl_2O_4 . *Journal of Luminescence*, 55 (5–6), 265–269.
- Kurajica, S., Tkalčec, E., Gržeta, B., Iveković, D., Mandić, V., Popović, J., and Kranzelić, D. (2011) Evolution of structural and optical properties in the course of thermal evolution of sol–gel derived cobalt-doped gahnite. *Journal of Alloys and Compounds*, 509 (7), 3223–3228.

- Laguna-Bercero, M. A., Sanjuán, M. L., and Merino, R. I. (2007) Raman spectroscopic study of cation disorder in poly- and single crystals of the nickel aluminate spinel. *Journal of Physics: Condensed Matter*, 19 (18), 1–10.
- Langer, K., and Andrut, M. (1996) The crystal field concept (CFC) in geoscience: Does the crystal field stabilization energy of Cr^{3+} rule its intercrystalline partitioning behavior? In: Dyar MD, McCammon C, Schaefer MW (eds.) *Mineral spectroscopy: a tribute to Roger G Burns*. The Geochemical Society Spec Pub, 29-40.
- Lavina, B., Salviulo, G., and Giusta, A.D. (2002) Cation distribution and structure modelling of spinel solid solutions. *Physics and Chemistry of Minerals*, 29(1), 10-18.
- Lazzeri, M., and Thibaudeau, P. (2006) Ab initio Raman spectrum of the normal and disordered MgAl_2O_4 spinel. *Physical Review B*, 74(14), 140301.
- Leeman, W.P. and Scheidegger, K.F. (1977) Olivine/liquid distribution coefficients and a test for crystal-liquid equilibrium. *Earth and Planetary Science Letters*, 35(2), 247–257.
- Lenaz, D. and Princivale, F. (2011) First occurrence of titanomagnetites from the websterite dykes within Balmuccia peridotite (Ivrea-Verbanò zone): crystal chemistry and structural refinement. *Periodico di Mineralogia*, 80 (1), 19–26.
- Lenaz, D., and Lughi, V. (2013) Raman study of $\text{MgCr}_2\text{O}_4\text{--Fe}^{2+}\text{Cr}_2\text{O}_4$ and $\text{MgCr}_2\text{O}_4\text{--MgFe}^{3+}_2\text{O}_4$ synthetic series: the effects of Fe^{2+} and Fe^{3+} on Raman shifts. *Physics and Chemistry of Minerals*, 40(6), 491-498.
- Lenaz, D., and Princivale, F. (2005) The crystal chemistry of detrital chromian spinel from the southeastern alps and outer dinarides: the discrimination of supplies from areas of similar tectonic setting?. *The Canadian Mineralogist*, 43(4), 1305-1314.
- Lenaz, D., and Skogby, (2013) H. Structural changes in the $\text{FeAl}_2\text{O}_4\text{--FeCr}_2\text{O}_4$ solid solution series and their consequences on natural Cr-bearing spinels. *Physics and Chemistry of Minerals*, 40(7), 587-595.
- Lenaz, D., Skogby, H., Princivale, F., and Hålenius, U. (2004) Structural changes and valence states in the $\text{MgCr}_2\text{O}_4\text{--FeCr}_2\text{O}_4$ solid solution series. *Physics and Chemistry of Minerals*, 31(9), 633-642.

- Lenaz, D., Skogby, H., Princivalle, F., and Hålenius, U. (2006) The MgCr_2O_4 – MgFe_2O_4 solid solution series: effects of octahedrally coordinated Fe^{3+} on T–O bond lengths. *Physics and Chemistry of Minerals*, 33(7), 465-474.
- Li, W., Li, J., and Guo, J. (2003) Synthesis and characterization of nanocrystalline CoAl_2O_4 spinel powder by low temperature combustion. *Journal of the European Ceramic Society*, 23 (13), 2289–2295.
- Llusar, M., Forés, A., Badenes, J.A., Calbo, J., Tena, M.A., and Monrós, G. (2001) Colour analysis of some cobalt-based blue pigments. *Journal of the European Ceramic Society*, 21(8), 1121-1130.
- Longerich, H.P., Jackson, S.E., and Gunther, D. (1996) Inter-laboratory note. Laser ablation inductively coupled plasma mass spectrometric transient signal data acquisition and analyte concentration calculation. *Journal of Analytical Atomic Spectrometry*, 11(9), 899-904.
- López-Moreno, S., Rodríguez-Hernández, P., Muñoz, A., Romero, A.H., Manjón, F.J., Errandonea, D., Rusu, E., and Ursaki, V.V. (2011) Lattice dynamics of ZnAl_2O_4 and ZnGa_2O_4 under high pressure. *Annalen der Physik*, 523(1-2), 157-167.
- Lucchesi, S., and Della Giusta, A. (1994) Crystal chemistry of non-stoichiometric Mg/Al synthetic spinels. *Zeitschrift für Kristallographie - Crystalline Materials*, 209(9), 714-719.
- Lucchesi, S., and Della Giusta, A. (1997) Crystal chemistry of a highly disordered Mg-Al natural spinel. *Mineralogy and Petrology*, 59(1-2), 91-99.
- Lucchesi, S., Della Giusta, A., and Russo, U. (1998) Cation distribution in natural Zn-aluminate spinels. *Mineralogical Magazine*, 62(1), 41-54.
- Malavasi, L., Galinetto, P., Mozzati, M.C., Azzoni, C.B., and Flor, G. (2002) Raman spectroscopy of AMn_2O_4 (A = Mn, Mg and Zn) spinels. *Physical Chemistry Chemical Physics*, 4(15), 3876-3880.
- Malézieux, J. M., Barbillat, J., Cervelle, B., Coutures, J. P., Couzi, M., and Piriou, B. (1983) Étude de spinelles de synthèse de la série $\text{MgCr}_x\text{Al}_{2-x}\text{O}_4$ et de chromites naturelles par microsonde Raman-laser. *Tshermaks Mineralogische und Petrographische Mitteilungen* 32, 171–185.
- Malézieux, J.M., and Piriou, B. (1988) Relation entre la composition chimique et le comportement vibrationnel de spinelles de synthèse et de chromites

- naturalles en microspectrométrie Raman, *Bulletin Minéralogique*, 111, 649–669.
- Maljuk, A., Tsurkan, V., Zestrea, V., Zaharko, O., Cervellino, A., Loidl, A., and Argyriou, D.N. (2009) Floating-zone growth of large high-quality CoAl_2O_4 single crystals. *Journal of Crystal Growth*, 311 (16), 3997–4000.
- Malsy, A.K., Karampelas, S., Schwarz, D., Klemm, L., Armbruster, T., and Tuan, D.A. (2012) Orange-red to orange-pink gem spinels from a new deposit at Lang Chap (Tan Huong-Truc Lau), Vietnam. *The Journal of Gemmology*, 33 (1–4), 19–27.
- Mantovani, L., Oleari, C., Tribaudino, M., Dondi, M., Zanelli, C., and Bromiley, G. (2012) Synthesis and characterization of a new ceramic pigment based on the pyroxene structure. *European Mineralogical Conference Vol. 1*, EMC2012-413.
- Marinković Stanojević, Z.V., Romčević, N., and Stojanović, B. (2007) Spectroscopic study of spinel ZnCr_2O_4 obtained from mechanically activated $\text{ZnO-Cr}_2\text{O}_3$ mixtures. *Journal of the European Ceramic Society*, 27(2–3), 903-907.
- Maslennikova, G.N. (2001) Pigments of the Spinel Type. *Glass and Ceramics*, 58(5-6), 216-220.
- Mattson, S.M. and Rossman, G.R. (1987a) Fe^{2+} - Fe^{3+} interactions in tourmaline. *Physics and Chemistry of Minerals*, 14 (1), 163-171.
- Mattson, S., and Rossman, G. (1987b) Identifying characteristics of charge transfer transitions in minerals. *Physics and Chemistry of Minerals*, 14(1), 94-99.
- Mayhew, L.E., Ellison, E.T., McCollom, T.M., Trainor, T.P., and Templeton, A.S. (2013) Hydrogen generation from low-temperature water-rock reactions. *Nature Geoscience*, 6 (6), 478–484.
- Melo, D.M.A., Cunha, J.D., Fernandes, J.D.G., Bernardi, M.I., Melo, M.A.F., and Martinelli, A.E. (2003) Evaluation of CoAl_2O_4 as ceramic pigments. *Materials Research Bulletin*, 38 (9–10), 1559–1564.
- Mimani, T. and Ghosh, S. (2000) Combustion synthesis of cobalt pigments: Blue and pink. *Current Science*, 78 (7), 892–896.

- Mindru, I., Marinescu, G., Gingasu, D., Patron, L., Ghica, C., and Giuginca, M. (2010) Blue CoAl_2O_4 spinel *via* complexation method. *Materials Chemistry and Physics*, 122 (2–3), 491–497.
- Minh, N.V., and Yang, I.-S. (2004) A Raman study of cation-disorder transition temperature of natural MgAl_2O_4 spinel. *Vibrational Spectroscopy*, 35(1–2), 93-96.
- Morris, T.F., Breaks, F.W., Averill, S.A., Crabtree, D.C., and McDonald, A. (1997) Gahnite composition; implications for base metal and rare-element exploration. *Exploration and Mining Geology*, 6(3), 253-260.
- Muralha, V.S.F., Rehren, T., and Clark, R.J.H. (2011) Characterization of an iron smelting slag from Zimbabwe by Raman microscopy and electron beam analysis. *Journal of Raman Spectroscopy*, 42(12), 2077-2084.
- Nakagomi, F., da Silva, S.W., Garg, V.K., Oliveira, A.C., Morais, P.C., and Franco Jr, A. (2009) Influence of the Mg-content on the cation distribution in cubic $\text{Mg}_x\text{Fe}_{3-x}\text{O}_4$ nanoparticles. *Journal of Solid State Chemistry*, 182(9), 2423-2429.
- Nakatsuka, A., Ikeda, Y., Yamasaki, Y., Nakayama, N., and Mizota, T. (2003) Cation distribution and bond lengths in CoAl_2O_4 spinel. *Solid State Communications*, 128 (2–3), 85–90.
- Nasdala, L., Götze, J., Hanchar, J.M., Gaft, M., and Krbetschek M.R. (2004a) Luminescence techniques in Earth Sciences. In: *Spectroscopic Methods in Mineralogy* (A. Beran & E. Libowitzky, editors). EMU Notes in Mineralogy 6, Eotvos University Press, Budapest, pp. 43-92.
- Nasdala, L., Smith, D.C., Kaindl, R., Gaft, M., and Ziemann, M.A. (2004b) Raman spectroscopy: Analytical perspectives in mineralogical research. In: *Spectroscopic Methods in Mineralogy* (A. Beran & E. Libowitzky, editors). EMU Notes in Mineralogy 6, Eotvos University Press, Budapest, pp. 281-343.
- Nassau, K. (1987) The fifteen causes of color: The physics and chemistry of color. *Color Research and Application*, 12(1), 4-26.
- Néel, L. (1948) Magnetic properties of ferrites: ferrimagnetism and antiferromagnetism. *Annales de Physique*, 3, 137-198.

- Novák, M., Houzar, S. and Rein, V. (1997) Gahnite-bearing marbles and their significance for regional classification of the eastern part of the Bohemian Massif. *Journal of the Czech Geological Society*, 42(1-2), 33–40.
- O'Neill, H.St.C. (1994) Temperature dependence of the cation distribution in CoAl_2O_4 spinel. *European Journal of Mineralogy*, 6 (5), 603–609.
- O'Neill, H.St.C., James, M., Dollase, W.A., and Redfern, S.A.T. (2005) Temperature dependence of the cation distribution in CuAl_2O_4 spinel. *European Journal of Mineralogy*, 17 (4), 581–586.
- Oh, S.K., Song, H.J., Kim, W.T., Kim, H.G., Lee, C.I., Park, T.Y., Jin, M.S., and Yoon, C.S. (2000) Impurity optical absorption of Co^{2+} -doped MgAl_2S_4 and CaAl_2S_4 single crystals. *Journal of Physics and Chemistry of Solids*, 61(8), 1243-1247.
- O'Horo, M.P., Frisillo, A.L., and White, W.B. (1973) Lattice vibrations of MgAl_2O_4 spinel. *Journal of Physics and Chemistry of Solids*, 34(1), 23-28.
- O'Neill, H.S., and Dollase, W.A. (1994) Crystal-structures and cation distributions in simple spinels from powder XRD structural refinements - MgCr_2O_4 , ZnCr_2O_4 , Fe_3O_4 and the temperature-dependence of the cation distribution in ZnAl_2O_4 . *Physics and Chemistry of Minerals*, 20(8), 541-555.
- O'Neill, H.S.C. (2003) The influence of next nearest neighbours on cation radii in spinels: the example of the Co_3O_4 - CoCr_2O_4 solid solution. *Mineralogical Magazine*, 67, 547–554.
- O'Neill, H.S.C., and Navrotsky, A. (1983) Simple spinels; crystallographic parameters, cation radii, lattice energies, and cation distribution. *American Mineralogist*, 68(1-2), 181-194.
- O'Neill, H.S.C., and Navrotsky, A. (1984) Cation distributions and thermodynamic properties of binary spinel solid solutions. *American Mineralogist*, 69(7-8), 733-753.
- O'Neill, H.S.C., and Wall, V.J. (1987) The Olivine–Orthopyroxene–Spinel Oxygen Geobarometer, the Nickel Precipitation Curve, and the Oxygen Fugacity of the Earth's Upper Mantle. *Journal of Petrology*, 28(6), 1169-1191.
- Osipov, A.A., and Osipova, L.M. (2009) Structure of glasses and melts in the Na_2O - B_2O_3 system from high-temperature Raman spectroscopic data: II. Superstructural units in melts. *Glass Physics and Chemistry*, 35(2), 132-140.

- Ospitali, F., Sabetta, T., Tullini, F., Nannetti, M.C., and Di Lonardo, G. (2005) The role of Raman microspectroscopy in the study of black gloss coatings on Roman pottery. *Journal of Raman Spectroscopy*, 36(1), 18-23.
- Ottinger, F., Kroslakova, I., Hametner, K., Reusser, E., Nesper, R., and Günther, D. (2005) Analytical evidence of amorphous microdomains within nitridosilicate and nitridoaluminosilicate single crystals. *Analytical and Bioanalytical Chemistry*, 383(3), 489-499.
- Palache, C., Berman, H., and Frondel, C. (1944) *Dana's System of Mineralogy*. 7th edition. 1, Wiley, New York.
- Pappalardo, R., and Dietz, R.E. (1961) Absorption Spectra of Transition Ions in CdS Crystals. *Physical Review*, 123(4), 1188-1203.
- Parr, J. (1992) A gahnite-garnet retrograde reaction from the Pinnacles Deposit, Broken Hill, New South Wales. *The Canadian Mineralogist*, 30(1), 145-152.
- Pasternak, M.P., Nasu, S., Wada, K., and Endo, S. (1994) High-pressure phase of magnetite. *Physical Review B*, 50(9), 6446-6449.
- Pirogova, G.N., Panich, N.M., Korosteleva, R.I., Voronin, Y.V., and Popova, N.N. (2001) Catalytic properties of chromites with a spinel structure in the oxidation of CO and hydrocarbons and reduction of nitrogen oxides. *Russian Chemical Bulletin*, 50(12), 2377-2380.
- Popović, J., Tkalčec, E., Gržeta, B., Kurajica, S., and Rakvin, B. (2009) Inverse spinel structure of Co-doped gahnite. *American Mineralogist*, 94(5-6), 771-776.
- Popp, J., Tarcea, N., Kiefer, W., Hilchenbach, M., Thomas, N., Hofer, S., Stuffer, T. (2001) Investigation on Mars model minerals by in situ laser Raman spectroscopy. *Proceedings of the First European Workshop on Exo-/Astro-Biology ESA SP-496*, Noordwijk: ESA Publications Division, ISBN 92-9092-806-9, p. 193 – 196.
- Pouchou, L.J. and Pichoir, F. (1984) New model quantitative x-ray microanalysis, 1. Application to the analysis of homogeneous samples. *La Recherche Aérospatiale*, 3, 13 –38.
- Praveen, M.N. and Ghosh, B. (2007) Multiple origins of gahnite associated with hydrothermal alteration from the Bhuyari base metal prospect of Proterozoic

- Betul Belt, Madhya Pradesh. *Journal Geological Society of India*, 69(6), 233–241.
- Preudhomme, J., and Tarte, P. (1971) Infrared studies of spinels—III: The normal II–III spinels. *Spectrochimica Acta Part A: Molecular Spectroscopy*, 27(9), 1817-1835.
- Princivalle, F., Della Giusta, A., and Carbonin, S. (1989) Comparative crystal chemistry of spinels from some suites of ultramafic rocks. *Mineralogy and Petrology*, 40(2), 117-126.
- Princivalle, F., Della Giusta, A., De Min, A., and Piccirillo, E.M. (1999) Crystal chemistry and significance of cation ordering in Mg-Al rich spinels from high-grade hornfels (Predazzo-Monzoni, NE Italy). *Mineralogical Magazine*, 63(2), 257-262.
- Putnis, A. (1992) *Introduction to mineral sciences*. Cambridge University Press, Cambridge, p. 457.
- Rangappa, D., Ohara, S., Naka, T., Kondo, A., Ishii, M., and Adschiri, T. (2007) Synthesis and organic modification of CoAl_2O_4 nanocrystals under supercritical water conditions. *Journal of Materials Chemistry*, 17 (41), 4426–4429.
- Redfern, S.A.T., Harrison, R.J., O'Neill, H.St.C., and Wood, D.R.R. (1999) Thermodynamics and kinetics of cation ordering in MgAl_2O_4 spinel up to 1600°C from in situ neutron diffraction. *American Mineralogist*, 84, 299-310.
- Reichmann, H.J., and Jacobsen, S.D. (2004) High-pressure elasticity of a natural magnetite crystal. *American Mineralogist*, 89(7), 1061-1066.
- Reichmann, H.J., and Jacobsen, S.D. (2006) Sound velocities and elastic constants of ZnAl_2O_4 spinel and implications for spinel-elasticity systematics. *American Mineralogist*, 91(7), 1049-1054.
- Righter, K., Sutton, S., Danielson, L., Pando, K., Le, L., and Newville, M. (2009) Using Vanadium in spinel as a sensor of oxygen fugacity in meteorites: applications to Mars, Vesta, and other asteroids. 40th Lunar and Planetary Science Conference, March 23-27, 2009, Texas, id.2213.
- Rodgers, K.A. (1993) Routine identification of aluminium hydroxide polymorphs with the laser Raman microprobe. *Clay Minerals*, 28(1), 85-99.

- Rossmann, G.R. (1975) Spectroscopic and magnetic studies of ferric iron hydroxy sulphates: intensification of color in iron (III) clusters bridged by a single hydroxide ion. *American Mineralogist*, 60 (7-8), 698-704.
- Rykhinskaya, K., and Fritzsche, S. (2004) Use of group theory for the analysis of vibrational spectra. *Computer Physics Communications*, 162(2), 124-142.
- Saalfeld, H. (1964) Strukturdaten von Gahnit, $ZnAl_2O_4$. *Zeitschrift für Kristallographie*, 120(6), 476–478.
- Sack, R.O., and Ghiorso, M.S. (1991) Chromian spinels as petrogenetic indicators; thermodynamics and petrological applications. *American Mineralogist*, 76(5-6), 827-847.
- Sales, M., Valentin, C., and Alarcon, J. (1997) Cobalt aluminate spinel-mullite composites synthesized by sol-gel method. *Journal of the European Ceramic Society*, 17 (1), 41–47.
- Sampath, S.K., and Cordaro, J.F. (1998) Optical Properties of Zinc Aluminate, Zinc Gallate, and Zinc Aluminogallate Spinels. *Journal of the American Ceramic Society*, 81(3), 649-654.8(3), 353–356.
- Sandhaus, D.J., and Craig, J.R. (1986) Gahnite in the metamorphosed stratiform massive sulfide deposits of the Mineral District, Virginia, U.S.A. *Tschermaks mineralogische und petrographische Mitteilungen*, 35(2), 77-98.
- Schmetzer, K. and Bank, H. (1985) Crystal chemistry of zincian spinels (gahnospinel) from Sri Lanka. *Neues Jahrbuch für Mineralogie*, 8, 353–356.
- Schmetzer, K., Haxel, C. and Bank, H. (1989) Colour of natural spinels, gahnospinel and gahnites. *Neues Jahrbuch für Mineralogie*, 160 (2), 159–180.
- Šepelák, V., Indris, S., Heitjans, P., and Becker, K.D. (2007) Direct determination of the cation disorder in nanoscale spinels by NMR, XPS, and Mössbauer spectroscopy. *Journal of Alloys and Compounds*, 434–435(0), 776-778.
- Shannon, R. (1976) Revised effective ionic radii and systematic studies of interatomic distances in halides and chalcogenides. *Acta Crystallographica Section A*, 32(5), 751-767.
- Shannon, R.D., and Prewitt, C.T. (1969) Effective ionic radii in oxides and fluorides. *Acta Crystallographica Section B*, 25(5), 925-946.

- Shebanova, O.N., and Lazor, P. (2003) Raman spectroscopic study of magnetite (FeFe_2O_4): a new assignment for the vibrational spectrum. *Journal of Solid State Chemistry*, 174(2), 424-430.
- Sheldrick, G. (2008) A short history of SHELX. *Acta Crystallographica Section A*, 64(1), 112-122.
- Shigley, J.E. and Stockton, C.M. (1984) Cobalt-blue gem spinels. *Gems & Gemology*, 20(1), 34-41.
- Shukla, S.J., Jadhav, K.M., and Bichile, G.K. (1999) Influence of Mg^{2+} substitution on magnetic properties of Co-Fe-Cr-O spinel ferrite system. *Journal of Magnetism and Magnetic Materials*, 195(3), 692-698.
- Singh, V., Chakradhar, R.P.S., Rao, J.L., and Kwak, H.Y. (2011) EPR and photoluminescence properties of combustion-synthesized $\text{ZnAl}_2\text{O}_4:\text{Cr}^{3+}$ phosphors. *Journal of Materials Science*, 46(7), 2331-2337.
- Skogby, H., and Hålenius, U. (2003) An FTIR study of tetrahedrally coordinated ferrous iron in the spinel-hercynite solid solution. *American Mineralogist*, 88(4), 489-492.
- Slotznick, S.P., and Shim, S.-H. (2008) In situ Raman spectroscopy measurements of MgAl_2O_4 spinel up to 1400°C. *American Mineralogist*, 93(2-3), 470-476.
- Smith, E. and Dent, G. (2005) *Modern Raman Spectroscopy: A Practical Approach*. Wiley Online Library, p. 210.
- Spry, P.G. (1987) Compositional zoning in zincian spinel. *The Canadian Mineralogist*, 25(1), 97-104.
- Spry, P.G., and Scott, S.D. (1986a) Zincian spinel and staurolite as guides to ore in the Appalachians and Scandinavian Caledonides. *The Canadian Mineralogist*, 24(1), 147-163.
- Spry, P.G., and Scott, S.D. (1986b) The stability of zincian spinels in sulfide systems and their potential as exploration guides for metamorphosed massive sulfide deposits. *Economic Geology*, 81(6), 1446-1463.
- Steffen, G., Langer, K., and Seifert, F. (1988) Polarized electronic absorption spectra of synthetic (Mg, Fe)-orthopyroxenes, ferrosilite and Fe^{3+} -bearing ferrosilite. *Physics and Chemistry of Minerals*, 16(2), 120-129.

- Sundblad, K. (1994) A genetic reinterpretation of the Falun and Åmmeberg ore types, Bergslagen, Sweden. *Mineralium Deposita*, 29(2), 170-179.
- Sunshine, J. M., and Cloutis, E. A. (1999) Absorption bands in spinels: Comparisons of laboratory and asteroid spectra. 30th Annual Lunar and Planetary Science Conference, March 15-29, 1999, Houston, TX, abstract no. 1640.
- Suszkiewicz, A. and Lobos, K. (2004) Gahnite from Siedlimowice, Strzegom-Sobótka. Granitic Massif, SW Poland. *Mineralogia Polonica*, 35 (2), 15–21.
- Suzuki, T., Nagai, H., Nohara, M., and Takagi, H.J. (2007) Melting of antiferromagnetic ordering in spinel oxide CoAl_2O_4 . *Journal of Physics: Condensed Matter*, 19 (14), 145265.
- Takahashi, E. (1978) Partitioning of Ni^{2+} , Co^{2+} , Fe^{2+} , Mn^{2+} and Mg^{2+} between olivine and silicate melts: compositional dependence of partition coefficient. *Geochimica et Cosmochimica Acta*, 42 (12), 1829–1844.
- Taran, M., Koch-Müller, M., and Langer, K. (2005) Electronic absorption spectroscopy of natural (Fe^{2+} , Fe^{3+})-bearing spinels of spinel s.s.-hercynite and gahnite-hercynite solid solutions at different temperatures and high-pressures. *Physics and Chemistry of Minerals*, 32(3), 175-188.
- Taran, M.N., Koch-Müller, M., and Feenstra, A. (2009) Optical spectroscopic study of tetrahedrally coordinated Co^{2+} in natural spinel and staurolite at different temperatures and pressures. *American Mineralogist*, 94(11-12), 1647-1652.
- Taylor, L. A., Nazarov, M. A., Shearer, C. K., McSween, H. Y., Cahill, J., Neal, C. R., Ivanova, M. A., Barsukova, L. D., Lentz, R. C., Clayton, R. N., Mayeda, T. K (2002) Martian meteorite Dhofar 019: A new shergottite. *Meteoritics and Planetary Science* 37(8), 1107–1128.
- Tielens, F., Calatayud, M., Franco, R., Recio, J.M., Pérez-Ramírez, J., and Minot, C. (2006) Study of the structural and electronic properties of bulk CoAl_2O_4 spinel. *The Journal of Physical Chemistry B*, 110 (2), 988–995.
- Tielens, F., Calatayud, M., Franco, R., Recio, J.M., Pérez-Ramírez, J., and Minot, C. (2009) Theoretical investigation of the inversion parameter in $\text{Co}_{3-s}\text{Al}_s\text{O}_4$ ($s=0-3$) spinel structures. *Solid State Ionics*, 180 (14–16), 1011–1016.

- Toriumi, K., Ozima, M., Akaogi, M., and Saito, Y. (1978) Electron-density distribution in crystals of CoAl_2O_4 . *Acta Crystallographica B*, 34 (4), 1093–1096.
- Uchida, H., Lavina, B., Downs, R.T., and Chesley, J. (2005) Single-crystal X-ray diffraction of spinels from the San Carlos Volcanic Field, Arizona: Spinel as a geothermometer. *American Mineralogist*, 90(11-12), 1900-1908.
- Urusov, V.S. (1992) A geometric model of deviations from Vegard's rule. *Journal of Solid State Chemistry*, 98(2), 223-236.
- Valenzuela, M.A., Jacobs, J.P., Bosch, P., Reijne, S., Zapata, B., and Brongersma, H.H. (1997) The influence of the preparation method on the surface structure of ZnAl_2O_4 . *Applied Catalysis A: General*, 148(2), 315-324.
- Van der Laag, N.J., Snel, M.D., Magusin, P.C.M.M., and de With, G. (2004) Structural, elastic, thermophysical and dielectric properties of zinc aluminate (ZnAl_2O_4). *Journal of the European Ceramic Society*, 24(8), 2417-2424.
- Verble, J.L. (1974) Temperature-dependent light-scattering studies of the Verwey transition and electronic disorder in magnetite. *Physical Review B*, 9(12), 5236-5248
- Visser, D., Thijssen, P.H.M. and Schumacher, J.C. (1992) Högbomite in sapphirine-bearing rocks from the Bamble Sector, south Norway. *Mineralogical Magazine*, 56(384), 343–351.
- Votyakov, S.L., Chashchukhin, I.S., Uimin, S.G., and Bykov, V.N. (1998) Oxygen thermometry and barometry of chromite-bearing ultramafic rocks, examples from the South Urals: I. Mössbauer Spectroscopy of chrome spinels and the problems of olivine-spinel thermometry. *Geochemistry International*, 36 (8), 706-716.
- Waerenborgh, J.C., Annersten, H., Ericsson, T., Figueiredo, M.O., and Cabral, J.M.P. (1990) A Mössbauer study of natural gahnite spinels showing strongly temperature-dependent quadrupole splitting distributions. *European Journal of Mineralogy*, 2(3), 267-271.
- Waerenborgh, J.C., Figueiredo, M.O., Cabral, J.M.P., and Pereira, L.C.J. (1994) Powder XRD structure refinements and ^{57}Fe Mössbauer effect study of synthetic $\text{Zn}_{1-x}\text{Fe}_x\text{Al}_2\text{O}_4$ ($0 < x \leq 1$) spinels annealed at different temperatures. *Physics and Chemistry of Minerals*, 21(7), 460-468.

- Wallwork, K., Kolitsch, U., Pring, A., and Nasdala, L. (2002) Decrespignyite-(Y), a new copper yttrium rare earth carbonate chloride hydrate from Paratoo, South Australia. *Mineralogical Magazine*, 66 (1), 181-188.
- Wang, A., Kuebler, K.E., Jolliff, B.L., and Haskin, L.A. (2004) Raman spectroscopy of Fe-Ti-Cr-oxides, case study: Martian meteorite EETA79001. *American Mineralogist*, 89(5-6), 665-680.
- Wang, C., Liu, S., Liu, L., and Bai, X. (2006) Synthesis of cobalt–aluminate spinels via glycine chelated precursors. *Materials Chemistry and Physics*, 96 (2–3), 361–370.
- Wang, Z., O'Neill, H.S.C., Lazor, P., and Saxena, S.K. (2002a) High pressure Raman spectroscopic study of spinel $MgCr_2O_4$. *Journal of Physics and Chemistry of Solids*, 63(11), 2057-2061.
- Wang, Z., Lazor, P., Saxena, S.K., and Artioli, G. (2002b) High-Pressure Raman Spectroscopic Study of Spinel ($ZnCr_2O_4$). *Journal of Solid State Chemistry*, 165(1), 165-170.
- Weakliem, H.A. (1962) Optical spectra of Ni^{2+} , Co^{2+} and Cu^{2+} in tetrahedral sites in crystals. *Journal of Chemical Physics*, 36(8), 2117–2140.
- Wildner, M., Andrut, M., and Rudowicz, C. Z. (2004) Optical absorption spectroscopy in geosciences. Part I: Basic concepts of crystal field theory. In: *Spectroscopic Methods in Mineralogy* (A. Beran & E. Libowitzky, editors). EMU Notes in Mineralogy 6, Eotvos University Press, Budapest, pp. 93-144.
- Wildner, M. (1996) Polarized Electronic Absorption Spectra of Tetrahedrally Coordinated Co^{2+} Ions in the New Compound $Ca_3Co(SeO_3)_4$ and Its Structural Characterization. *Journal of Solid State Chemistry*, 124(1), 143-150.
- Winell, S., Annersten, H., and Prakapenka, V. (2006) The high-pressure phase transformation and breakdown of $MgFe_2O_4$. *American Mineralogist*, 91(4), 560-567.
- Winkler, B.r., Harris, M.J., Eccleston, R.S., Knorr, K., and Hennion, B. (1997) Crystal field transitions in $Co_2[Al_4Si_5]O_{18}$ cordierite and $CoAl_2O_4$ spinel determined by neutron spectroscopy. *Physics and Chemistry of Minerals*, 25(1), 79-82.

- Xirouchakis, D., Draper, D.S., Schwandt, C.S., and Lanzirotti, A. (2002) Crystallization conditions of Los Angeles, a basaltic Martian meteorite. *Geochimica et Cosmochimica Acta*, 66(10), 1867-1880.
- Yalçın, Ü., Schreyer, W., and Medenbach, O. (1993) Zn-rich högbomite formed from gahnite in the metabauxites of the Menderes Massif, SW Turkey. *Contributions to Mineralogy and Petrology*, 113(3), 314-324.
- Yoneda, A. (1990) Pressure derivatives of elastic constants of single crystal MgO and MgAl₂O₄. *Journal of Physics of the Earth*, 38 (1), 19-55.
- Yong, W., Botis, S., Shieh, S.R., Shi, W., and Withers, A.C. (2012) Pressure-induced phase transition study of magnesiochromite (MgCr₂O₄) by Raman spectroscopy and X-ray diffraction. *Physics of the Earth and Planetary Interiors*, 196–197(0), 75-82.
- Yu, Y., and Gee, J.S. (2005) Spinel in Martian meteorite SaU 008: implications for Martian magnetism. *Earth and Planetary Science Letters*, 232(3–4), 287-294.